

DISSERTATION ZUR ERLANGUNG DES DOKTORGRADES DER FAKULTÄT FÜR CHEMIE UND
PHARMAZIE DER LUDWIG-MAXIMILIANS-UNIVERSITÄT MÜNCHEN

ON STRUCTURING AND SENSING
WITH METAL-ORGANIC FRAMEWORKS:
FROM MOLECULES
TO STRUCTURAL COLOR

Annekathrin Ranft

aus

München, Deutschland

2015

ERKLÄRUNG

Diese Dissertation wurde im Sinne von §7 der Promotionsordnung vom 28. November 2011 von Frau Prof. Dr. Bettina Lotsch betreut.

EIDESSTATTLICHE VERSICHERUNG

Diese Dissertation wurde eigenständig und ohne unerlaubte Hilfe erarbeitet.

München, 24.03.2016

Annekathrin Ranft

Dissertation eingereicht am	20.11.2015
Erstgutachterin	Prof. Dr. Bettina Lotsch
Zweitgutachter	Prof. Dr. Achim Hartschuh
Mündliche Prüfung am	15.12.2015

Wenn du nicht irrst, kommst du nicht zu Verstand;
Willst du entstehn, entsteh´ auf eigne Hand!

J. W. Goethe, *Faust. Der Tragödie zweiter Teil*, Zweiter Akt.

DANKE!

Für die zurückliegende, besondere Zeit möchte ich mich ganz herzlich bedanken:

Bei meiner Doktormutter Bettina Lotsch; für das schöne Forschungsthema, für deine Unterstützung sowohl bei Problemen als auch durch die häufig gebotenen Gelegenheiten zum wissenschaftlichen Austausch (viele Tagungsreisen!), und für die ansonsten freie Hand beim Forschen.

Bei meinem Prüfungskomitee, bestehend aus Achim Hartschuh, Dirk Johrendt, Konstantin Karaghiosoff, Wolfgang Schmahl und Christian Ochsenfeld; für ihre Zusage zur Teilnahme an der Prüfung und für die angeregte Diskussion meiner Arbeit.

Bei all meinen Arbeitskollegen in München und in Stuttgart, insbesondere meinen BFF-Kolleginnen Ida Pavlichenko und Katharina Schwinghammer; dafür, dass ich mich seit dem 1. Tag im Arbeitskreis Lotsch wohl gefühlt habe und ich wundervolle Momente mit euch erleben durfte.

Bei meinen Praktikanten Frederik Haase, Sophia Betzler, Alberto von Mankowski, Julia Stanek, Berenice Jahn, Yinghong Hu, Maximilian Lamothe, Anna Siodmak und Laura Nichols; für die tolle Zusammenarbeit mit euch, die mit Sicherheit den größten Teil meiner Forschungsergebnisse ermöglicht hat.

Bei meinen Kooperationspartnern, allen voran Felicitas Niekkel, Polina Davydovskaya und Florian Hinterholinger; für ihre Ausdauer und Unterstützung beim Publizieren, für ihren Arbeitseifer und für die netten Gespräche auch außerhalb der Arbeit.

Bei allen Mitgliedern der Nachbar-Arbeitskreise, insbesondere Christian Minke, Tina Reuther, Wolfgang Wunschheim und Thomas Miller (für die technische Unterstützung), Catrin Löhnert und Olga Lorenz (für eure Hilfsbereitschaft in allen sozialen Bereichen), Erwin Wiesenmayer, Franziska Hummel, Alesja Ivanova und Halina Dunn (für eine schöne Zeit im Labor und außerhalb dessen) und Dajana Durach (die mir beim Drucken dieser Arbeit Beistand geleistet hat).

Bei Cristoph Hohmann; für seine Kreativität und die gute Zusammenarbeit beim Erstellen unseres Covers für das Nanopartikel-Paper.

Bei meinen Freundinnen Ellen Broda, Veronika Weiß, Stefanie Riedt, Monika Beirer, Katharina Will, Tanja Ossiander und Diana Gabriel, und bei meinen Lieblingskollegen Christian Ziegler und Linus Stegbauer; dafür, dass sie trotz langer Seh-Pausen und jetzigem Berufswechsel immer noch für mich da sind. Auf dass wir uns auch weiterhin gegenseitig unterstützen!

Bei meinen neuen Arbeitskollegen aus dem Deutschen Museum, allen voran Daniela Schneevoigt und meine Mit-Volos Melanie Saverimuthu, Franca Langenwalder, Lena Bockreiß, Carola Dahlke, Andreas Hempfer, Neslihan Becerici-Schmidt und Helene Hoffmann; für ihr Mitfiebern auf die Prüfung, das Feiern danach und die schöne Zeit, die wir miteinander im Arbeitsalltag verbringen.

Bei meiner tollen Familie: Thomas, Sabine, Susu, Lala, Britta und Frida; bei meinem liebsten Dodo; und bei seiner ganzen Familie; für eure jahrelange Unterstützung, für die Gespräche, für euren Glauben an die Durchführung dieser Arbeit, für die Spaziergänge, für die schönsten Wochenenden mit Erholen, Spielen, Essen!

1 INTRODUCTION

1.1 HIERARCHY AND EMERGENCE: ORDER IN NATURE AND SYNTHETIC CHEMISTRY

1.1.1 Materials and Voids

Nature uses a number of engineering strategies which have blossomed into some remarkable properties, such as the “lotus effect” referring to water-repellant leaves.¹ In many cases, the origin of these properties may be traced back to the material’s *structure* and *morphology* (i.e. patterned surfaces and hierarchical organization of the constituting components) rather than on its particular *composition*. In structured systems, each level represents the building units for the next higher level thus leading to an overall complex architecture. – In philosophy, biology and physics, among other disciplines, hierarchical organization is discussed as a “self-organized” process which is associated with the development of properties called “emergent”; that is, the properties found at one hierarchical level are present only because of the appropriate arrangement and interplay of all sub-levels.² Moreover, emergent properties are argued to be *synergistic* phenomena different from simple *results*:^{2,3} For instance, a single *letter* (a, b, ...) is characterized only by a particular sound and for being a building unit for the next higher level (a *word*). The new level, however, is now additionally fashioned with an individual *meaning* (for a specific group of humans) which seems to be not simply reducible to the plain linking of some letters. Being a central theme for diverse sciences, Aristotle condensed this phenomenon into the famous phrase: “The whole is something over and above its parts, and not just the sum of them all...”.²

1 Introduction

In natural matter such as bones, wood and mollusk shells, the hierarchical arrangement is believed to allow for controlling mechanical and other properties, depending on the interaction of all levels of organization.⁴⁻⁷ For instance, glass is widely used in nature as a building material, despite its apparent fragility. To strengthen the toughness of this material, nature has evolved effective means such as in the glass sponge *Euplectella* sp. (**Fig. 1**): In total, seven different hierarchical levels were identified using scanning electron microscopy, ranging from the nano- to the macroscale.⁸ The first level is composed of consolidated silica nanospheres (50–200 nm) deposited around a protein filament (**Fig. 1i**). The low strength of SiO₂ is balanced at the next structural levels: According to the authors,⁸ organic interlayers in the laminated spicule structure (**Figs. 1g and h**) are likely to prevent cracking events, while the packing of slightly different spicules (**Fig. 1f**) seems to allow for a larger defect tolerance than for the individual fiber. The complexity of the entire skeleton (**Fig. 1a**) shows impressively how inherently poor building materials may be improved through hierarchical structuring. Moreover, the seven identified levels of the sponge represent fundamental construction strategies such as laminated structures, bundled fibers and diagonally reinforced square-grid cells.⁸ Biological materials and their design principles are therefore a constant inspiration source for engineers to fabricate nature-like materials: This way, existing engineering concepts may be improved and newly emerging issues may be faced, such as the need for adapting to environmental changes.⁹⁻¹⁴

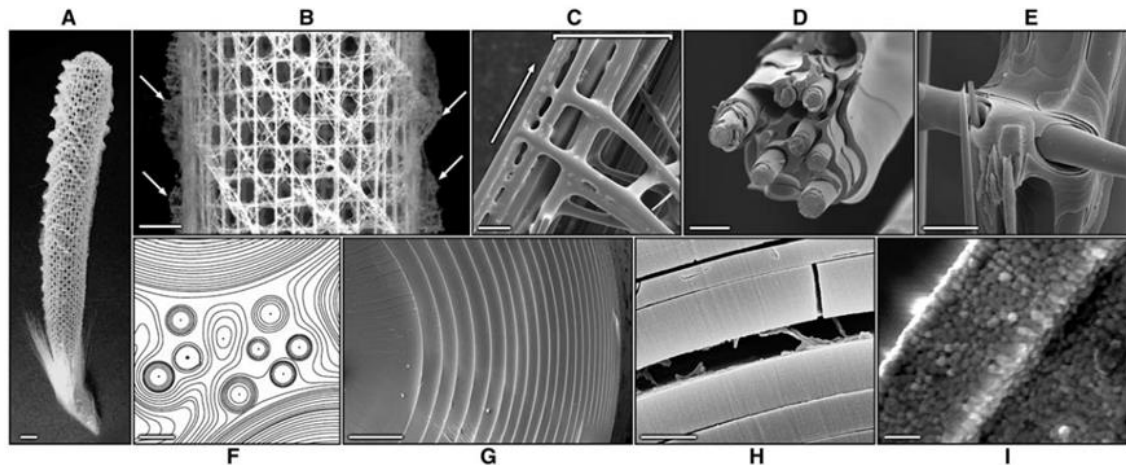


Figure 1. Hierarchical structuring in nature by the example of the skeletal system of *Euplectella* sp. (a) Photograph of the skeleton. (b) Square-grid lattices in the cage structure with diagonal elements. (c) Strut composed of multiple spicules. (d) Single beam with ceramic fiber-composite structure. (e) Junction area with laminated silica layers. (f) Cross-section through a spicular strut. (g) Cross-section through a single spicule. (h) Fractured spicule revealing an organic interlayer. (i) Consolidated nanospheres. – Scale bars: (a) 1 cm, (b) 5 mm, (c) 100 μm , (d) 20 μm , (e) 25 μm , (f) 10 μm , (g) 5 μm , (h) 5 μm , (i) 500 nm. Reproduced from ref. 8. Reprinted with permission from AAAS.

1 Introduction

Successful translation of bio-inspired ideas into our engineering world requires a careful analysis of structure–function relationships in natural tissues.⁹ Apparently, biological materials allow for an enormous functional range including the interaction with the environment (e.g. capture of light, metabolism, adaptation to changing conditions), movements and growth, or withstanding mechanical forces. Nevertheless, relatively few constituent elements are used in nature as basis for either (inorganic) minerals, (organic) polymers or composite structures;^{13,15} these are apparently sufficient for covering all required functions. For engineers, by contrast, the range of choice of elements is far greater (**Fig. 2**); while, however, ceramics and polymers are not the first choice of an engineer to build strong and robust structures, nature uses them to build skeletons.¹⁵ In biological designs, a few basic concepts exist from which engineers can learn including growth, hierarchical structuring, and adaptation to external conditions (e.g. self-healing).^{5,9}

A nearly pervasive feature found in natural materials is the complex structuring which results from a rather dynamic strategy in material fabrication (**Fig. 2**): Instead of using a fixed design (as in the case for engineering materials), the material is *grown* according to its genetic code, which allows for more flexibility.⁹ According to ref. 9, this strategy permits, on the one hand, adaptation to a function without the need for changing the complete fabrication strategy (e.g. a branch can grow in different directions as a response to adverse conditions). On the other hand, natural materials are thus capable of withstanding and adapting to different environments (bones carry us a whole lifetime!) by retaining its strength even in damaged states.^{7,16} It thus seems plausible that the particular way in which the components are arranged in space is much more important than the material itself used to build the structure (e.g. calcite, aragonite, apatite or silica as mineral parts in various tough materials).⁴

In hierarchically structured materials, empty space such as pores, channels and cavities, is a common feature and may also serve multiple functions.¹³ For example, many bird skeletons possess hollow bones, thus leading to very low body weights; flying birds, in particular, seem to have more hollow bones (i.e. not filled with marrow; see also **Fig. 3a**) than flightless birds (e.g. penguins) or diving birds, where a higher density skeleton may help to propel them through water.¹³ Other biological examples with porous structures are wood, diatoms and sponges, honeycombs or lung tissue;^{5,13} in each case, the emergence of porosity enables the material to fulfill characteristic functions (e.g. gas exchange in human lungs). – Form–function principles found in nature’s materials have ultimately triggered the fabrication of biomimetic replicas: Lightweight driven architectures can be found, for

1 Introduction

instance, in the design of the Eiffel tower. Artificial inverse opal structures which resemble honeycombs (**Fig. 3b**) are attractive for the development of smart materials with multiple functions (e.g. guest accommodation or enhanced transport properties).¹⁹ The distribution of size, shape and organization of the pores is directly related with the properties of the material and its capability of carrying out a specific function. In the special case of inverse opals, novel qualities may emerge from its ordered structuring which are unrelated to the formerly named ones, that is, for instance: vivid coloration (see **chapter 1.2**).¹⁹

<p style="text-align: center;"><i>Biological material</i></p> <p style="text-align: center;">light elements dominate: C, N, O, H, Ca, P, S, Si ...</p> <p style="text-align: center;">growth by biologically controlled self-assembly (approximate design)</p>	<p style="text-align: center;"><i>Engineering material</i></p> <p style="text-align: center;">large variety of elements: Fe, Cr, Ni, Al, Si, C, N, O ...</p> <p style="text-align: center;">fabrication from melts, powders, solutions etc. (exact design)</p>
<p>hierarchical structuring at all size levels</p>	<p>forming of parts and microstructuring of the material</p>
<p>adaption of form and structure to the function</p>	<p>selection of material according to function</p>
<p style="text-align: center;">(re-)modelling & healing: adaption to changing environmental conditions, self-repair</p>	<p style="text-align: center;">secure design (considering possible maximum loads or fatigue)</p>

Figure 2. Building blocks and fabrication modes that are used by nature to create material (upper left side) in comparison to an engineer's approach (upper right side). Due to the unequal proceedings, different strategies have to be pursued to achieve the desired functionality (bottom levels). Adapted from ref. 9.

The key issue for the artificial synthesis of porous structures is how to template the pores, and how to order and shape them.^{20,21} In the fabrication of biomimetic replica, biotemplate-based strategies may serve as proof-of-principle experiments, as they allow for convenient duplication of complex biological structures.^{22,23} Basically, a biomaterial (e.g. a butterfly wing) is used as a sacrificial template, and precursors (vapor, liquid or solid) are deposited on or infiltrated into the template. Replica or inverse replica are obtained after removal of the template (e.g. by heat treatment).²² Non-biotemplate approaches, by contrast, provide a higher controllability and can allow for the generation of structures not seen in nature. Both top-down (such as lithography or nanoimprinting) and bottom-up methods can be used, or

1 Introduction

a combination of both to achieve more complex structures.^{22,23} Liquid-phase deposition is such a commonly used bottom-up technique for the preparation of thin films and multilayers.^{12,24-26} It implies the preparation of a colloidal suspension, followed by film patterning through self-assembly,²⁷ and heat treatment for solvent removal.

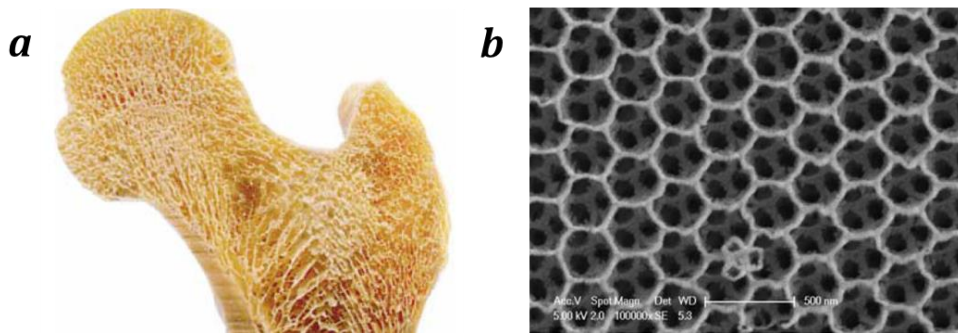


Figure 3. Porosity in a femoral head (a), and in an artificial inverse opal structure (b) serving different functions. (a) © 2002 WILEY-VCH Verlag GmbH & Co. KGaA, Weinheim. Reproduced with permission from ref. 17; (b) © 2007 Elsevier Ltd. Reprinted with permission from Elsevier and adapted from ref. 18.

The pores of template-driven structures are characterized by the dimensions of the respective template and may range from the nano- to macroscale. Generally, voids are classified as either micropores (smaller than 2 nm), mesopores (2–50 nm) or macropores (larger than 50 nm).²⁸ Sacrificial templates can be micelle forming agents such as surfactants and block copolymers,^{11,21} or polymeric beads which are available in a broad size range.^{29,30} The general concept of non-biotemplating strategies relies on the preparation of a solution containing the inorganic precursors and the templating agents (thus allowing for microphase separation); this is then processed in order to define the macroscopic shape of the final material (films, powders, monoliths, fibers etc.).³¹ For films, processing is typically achieved *via* self-assembly through evaporation of the solvent.^{26,27} Mixed porous structures may be obtained, if several strategies are coupled such as the use of both nanocrystals and structure-directing polymers in a solvent. During solvent evaporation the particles regularly assemble with respect to the polymer micelles, and after thermal processing, ordered frameworks are obtained with pores in the meso- to macrorange; the pore walls are built up from the particles and thus feature textural microporosity.³²

Micropores can be intrinsically present in both natural and artificial materials as molecular cavities such as in zeolites, which have already found their way into industrial processes, and the rather new class of metal-organic frameworks (MOFs). The latter are inorganic-organic hybrid materials comprised of single metal ions, or metal oxo clusters linked by organic ligands through coordination bonds.³³⁻³⁵ As the strength of these bonds is rather weak and, hence, their formation reversible, eventually well-defined structures are obtained in terms of geometry and crystallographic parameters. During the synthesis of a MOF, solvent molecules, excessive building blocks, or auxiliary agents may be trapped in the MOF pores: In most cases, such guest species may be removed through simple heat treatment or pressure reduction, thus leading to permanent porosity.³⁶ Synthetic zeolites and MOFs have thus attracted great attention owing to the presence of these nanocavities and their potential applications in gas storage, adsorption, separation, heterogenous catalysis or molecular sensing.^{37,38} In comparison to zeolites, MOFs are synthesized under rather mild conditions: Typically, a self-assembly reaction is initiated between a metal source and the organic linkers, which often proceeds in a one-step solvothermal reaction, and the cavities are usually formed without the need for any auxiliary templates.³⁶ Consequently, MOFs represent promising materials in terms of processability, flexibility, structural diversity and geometrical control;³⁷ in the following, all of these qualities are discussed in more detail, starting with the most characteristic one: structural variability.

1.1.2 Metal-Organic Frameworks

Beside zeolites, MOFs exhibit one of the highest degrees of structural flexibility. The dimensions of the pore system and other structural properties such as surface area, crystal density and rigidity of the network are controllable by choosing the “right” metal source and ligand (termed “reticular synthesis”). Zeolites, by contrast, are characterized by more rigid tetrahedral oxide frames (held through covalent bonds) that are rather difficult to alter, and compositionally limited.³⁶ The MOF backbone also allows for facile modification of the pore structure, e.g. by introducing functional groups.^{39,40}

There are currently a few approaches to the synthesis of new MOF structures, according to ref. 41:

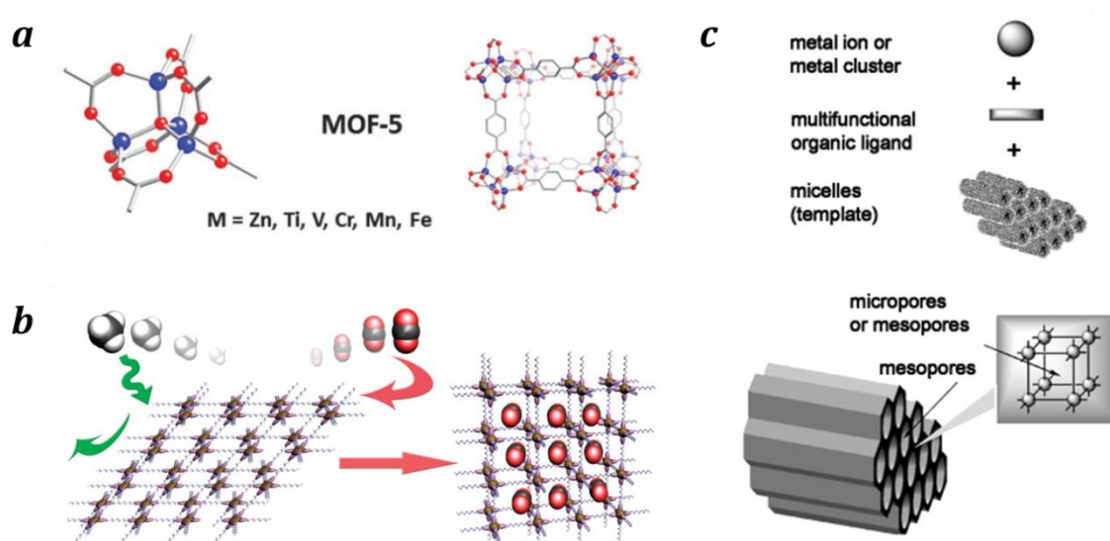


Figure 5. A choice of different MOF classes. (a) Metal oxo cluster and lattice structure of MOF-5 (blue: metal, red: oxygen, grey: carbon), which may be built up from a variety of different metal ions. (b) Schematic illustration of selective gas adsorption in a flexible MOF, showing guest-dependent structural changes. (c) Formation of a mesostructured MOF assembled from metal ions and organic ligands in the presence of surfactant micelles as supramolecular templates. The mesopore walls are constructed from the MOF which itself can feature micro- and/or mesopores. (a) Reproduced with permission and adapted from ref. 45 – Published by The Royal Society of Chemistry; (b) Reproduced from ref. 36 with permission of The Royal Society of Chemistry; (c) © 2008 Wiley-VCH Verlag GmbH & Co. KGaA, Weinheim. Reproduced with permission and adapted from ref. 37.

1) Introduction of functional ligands, either directly or *via* post-synthetic modification. For the latter, typical examples include the formation of amide and urea linkages *via* reaction of $-\text{NH}_2$ with appropriate target molecules (acetic anhydrides, isocyanates);⁴¹

2) Isomorphous structures of a certain crystal structure type (**Fig. 5a**). This approach is based on the integration of either metal ions with the same charge or coordination environment, or different ligands with the same denticity, to achieve similar structure types (e.g. the MIL-53 or MIL-101 families⁴²);

3) Isorecticular synthesis. By introducing ligands with the same denticity but different lengths of their backbones, the pore dimensions may be varied (e.g. the IRMOF or UIO-66 families^{43,44});

4) Hybridization (or “defect engineering”), meaning the modification of parent host structures. Hybridization can include mixing at the atomic scale (i.e. the introduction of more than one type of metal/ligand into the host MOF structure, or partial replacement of original building blocks^{45,46}), or the formation of two (or more) distinct phases in so-called

1 Introduction

core-shell heterostructures.⁴⁷ A third class of hybrid MOF structures accommodates functional guests in their pores such as, for instance, enzymes.⁴¹ The development of hybridization strategies may be rationalized by the observation that some desired structures are not accessible by reacting the appropriate building blocks due to steric or electronic constraints.⁴¹

MOF structures can be produced also with differing flexibility degrees ranging from rigid MOFs which are comparatively robust and feature permanent porosity, to rather dynamic ones.³⁶ These are capable of responding to external stimuli (e.g. guest molecules) through more or less pronounced structural transformations (**Fig. 5b**).^{36,48,49} Such tunable porosity, as well as usually large surface areas, and reasonable thermal stability make MOFs potential candidates for many different applications including gas storage, separation, and sensing. – In industry, for instance, adsorption-based separation processes are important to remove a certain gas from a mixture (e.g. CO₂ removal for fuel cell technology) or for purification purposes.³⁶ Principally, gas separation is controlled by the adsorption capacity and selectivity of an adsorbent. In zeolites and rigid MOFs, one or more of the following mechanisms are most likely to occur, according to ref. 36:

- 1) Size and/or shape exclusion (distinct components are prevented from entering the pores, while others are able to pass), termed *molecular sieving effect* or *steric separation*;
- 2) Different adsorbate–surface or adsorbate packing interactions (preferential adsorption), termed *thermodynamic equilibrium effect*.

(Besides, other adsorption mechanisms are discussed such as the *kinetic* and the *quantum sieving effect*.)³⁶ For the former (molecular sieving), the cross-sectional size and the shape of the gas molecule determine the separation process. Hence, restricted small pores may favor molecular sieving to occur, which can be achieved, for instance, by using rather short or bulky ligands.³⁶ (Note that adsorbent selection is apparently a complex problem: While larger pores are in favor for allowing guest molecules to be transported to the interior of the material, the opposite may be desired to achieve good separation efficiency.³⁷) – In terms of preferential adsorption, the interaction strength between adsorbate and adsorbent becomes crucial for separation: This is determined by polarizability, magnetic susceptibility, or permanent dipole moments, as well as by weak interactions (hydrogen or pi-bonds).³⁶ In addition, the presence of uncoordinated nitrogen atoms or metal sites in the MOF pores may affect the interaction strength between the MOF and the target molecule.^{36,50} There are a

couple of MOFs known to have only very small pores which, however, may expand when exposed to certain gases and/or at specific threshold pressures (dubbed *gate opening*): This way the entrance of a guest molecule to the MOF interior may be facilitated e.g. through a favorable adsorbate–surface interaction.^{36,51}

In many industrial applications, accessible interfaces and specific morphologies play an important role for the performance of a material, which on first glance may appear non-relevant to the desired qualities (e.g. selectivity for sensing purposes). As such, gaining control of size, shape and morphology is mandatory in order to fashion MOFs or other porous materials according to a desired application. A wide range of different synthesis routes render MOFs now accessible within a broad length scale from microsized crystals to nanoparticles. For instance, MOFs can be processed in the form of thin films suitable for sensing applications: Here, it is found that decreased film thicknesses as well as porous and particulate morphologies allow for improved sensing properties as the analyte can infiltrate the film more easily, and the surface area and activity are increased.³⁷ Thin films can be achieved, for instance, by spin- or dip-coating protocols^{12,24,52,53} requiring the dispersion of uniformly sized nanoparticles in a volatile solvent. Examples for the preparation of MOF nanoparticles include solvothermal synthesis, either without⁵⁴ or with the assistance of ultrasound/microwave heating,^{55,56} or even room temperature synthesis.⁵⁷ Besides, the use of capping agents⁵⁸ or ligands built in a similar fashion to the linking precursor (“coordination modulation”)^{53,59} has been found to affect both the MOF’s size and morphology.

MOF structures, however, are not solely restricted to the microporous regime: Supramolecular template strategies can be used to create mesostructured frameworks (**Fig. 5c**). In the presence of surfactant-directed micelles, a mesoporous structure may form upon the self-assembly of the MOF from metal ions and the organic ligand. Nanocrystalline domains of the MOF constitute the walls of the mesoporous structure,³⁷ similar to the strategy reported earlier for hierarchically porous materials. – Besides defined environments for guest adsorption, structuring of MOFs can pave the way to other interesting features and applications, such as the emergence of “structural coloration”: Here, the particular ordering of the MOF crystals can act as a diffraction grating for visible light thus leading to intense reflections. Structural coloration is a common theme in nature’s materials, e.g. on the skin and wings of animals, and has already found its way into several biomimetic optical devices;¹² all of which will be discussed in the next chapter.

1.2 BIO-INSPIRATION: FROM COLOR TO OPTICAL DEVICES

1.2.1 Color Generating Principles

Colors in nature, especially the vivid ones found in peacock feathers or pearlescent mollusk shells, are a fascinating subject for both scientists and non-scientists. In the last few centuries, researchers began to explore how colors were produced in nature, and what kind of role coloration plays among animals. Beside intraspecific communication and sexual selection, the coloration may help to avoid predation or serve even non-communicative functions such as enhancing vision, or strengthening integumentary tissues (compare also with *chapter 1.1*).⁶⁰ Colors in animals are typically achieved through pigments or through structural coloration, or by a combination of these mechanisms.⁶⁰ Besides, some animals use bioluminescence as light source, which is particularly common among marine organisms in the open or deep sea.⁶¹ – Pigments interact with light by selectively absorbing certain wavelength ranges. For example, natural orange colorations are typically achieved through carotenoid pigments which absorb light in the blue part of the electromagnetic spectrum.⁶⁰ Nevertheless, carotenes can also come in blue or black if they are bound to proteins. Lobsters, for instance, are black when alive, but turn red when they are cooked. This color change is attributed to the heat-induced denaturation of the protein part in the pigment, leaving visible the red color of the carotene when the lobster is boiled.⁶² Melanins, by contrast, absorb light across the entire visible range, which results in black or brown colors (as, for example, in the human skin).

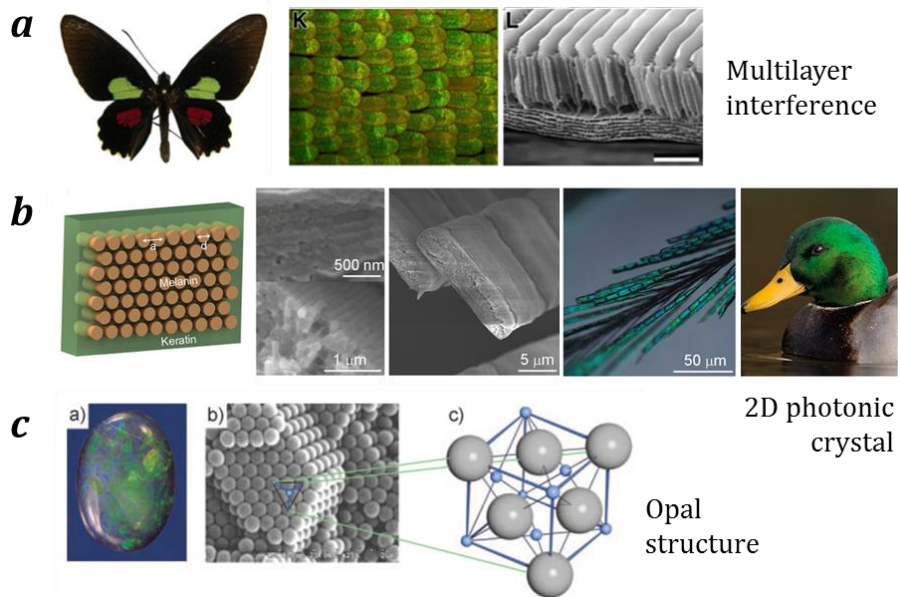


Figure 6. Structural coloration in nature and underlying optical principles. (a) The dorsal forewings of *Parides aeneas bolivar* have green-colored areas, which are attributed to the underlying multilayer structure in the scale lumen. (b) Hexagonal arrays of melanin rods embedded in a keratin matrix form a 2D photonic crystal which causes the green-blueish color of the duck feathers. (c) The color effects of a natural opal are caused by the underlying nanostructure which can be described by a fcc lattice. (a) © 2014 Wilts et al.; licensee BioMed Central Ltd. Reproduced with permission and adapted from ref. 63; (b) Reproduced and adapted from ref. 64; (c) © 2009 Wiley-VCH Verlag GmbH & Co. KGaA, Weinheim. Reproduced with permission from ref. 65.

In contrast to pigmentary colorations, structural colors are produced when light physically interacts with structures on the nanoscale: More specifically, the light is controlled by the interfaces between materials that differ in their individual refractive indices (RIs). Here, three different processes may occur: a) interference, b) diffraction or c) scattering.^{60,66} – Typical structures for interference-based colors include thin films and multilayer structures (**Fig. 6a**; see **Figs. 7a** and **b** for the respective optical mechanisms). The interaction of light with a multilayer can be described as follows: A wave propagating in the stack undergoes reflection at each interface for a defined wavelength range (**Fig. 7b**); the observed color is a product of the interference of all reflected beams and depends on the periodicity of the stack, i.e. the optical thickness of a bilayer.

Diffraction gratings are regularly ordered surfaces which disperse light in different directions (**Fig. 7c**), depending on the wavelength of light striking the surface and the spacing of the grating.⁶⁰ Examples in our everyday life include the parallel lines in a very fine cloth, or the pits and lands on optical storage disks. The processes of interference and diffraction can be combined to produce more complex optical effects, such as, for instance,

in the multilayered structure of the beetle *Chlorophila obscuripennis*. Here, the multilayers form ridges and pits, which interact differently with incident light and thus generate a mixed overall color appearance of the beetle.⁶⁷ The colors of the butterfly in **Fig. 6a** are a result of both structural and pigmentary coloration, and show angle-dependence of the reflection (termed *iridescence*).⁶³ – Scattering of light represents a different type of color generation, in comparison to the processes described above: Here, the color is caused by a rather irregular structuring (**Fig. 7d**).⁶⁶ The thus produced colors are usually less saturated, more diffuse and generally non-iridescent (see the blue color of the sky).⁶⁰ Scattering is also the main optical mechanism for generating whiteness in nature, including the white appearance of milk, or the scales of some butterflies, by scattering all visible wavelengths.²²

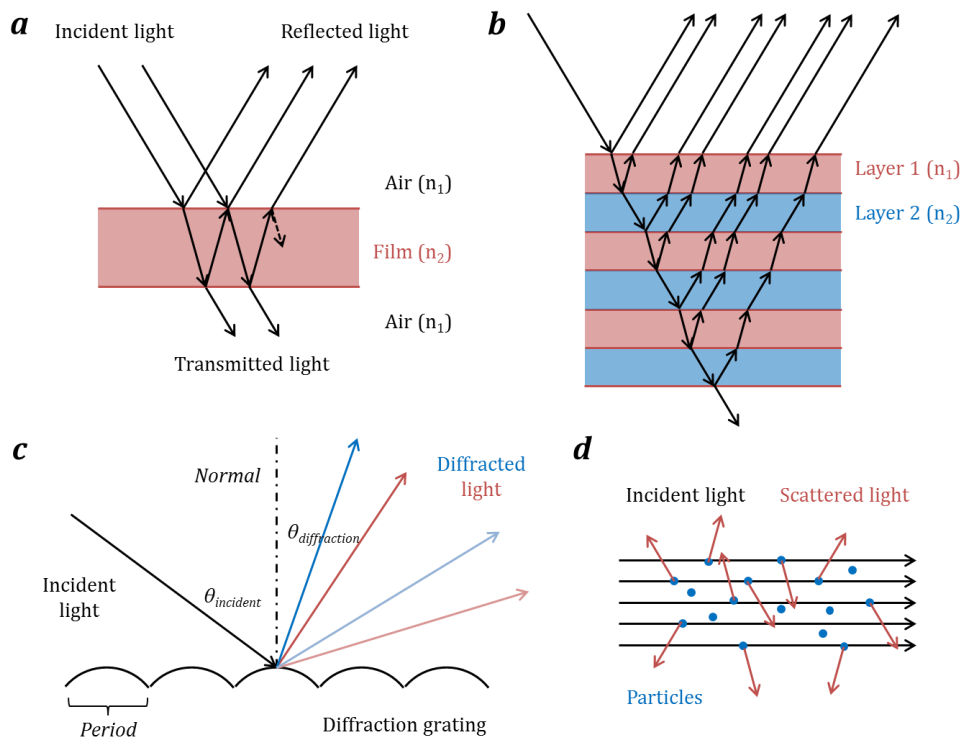


Figure 7. Physical basis of structural colors. (a) Thin film interference; (b) multilayer interference (materials with different RIs (n_1 , n_2) are marked by different colors); (c) diffraction grating dividing light into spectra (the dispersion is illustrated by blue and red arrows, and less saturated colors for the 2nd order spectrum); (d) scattering process. Adapted from ref. 68.

Among color-producing structures, so-called photonic crystals (PCs) are particularly attractive materials for controlling the qualities of light.⁶⁹ Basically, PCs can be regarded as crystal-like structures in the sense that they contain building blocks (e.g. thin films) arranged in a periodic pattern. Important parameters are the size (or thickness) of the

1 Introduction

periodic units (i.e. the lattice constants), and the variation in their RI in one, two or three dimensions (**Fig. 6**). The result is a distribution of energy levels with allowed modes and forbidden wavelength bands (occurrence of band gaps), similar to electronic semiconductors. In the special case of visible light, this phenomenon generates very intense colors resulting from the interference of the “forbidden” (and thus reflected) light frequencies. A prominent example for exhibiting this structural color effect is the gemstone opal (**Fig. 6c**). Its vivid coloration arises from its three-dimensional nanostructure consisting of densely packed, monodisperse silica spheres.⁶⁵ Here, the relation with “crystals” becomes even clearer as the ordering (or packing) of the spheres can be described similarly to regular crystal lattice arrangements (e.g. fcc). – A way more simple PC structure is a multilayer consisting of alternately stacked materials in the form of thin films, and with differing RIs (**Figs. 6a** and **7b**). 1D PCs are also referred to as *Bragg stacks* (BSs), as the interaction of the stack with light can be appropriately described through a modified version of the Bragg law (i.e. the Bragg-Snell law):⁷⁰

$$m\lambda = 2d(n_{\text{eff}}^2 - \sin^2\theta)^{1/2}$$

Here, m is the diffraction order, λ is the wavelength of the reflected light, d is the physical thickness, n_{eff} is the mean effective RI and θ is the angle of incident light. If not combined with other color-generating processes, PCs typically show iridescent behavior which is particularly appealing in 2D and 3D structures.

Iridescence (i.e. a change in color with an altered viewing angle) is a common feature in nature, ranging from minerals to living organisms: Many iridescent colorations are observed in arthropods and molluscs – e.g. on the wings, bodies or shells of flies and bees, in butterflies and beetles, or for nacre – whereas fewer examples exist among vertebrates.⁶⁰ In some birds, keratin and melanin are appropriately arranged in the feather barbules to achieve the interaction with visible light (see also **Fig. 6b**).⁶⁴ – Changes in the viewing angle can produce drastic changes in hue and intensity. The reflectance spectra can in fact exceed 100 % reflectance (for an optimal viewing angle) when measured relative to a diffuse white standard;⁷¹ when the angle is changed, the iridescence can disappear, leaving visible only the color produced by underlying pigments (e.g. black melanins).⁶⁰ This specific feature of iridescent coloration could serve animals in a number of ways. For instance, birds may direct their display more specifically to an intended receiver (e.g. to attract the attention of a female) by showing the bright color,⁷² while a potential rival might be faced by the less brilliant coloration. Another feature of structural colors is that the whole range of visible

colors can be produced, even short wavelengths (blue to violet), which are rarely known in pigmentary coloration.⁶⁰

As mentioned above, the origin of structural colors is related to the (nanoscale) dimensions and RIs of a structure. Variations in these characteristics will generally affect the final optical appearance; this feature, in turn, might allow an animal to alter its coloration in response to changes in its environment. For instance, the reed frog changes its color as a consequence of increasing temperatures (e.g. during dry seasons), which seems to help the frog for thermoregulation due to a higher overall reflectance.⁶⁰ – Similarly, one could use such strategies to also detect changes in the anthropogenic environment: Indeed, various artificial humidity sensors have already been realized inspired by natural role models and relying on optical detection. For instance, it was shown that paradise whiptails can change the color of stripes on their bodies within seconds under control of the sympathetic nervous system.²² Physiological experiments, mimicking these processes, achieved swelling and shrinking of the spaces between iridosphore plates upon changes in the osmotic pressure, which ultimately resulted in strong color shifts. Artificially generated nanostructures based on a hydrogel have shown to act in a similar way upon water adsorption.^{22,73}

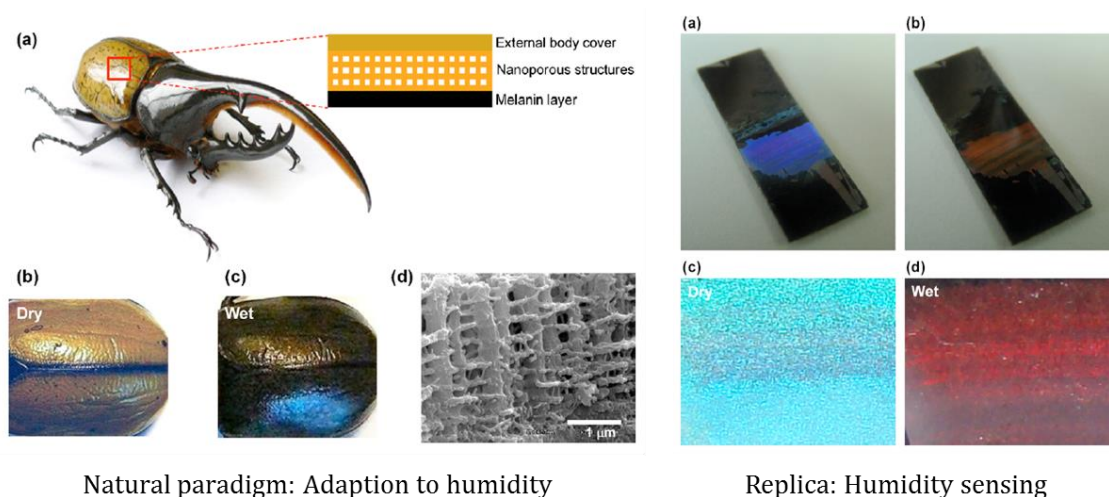


Figure 8. Color changes in natural and synthetic materials as a response to humidity variations. Left: The *Dynastes Hercules* (a) is greenish in a dry atmosphere (b). When exposed to a high level of humidity, the beetle's body turns black (c). (d) SEM image of the cuticle of the beetle. – Right: Photographs of the biomimetic sensor in dry state (a) and in wet state (b). Microscope images of the film confirm the change in color from blue-green (c) to red (d) with relative humidity. All images reprinted with permission from ref. 75. © 2010, AIP Publishing LLC.

1 Introduction

While these examples display stimuli-induced changes in the lattice constants of nanostructures (i.e. expansion/contraction upon heating or water adsorption), dynamic changes in the RI can be likewise imagined (e.g. through solvent or vapor infiltration). For instance, the color of the Hercules beetle (*Dynastes Hercules*) changes from iridescent olive green to black with changes in humidity (**Fig. 8**, left).⁷⁴ The beetle's elytra is composed of a porous internal structure which, at high humidity levels, is filled with water and thus causes the elytra to appear black. – Inspired by the Hercules beetle, biomimetic humidity sensors have been fabricated such as the film shown in **Fig. 8** (right).⁷⁵ Here, silica spheres were assembled to form a 3D colloidal crystal and infiltrated with a polymer solution; after exposure to UV light an inverse replica was obtained similar to the porous structure of the beetle's cuticle. The porous replica shows reflection peak shifts upon water infiltration which is attributed to a change in the effective RI.⁷⁵

Besides humidity, solvents and gases, a range of other stimuli can be imagined such as heat, stress, light, electric or magnetic fields.²² In comparison to conventional humidity sensors relying on electrical signals, optical readout schemes offer a convenient and fast alternative sensing mechanism as, for instance, no externally wired electronics are needed for measurements; besides, they do not afford complicated fabrication processes (compare with **chapter 1.1**).²² Moreover, optical sensors can in principle be adapted to any material that can be fashioned into thin films, multilayers and the like. The change in the optical properties can then be monitored by UV-Vis spectroscopy as the stimulus induces a shift in the position of the reflection spectrum.⁷⁶ Even more simple, the response can be detected by the naked eye (if the color change is significantly large), similar to the principle of indicator papers (see **Fig. 8**, right).⁷⁵

1.2.2 Sensor Performance Parameters

As in other sensors, the sensing performance of optical devices (e.g. selectivity, sensitivity, response time and detection limit) depends on which materials and how they are implemented in the sensor, namely their chemical composition and their “structuring” (morphology, size of the building blocks, surface area etc.). A range of strategies have been developed suitable to control these issues and therefore, to improve the sensor’s output. For instance, the selectivity of a sensing system may be greatly enhanced by the introduction of inherent functional materials such as the afore mentioned MOF structures (see **chapter 1.1**). In comparison to metal oxides which are commonly used as building blocks for thin films and PCs, they provide more possibilities for responding to a distinct chemical stimulus, namely size exclusion, tunable host-guest interactions and the option for post-synthetic modification.

An alternative strategy to increase the specificity towards certain analytes is the concept of combinatorial sensing: Here, the single sensor is replaced by an array of different sensors of which each responds to the analyte in a characteristic way. Since we deal with an optical readout scheme, digital images can be taken before and after analyte exposure, from which a difference profile is generated for each sensor (**Fig. 9a**). The combined response of all sensors provides – in the best case – a unique signal (i.e. a colorimetric fingerprint) which in turn can be used to identify a single analyte or to discriminate between similar complex mixtures (e.g. coffee aromas, see **Fig. 9b**).⁷⁷ Ultimately, principal component analysis (PCA) can be used which may allow for predicting whether an unknown sample shows similarities to already identified groups or not (**Fig. 9c**).⁷⁸

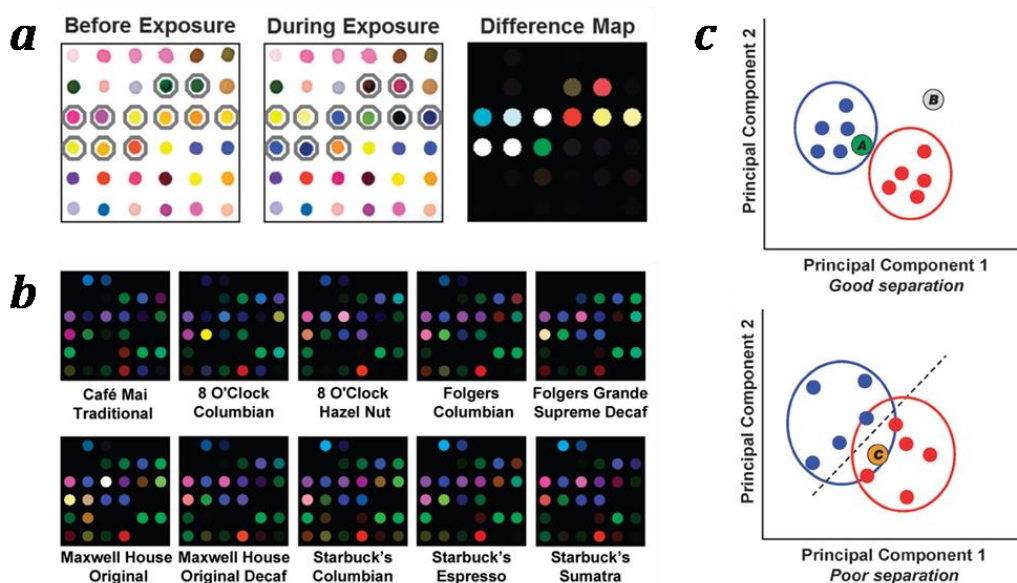


Figure 9. The concept of combinatorial sensing. (a) A colorimetric sensing array consisting of 36 different dyes is exposed to a gaseous analyte (here: ammonia). Digital images are taken before and after exposure, from which a difference map is generated. (b) Color difference profiles can be generated for a range of different analytes (here: ten commercial coffee aromas), representing unique colorimetric fingerprints for each investigated analyte. (c) Quantitative comparison of the difference maps can be done by principal component analysis (PCA), and can help to predict the identity of a sample. If a large separation exists among the sample classes (blue and red circle in the top image), it can be inferred that unknown samples either belong to a class (A, within the blue circle), or rather not (B, outside the circles). Using a dataset with poor separation (bottom), no unambiguous identification is possible. (a) Reproduced from ref. 78 with permission of The Royal Society of Chemistry; (b) Reprinted with permission from ref. 77. © 2010 American Chemical Society; (c) Reproduced and adapted from ref. 78 with permission of The Royal Society of Chemistry.

In order to facilitate the transport of molecules to the active components in the photonic architecture, films made of randomly oriented particles may be favoured over dense structures, as they provide a highly accessible pore system (textural porosity). This way, both the response time and sensitivity of the detection platforms could be enhanced (see **chapter 1.1**). – Along with the sensitivity, the limit of detection is linked to not only the chemical composition and microstructure of the film, but also the experimental conditions i.e. the resolution of the applied instrument and readout scheme. For the latter, the introduction of a so-called “defect layer” into the periodic structure has shown to provide an effective means to facilitate the detection of even small spectral changes; the defect produces a sharp band of allowed states in the photonic band gap which can be utilized for the precise determination of the optical response (**Fig. 10**, principle shown by the example of a regular $\text{SiO}_2/\text{TiO}_2$ BS, top images, and a similar stack with a SiO_2 defect layer, bottom images).⁷⁹

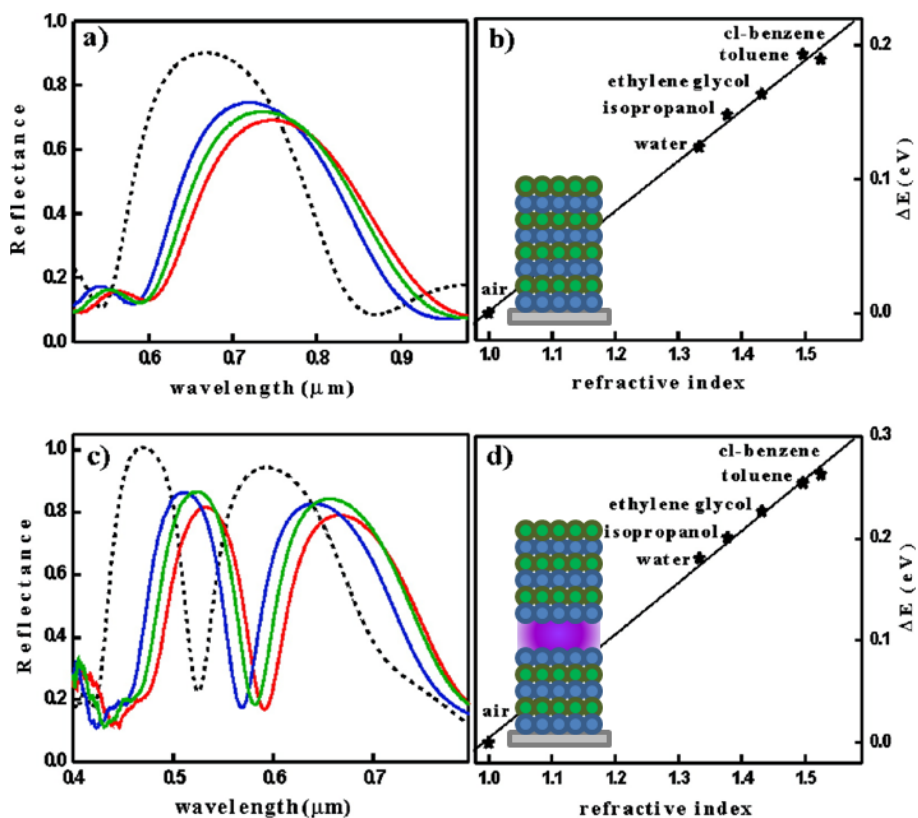


Figure 10. Introduction of defect layers in 1D PCs and solvent sensing. (a) Optical response of a regular $\text{SiO}_2/\text{TiO}_2$ BS infiltrated with different solvents (blue: water, green: ethylene glycol, red: Cl-benzene) in comparison to air (dotted line). (b) Spectral shifts measured for different solvents. (c-d) Optical response and measured spectral shifts for a BS with a sandwiched SiO_2 defect layer, infiltrated with the same solvents. Reprinted and adapted with permission from ref. 79. © 2008 American Chemical Society.

1.3 OBJECTIVES OF THIS THESIS

In *chapters 1.1* and *1.2*, the concepts of hierarchy and emergent properties have been introduced, namely defined porosity and structural coloration. The materials explored in this thesis and its contents are likewise based on a hierarchical order (**Fig. 11**): Inherently (micro)porous and functional MOF nanoparticles (1) are integrated into texturally (micro- and meso)porous thin films (2) and multilayers with submicron scale periodicity (3) *via* bottom-up assembly. By using interference-based readout (4), we aim for creating versatile detection platforms (5) with enhanced selectivity for different chemical stimuli. In the following, the objectives of this thesis and their organization in *chapters 2* and *3* are described in more detail.

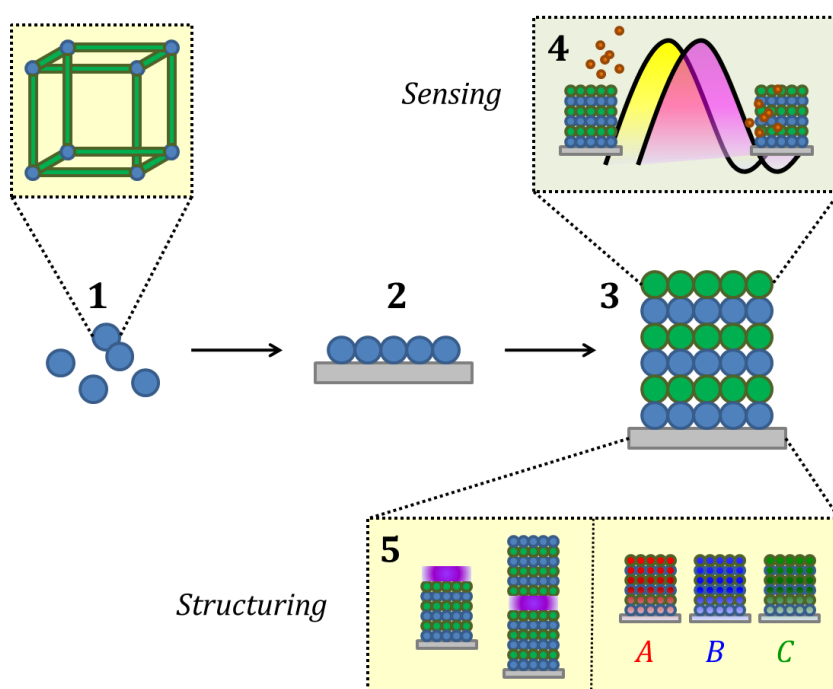


Figure 11. Objects of interest in this thesis. MOF nanoparticles (1) are integrated into thin films (2) and multilayers (3) *via* bottom-up assembly. The sensing performance of (3) is investigated by using an interference-based readout scheme (4). To increase the sensitivity and selectivity, the stack components and/or their order were varied (5; left: two defect structures; right: MOF-based BSs with differing MOF structures).

The fabrication of sensitive thin MOF films and multilayers requires the availability of nanosized MOF structures, and a preferably easy access *via* generally applicable strategies. In **chapter 2.1**, newly developed synthesis routes are discussed by the example of two prototypic MOF structures (HKUST-1, IRMOF-3). Downsizing of the MOFs is achieved by the addition of polymers and/or surfactants to the reaction solution thereby suggesting a mild and universal approach toward nanoscale MOFs. In addition, the formation of thin MOF films is demonstrated using stable colloidal suspensions of the MOFs, and the effective RI is determined being an important parameter in the design of photonic multilayers.

In **chapter 3**, the synthesis of various MOF-based PCs is demonstrated and the respective sensing properties are discussed. As a proof-of-concept, the integration of a MOF thin film into photonic multilayers is shown for the first time (ZIF-8/TiO₂) and for two different synthesis routes (nanoparticulate vs dense ZIF-8 films). The sensing performance of these platforms is demonstrated by vapor sorption measurements and *in situ* monitoring of the spectral response (**chapter 3.1**). – In our next attempt, we aim at enhancing the selectivity of nanoparticulate MOF-based BSs by introducing two additional MOF structures (HKUST-1, CAU-1) which differ in their individual sorption properties (i.e. polarity, pore sizes etc). The MOFs are integrated into the BSs either in single form (TiO₂/MOF), in combination with another MOF (MOF-1/MOF-2), or as multiple sensors in the form of an array (combinatorial sensing; **chapter 3.2**). – Finally, the introduction of ZIF-8 nanoparticles as a defect layer in 1D PCs is shown, either on top or sandwiched between regular SiO₂/TiO₂ BSs. The emerging optical properties are discussed for each architecture, and the sensing performance is surveyed in dependence on the stacking order (top vs sandwich) and morphology of the constituents (dense vs porous; **chapter 3.3**).

1.4 REFERENCES

- 1 H.C. Von Baeyer, *The Sciences* **2000**, *40*, 12-15.
- 2 P.A. Corning, *Complexity* **2002**, *7*, 18-30.
- 3 P.W. Anderson, *Science* **1972**, *177*, 393-396.
- 4 J.D. Currey, *Science* **2005**, *309*, 253-254.
- 5 P. Fratzl and R. Weinkamer, *Prog. Mater Sci.* **2007**, *52*, 1263-1334.
- 6 J.W.C. Dunlop and P. Fratzl, *Annu. Rev. Mater. Res.* **2010**, *40*, 1-24.
- 7 R.O. Ritchie, *Nat Mater* **2011**, *10*, 817-822.
- 8 J. Aizenberg, J.C. Weaver, M.S. Thanawala, V.C. Sundar, D.E. Morse and P. Fratzl, *Science* **2005**, *309*, 275-278.
- 9 P. Fratzl, *J. R. Soc. Interface* **2007**, *4*, 637-642.
- 10 K. Liu and L. Jiang, *Nano Today* **2011**, *6*, 155-175.
- 11 K.J.C. van Bommel, A. Friggeri and S. Shinkai, *Angew. Chem. Int. Ed.* **2003**, *42*, 980-999.
- 12 H.K. Raut, V.A. Ganesh, A.S. Nair and S. Ramakrishna, *Energy Environ. Sci.* **2011**, *4*, 3779-3804.
- 13 P.-Y. Chen, J. McKittrick and M.A. Meyers, *Prog. Mater Sci.* **2012**, *57*, 1492-1704.
- 14 C. Sanchez, H. Arribart and M.M. Giraud Guille, *Nat Mater* **2005**, *4*, 277-288.
- 15 U.G.K. Wegst, H. Bai, E. Saiz, A.P. Tomsia and R.O. Ritchie, *Nat Mater* **2015**, *14*, 23-36.
- 16 J.F.V. Vincent, *Proc. Inst. Mech. Eng. H J. Eng. Med.* **2009**, *223*, 919-939.
- 17 S.V. Dorozhkin and M. Epple, *Angew. Chem. Int. Ed.* **2002**, *41*, 3130-3146.
- 18 G.I.N. Waterhouse and M.R. Waterland, *Opal and inverse opal photonic crystals: Fabrication and characterization*, *Polyhedron* **2007**, *26*, 356-368.

1 Introduction

- 19 C.F. Blanford, H. Yan, R.C. Schroden, M. Al-Daous and A. Stein, *Adv. Mater.* **2001**, *13*, 401-407.
- 20 P. Innocenzi, L. Malfatti and G.J.A.A. Soler-Illia, *Chem. Mater.* **2011**, *23*, 2501-2509.
- 21 D. Wu, F. Xu, B. Sun, R. Fu, H. He and K. Matyjaszewski, *Chem. Rev.* **2012**, *112*, 3959-4015.
- 22 K. Yu, T. Fan, S. Lou and D. Zhang, *Prog. Mater. Sci.* **2013**, *58*, 825-873.
- 23 S. Sotiropoulou, Y. Sierra-Sastre, S.S. Mark and C.A. Batt, *Chem. Mater.* **2008**, *20*, 821-834.
- 24 N. Sahu, B. Parija and S. Panigrahi, *Indian J. Phys.* **2009**, *83*, 493-502.
- 25 K. Ariga, J.P. Hill and Q. Ji, *Phys. Chem. Chem. Phys.* **2007**, *9*, 2319-2340.
- 26 L. Mahoney and R. Koodali, *Materials* **2014**, *7*, 2697.
- 27 D.V. Talapin, *ACS Nano* **2008**, *2*, 1097-1100.
- 28 K.S.W. Sing, *Pure Appl. Chem.* **1985**, *57*, 603.
- 29 B. Hatton, L. Mishchenko, S. Davis, K.H. Sandhage and J. Aizenberg, *Proc. Natl. Acad. Sci.* **2010**, *107*, 10354-10359.
- 30 M.H. Lash, M.V. Fedorchak, J.J. McCarthy and S.R. Little, *Soft Matter* **2015**.
- 31 C. Sanchez, C. Boissiere, S. Cassaignon, C. Chaneac, O. Durupthy, M. Faustini, D. Grosso, C. Laberty-Robert, L. Nicole, D. Portehault, F. Ribot, L. Rozes and C. Sasseoye, *Chem. Mater.* **2014**, *26*, 221-238.
- 32 B.A. Helms, T.E. Williams, R. Buonsanti and D.J. Milliron, *Adv. Mater.* **2015**.
- 33 C. Janiak and J.K. Vieth, *New J. Chem.* **2010**, *34*, 2366-2388.
- 34 M. Eddaoudi, D.B. Moler, H. Li, B. Chen, T.M. Reineke, M. O'Keeffe and O.M. Yaghi, *Acc. Chem. Res.* **2001**, *34*, 319-330.
- 35 H. Furukawa, K.E. Cordova, M. O'Keeffe and O.M. Yaghi, *Science* **2013**, *341*.
- 36 J.-R. Li, R.J. Kuppler and H.-C. Zhou, *Chem. Soc. Rev.* **2009**, *38*, 1477-1504, <http://dx.doi.org/10.1039/B802426J>.

1 Introduction

- 37 L.-G. Qiu, T. Xu, Z.-Q. Li, W. Wang, Y. Wu, X. Jiang, X.-Y. Tian and L.-D. Zhang, *Angew. Chem.* **2008**, *120*, 9629-9633.
- 38 J. Perez-Ramirez, C.H. Christensen, K. Egeblad, C.H. Christensen and J.C. Groen, *Chem. Soc. Rev.* **2008**, *37*, 2530-2542.
- 39 S.M. Cohen, *Chem. Rev.* **2012**, *112*, 970-1000.
- 40 M. Lammert, S. Bernt, F. Vermoortele, D.E. De Vos and N. Stock, *Inorg. Chem.* **2013**, *52*, 8521-8528.
- 41 M.L. Foo, R. Matsuda and S. Kitagawa, *Chem. Mater.* **2014**, *26*, 310-322.
- 42 L. Hamon, C. Serre, T. Devic, T. Loiseau, F. Millange, G. Férey and G.D. Weireld, *J. Am. Chem. Soc.* **2009**, *131*, 8775-8777.
- 43 M. Eddaoudi, J. Kim, N. Rosi, D. Vodak, J. Wachter, M. O'Keeffe and O.M. Yaghi, *Science* **2002**, *295*, 469-472.
- 44 S.J. Garibay and S.M. Cohen, *Chem. Commun.* **2010**, *46*, 7700-7702.
- 45 P. Deria, J.E. Mondloch, O. Karagiari, W. Bury, J.T. Hupp and O.K. Farha, *Chem. Soc. Rev.* **2014**, *43*, 5896-5912.
- 46 H. Furukawa, U. Müller and O.M. Yaghi, *Angew. Chem. Int. Ed.* **2015**, *54*, 3417-3430.
- 47 K. Koh, A.G. Wong-Foy and A.J. Matzger, *Chem. Commun.* **2009**, 6162-6164.
- 48 F.-X. Coudert, A. Boutin, A.H. Fuchs and A.V. Neimark, *J. Phys. Chem. Lett.* **2013**, *4*, 3198-3205.
- 49 A. Schneemann, V. Bon, I. Schwedler, I. Senkovska, S. Kaskel and R.A. Fischer, *Chem. Soc. Rev.* **2014**, *43*, 6062-6096.
- 50 Q. Yang and C. Zhong, *J. Phys. Chem. B* **2006**, *110*, 655-658.
- 51 C. Gücüyener, J. van den Bergh, J. Gascon and F. Kapteijn, *J. Am. Chem. Soc.* **2010**, *132*, 17704-17706.
- 52 A. Demessence, C. Boissiere, D. Grosso, P. Horcajada, C. Serre, G. Férey, G.J.A.A. Soler-Illia and C. Sanchez, *J. Mater. Chem.* **2010**, *20*, 7676-7681.

1 Introduction

- 53 H. Guo, Y. Zhu, S. Qiu, J.A. Lercher and H. Zhang, *Adv. Mater.* **2010**, *22*, 4190-4192.
- 54 E. Haque, N.A. Khan, J.H. Park and S.H. Jhung, *Chem. Eur. J.* **2010**, *16*, 1046-1052.
- 55 N.A. Khan, I.J. Kang, H.Y. Seok and S.H. Jhung, *Chem. Eng. J.* **2011**, *166*, 1152-1157.
- 56 Z.-Q. Li, L.-G. Qiu, T. Xu, Y. Wu, W. Wang, Z.-Y. Wu and X. Jiang, *Mater. Lett.* **2009**, *63*, 78-80.
- 57 J. Cravillon, S. Münzer, S.-J. Lohmeier, A. Feldhoff, K. Huber and M. Wiebcke, *Chem. Mater.* **2009**, *21*, 1410-1412.
- 58 M. Ma, D. Zacher, X. Zhang, R.A. Fischer and N. Metzler-Nolte, *Cryst. Growth Des.* **2011**, *11*, 185-189.
- 59 A. Umemura, S. Diring, S. Furukawa, H. Uehara, T. Tsuruoka and S. Kitagawa, *J. Am. Chem. Soc.* **2011**, *133*, 15506-15513.
- 60 S.M. Doucet and M.G. Meadows, *J. R. Soc. Interface* **2009**, *6*, S115-S132.
- 61 E.A. Widder, *Bioscience Explained* **2001**, *1*, 1-9.
- 62 M. Wallin, *Bioscience Explained* **2002**, *1*, 1-12.
- 63 B. Wilts, N. Ijbema and D. Stavenga, *BMC Evol. Biol.* **2014**, *14*, 1-11, <http://creativecommons.org/licenses/by/4.0>.
- 64 T. Khudiyev, T. Dogan and M. Bayindir, *Sci. Rep.* **2014**, *4*, 4718, <http://creativecommons.org/licenses/by-nc-sa/3.0/>.
- 65 F. Marlow, Muldarisnur, P. Sharifi, R. Brinkmann and C. Mendive, *Angew. Chem. Int. Ed.* **2009**, *48*, 6212-6233.
- 66 S. Kinoshita and S. Yoshioka, *ChemPhysChem* **2005**, *6*, 1442-1459.
- 67 F. Liu, H. Yin, B. Dong, Y. Qing, L. Zhao, S. Meyer, X. Liu, J. Zi and B. Chen, *Phys. Rev. E* **2008**, *77*, 012901.
- 68 A.R. Parker, *J. R. Soc. Interface* **2005**, *2*, 1-17.
- 69 G. von Freymann, V. Kitaev, B.V. Lotsch and G.A. Ozin, *Chem. Soc. Rev.* **2013**, *42*, 2528-2554.

1 Introduction

- 70 C. Fenzl, T. Hirsch and O.S. Wolfbeis, *Angew. Chem. Int. Ed.* **2014**, *53*, 3318-3335.
- 71 D. Osorio and A.D. Ham, *J. Exp. Biol.* **2002**, *205*, 2017-2027.
- 72 F.G. Stiles, *The Condor* **1982**, *84*, 208-225.
- 73 R.A. Barry and P. Wiltzius, *Langmuir* **2006**, *22*, 1369-1374.
- 74 M. Rassart, J.F. Colomer, T. Tabarrant and J.P. Vigneron, *New J. Phys.* **2008**, *10*, 033014, 033011-033014.
- 75 J.H. Kim, J.H. Moon, S.-Y. Lee and J. Park, *Appl. Phys. Lett.* **2010**, *97*, 103701.
- 76 B.V. Lotsch and G.A. Ozin, *Adv. Mater.* **2008**, *20*, 4079-4084.
- 77 B.A. Suslick, L. Feng and K.S. Suslick, *Anal. Chem.* **2010**, *82*, 2067-2073.
- 78 J.R. Askim, M. Mahmoudi and K.S. Suslick, *Chem. Soc. Rev.* **2013**, *42*, 8649-8682, <http://dx.doi.org/10.1039/C3CS60179J>.
- 79 S. Colodrero, M. Ocaña and H. Míguez, *Langmuir* **2008**, *24*, 4430-4434.

2 NOVEL STRATEGIES IN NANOSCALE MOF SYNTHESIS

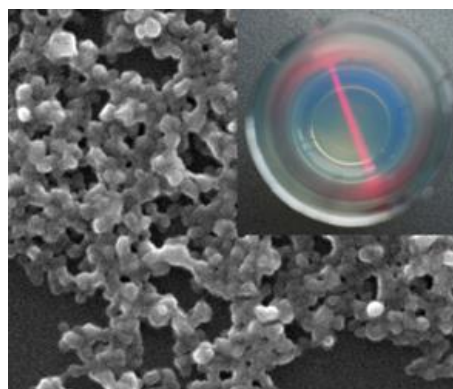
SUMMARY

The possibility to cast a material into any suitable form, such as thin films for sensing devices, can play a key role in controlling and improving its properties relevant to the desired application field. Nanoparticles represent versatile building blocks for the synthesis of thin films as they allow for precise adjustment of the film microstructure depending on the particle size and shape. Besides surface chemistry, the morphology and the chemical composition of the active material ultimately determine the device's output. As an example, parameters related to real-time sensors, such as analyte specificity and fast recovery, require the use of materials with inherent selectivity and moderate host-guest interaction strength (physisorption). These issues have been addressed recently by the incorporation of *metal-organic frameworks* (MOFs), e.g. into photonic crystal sensors (a detailed report on such MOF-based platforms realized in our group is given in **chapter 3**); these crystalline porous network structures are built up from metal ions and bridging organic linkers which can bear additional functionality.

In order to implement any desired MOF structure in the form of nanoparticulate films, generally applicable size- and shape-controlled strategies are required. Access to MOF nanoparticles has been obtained by a number of methods so far, including ultrasonic or microwave assisted heating. The use of chemical additives – such as surfactants or

polymers – has also been proven beneficial for nanoscale MOF synthesis due to several reasons: The additive can act as a *competitor* to the ligand, allow for controlling the particle's *morphology* through weak interactions with the particle surface, or help to *stabilize* a distinct size distribution in the colloidal suspension. The combination of two or more differently acting auxiliary agents is expected to result in superior control of growth mechanisms at the nanoscale.

In this study presented in **chapter 2.1**, we report on the preparation of two prototypical MOFs *via* an additive-mediated approach. Fine-tuning of the particle size was achieved by adjusting the type and amount of additives, along with the temperature. MOF nanoparticles were thus formed within 5 minutes under mild conditions. – Besides, the formation of optically homogeneous thin MOF films was demonstrated. Characteristic properties of the films, i.e. layer thickness and refractive index, were determined which can ultimately be used in the design of (optical) thin film-based devices.



2.1 ADDITIVE-MEDIATED SIZE CONTROL OF MOF NANOPARTICLES

Annekathrin Ranft, Sophia B. Betzler, Frederik Haase and Bettina V. Lotsch

published in *CrystEngComm* **2013**, 15, 9296-9300
DOI: 10.1039/c3ce41152d
<http://pubs.rsc.org/en/Content/ArticleLanding/2013/CE/c3ce41152d>
Reproduced by permission of The Royal Society of Chemistry

Abstract

A fast synthesis approach toward sub-60 nm sized MOF nanoparticles was developed by employing auxiliary additives. Control over the size of HKUST-1 and IRMOF-3 particles was gained by adjusting the concentration and type of stabilizers. Colloidal solutions of the MOFs were used for the formation of optically homogeneous thin films by spin-coating.

2.1.1 Introduction

Metal-organic frameworks (MOFs) represent a class of crystalline porous materials featuring intriguing properties such as chemical functionality combined with high porosity, which can be tailored for desired applications through the choice of the constituting building blocks.¹ Possible fields of application range from gas adsorption and storage² over catalysis³ and molecular sieving⁴ to the use of MOFs as active components in chemical sensors.⁵ Especially in the field of sensing, the possibility to cast the sensing material into a suitable form, such as thin films, is a key prerequisite to ensure diffusion throughout the entire active material and to keep response times low.⁶ MOF nanoparticles (NPs) can serve as versatile building blocks for thin films, which can be obtained by straightforward, low temperature solution processing protocols such as spin- and dip-coating.⁷ At the same time,

the use of nanoparticulate MOFs in principle allows for the precise adjustment of the material's properties, such as surface chemistry and shape, which in turn will affect the microstructure and, hence, performance of the resulting MOF film; besides, shape-specific synthesis strategies could reveal a better insight into MOF crystal growth mechanisms at the nanoscale.⁸

Among a range of well-studied MOF systems, HKUST-1 ($\text{Cu}_3(\text{BTC})_2$, BTC = benzene-1,3,5-tricarboxylate) belongs to the most prominent ones owing to its structural stability on adsorption and desorption of water molecules, which coordinate to unsaturated Cu(II) sites of the framework.⁹ In addition, such open metal sites are proposed to show increased affinity towards H_2 molecules resulting in improved hydrogen storage capacity,¹⁰ which may be even enhanced by tailoring the morphology and size of HKUST-1 crystals on the nanoscale. Access to MOF NPs has been obtained by a number of methods so far, upon which ultrasonic (US) or microwave (MW) assisted heating have been found to significantly accelerate the crystallization of MOFs as compared to traditional electric heating.¹¹⁻¹³ However, these strategies have shown to lack reproducibility owing to the use of different types of synthesis set-ups which may affect the particle properties significantly.¹⁴ The need for high temperatures for enhanced crystallinity has been circumvented by the development of direct mixing approaches,^{12,15-17} mechanochemical routes,¹⁸ freeze-drying approaches¹⁹ or continuous-flow methods which allow for the high-throughput preparation of MOF crystals by rapid mixing of pre-heated solvent streams.²⁰ Such routes suffer, however, in some cases from comparatively long reaction times (20 min at least for the synthesis of HKUST-1 based on a mechanochemical route¹⁸) or a complex synthesis set-up (synthesis in a continuous flow reactor²⁰) which hampers their generalization and implementation. Moreover, fine-tuning of the crystal size below 100 nm remains a challenge for the above mentioned synthesis strategies. Another attractive route to the size-controlled MOF synthesis is the use of auxiliary additives which can act as competitors to the bridging ligand ("coordination modulation"),^{13,21,22} or the use of surfactants to control the influx of monomers in order to stabilize the growing particles and to control the particles' morphology through weak interactions of the additive with the particle surface ("surfactant-mediated synthesis").²³⁻²⁶ These synthesis schemes have been successfully utilized not only for HKUST-1 with the help of PAA (poly(acrylic acid)) salts²⁵ or dodecanoic acid as size modulating agents,¹³ but also for other well-studied MOFs such as isorecticular IRMOF-3 ($\text{Zn}_4\text{O}(\text{BDC-NH}_2)_3$, BDC-NH₂ = 2-aminoterephthalate). In the case of IRMOF-3, superior control of the crystal size has been achieved by the addition of CTAB (hexadecyltrimethylammonium bromide) to slow down

nucleation times, and by fine-tuning the synthesis conditions through a four-step strategy.²⁶ Based on these studies realizing the size-controlled formation of MOFs at ambient rather than high-temperature conditions,²⁷⁻²⁹ the controlled synthesis of nanosized MOFs seems feasible. Nevertheless, only a few generally applicable synthetic strategies toward nanoMOFs with sizes less than 100 nm have been developed as yet.

In this study, we report on the preparation of ultrasmall versions of HKUST-1 and IRMOF-3, using an additive-mediated synthesis strategy. Our approach involves the use of chemical additives (polymers or polymer-surfactant combinations), which are mixed with the ligand before being reacted with the respective metal source, upon which MOF NPs form within 5 minutes under mild conditions. By altering the synthetic conditions such as reaction temperature, concentration, ratio and type of additive, we gain control over the particle size of the respective MOF.

2.1.2 Results and Discussion

HKUST-1 NPs were successfully prepared by mixing precursor solutions ($\text{Cu}(\text{OAc})_2 \cdot \text{H}_2\text{O}$ and trimesic acid (H_3BTC) in a water-ethanol-DMF mixture) with PAA at different temperatures (0 °C, room temperature (RT), 55 °C). Powder X-ray diffraction (PXRD) patterns of the products obtained at 0 °C and at RT, respectively, confirm the structure of the as-synthesized materials (**Fig. 1a**), apart from peak broadening, which is attributed to the small grain size of the products (29 nm deduced through the Scherrer formula). The morphology of the MOF NPs was examined by scanning electron microscopy (SEM), atomic force microscopy (AFM) and dynamic light scattering (DLS). SEM images of HKUST-1 synthesized at RT and 0 °C, respectively, reveal small particles with diameters between 30 nm and 50 nm (**Fig. 2a**), which was confirmed additionally through AFM (see **Figs. 2b** and **S1, SI**). DLS measurements (**Fig. S2, SI**) suggest that an increase of the reaction temperature from 0 °C to RT leads to a small shift of the mean particle radius from 50 nm to 60 nm (note that DLS measures the hydrodynamic radius including a solvating shell, leading to larger particle sizes than obtained by direct imaging techniques). This observation is supported by SEM images showing a comparatively larger amount of particles with diameters >40 nm for the synthesis at RT (see **Fig. S3, SI**). Heating the reaction mixture to 55 °C, however, leads to a more significant increase of the particle radius from 60 nm to 80 nm, as confirmed by DLS measurements (**Fig. S2, SI**). Low temperatures, therefore, seem to be beneficial to slow down crystal growth and reduce the particle size of HKUST-1; this tendency is in agreement

with other reports where size-control was gained by using rather mild synthesis conditions.¹⁶ We observed a similar size-controlling effect by varying the polymer concentration, i.e. the ratio of H₃BTC to PAA, from 1:2 up to 1:15 (corresponding to 0.082 mmol up to 0.615 mmol of PAA), while keeping the temperature at 0 °C and monitoring the change of the particle size with DLS (**Fig. S4, SI**). We observe that on decreasing the amount of PAA, the particle radius decreases from 57 nm (for a ratio of 1:6, 0.246 mmol PAA) to 48 nm (for a ratio of 1:3, 0.123 mmol PAA) while the size distribution is significantly narrowed as indicated by a change of the polydispersity index (PDI) from 0.184 (1:6, 0.246 mmol PAA) to 0.091 (1:3, 0.123 mmol PAA).

However, for an even lower ratio of 1:2 (0.082 mmol PAA), the PDI was found to rise again (0.176). While the size distribution is broadened – in general – with increasing amounts of PAA, the product yield is decreased, and at the highest PAA concentration (1:15, 0.615 mmol PAA) no precipitation was observed at all. We rationalize these findings by invoking the observation that HKUST-1 is formed within seconds upon the reaction of the starting materials and further growth of the particles seems to be inhibited by the formation of a protective PAA shell coordinating to the Cu(II) ions.³⁰ At increasing amounts of PAA (and, hence, increasing acidity of the reaction mixture) the network formation (i.e. nucleation) is slowed down owing to a comparatively low supply of the network constituting deprotonated linker BTC³⁻, along with a low availability of free copper ions not coordinated to PAA.³¹ On the contrary, at very low PAA concentrations, the amount of stabilizing agent is insufficient to slow down monomer addition; thus, size defocusing is observed for both particularly low and high amounts of PAA (for a given concentration of H₃BTC and copper acetate). A ratio of 1:3 (0.123 mmol PAA) turned out to be most suitable to obtain a narrow size distribution (PDI = 0.091) and a reasonably high product yield (65–70%). Using these synthesis conditions, we observed no significant change of the size of the particles by increasing the reaction time from 5 min to 30 min (see **Figs. S5 and S6, SI**), which we attribute to the rapid formation and protection of the particles upon mixing of the starting materials with PAA.³²

Nanosized IRMOF-3 was obtained by mixing $\text{Zn}(\text{OAc})_2 \cdot 2\text{H}_2\text{O}$, 2-aminoterephthalic acid, CTAB and polyvinylpyrrolidone (PVP) in DMF at RT, and the formation of IRMOF-3 NPs was confirmed by PXRD (a mean diameter of 27 nm was deduced through the Scherrer formula). The diffraction pattern of the as-synthesized material matches with the simulated pattern, whereas the completely dry product shows an intensity reversion of the peaks at 6.7° and 9.6° (**Fig. 1b**). Similar findings for such an intensity change have been rationalized by porefilling effects caused by residual guest species from the synthesis solution.³³

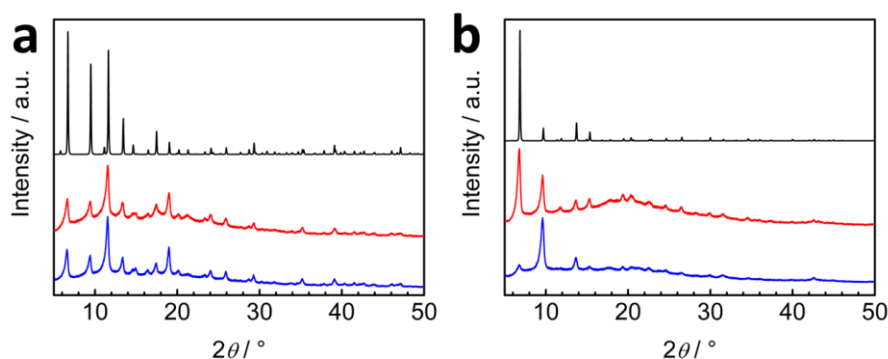


Figure 1. PXRD patterns of HKUST-1 and IRMOF-3 nanoparticles. (a) Simulated XRD pattern for HKUST-1 (black) and PXRD patterns of HKUST-1 synthesized at 0°C (red) and at RT (blue), (b) simulated XRD pattern for IRMOF-3 (black) and PXRD patterns of as-synthesized IRMOF-3 (red) and after drying (blue).

The nanoparticulate morphology of IRMOF-3 was confirmed by SEM (**Fig. 2c**); we deduce a mean diameter of 36 nm from the SEM images, whereas AFM measurements suggest particle sizes between 12 nm and 45 nm (see **Figs. 2d** and **S7, S1**). We successfully achieved size control of the particles by varying the concentration of the CTAB–PVP mixture at a constant weight ratio of 1:1 between 0.0135 mmol/0.00013 mmol and 0.054 mmol/0.0005 mmol. DLS measurements suggest that higher amounts of the additives reduce the mean particle radius from 80 nm to <30 nm (see **Fig. S8, S1**). The combination of two differently acting stabilizers shows a synergetic effect on the size distribution of IRMOF-3 particles: while the use of either CTAB or PVP as size-controlling agent has shown to reduce the hydrodynamic radius of IRMOF-3 to around 40 nm with a broad size distribution in particular for PVP ($n_{\text{CTAB}} = 0.027$ mmol, and $n_{\text{PVP}} = 0.00025$ mmol, respectively; see **Fig. S9, S1**), the combination of both materials allows for the synthesis of even smaller particles (≈ 30 nm in radius for 0.027 mmol/0.00025 mmol of CTAB–PVP). To our knowledge, these sizes are among the smallest which have been reported so far for IRMOF-3 NPs and most other MOFs.^{26–28} In order to investigate the effect of the additive combination on the particle size

of IRMOF-3 in more detail, we conducted purely PVP-mediated syntheses as well as a direct mixing approach without the addition of any auxiliary material. DLS measurements suggest that increasing concentrations of PVP lead to a decrease of the particle radius from 280 nm down to 40 nm for the highest PVP concentration (0.00125 mmol) (**Fig. S10, SI**). This observation is in agreement with a report about PVP protected Prussian Blue particles where an increased content of stabilizing PVP at given concentrations of the starting materials led to smaller diameters.³⁴ Besides size-modulating effects, PVP may prevent the particles from aggregating in solution.³⁵ The role of CTAB in the additive-mediated synthesis of IRMOF-3 may become clear by looking at the synthesis without mediators: in addition to small particles in the size range below 50 nm, SEM images reveal the presence of larger particles (80–180 nm) exhibiting a cubic morphology, which we did not observe in the presence of additives (**Fig. S11, SI**). According to previously described synthetic routes developed for the size- and shape-control of MOF NPs, CTAB has been shown to slow down the nucleation and growth of MOFs and, hence, to affect the resulting size distribution.^{24,36,37} Here, it seems likely that the addition of CTAB in combination with PVP does not only restrict particle growth (for a given concentration of the additives), but also contributes to an increased uniformity in size. Interestingly, additional time-dependent experiments suggest that further increase of the reaction time from 5 min to 60 min in the presence of the additive mixture has little impact on the particle size and crystallinity of the final product (**Figs. S12 and S13, SI**). In contrast to the reaction of the pure starting materials (Zn source and H₂BDC-NH₂), which instantaneously causes turbidity of the reaction solution due to particle formation, the reaction speed for the additive-controlled synthesis of IRMOF-3 is slowed down dramatically such that (visible) crystal formation is delayed for a few minutes after combining the starting materials, which emphasizes the importance of CTAB and PVP as stabilizers (see **Fig. S14, SI**). Even after 11 days, the size distribution within the reaction mixture has changed only marginally from 30 nm (mean radius) to 48 nm (see **Fig. S12, SI**), suggesting a facile handling of the product and, moreover, the possibility to isolate a particular particle size within a narrow size range as a function of time.

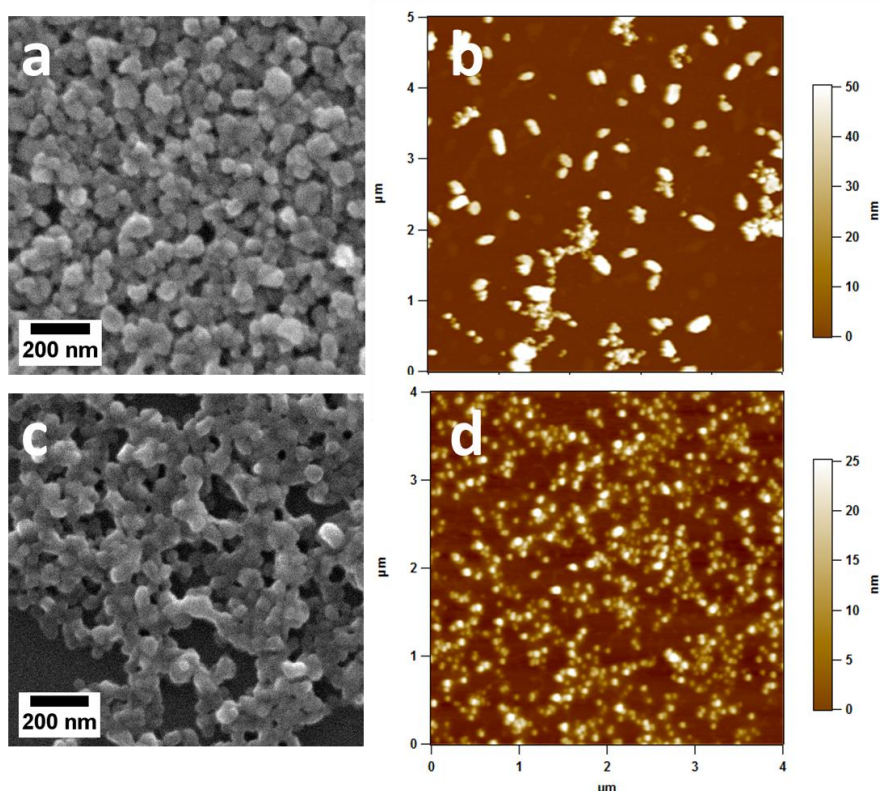


Figure 2. SEM and AFM images of HKUST-1 and IRMOF-3 particles. (a) SEM image of HKUST-1 synthesized at RT, (b) AFM image of HKUST-1 synthesized at 0 °C, (c) SEM image and (d) AFM image of IRMOF-3 synthesized with a ratio of CTAB/PVP = 0.027 mmol/0.00025 mmol.

MOF NPs with a uniform size of smaller than ≈ 100 nm can be used to build up optically homogeneous thin films exhibiting minimum scattering of visible light, which can serve as building blocks in MOF-based optical sensors.³⁸ MOF NP-based thin films may be deposited on a suitable substrate by solution processing, for example by spin- or dip-coating. As the layer thickness is affected by the concentration of particles in solution as well as by the volatility and wetting properties of the solvent, the use of well-dispersed MOF particles in an appropriate solvent is mandatory. Stable colloidal suspensions of HKUST-1 and IRMOF-3 were obtained by redispersing the particles in DMF, whereas their dispersion in other more volatile solvents such as ethanol or methanol was found to be impeded by the sedimentation of the particles within minutes. Thin films composed of HKUST-1 or IRMOF-3 particles were obtained by spin-coating DMF-based suspensions (conditions see [SI](#)) and characterized by cross-sectional SEM and ellipsometry. **Fig. 3** shows a representative section of the MOF layers which exhibit uniform thicknesses ($173 \text{ nm} \pm 15 \text{ nm}$ for HKUST-1, $147 \text{ nm} \pm 5 \text{ nm}$ for IRMOF-3) over a large lateral range; this thickness range is supported by ellipsometry

(176.2 nm \pm 0.6 nm for HKUST-1, 143.1 nm \pm 0.2 nm for IRMOF-3). Besides layer thicknesses, ellipsometry allows us to determine the effective refractive index (RI) of a dielectric material (or composite) fashioned into a reflective thin film. We obtained effective RIs of 1.21 and 1.27 for HKUST-1 and IRMOF-3, respectively (note that textural porosity as well as possible residues of the respective additives contribute to the experimental value), which is slightly smaller than the RI of other MOF films (e.g. ZIF-8: 1.34–1.39).^{38,39} The film assembly based on NPs imparts the MOF layer with textural porosity, which may be beneficial for MOF-based sensing devices: interstitial voids guarantee free diffusion throughout the entire film, thereby enhancing the sensitivity, whereas the MOF adds chemical selectivity to the system.^{32,38}

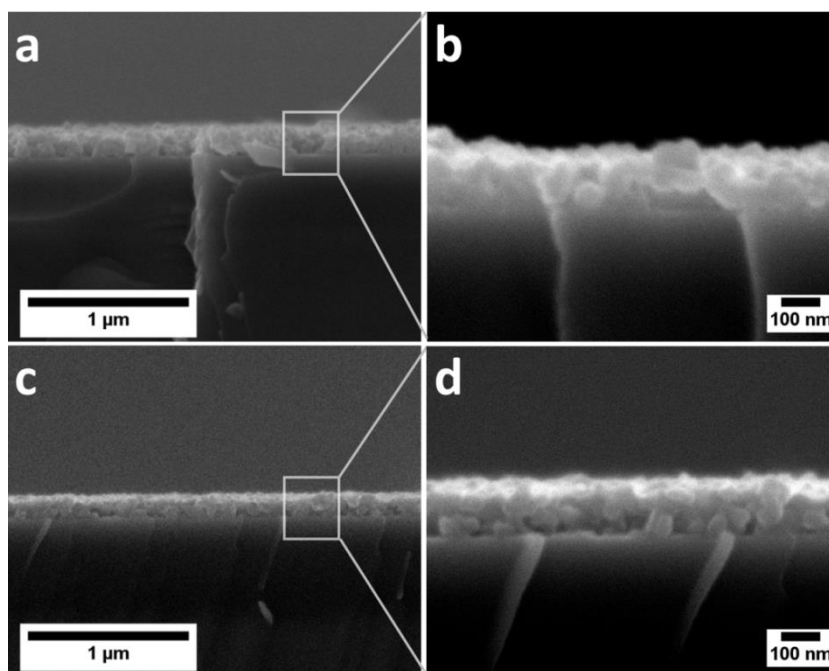


Figure 3. Cross-sectional SEM images of MOF thin films assembled from colloidal solutions of the respective MOFs by spin-coating. (a) HKUST-1 film, (b) magnified detail, (c) IRMOF-3 film, (d) magnified detail.

2.1.3 Conclusions

In summary, we have developed a fast solvothermal synthesis approach toward sub-60 nm sized MOF NPs (HKUST-1 and IRMOF-3) under mild conditions. Our method allows fine-tuning of the particle size within a large range (30–300 nm) by adjusting the type and amount of polymer (PAA for HKUST-1) or polymer–surfactant combination (PVP–CTAB for IRMOF-3), along with the temperature and reaction time. The synergistic action of two different additives having characteristic stabilizing properties results in superior control of the IRMOF-3 particle size and monodispersity. Opening generally applicable synthetic avenues to MOF NPs with diameters smaller than commonly achieved size ranges (≈ 30 nm) is of importance for several fields of applications relying on ultras-small MOF particles or thin films, such as in drug delivery or sensing. Along these lines, we have demonstrated the fabrication of optically homogenous HKUST-1 and IRMOF-3 thin films derived from stable colloidal MOF suspensions by spin-coating. Such hierarchically porous structures bode well for the development of highly accessible and sensitive MOF-based sensing devices.

Acknowledgments

Financial support by the Max Planck Society, Deutsche Forschungsgemeinschaft (SPP-1362), the Fond der Chemischen Industrie (FCI), the cluster of excellence “Nanosystems Initiative Munich” (NIM), and the Center for NanoScience (CeNS) is gratefully acknowledged. We thank Prof. T. Bein for granting access to the ellipsometer and I. Pavlichenko, C. Minke, V. Duppel, S. Werner and C. Ziegler for their assistance with the material analysis.

2.1.4 References

- 1 (a) M. Eddaoudi, D. B. Moler, H. Li, B. Chen, T. M. Reineke, M. O'Keeffe and O. M. Yaghi, *Acc. Chem. Res.* **2001**, *34*, 319-330; (b) M. Eddaoudi, J. Kim, N. Rosi, D. Vodak, J. Wachter, M. O'Keeffe and O. M. Yaghi, *Science* **2002**, *295*, 469-472; (c) C. Janiak and J. K. Vieth, *New J. Chem.* **2010**, *34*, 2366-2388; (d) W. Xuan, C. Zhu, Y. Liu and Y. Cui, *Chem. Soc. Rev.* **2012**, *41*, 1677-1695; (e) L. Song, J. Zhang, L. Sun, F. Xu, F. Li, H. Zhang, X. Si, C. Jiao, Z. Li, S. Liu, Y. Liu, H. Zhou, D. Sun, Y. Du, Z. Cao and Z. Gabelica, *Energy Environ. Sci.* **2012**, *5*, 7508-7520; (f) S. M. Cohen, *Chem. Rev.* **2012**, *112*, 970-1000; (g) T. R. Cook, Y. Zheng and P. J. Stang, *Chem. Rev.* **2013**, *113*, 734-777.
- 2 (a) M. P. Suh, H. J. Park, T. K. Prasad and D. Lim, *Chem. Rev.* **2012**, *112*, 782-835; (b) K. Sumida, D. L. Rogow, J. A. Mason, T. M. McDonald, E. D. Bloch, Z. R. Herm, T. Bae and J. R. Long, *Chem. Rev.* **2012**, *112*, 724-781.
- 3 (a) J. Lee, O. K. Farha, J. Roberts, K. A. Scheidt, S. T. Nguyen and J. T. Hupp, *Chem. Soc. Rev.* **2009**, *38*, 1450-1459; (b) M. Ranocchiari and J. A. van Bokhoven, *Phys. Chem. Chem. Phys.* **2011**, *13*, 6388-6396; (c) P. Valvekens, F. Vermoortele and D. De Vos, *Catal. Sci. Technol.* **2013**, *3*, 1435-1445.
- 4 (a) J. Li, J. Sculley and H. Zhou, *Chem. Rev.* **2012**, *112*, 869-932; (b) M. Shah, M. C. McCarthy, S. Sachdeva, A. K. Lee and H. Jeong, *Ind. Eng. Chem. Res.* **2012**, *51*, 2179-2199.
- 5 (a) B. Chen, S. Xiang and G. Qian, *Acc. Chem. Res.* **2010**, *43*, 1115-1124; (b) L. E. Kreno, K. Leong, O. K. Farha, M. Allendorf, R. P. Van Duyne and J. T. Hupp, *Chem. Rev.* **2012**, *112*, 1105-1125; (c) Y. Cui, Y. Yue, G. Qian and B. Chen, *Chem. Rev.* **2012**, *112*, 1126-1162.
- 6 (a) O. Shekhah, J. Liu, R. A. Fischer and C. Wöll, *Chem. Soc. Rev.* **2011**, *40*, 1081-1106; (b) D. Bradshaw, A. Garai and J. Huo, *Chem. Soc. Rev.* **2012**, *41*, 2344-2381.
- 7 (a) P. Horcajada, C. Serre, D. Grosso, C. Boissière, S. Perruchas, C. Sanchez and G. Férey, *Adv. Mater.* **2009**, *21*, 1931-1935; (b) A. Demessence, P. Horcajada, C. Serre, C. Boissière, D. Grosso, C. Sanchez and G. Férey, *Chem. Commun.* **2009**, 7149-7151; (c) A. Demessence, C. Boissière, D. Grosso, P. Horcajada, C. Serre, G. Férey, G. J. A. A.

- Soler-Illia and C. Sanchez, *J. Mater. Chem.* **2010**, *20*, 7676-7681; (d) D. Jiang, A. D. Burrows, Y. Xiong and K. J. Edler, *J. Mater. Chem. A* **2013**, *1*, 5497-5500.
- 8 (a) M. P. Attfield and P. Cubillas, *Dalton Trans.* **2012**, *41*, 3869-3878; (b) N. Stock and S. Biswas, *Chem. Rev.* **2012**, *112*, 933-969; (c) E. A. Flügel, A. Ranft, F. Haase and B. V. Lotsch, *J. Mater. Chem.* **2012**, *22*, 10119-10133; (d) V. Valtchev and L. Tosheva, *Chem. Rev.* **2013**, *113*, 6734-6760.
- 9 (a) S. S. Y. Chui, S. M. F. Lo, J. P. H. Charmant, A. G. Orpen and I. D. Williams, *Science* **1999**, *283*, 1148-1150; (b) P. M. Schoenecker, C. G. Carson, H. Jasuja, C. J. J. Flemming and K. S. Walton, *Ind. Eng. Chem. Res.* **2012**, *51*, 6513-6519.
- 10 Q. Yang and C. Zhong, *J. Phys. Chem. B* **2006**, *110*, 655-658.
- 11 (a) Z. Li, L. Qiu, T. Xu, Y. Wu, W. Wang, Z. Wu and X. Jiang, *Mater. Lett.* **2009**, *63*, 78-80; (b) N. A. Khan and S. H. Jhung, *Bull. Korean Chem. Soc.* **2009**, *30*, 2921-2926; (c) Z. Ni and R. I. Masel, *J. Am. Chem. Soc.* **2006**, *128*, 12394-12395; (d) Z. Xiang, D. Cao, X. Shao, W. Wang, J. Zhang and W. Wu, *Chem. Eng. Sci.* **2010**, *65*, 3140-3146; (e) N. A. Khan, E. Haque and S. H. Jhung, *Phys. Chem. Chem. Phys.* **2010**, *12*, 2625-2631.
- 12 S. Loera-Serna, M. A. Oliver-Tolentino, Ma. de Lourdes López-Núñez, A. Santana-Cruz, A. Guzmán-Vargas, R. Cabrera-Sierra, H. I. Beltrán and J. Flores, *J. Alloys Compd.* **2012**, *540*, 113-120.
- 13 S. Diring, S. Furukawa, Y. Takashima, T. Tsuruoka and S. Kitagawa, *Chem. Mater.* **2010**, *22*, 4531-4538.
- 14 (a) M. Schlesinger, S. Schulze, M. Hietschold and M. Mehring, *Microporous Mesoporous Mater.* **2010**, *132*, 121-127; (b) J. Klinowski, F. A. Almeida Paz, P. Silva and J. Rocha, *Dalton Trans.* **2011**, *40*, 321-330.
- 15 J. Zhuang, D. Ceglarek, S. Pethuraj and A. Terfort, *Adv. Funct. Mater.* **2011**, *21*, 1442-1447.
- 16 G. Majano and J. Pérez-Ramírez, *Helv. Chim. Acta* **2012**, *95*, 2278-2286.
- 17 L. Brinda, K. S. Rajan and J. B. B. Rayappan, *J. Appl. Sci.* **2012**, *12*, 1778-1780.
- 18 H. Yang, S. Orefuwa and A. Goudy, *Microporous Mesoporous Mater.* **2011**, *143*, 37-45.

- 19 L. H. Wee, M. R. Lohe, N. Janssens, S. Kaskel and J. A. Martens, *J. Mater. Chem.* **2012**, *22*, 13742-13746.
- 20 M. Gimeno-Fabra, A. S. Munn, L. A. Stevens, T. C. Drage, D. M. Grant, R. J. Kashtiban, J. Sloan, E. Lester and R. I. Walton, *Chem. Commun.* **2012**, *48*, 10642-10644.
- 21 (a) S. Hermes, T. Witte, T. Hikov, D. Zacher, S. Bahnmüller, G. Langstein, K. Huber and R. A. Fischer, *J. Am. Chem. Soc.* **2007**, *129*, 5324-5325; (b) J. Cravillon, R. Nayuk, S. Springer, A. Feldhoff, K. Huber and M. Wiebcke, *Chem. Mater.* **2011**, *23*, 2130-2141; (c) M. Pham, G. Vuong, F. Fontaine and T. Do, *Cryst. Growth Des.* **2012**, *12*, 3091-3095.
- 22 F. Wang, H. Guo, Y. Chai, Y. Li and C. Liu, *Microporous Mesoporous Mater.* **2013**, *173*, 181-188.
- 23 K. M. L. Taylor, A. Jin and W. Lin, *Angew. Chem.* **2008**, *120*, 7836-7839.
- 24 Q. Liu, L. Jin and W. Sun, *Chem. Commun.* **2012**, *48*, 8814-8816.
- 25 D. Jiang, T. Mallat, F. Krumeich and A. Baiker, *Catal. Commun.* **2011**, *12*, 602-605.
- 26 M. Ma, D. Zacher, X. Zhang, R. A. Fischer and N. Metzler-Nolte, *Cryst. Growth Des.* **2011**, *11*, 185-189.
- 27 L. Huang, H. Wang, J. Chen, Z. Wang, J. Sun, D. Zhao and Y. Yan, *Microporous Mesoporous Mater.* **2003**, *58*, 105-114.
- 28 Z. Gu, J. Jiang and X. Yan, *Anal. Chem.* **2011**, *83*, 5093-5100.
- 29 J. Cravillon, S. Münzer, S. Lohmeier, A. Feldhoff, K. Huber and M. Wiebcke, *Chem. Mater.* **2009**, *21*, 1410-1412.
- 30 Y. Gotoh, R. Igarashi, Y. Ohkoshi, M. Nagura, K. Akamatsu and S. Deki, *J. Mater. Chem.* **2000**, *10*, 2548-2552.
- 31 T. Uemura, Y. Hoshino, S. Kitagawa, K. Yoshida and S. Isoda, *Chem. Mater.* **2006**, *18*, 992-995.
- 32 D. Tanaka, A. Henke, K. Albrecht, M. Moeller, K. Nakagawa, S. Kitagawa and J. Groll, *Nat. Chem.* **2010**, *2*, 410-416.

- 33 (a) J. Hafizovic, M. Bjorgen, U. Olsbye, P. D. C. Dietzel, S. Bordiga, C. Prestipino, C. Lamberti and K. P. Lillerud, *J. Am. Chem. Soc.* **2007**, *129*, 3612-3620; (b) L. Zhang and Y. H. Hu, *Appl. Surf. Sci.* **2011**, *257*, 3392-3398.
- 34 (a) T. Uemura and S. Kitagawa, *J. Am. Chem. Soc.* **2003**, *125*, 7814-7815; (b) T. Uemura, M. Ohba and S. Kitagawa, *Inorg. Chem.* **2004**, *43*, 7339-7345.
- 35 Z. Li and Y. Zhang, *Angew. Chem. Int. Ed.* **2006**, *45*, 7732-7735.
- 36 P. Sarawade, H. Tan and V. Polshettiwar, *ACS Sustainable Chem. Eng.* **2013**, *1*, 66-74.
- 37 Y. Pan, D. Heryadi, F. Zhou, L. Zhao, G. Lestari, H. Su and Z. Lai, *CrystEngComm* **2011**, *13*, 6937-6940.
- 38 (a) G. Lu and J. T. Hupp, *J. Am. Chem. Soc.* **2010**, *132*, 7832-7833; (b) F. M. Hinterholzinger, A. Ranft, J. M. Feckl, B. Rühle, T. Bein and B. V. Lotsch, *J. Mater. Chem.* **2012**, *22*, 10356-10362.
- 39 S. Eslava, L. Zhang, S. Esconjauregui, J. Yang, K. Vanstreels, M. R. Baklanov and E. Saiz, *Chem. Mater.* **2013**, *25*, 27.

3 INTERFERENCE-BASED READOUT OF SORPTION EVENTS IN MOF MULTILAYER SYSTEMS

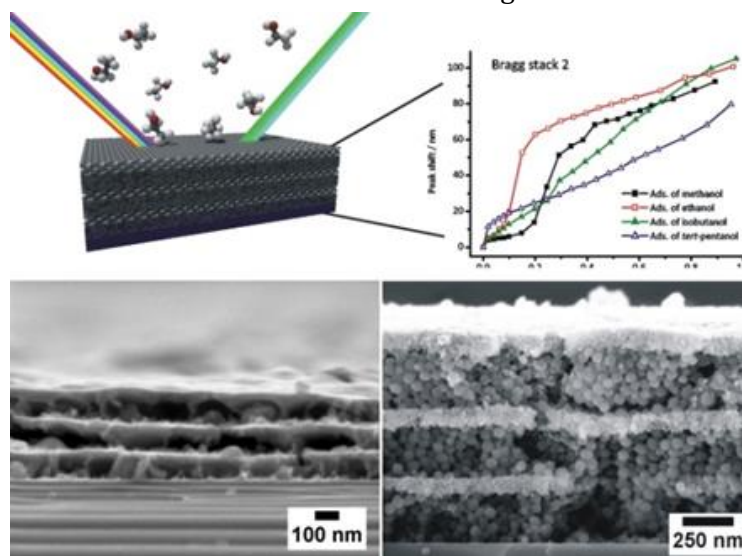
SUMMARY

Nanoparticulate MOFs, primarily those having diameters below 100 nm, lend themselves well for the formation of optically homogeneous thin films, as demonstrated in the previous chapter (2.1). For the design of multilayered sensors relying on an optical readout (i.e. interference), refractive indices (RIs) of the materials and their layer thicknesses (z) constitute the most relevant properties: Depending on how these parameters are chosen, specific spectral qualities are achieved such as hue and intensity of the reflected color. In 1D photonic crystals (PCs), two materials with differing RIs are alternately arranged in the form of thin films. The resulting color (reflection maximum or Bragg peak) is determined by the Bragg-Snell law and changes with respect to variations in the optical thickness (i.e. RI and z). These variations can be either static or dynamic: For the former, different synthetic conditions or material compositions can lead to altered thicknesses and RIs; the latter is characterized by spectral shifts induced, for instance, through the capability of the stack constituting materials to adsorb particular guest molecules. This quality can be utilized, in turn, to detect changes in the environment such as the presence of toxic gases.

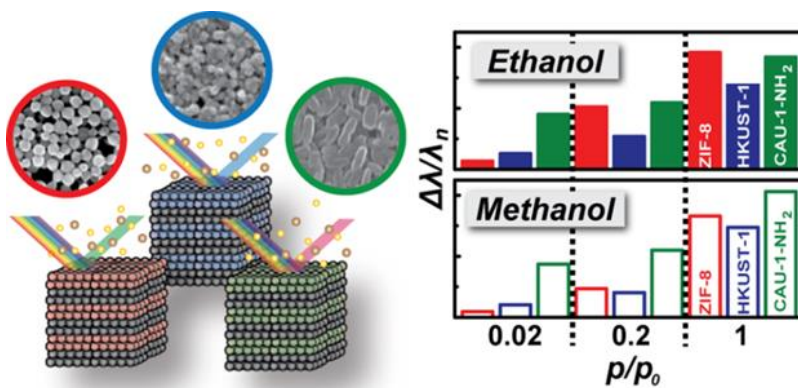
Due to their unique structure, MOFs are suitable for adsorbing molecules and, hence, also reporting on such events. Here, tunable sorption properties are achieved as a function of the building blocks constituting the MOF lattice, including size exclusion, polarity effects, and specific host-guest interactions (e.g. H-bonds). Besides, MOFs are typically characterized through adsorption isotherms showing specific analyte uptake in dependence of the partial pressure; it is thus expected that MOF-based photonic architectures are capable of specifying even slight variations in analyte concentration. – A particularly appealing property of interference-based readout is the fact that no additional labelling of the sensing material is required to achieve monitoring of sorption events, as the observed parameter, the (effective) RI, is a quality inherent to the investigated material (or a combination of different materials/morphologies); hence, in principle, any desired MOF structure could be implemented in PC devices, if it can be accessed in nanoscale form or otherwise processed into thin films. Moreover, this approach allows for real-time sensing, as the response induced by RI variations is expected to occur fast (i.e. on the order of seconds).

In the following **chapters 3.1–3.3**, three examples are reported of how MOFs may be implemented in 1D PC sensors. Besides structural and optical characteristics, the sensing performance of these platforms is discussed in view of different design aspects: tuning of the MOF composition, morphology of the layers, and ordering of the stack constituting materials; as well as in relation to general sensing characteristics, namely selectivity, response time and sensitivity. In order to monitor the RI-induced spectral changes, both the reflectance spectra and the color appearance were used for detection. The thus obtained data were evaluated through optically encoded isotherms (concentration-dependent spectral shifts induced by analyte adsorption), changes in reflectance at a certain wavelength (for a time-resolved response toward varying analyte concentrations) or color image analysis coupled with principle component analysis (identification and separation of single solvents/solvent mixtures with sensor arrays).

In **chapter 3.1**, the integration of a prototypic MOF into 1D PCs is demonstrated for the first time. For the realization of the photonic architecture, ZIF-8 and TiO_2 were chosen as PC components with different RIs. While the latter is used to assure a high RI contrast and, hence, good optical quality of the stack, ZIF-8 is intended to impart molecular selectivity to the Bragg stack (BS) as a result of its defined pore system and pore size. – For the fabrication of the BSs, two different synthesis approaches were used: In the first approach, the ZIF-8 layers were *grown* onto the substrate, while the second stack was assembled from ZIF-8 *nanoparticles*; in both cases, TiO_2 films with textural porosity were used to enable molecular diffusion within the entire stack. – The sensing performance of the two different stacks was investigated by exposing them towards chemically similar solvent vapors at varying concentrations. By plotting the observed spectral shifts as a function of the partial pressure (similar to an isotherm), the differences in sensitivity and selectivity were identified for both platforms.



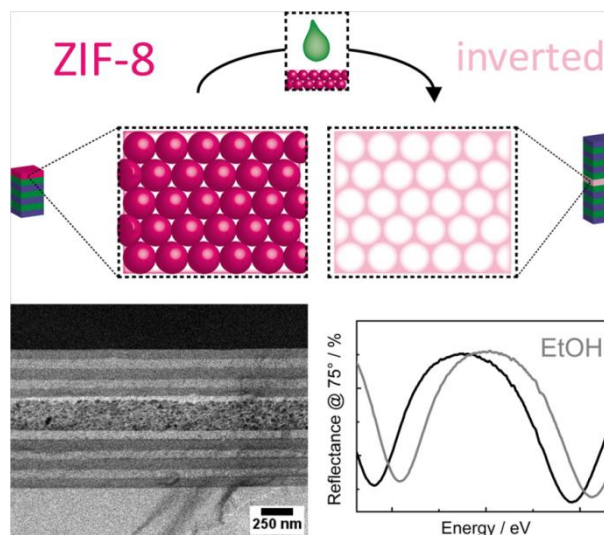
In **chapter 3.2**, the integration of three different types of MOFs into photonic multilayers is reported. Here, we aimed at achieving different sorption properties of the BSs, including enhanced selectivity and sensitivity for particular analytes; to this end, different MOF structures were chosen featuring characteristic pore sizes and environments. – The fabrication of the BSs was



accomplished by assembling MOF nanoparticles in alternation with another component. In total, three different synthesis approaches were used: In the first approach, the MOFs were stacked with the high RI-material TiO_2 , similar to the approach reported in **chapter 3.1**; in the second, purely MOF-based BSs were produced, dubbed *tandem MOF BSs*, in which two of

the MOF structures were alternately arranged; in the third approach, three of the regular TiO_2/MOF BSs were organized in a pattern to serve as a *colorimetric fingerprint*. – The sensing performance of all three systems was tested by recording a) the pressure-dependent adsorption of solvent vapors (for TiO_2/MOF BSs and tandem MOF BSs), b) the kinetics of TiO_2/MOF BSs, and c) the combined response of the array, with respect to different solvents and solvent mixtures at a fixed concentration. In summary, these experiments reveal a sensing performance of the stacks that allows for both identifying and quantifying an analyte; fast response times; and the potential for combinatorial sensing by specifying even complex analytes.

In **chapter 3.3**, the introduction of a stimuli-responsive ZIF-8 “defect” layer into regular $\text{SiO}_2/\text{TiO}_2$ multilayers is shown. With the addition of this dopant layer, we aimed at the emergence of an additional narrow band of allowed states in the photonic band gap; the sharpness of this band may help to provide a more precise means to detect even small spectral changes upon analyte adsorption. The defect layer has therefore been deposited either on top of the metal oxide stacks (*top defect structures*) or sandwiched between two regular stacks (*sandwich defect structures*). In addition, we tried different TiO_2 film morphologies (either TiO_2 sol or nanoparticles) to investigate a potential impact on the stack’s sensing properties.



– Vapor sorption measurements were conducted as a function of the layer morphology, layer sequence and the position of the defect layer in the stack; in summary, we identified a “gating” function of the uppermost layers for the sensitivity of the overall detection platform. – Besides, the conversion of the ZIF-8 layer into an optically homogenous mesoporous film (under defined conditions) was observed, and discussed as a generic approach toward hierarchically structured films and multilayers.

3.1 ONE-DIMENSIONAL METAL–ORGANIC FRAMEWORK PHOTONIC CRYSTALS USED AS PLATFORMS FOR VAPOR SORPTION

Florian M. Hinterholzinger, Annekathrin Ranft, Johann M. Feckl, Bastian Rühle, Thomas Bein and Bettina V. Lotsch

published in *J. Mater. Chem.* **2012**, *22*, 10356-10362

DOI: 10.1039/c2jm15685g

<http://pubs.rsc.org/en/Content/ArticleLanding/2012/JM/c2jm15685g>

Reproduced by permission of The Royal Society of Chemistry

Abstract

We present the fabrication of one-dimensional photonic crystals (Bragg stacks) based on a microporous metal–organic framework material and mesoporous titanium dioxide. The Bragg stack heterostructures were obtained using two complementary synthesis approaches utilizing the bottom-up assembly of heterogeneous, i.e. two-component photonic crystal multilayer structures. Zeolitic imidazolate framework ZIF-8 and mesoporous titanium dioxide were chosen as functional components with different refractive indices. While ZIF-8 is intended to impart molecular selectivity, mesoporous TiO₂ is used to ensure high refractive index contrast and to guarantee molecular diffusion within the Bragg stack. The combination of micro- and mesoporosity within one scaffold endows the 1D-MOF PC with characteristic adsorption properties upon exposure to various organic vapors. In this context, the sorption behavior of the photonic material was studied as a function of partial pressure of organic vapors. The results show that the multilayered photonic heterostructures are sensitive and selective towards a series of chemically similar solvent vapors. It is thus anticipated that the concept of multilayer heterogeneous photonic structures will provide a versatile platform for future selective, label-free optical sensors.

3.1.1 Introduction

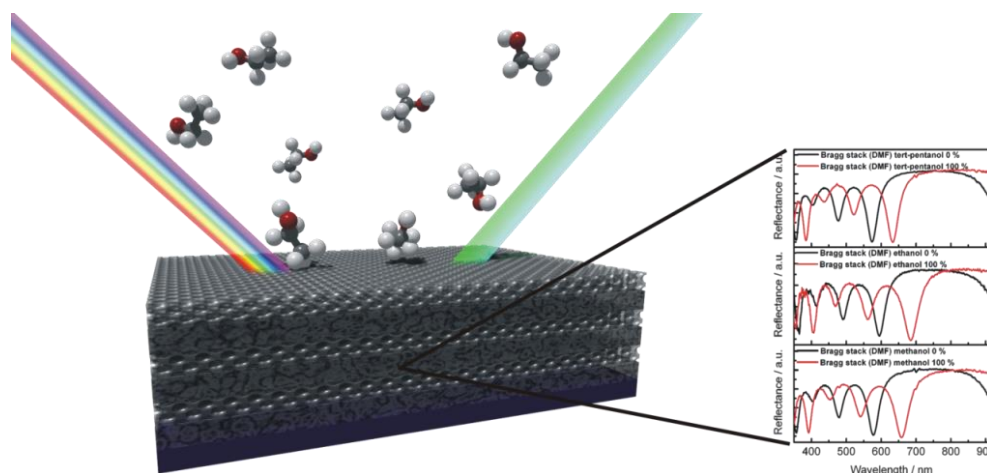
Metal–organic frameworks represent a class of hybrid materials with promising properties for various applications.^{1–5} In particular, the modular tailorability, the rich host–guest interactions, and the widely tunable sorption behavior make MOFs attractive candidates for chemical sensing.^{6,7} However, only a few reports are dealing with MOF-based sensors,^{8,9} in which the intrinsic framework luminescence^{10–14} or the refractive index modulation of Fabry–Perot interference peaks have been explored for signal transduction.¹⁵ The tunability of the effective refractive index (RI) of MOFs *via* adsorption of guests inspired us to correlate these properties with the underlying optics of photonic crystals (PCs), which are composed of alternating dielectric layers featuring periodic changes in their effective refractive indices.^{16–18}

One-dimensional assemblies, which represent the structurally simplest form of photonic crystals, are also known as Bragg stacks (BS) or Bragg mirrors. 1D-PC multilayer structures interacting with visible light require layer thicknesses corresponding to optical wavelengths.¹⁹ As a consequence of the periodicity in the dielectric function, specific wavelengths are efficiently reflected due to diffraction and interference of incident light at each interface of the periodically stacked composite.²⁰ Enhanced reflectivity is achieved by increasing the number of bilayers or by choosing dielectric materials featuring a high refractive index contrast (**Scheme 1**).²¹

Currently, intensive research efforts are focused on the development of tunable optical sensors with a label-free operation and compact set-up. There are several approaches ranging from plasmonic noble metal nanotubes²² or field effect transistors based on reduced graphene²³ to Bragg stacks built up from an alternating polymer architecture,²⁴ which deal with the implementation of these materials as tunable and label-free sensors. In particular, detection platforms based on Bragg stacks can be realized by translating stimuli-induced optical thickness changes of the constituent materials into a color change of the multilayer photonic structure. So far, several studies are dealing with tailor-made inorganic or hybrid materials to implement functionality within one-dimensional photonic crystals.²⁵ While there are several examples of versatile SiO₂–TiO₂ systems,^{26–28} including both dense and porous morphologies as well as nanoparticle-based Bragg stacks,^{29,30} smart hybrid photonic materials with intrinsic functionality are still rare.

3 Interference-Based Readout

In principle, a Bragg stack offers a versatile platform for the detection of molecular interactions and the development of chemical sensors, whereas the realization of chemical selectivity in sensors remains a great challenge.



Scheme 1. Schematic representation of a multilayered photonic crystal architecture illustrating the structure- and angle-dependent reflection of incident light as well as the optical response upon exposure to external stimuli.

Very recently, several groups reported a new transduction scheme based on the fabrication of MOF-containing ordered 3D photonic structures.^{31,32} The selectivity issue is addressed by integrating metal-organic frameworks into three-dimensional inverse opal structures. While Wu *et al.*³² employed a colloidal crystal templating approach using a polystyrene opaline “mold”, the group of J. Hupp³¹ deposited MOF crystals onto a silica template to obtain hybrid MOF-silica colloidal crystal (MOF-SCC) films. The authors have shown that the introduction of an ordered porous structure imparts useful optical features to HKUST-1 and ZIF-8. For MOF-SCC an optical signal displayed by distinct stop band shifts upon analyte sorption is readily observed.

Contrary to 3D photonic materials, we introduce herein a one-dimensional photonic architecture based on a microporous metal-organic framework and titanium dioxide. Thus, an optical transducer system is built, which is used to efficiently convert molecular adsorption into an optical response. As a microporous material, the intensively studied zeolitic imidazolate framework ZIF-8³³ was chosen; this is expected to impart size- and

chemoselectivity and, thus, functionality to the 1D-MOF PC. Complementary material properties in one single platform, such as hydrophobicity/hydrophilicity, dual pore-size regimes, and high refractive index contrast, can be additionally integrated by our combined assembly approach.

Ultimately, the presented results are expected to extend the toolbox for designing nanoporous and at the same time highly selective photonic crystals, to promote our understanding of molecular interactions in porous materials, and to provide novel concepts for label-free chemo-optical sensors.

3.1.2 Experimental

All chemicals (zinc nitrate hexahydrate, 2-methylimidazole; nitric acid (0.1 M), titanium(IV) ethoxide, titanium tetrachloride) as well as solvents are commercially available and were used as received. *Tert*-butyl alcohol was dried over a 4 Å molecular sieve at 28 °C and filtered prior to use.

Route A

Preparation of dense ZIF-8 films

ZIF-8 thin films were prepared on silicon wafers, similar to the approach reported in refs. 14 and 15. The substrates were pre-cleaned in Piranha solution ($\text{H}_2\text{SO}_4/\text{H}_2\text{O}_2$, 70:30 (v/v)) at 70 °C for 30 minutes, rinsed with distilled water and dried under nitrogen flow.

For ZIF-8 thin film preparation, 500 mL methanolic stock solutions of $\text{Zn}(\text{NO}_3)_2 \cdot 6\text{H}_2\text{O}$ (25 mM, 99%, Aldrich) as well as of 2-methylimidazole (mIm) (50 mM, 99%, Aldrich) were prepared. A ZIF-8 thin film was obtained by immersing the cleaned substrates in a fresh mixture of 10 mL $\text{Zn}(\text{NO}_3)_2$ stock solution and 10 mL mIm stock solution for 30 minutes at room temperature. For optimization of homogeneity and to enhance surface smoothness, two different strategies were employed. The beakers were either put in an ultrasonic bath or fixed on a shaker during film growth. The as-prepared ZIF-8 thin film was washed with methanol and dried under nitrogen flow. Thicker films could be obtained by simply repeating the process with fresh solutions.

3 Interference-Based Readout

Synthesis of ultrasmall titanium dioxide nanoparticles and film preparation

Titanium dioxide nanoparticles were synthesized as described earlier.³⁴ In brief, a nonaqueous sol-gel route in tertbutyl alcohol under microwave irradiation was used to yield ultrasmall (3 nm), crystalline (anatase), non-agglomerated and highly dispersible nanoparticles.

For all syntheses, titanium tetrachloride (0.7 mL, 6.4 mmol, 99.995%, Aldrich) was dissolved in toluene (5 mL) and added to tert-butyl alcohol (15 mL, 160 mmol, Aldrich) under continuous stirring. Microwave heating was performed in microwave autoclaves with an initial heating power of 1200 W (Synthos 3000, Anton Paar). The solution was heated to 80 °C within 1 min and then kept at 50 °C for 20 min resulting in a slightly yellow, transparent solution of nanoparticles. To obtain the fully crystalline nanoparticles, this heating procedure was repeated one more time after a cooling period to room temperature. The solution was then colorless and titaniumdioxide could be flocculated by the addition of n-heptane (n-heptane:tert-butanol/toluene 2:1 volume ratio; Sigma) and separated by centrifugation at 50 000 rcf for 15 min.

For the preparation of the mesoporous (mp) titania films the nanoparticle pellet (0.4 g) was redispersed in ethanol (8.3 mL) and Pluronic F127 (0.1 g, BASF) was added as structure directing agent (SDA).

Fabrication of Bragg stack 1 (BS-1)

For the fabrication of Bragg stack 1 (BS-1), thoroughly washed and dense ZIF-8 thin films were coated with a fresh colloidal suspension of redispersed ultrasmall titanium dioxide nanoparticles. The films were deposited by spin-coating using a Laurell WS-400B-6NPP-Lite-AS spin-coater at a speed of 5000 rpm to give a film thickness of ~50 nm. To remove the SDA, the films were first heated to 100 C (3 h ramp, 1 h dwell time) to increase the film stability followed by an extraction of the SDA with ethanol under reflux for 1 h. The complete removal was confirmed by reflection absorption infrared (RAIR) spectroscopy in addition to scanning electron microscopy (SEM) (see [SL](#), **Figs. S11** and **S12**).

The whole procedure was repeated 3 times to obtain multiple alternating ZIF-8-mp-TiO₂ architectures.

Route B

Synthesis of ZIF-8 nanoparticles

ZIF-8 nanoparticles were prepared by a modified literature synthesis.³⁵ In a typical experiment, $\text{Zn}(\text{NO}_3)_2 \cdot 6\text{H}_2\text{O}$ (1.03 g, 3.45 mmol, 99%, Grüssing) was dissolved in methanol (70 mL, puriss, Sigma) and rapidly added to a pre-cooled (0 °C) solution of 2-methylimidazole (2.27 g, 27.7 mmol, 99%, Aldrich) in methanol (70.0 mL). The mixture was stirred and cooled constantly throughout the reaction until the solution slowly turned turbid. After 30 min, the nanocrystals were separated from the solvent by centrifugation. Colloidal suspensions of ZIF-8 were obtained by redispersing the particles after centrifugation in DMF (or methanol) (670 mg ZIF-8/1 mL DMF).

Synthesis of titania nanoparticles

Titania nanoparticles were synthesized according to the literature.³⁶ In a typical procedure, $\text{Ti}(\text{OEt})_4$ (6.25 mL, Aldrich) was slowly added to HNO_3 (0.1 M, 37.5 mL, puriss, Acros) under stirring and heated to 80 °C for 8 h. After cooling to room temperature, the opalescent mixture was sonicated for at least 3 h in order to break up agglomerates. Colloidal suspensions of titania in a solvent sufficiently volatile for spin-coating were obtained by repeated collection of the particles by centrifugation and redispersion in DMF (or methanol) (130 mg TiO_2 /1 mL DMF).

Fabrication of Bragg stack 2 (BS-2)

Silicon wafers were used as substrates for the film deposition by spin-coating. The substrates were pre-cleaned with soap and water and subsequently treated with Piranha solution ($\text{H}_2\text{SO}_4/\text{H}_2\text{O}_2$, 2:1 (v/v)). After thoroughly rinsing with deionized water, the wafers were dried under nitrogen flow and stored in ethanol. Before film deposition, the substrates were plasma-cleaned and rinsed with ethanol under spinning for 5 s. The preparation of the Bragg stack was performed by alternately spin-coating colloidal suspensions of ZIF-8 and titania onto the substrate at a speed of 4000 rpm (1500 acceleration) for 60 s, starting with ZIF-8. The film thickness was adjusted by the particle concentration in the suspensions and by multiple coating steps. After each deposition, the film was annealed at 200 °C for 30 min.

3.1.3 Characterization

X-ray diffraction (XRD) measurements of powders and thin films were performed using a Bruker D8 (Cu- $K_{\alpha 1}$ = 1.5406 Å; Cu- $K_{\alpha 2}$ = 1.5444 Å) in theta–theta geometry. The films were measured between 5° and 20° two theta, with a step-size of 0.05° two theta and a scan-speed of 3°/min. The data of the powder samples were collected between 5° and 45° two theta with a stepsize of 0.05° two theta and a scan-speed of 0.3°/min.

SEM micrographs of BS-1 were recorded with a JEOL JSM-6500F scanning electron microscope (SEM) equipped with an Oxford EDX analysis system; those of BS-2 with a Merlin (Zeiss) FE-SEM. Ellipsometry measurements were performed with a Woollam M2000D at an angle of 75° in the spectral range of 190–1000 nm. The data were fitted between 350 and 1000 nm using a Cauchy-type material as the model layer. Reflectance measurements were recorded with the same ellipsometer using s-polarized light at an incident angle of 75°.

The recording of isotherms was performed at ambient temperature using a home-made Labview-controlled gas mixer. Digital mass flow controllers (W-101A-110-P, F-201C, Bronkhorst High-Tech) ensured the accurate dosing of the carrier gas nitrogen and the liquid analyte, which was vaporized in a controlled evaporation and mixing element (W-101A, Bronkhorst High-Tech). Partial pressures (p) were calculated using the van der Waals equation.^{28,37} The relative pressure p/p_0 relates to the saturation pressure p_0 .

3.1.4 Results and Discussion

Bragg stack preparation and structural properties

Two different strategies were employed for the fabrication of 1D-MOF photonic crystals consisting of either dense or porous ZIF-8 layers, and differently sized mesoporous titanium dioxide nanoparticle derived films. Stability, pore accessibility as well as high optical quality multilayer films are key requirements for the fabrication of analyte-responsive transducer systems. Those features were addressed by the choice of suitable deposition and post-treatment parameters. For the mp-TiO₂ deposition in BS-1, both a complete removal of the

template (see [SI Figs. S11](#) and [S12](#)) as well as minimum etching of the ZIF-8 underlayer had to be achieved. In [Fig. 1](#) the X-ray diffraction patterns of both 3-bilayer Bragg stacks (photographs shown in [Fig. 2](#)) are depicted and compared to simulated data. The mild annealing temperatures employed in either case, in addition to the solvent extraction carried out under non-acidic conditions (BS-1), retain the crystallinity and stability of the ZIF-8 layers. The diffraction patterns of the multilayered ZIF-8–TiO₂ composites show excellent agreement with the simulated ZIF-8 data, apart from peak broadening, indicating a slightly smaller grain size of the ZIF-8 crystals within the BSs.

In contrast to BS-1, which features dense ZIF-8 layers, BS-2 is composed of ZIF-8 nanocrystals (approx. 50 nm diameter, see [SI Fig. S2](#)), forming uniform layers, and nanoparticle-based TiO₂ layers with TiO₂ particles around 10–15 nm in diameter. Therefore, we expect BS-2 to exhibit a fairly high degree of textural mesoporosity in both layers, in addition to the intrinsic microporosity provided by the ZIF-8 crystals.

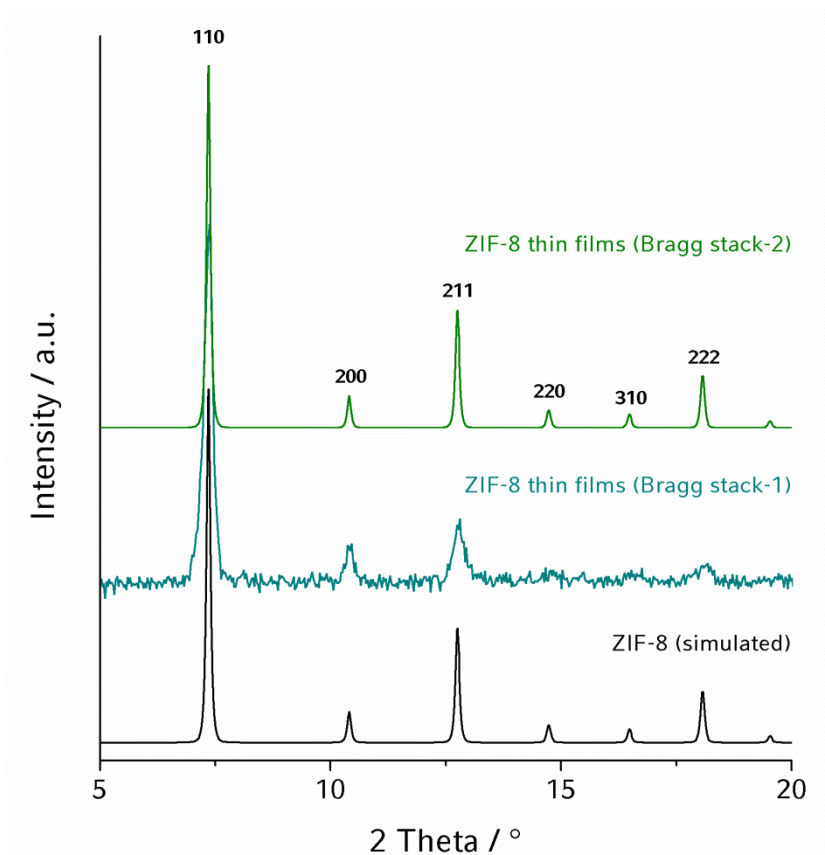


Figure 1. X-ray diffraction patterns (background corrected) of the 3-bilayer Bragg stack 1 (middle) as well as Bragg stack 2 (top) after temperature treatment and complete removal of the structure-directing agent (F127), compared to simulated data (bottom line).



Figure 2. Photographs of 3-bilayer Bragg stack 1 (left) and Bragg stack 2 (right) on a $5 \times 2.5 \text{ cm}^2$ Si substrate in air.

The coexistence of both materials embedded in the 1D-MOF PC structure is confirmed by scanning electron microscopy (SEM). In **Fig. 3** representative 3-bilayer Bragg stacks composed of alternating microporous ZIF-8 layers and porous titania layers deposited on a silicon substrate are depicted. The differently prepared Bragg stacks exhibit a ZIF-8 layer thickness of approximately 70 nm in BS-1 and about 200 nm in BS-2, respectively. TiO_2 layers deposited on each ZIF-8 film have a thickness of about 50 nm in both Bragg stacks. The cross-sectional SEM micrographs reveal that both fabrication methods yield fairly uniform layer thicknesses throughout the entire architecture. **Fig. 3** also demonstrates the alteration of both materials seen by the differences in material contrast. While the dark layers represent the ZIF-8 material exhibiting a lower electron density, the brighter thin films consist of TiO_2 nanoparticles. Not only the deposition of ZIF-8 layers on silicon, as already shown by several groups,^{15,38} but also adhesion between ZIF-8 and mesoporous/nanoparticle titania layers was achieved using our dual assembly approach. In contrast to the deposition of MOF material on inverse opal structures,^{31,32} no surface modification is necessary when preparing ZIF-8-based one-dimensional photonic structures. Regarding the stability and crystallinity of the multilayered Bragg stacks, no delamination or amorphization upon heating, extraction or adsorption of volatile species is observed, which is consistent with the corresponding XRD results (see **Fig. 1**). In conclusion, robust, uniform and high-optical quality multilayered photonic crystals composed of two different materials with varying morphologies can reproducibly be fabricated and thus provide the basis for chemical sensing studies.

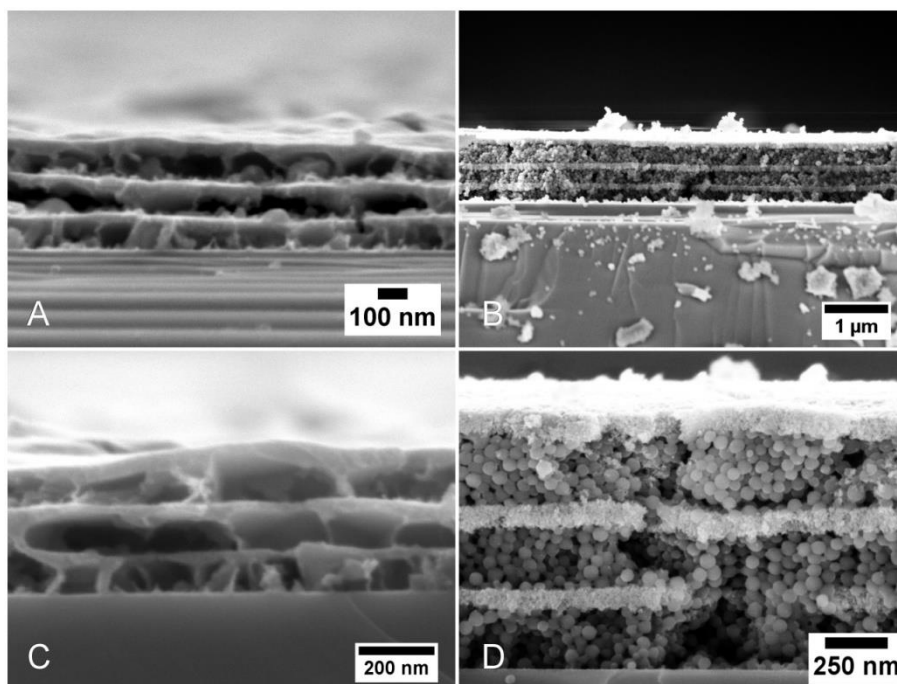


Figure 3. Scanning electron micrographs showing cross-sections of both 3-bilayer Bragg stacks with an average film thickness of ~ 50 nm for each titania layer and ~ 70 nm for each ZIF-8 layer for BS-1 (A and C) as well as for BS-2 (DMF, B and D) exhibiting a layer thickness of ~ 50 nm for each titania layer and ~ 200 nm for ZIF-8 layers, respectively. ZIF-8-TiO₂-BSs are depicted for different magnifications (A: $\times 80\,000$; B: $\times 15\,000$; C: $\times 100\,000$; D: $\times 60\,000$).

Vapor adsorption and optical sensing

The combination of a microporous MOF material with mesoporous metal oxide layers is supposed to endow the material with a unique combination of size-selectivity and analyte sensitivity. The integration of both morphologies within one photonic structure is expected to act as a molecular sieving platform, readily adsorbing analyte molecules with small kinetic diameters in both layers, whereas the access of larger guests is exclusively possible into the mesoporous titania layers. Essentials such as high specific surface areas, pore accessibility, efficient diffusion and molecular sieving abilities are all addressed by our highly porous 1D-MOF photonic crystals.

The optical response of the 1D-MOF PCs to guest adsorption was investigated by performing sorption experiments of volatile analyte molecules. According to the optical Bragg equation, sorption of volatile species into the porous layers influences the effective refractive index of a bilayer by which analyte-induced color changes can be efficiently monitored. In **Fig. 4** the reflectance spectra of both Bragg stacks are demonstrated. Here, the

optical response is triggered by the adsorption of ethanol vapor at the highest partial pressure ($p/p_0 \approx 1.0$), which entails pronounced red-shifts of the Fabry–Perot fringe of BS-1 from $\lambda \approx 585$ to $\lambda \approx 630$ nm as well as of the stop band of BS-2, derived from nanoparticles redispersed in DMF, from $\lambda \approx 740$ to $\lambda \approx 840$ nm, respectively. We attribute the significantly larger optical shift of BS-2 to the thicker ZIF-8 layers and amplified external surface area (and hence accessibility), which underlines the enhanced contribution of the “active” component to the observed overall optical shift of the BS.³⁹ Compared to the 3D-MOF (HKUST-1) hybrid photonic crystals recently reported by the groups of J. Hupp and G. Li,^{31,32} which show optical shifts of 9 nm and 16 nm upon ethanol sorption, respectively, a significant increase with respect to the optical response can be monitored in our system. However, when infiltrating 30 nm thick polystyrene template films with ZIF-8, Wu *et al.* observed a distinct shift of about 75 nm upon methanol adsorption.³² Compared to the inherently smaller absolute shifts observed with BS-1, which are presumed to result from the significantly smaller thickness of the ZIF-8 films, an even higher sensitivity upon sorption of organic vapors can be deduced from the reflectance spectrum of BS-2 (**Figs. 4** and **S21**, **SI**). Note that only a short heating period of 15 minutes at 200 °C was applied to Bragg stack 2 prior to the sorption experiments compared to the activation procedure reported by Wu *et al.*³² The samples were additionally subjected to a high-rate flow of dry nitrogen (Varian Chrompack Gas-clean Moisture Filter CP 17971, outlet concentration <0.1 ppm), which highlights the facile analyte uptake and release during a series of sorption measurements.

Analyte-induced variations of the optical thickness give rise to distinct optical shifts not only for ethanol and methanol but also for other larger analytes such as isobutanol and *tert*-pentanol. Adsorption isotherms monitoring the optical shift as a function of relative vapor pressure were recorded for BS-2 (**Fig. 5c**) as well as for the dense and porous ZIF-8 films as reference (**Figs. 5a** and **b**). The latter show that the smaller alcohols are readily adsorbed by this MOF, including analyte molecules with larger kinetic diameters compared to the aperture size of ZIF-8 (3.4 Å).³³ These results are consistent with literature data, as it was previously shown that molecules such as ethanol or isobutanol exhibiting kinetic diameters of 4.5 Å (ref. 40) and 5 Å (ref. 41) are readily adsorbed owing to the flexibility of the pore apertures in ZIF-8.^{41,42} Hence, *tert*-pentanol (2-methyl-1-propanol) was chosen as a sterically demanding analyte molecule with a kinetic diameter larger than 5 Å.⁴³ The dense ZIF-8 reference film only shows a minute optical shift of 4 nm, which is consistent with the almost complete exclusion of *tert*-pentanol from the ZIF-8 pore system (**Fig. 5a**). The

nanoparticle-based ZIF-8 film shows a larger optical shift of about 30 nm at the highest partial pressure ($p/p_0 \approx 1.0$, **Fig. 5b**), which is in agreement with the presence of a significant degree of textural mesoporosity.

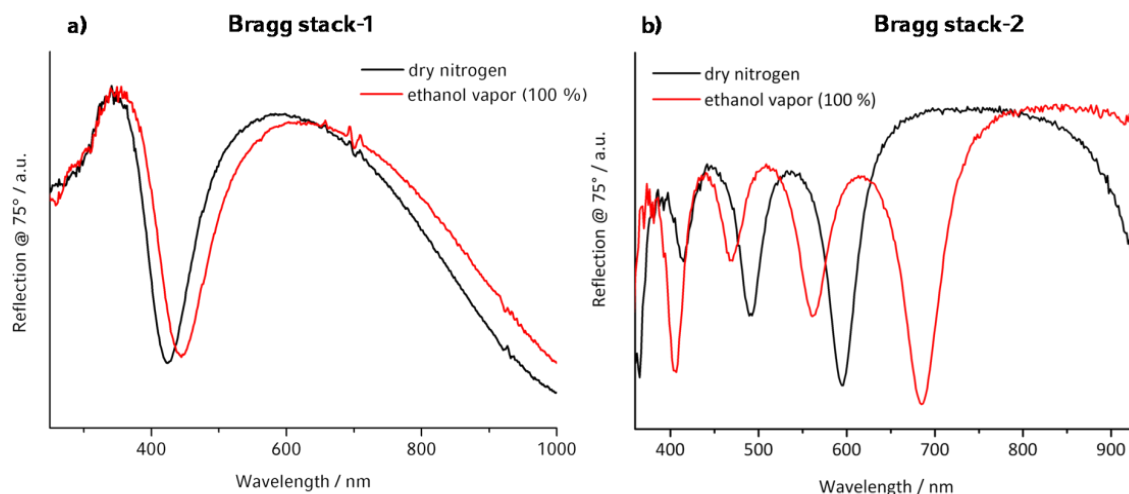


Figure 4. Reflectance spectra of Bragg stack 1 (a) and Bragg stack 2 (DMF) (b) illustrating the optical shift upon ethanol exposure recorded at the highest partial pressure ($p/p_0 \approx 1.0$).

In order to probe the host–guest interactions within the comparatively more complex Bragg stack environment, optical adsorption isotherms were recorded exemplarily for BS-2, as depicted in **Fig. 5c**. Specifically, the initial stages during adsorption of alcohol vapors and the expected pore size-specific adsorption isotherms achieved through the incorporation of different porosities are of key interest.

During the first two dosing steps the 1D-MOF Bragg stack rapidly responds to all analyte molecules, indicated by varying red-shifts ranging from 5 to 15 nm (**Fig. 5c**). At a partial pressure of $p/p_0 = 0.1$ and $p/p_0 = 0.2$, respectively, a steep increase in the methanol and ethanol isotherms is observed. However, a larger optical shift is recorded for ethanol, which is attributed to more beneficial interactions between ethanol and ZIF-8 owing to the larger hydrophobicity of ethanol compared to that of methanol. At the respective threshold pressures, pronounced optical shifts of about 50–60 nm are recorded, which gradually increase up to saturation pressure. The S-shaped isotherms upon methanol and ethanol adsorption recorded for both the single ZIF-8 films and for BS-2 are in good agreement with the results obtained by Remi *et al.*⁴⁴ The authors attribute the S-shaped isotherms to

changes in the framework triggered by interactions with guest-molecules, which was additionally confirmed and described elsewhere.⁴² In contrast to the distinct S-shaped isotherms, isobutanol sorption experiments yield an almost linearly increasing adsorption behavior with an absolute shift of about 100 nm at the highest partial pressure. In contrast, the adsorption isotherm of *tert*-pentanol exhibits a convex shape featuring the highest uptake during the first dosing steps, which we attribute to the textural porosity of both ZIF-8 and titania layers arising from the nanoparticle architecture, as seen also for the porous ZIF-8 film (**Fig. 5b**). However, this analyte exhibits the smallest overall uptake, which is consistent with the exclusion of *tert*-pentanol from the ZIF-8 pores, as demonstrated also for the porous ZIF-8 film (**Fig. 5b**). However, this analyte exhibits the smallest overall uptake, which is consistent with the exclusion of *tert*-pentanol from the ZIF-8 pores, as demonstrated also for the individual ZIF-8 films. In contrast, the smaller analytes (methanol, ethanol, isobutanol) are more readily adsorbed owing to their smaller kinetic diameters.

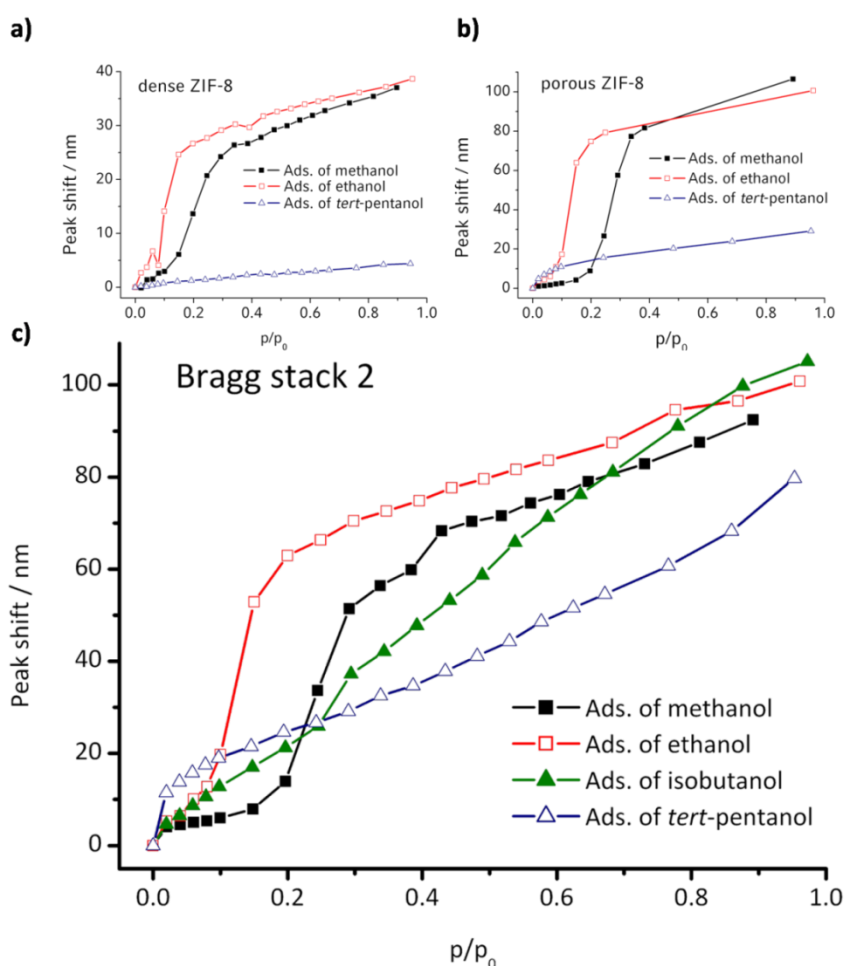


Figure 5. Optical vapor sorption isotherms demonstrating the adsorption performance of (a) dense and (b) nanoparticulate ZIF-8 reference samples as well as of (c) BS-2 (DMF) during exposure to a series of alcohol vapors.

As discussed above, an important finding is the fact that distinctly shaped isotherms are obtained for each of the four analytes over the entire relative pressure range, as additionally demonstrated by reproduced sorption experiments using Bragg stacks derived from two different synthesis batches (see [SL](#), **Fig. S22**). The characteristic sorption behavior indicates a high degree of chemical selectivity inherent to the MOF-BS, which is especially noticeable at low relative pressures. Comparison of the shapes of the isotherms for the BS and the individual ZIF-8 thin films (**Fig. 5**) confirms that the optical response is dominated by ZIF-8.

3.1.5 Conclusions

In summary, a one-dimensional MOF-based photonic crystal heterostructure with embedded micro- and mesoporosity is presented. The fabrication of the 1D-MOF PC was achieved *via* two different inexpensive bottom-up synthesis approaches. The strategy of combining a microporous MOF material with mesoporous titanium dioxide layers provides the basis for a highly sensitive signal transduction scheme with an amplified overall optical response, while maintaining high chemical specificity. Hence, molecular recognition is translated into a readable optical signal without the use of any reporter systems.

The concept of MOF-based one-dimensional photonic crystal structures extends the scope of chemoselective optical signal transducer systems. We anticipate a generalization of the assembly of 1D photonic materials in terms of the large variety and tunability of MOFs or related materials. Thus, we believe that the above proof-of-concept experiments provide a basis for the design of highly sensitive and chemically selective optical sensors.

Acknowledgments

Financial assistance from DFG (SPP 1362), the Center for Nanoscience (CeNS) and the cluster of excellence Nanosystems Initiative Munich (NIM) is gratefully acknowledged. The authors thank Dr. Steffen Schmidt and Viola Duppel for assistance with SEM data acquisition.

3.1.6 References

- 1 O. M. Yaghi, M. O’Keeffe, N. W. Ockwig, H. K. Chae, M. Eddaoudi and J. Kim, *Nature* **2003**, *423*, 705-714.
- 2 G. Férey, *Chem. Soc. Rev.* **2008**, *37*, 191-214.
- 3 U. Mueller, M. Schubert, F. Teich, H. Puetter, K. Schierle-Arndt and J. Pastre, *J. Mater. Chem.* **2006**, *16*, 626-636.
- 4 J.-R. Li, R. J. Kuppler and H.-C. Zhou, *Chem. Soc. Rev.* **2009**, *38*, 1477-1504.
- 5 S. T. Meek, J. A. Greathouse and M. D. Allendorf, *Adv. Mater.* **2011**, *23*, 249-267.
- 6 C. Scherb, J. J. Williams, F. Hinterholzinger, S. Bauer, N. Stock and T. Bein, *J. Mater. Chem.* **2011**, *21*, 14849-14856.
- 7 O. Shekhah, J. Liu, R. A. Fischer and C. Wöll, *Chem. Soc. Rev.* **2011**, *40*, 1081-1106.
- 8 M. D. Allendorf, C. A. Bauer, R. K. Bhakta and R. J. T. Houk, *Chem. Soc. Rev.* **2009**, *38*, 1330-1352.
- 9 L. E. Kreno, K. Leong, O. K. Farha, M. Allendorf, R. P. Van Duyne and J. T. Hupp, *Chem. Rev.* **2011**, *112*, 1105-1125.
- 10 H. Xu, F. Liu, Y. Cui, B. Chen and G. Qian, *Chem. Commun.* **2011**, *47*, 3153-3155.
- 11 B. Chen, L. Wang, Y. Xiao, F. R. Fronczek, M. Xue, Y. Cui and G. Qian, *Angew. Chem.* **2009**, *121*, 508-511.
- 12 B. Gole, A. K. Bar and P. S. Mukherjee, *Chem. Commun.* **2011**, *47*, 12137-12139.
- 13 K. C. Stylianou, R. Heck, S. Y. Chong, J. Bacsá, J. T. A. Jones, Y. Z. Khimyak, D. Bradshaw and M. J. Rosseinsky, *J. Am. Chem. Soc.* **2010**, *132*, 4119-4130.
- 14 Y. Takashima, V. M. Martínez, S. Furukawa, M. Kondo, S. Shimomura, H. Uehara, M. Nakahama, K. Sugimoto and S. Kitagawa, *Nat. Commun.* **2011**, *2*, 1681-1682.
- 15 G. Lu and J. T. Hupp, *J. Am. Chem. Soc.* **2010**, *132*, 7832-7833.

- 16 L. D. Bonifacio, B. V. Lotsch, D. P. Puzzo, F. Scotognella and G. A. Ozin, *Adv. Mater.* **2009**, *21*, 1641-1646.
- 17 S. John, *Phys. Rev. Lett.* **1987**, *58*, 2486-2489.
- 18 A. Arsenault, S. Fournier-Bidoz, B. Hatton, H. Miguez, N. Tetreault, E. Vekris, S. Wong, S. M. Yang, V. Kitaev and G. A. Ozin, *J. Mater. Chem.* **2004**, *14*, 781-794.
- 19 J. D. Joannopoulos, P. R. Villeneuve and S. Fan, *Nature* **1997**, *386*, 143-149.
- 20 H.-Y. Lee and T. Yao, *J. Appl. Phys.* **2003**, *93*, 819-830.
- 21 M. Bardosova, M. E. Pemble, I. M. Povey, R. H. Tredgold and D. E. Whitehead, *Appl. Phys. Lett.* **2006**, *89*, 0931161-0931163.
- 22 J. McPhillips, A. Murphy, M. P. Jonsson, W. R. Hendren, R. Atkinson, F. Höök, A. V. Zayats and R. J. Pollard, *ACS Nano* **2010**, *4*, 2210-2216.
- 23 R. Stine, J. T. Robinson, P. E. Sheehan and C. R. Tamanaha, *Adv. Mater.* **2010**, *22*, 5297-5300.
- 24 Z. Wang, J. Zhang, J. Xie, Z. Wang, Y. Yin, J. Li, Y. Li, S. Liang, L. Zhang, L. Cui, H. Zhang and B. Yang, *J. Mater. Chem.* **2012**, *22*, 7887-7893.
- 25 S. I. Khartsev and A. M. Grishin, *Appl. Phys. Lett.* **2005**, *87*, 1225041-1225043.
- 26 M. C. Fuertes, F. J. Lopez-Alcaraz, M. C. Marchi, H. E. Troiani, V. Luca, H. Miguez and G. J. A. A. Soler-Illia, *Adv. Funct. Mater.* **2007**, *17*, 1247-1254.
- 27 S. Y. Choi, M. Mamak, G. von Freymann, N. Chopra and G. A. Ozin, *Nano Lett.* **2006**, *6*, 2456-2461.
- 28 J. Kobler, B. V. Lotsch, G. A. Ozin and T. Bein, *ACS Nano* **2009**, *3*, 1669-1676.
- 29 D. Lee, M. F. Rubner and R. E. Cohen, *Nano Lett.* **2006**, *6*, 2305-2312.
- 30 S. Colodrero, M. Ocaña, A. R. González-Elipé and H. Míguez, *Langmuir* **2008**, *24*, 9135-9139.
- 31 G. Lu, O. K. Farha, L. E. Kreno, P. M. Schoenecker, K. S. Walton, R. P. Van Duyne and J. T. Hupp, *Adv. Mater.* **2011**, *23*, 4449-4452.

3 Interference-Based Readout

- 32 Y.-n. Wu, F. Li, W. Zhu, J. Cui, C.-a. Tao, C. Lin, P. M. Hannam and G. Li, *Angew. Chem. Int. Ed.* **2011**, *50*, 12518-12522.
- 33 K. S. Park, Z. Ni, A. P. Côté, J. Y. Choi, R. Huang, F. J. Uribe-Romo, H. K. Chae, M. O’Keeffe and O. M. Yaghi, *Proc. Natl. Acad. Sci. U. S. A.* **2006**, *103*, 10186-10191.
- 34 J. M. Szeifert, J. M. Feckl, D. Fattakhova-Rohlfing, Y. Liu, V. Kalousek, J. Rathousky and T. Bein, *J. Am. Chem. Soc.* **2010**, *132*, 12605-12611.
- 35 J. Cravillon, S. Münzer, S.-J. Lohmeier, A. Feldhoff, K. Huber and M. Wiebcke, *Chem. Mater.* **2009**, *21*, 1410-1412.
- 36 B. V. Lotsch, F. Scotognella, K. Moeller, T. Bein and G. A. Ozin, *Proc. SPIE* **2010**, *7713*, 7713V.
- 37 C. Scherb, R. Koehn and T. Bein, *J. Mater. Chem.* **2010**, *20*, 3046-3051.
- 38 A. Demessence, C. Boissière, D. Grosso, P. Horcajada, C. Serre, G. Férey, G. J. A. A. Soler-Illia and C. Sanchez, *J. Mater. Chem.* **2010**, *20*, 7676-7681.
- 39 M. D. Allendorf, R. J. T. Houk, L. Andruszkiewicz, A. A. Talin, J. Pikarsky, A. Choudhury, K. A. Gall and P. J. Hesketh, *J. Am. Chem. Soc.* **2008**, *130*, 14404-14405.
- 40 G. Zhu, Y. Li, H. Zhou, J. Liu and W. Yang, *Mater. Lett.* **2008**, *62*, 4357-4359.
- 41 X.-L. Liu, Y.-S. Li, G.-Q. Zhu, Y.-J. Ban, L.-Y. Xu and W.-S. Yang, *Angew. Chem. Int. Ed.* **2011**, *50*, 10636-10639.
- 42 D. Fairen-Jimenez, S. A. Moggach, M. T. Wharmby, P. A. Wright, S. Parsons and T. Düren, *J. Am. Chem. Soc.* **2011**, *133*, 8900-8902.
- 43 M. Kodaka, *J. Phys. Chem. B* **2003**, *108*, 1160-1164.
- 44 J. Cousin Saint Remi, T. Remy, V. Van Hunskerken, S. van de Perre, T. Duerinck, M. Maes, D. De Vos, E. Gobechiya, C. E. A. Kirschhock, G. V. Baron and J. F. M. Denayer, *ChemSusChem* **2011**, *4*, 1074-1077.

3.2 TANDEM MOF-BASED PHOTONIC CRYSTALS FOR ENHANCED ANALYTE-SPECIFIC OPTICAL DETECTION

Annekathrin Ranft, Felicitas Niekiel, Ida Pavlichenko, Norbert Stock, and Bettina V. Lotsch

published in *Chem. Mater.* **2015**, 27, 1961-1970

DOI: 10.1021/cm503640c

<http://pubs.acs.org/doi/abs/10.1021/cm503640c>

Reprinted with permission. © 2015 American Chemical Society

Abstract

Owing to their structural variability, metal–organic frameworks (MOFs) lend themselves well as chemical sensing materials by providing both high sensitivity and selectivity. Here, we integrate different types of MOFs (ZIF-8, HKUST-1, CAU-1-NH₂) into photonic multilayers referred to as Bragg stacks (BSs), which report on adsorption events through changes in their effective refractive index (RI). The fabrication of photonic multilayers is accomplished by spin-coating colloidal suspensions of MOF nanoparticles and/or the high RI-material TiO₂. While their incorporation in BSs allows for the label-free readout of host–guest interactions, the choice of particular types of MOFs determines the sensing properties of the BS. Here, we present MOF-based BSs with enhanced specificity toward molecular analytes by combining two different MOFs in a single platform. The sensing performance of our BSs is demonstrated by a combined spectroscopic and principal component analysis of their vapor response. Time-dependent measurements reveal fast response times and good recoverability of the multilayers. Moreover, we demonstrate that combinatorial sensing is feasible by arranging different MOF BSs in a basic color pattern, which highlights the potential of MOF-based multilayers in arrayed sensor devices.

3.2.1 Introduction

Metal-organic frameworks (MOFs) constitute a class of permanently porous materials featuring high surface areas combined with chemical functionality. Tuning the framework through the choice of the constituting building blocks¹⁻⁴ as well as through the introduction of functional groups by either direct or postsynthetic approaches⁵⁻⁷ allows the size and chemistry of the pores to be modified and, hence, the host-guest interactions between the MOF and analyte being adsorbed in the MOF structure to be controlled. Owing to their structural variability and the possibility to control their sorption properties, MOFs lend themselves well for applications where analyte-specific interactions are key to their functionality. Potential fields of application range from catalysis^{8,9} and molecular sieving or separation^{10,11} to sensing devices.^{12,13} Along with the possibility to downsize MOFs to the nanoscale and fashion them into various shapes and sizes matching the application that is sought,¹⁴⁻¹⁶ the inherent functionality of MOFs can be amplified by increasing their external surface area, which may help to improve the sensitivity of sensors or the like.¹⁷ To develop highly selective sensors, decoding MOF-analyte interactions on a molecular level is of particular importance to understand and control possible signal transduction pathways. Suitable techniques for monitoring sorption events in MOFs rely on an optical readout such as luminescence quenching¹⁸ or solvatochromism,¹⁹ on gravimetric²⁰ or mechanical transduction schemes,²¹ or X-ray diffraction²² and NMR spectroscopy²³ used as probes to monitor sorptive-induced structural changes in the framework. Despite the availability of numerous properties that can be used for signal detection, identification of appropriate transduction pathways constitutes one of the key challenges in the design of MOF sensors.¹³ For example, quartz crystal microbalance (QCM) has recently been explored as a promising transduction scheme.²⁴⁻²⁷ Here, the event of molecular adsorption is monitored by guest-dependent mass changes, which can be used, for instance, to determine diffusion constants of small molecules within MOFs.²⁷

Some MOF structures show photoluminescent behavior that can be modulated through molecular adsorption.¹⁸ However, such turn-off sensors often lack sufficient chemical selectivity and may undergo signal losses caused by phenomena other than analyte adsorption.¹³ In addition, optical transduction schemes based on interferometry have been successfully implemented into MOF-based sensing platforms, which are capable of readily detecting adsorption events in the MOF pores.²⁸⁻³⁴ Interference-based schemes benefit from

providing a label-free transduction pathway that is independent of the investigated sensing material, and they offer real-time decoding of host–guest interactions. Consequently, this route has been extended to photonic multilayer systems,^{30,31} christened 1D photonic crystals (PCs) or Bragg stacks (BSs), as well as to 3D opal structures and films,^{32–34} harnessing the change in the effective refractive index (RI) as a result of analyte adsorption in the porous MOF structure. We recently demonstrated the adsorption performance of multilayer stacks composed of alternating ZIF-8 layers and the high-RI material TiO₂ toward a range of organic vapors using spectrophotometric ellipsometry.³⁰

Besides signal transduction, the integration of MOFs into sensing devices through thin film growth techniques and the design of MOFs with desirable properties are considered to be central tasks for the development of MOF-based chemical sensors.¹³ Sensing performance is generally associated with surface properties and the microstructure of the sensing material, i.e., surface area, porosity, and film thickness. Consequently, thin layers with thicknesses up to a few hundred nanometers are commonly preferred because they permit rapid analyte uptake. Along with the detection limit and sensitivity, the response time may further be improved by using porous and particulate morphologies.¹⁷ Toward this end, a number of different growth techniques have been developed for the fabrication of thin MOF films that differ in their focus: thickness, microstructure, or crystallite orientation.^{14–16,24–29,35–37} These techniques include direct or secondary growth methods,²⁴ gel-layer deposition,³⁶ layer-by-layer (LbL) techniques,²⁶ or the use of colloidal suspensions for film deposition by spin- or dip-coating protocols.^{28,35,37} Some of these methods require pretreatment of the substrate with anchor molecules that provide a suitable interface or linkage to the growing MOF crystal.^{24,26,36} In contrast to sequential growth methods, the fabrication of thin films from colloidal suspensions offers the advantages of fast deposition and facile thickness adjustment through the choice of particle concentration and deposition speed.³⁷ In addition, such low-temperature solution processing methods are adaptive to any MOF structure that can be stabilized as a colloidal suspension and are, therefore, a generalizable route toward thin MOF films.

Besides film fabrication and choosing an appropriate transduction scheme, the rational choice of the MOF used for detection represents a key element in the fabrication of selective sensing systems. According to the application that is sought, the sorption properties of the device can be tailored by choosing a MOF with appropriate characteristic sensing features, such as hydrophilic HKUST-1 for water sensing applications.^{24,38} In this context, the challenge to specifically detect one out of a mixture of interfering analytes may be addressed

by integrating MOFs in the sensing device that show low cross-responsiveness to other analytes or through “fingerprint” approaches^{39–43} utilizing an array of different MOF sensors. Immobilized metalloporphyrin dyes, for instance, have been used to create unique color profiles that allow for the identification of chemically similar vapors by ligation of open coordination metal sites.⁴⁰ While the concept of combinatorial sensing has already been well-established in the field of metal oxides⁴² and porous silicon-based PCs,⁴³ to our knowledge, it has not been extended to optically encoded MOF sensors so far. In comparison to these materials, MOFs could offer both inherent chemo- and size-selectivity as well as enhanced chemical stability, circumventing the need for additional functionalization.

Here, we present a generic analyte detection platform based on MOF nanoparticle multilayer systems that allows for the specific and label-free detection of molecular adsorption events in real time. This strategy takes advantage of the inherent sorption properties of the MOFs and translates them into an analyte-specific optical readout. To demonstrate the feasibility of our approach, we selected ZIF-8, HKUST-1, and CAU-1-NH₂ as prototypic, well-investigated MOF structures with different framework polarities, which are available in nanoparticulate form.

To obtain a high level of specificity, we have integrated multiple MOF species into a single sensing platform (christened tandem MOF BS), which thus simultaneously encodes different types of host–guest interactions. In addition, we have developed an array-based platform utilizing the combinatorial response of multiple MOF films for analyte detection. We demonstrate the arrangement of TiO₂/MOF BSs and their response to different vapors, yielding specific color patterns that can be correlated to changes in the respective reflection spectra. Using color image analysis and principal component analysis (PCA), we show that the stacks are capable of discriminating between both single solvents and solvent mixtures.

3.2.2 Experimental Section

Chemicals

All chemicals were obtained from commercial sources and were used without further purification. Zinc nitrate hexahydrate (Zn(NO₃)₂·6H₂O, 99%) and aluminum chloride hexahydrate (AlCl₃·6H₂O, ≥99%) were purchased from Grüssing. 2-Methylimidazole (C₄H₆N₂, 99%), poly(acrylic acid) (PAA, MW = 1,800), and titanium(IV) ethoxide (Ti(OEt)₄) were purchased from Sigma-Aldrich. Benzene-1,3,5-tricarboxylic acid (H₃BTC, 98%), N,N-

3 Interference-Based Readout

dimethylformamide (DMF, p.a.), copper acetate monohydrate ($\text{Cu}(\text{OAc})_2 \cdot \text{H}_2\text{O}$, 98+%), and nitric acid (HNO_3 , puriss) were purchased from Acros. Ethanol (99%) was purchased from BfB. 2-Aminoterephthalic acid ($\text{H}_2\text{BDC-NH}_2$, $\geq 98\%$) was purchased from ABCR. Methanol was purchased from either Sigma-Aldrich (puriss) or BASF (purum).

Syntheses

Preparation of ZIF-8 nanoparticles

ZIF-8 particles were synthesized by a modified literature synthesis method.⁴⁴ $\text{Zn}(\text{NO}_3)_2 \cdot 6\text{H}_2\text{O}$ (0.73 g, 2.44 mmol) was dissolved in methanol (50 mL) and rapidly added to a solution of $\text{C}_4\text{H}_6\text{N}_2$ (1.62 g, 19.6 mmol) in 50 mL of methanol. The mixture was stirred constantly throughout the reaction until the solution turned turbid. After 1 h, the product was separated from the reaction mixture by centrifugation and washed in methanol three times. Stable colloidal suspensions of ZIF-8 were obtained by redispersing the washed product in methanol using ultrasound (Elmasonic S100H ultrasonic bath, 550 W).

Preparation of HKUST-1 nanoparticles

HKUST-1 particles were synthesized similarly to that in the literature.⁴⁵ H_3BTC (0.738 g, 3.44 mmol) was dissolved in ethanol (14 mL) and DMF (42 mL) and combined with PAA (2.21 g, 1.23 mmol). To this mixture was added a solution of $\text{Cu}(\text{OAc})_2 \cdot \text{H}_2\text{O}$ (0.7 g, 3.44 mmol) in 28 mL of deionized water under vigorous stirring, which rapidly induced the formation of a blue precipitate. After 30 min, the product was separated from the reaction mixture by centrifugation and washed in DMF at least three times. Stable colloidal suspensions of HKUST-1 were obtained by redispersing the washed product in DMF using ultrasound.

Preparation of CAU-1-NH₂ nanoparticles

CAU-1-NH₂ particles were synthesized by a modified literature protocol.⁴⁶ A mixture of $\text{H}_2\text{BDC-NH}_2$ (0.087 g, 0.468 mmol) and $\text{AlCl}_3 \cdot 6\text{H}_2\text{O}$ (0.348 g, 1.44 mmol) was suspended in 3.175 mL of methanol in a microwave tube (Biotage, 2–5 mL glass reactor) and sealed with a septum. After a prestirring time of 10 s, the reaction mixture was heated under stirring in a microwave oven (Biotage Injector) for 6 min at 145 °C. The reaction mixture was then rapidly cooled to ambient temperature using a forced air cooler, yielding a milky yellow dispersion. The product was separated from the reaction mixture by centrifugation and

3 Interference-Based Readout

washed in methanol five times. Stable colloidal suspensions of CAU-1-NH₂ were obtained by redispersing the washed product in methanol using ultrasound.

Preparation of TiO₂ nanoparticles

TiO₂ particles were synthesized according to the literature.⁴⁷ Ti(OEt)₄ (6.25 mL) was slowly added to HNO₃ (0.1 M, 37.5 mL) under stirring and heated at 80 °C for 8 h. After cooling to room temperature, the opalescent mixture was sonicated for at least 3 h. Stable colloidal suspensions of TiO₂ were obtained by repeated collection of the product by centrifugation, washing, and finally redispersing in methanol using ultrasound.

Fabrication of TiO₂/MOF Bragg stacks

Multilayer stacks consisting of thin MOF (MOF = ZIF-8, HKUST-1, CAU-1-NH₂) and TiO₂ layers were obtained in an analogous manner to that in the literature³⁰ by spin-coating the respective colloidal suspensions alternately on silicon substrates, beginning with either TiO₂ (referred to as TiO₂/MOF BS) or a MOF layer (referred to as MOF/TiO₂ BS). Prior to film deposition, silicon substrates (1×1 cm²) were treated with piranha acid (96% H₂SO₄/30% H₂O₂, 2:1 (v/v)) for 1 h, rinsed intensively with water, dried under a nitrogen stream, and plasma-cleaned (Femto plasma cleaner, Diener Electronic GmbH, air, 100 W) for 5 min. A rotational speed of 3000–4000 rpm for 30–60 s was used for the deposition of the layers, and the acceleration speed was fixed to 1500 rpm/s. The film thickness was adjusted by the particle concentration in the suspensions and by multiple coating steps. After each deposition, the film was annealed at 40 °C (for BSs containing CAU-1-NH₂) or 200 °C (all other BSs) for 15 min.

Fabrication of tandem MOF Bragg stacks

Multilayer stacks consisting of thin layers of two different MOFs (christened ZIF-8/HKUST-1 BS and ZIF-8/CAU-1-NH₂ BS) were obtained by spin-coating the respective colloidal suspensions alternately on silicon substrates, beginning with ZIF-8. The cleaning process of the substrates and the fabrication of the Tandem MOF BSs were conducted similarly to that for the fabrication of TiO₂/MOF BSs.

Characterization

XRD patterns of powders were collected using either a Huber G670 diffractometer in Guinier geometry or a Stoe Stadi P diffractometer with an image plate detector system in transmission with Ge(111)-monochromated Cu-K $_{\alpha 1}$ radiation ($\lambda = 1.54051 \text{ \AA}$). Data were collected between 5° and 45°. IR spectroscopy for the bulk material was carried out with the help of either a PerkinElmer Spektrum BX II spectrometer including an attenuated total reflectance (ATR) unit or a Bruker ALPHA-P FT-IR spectrometer in the spectral range of 4000–650 cm $^{-1}$. IR spectra of BSs were detected with a Nicolet iN10 IR microscope (Thermo Scientific) in the spectral range of 4000–675 cm $^{-1}$. Scanning electron (SE) micrographs were recorded either with a Merlin (Zeiss) FE-SEM or a JEOL JSM-6500F SEM equipped with an Oxford EDX analysis system. EDX analysis was performed using either the Oxford EDX system or a Philips ESEM XL 30 with an EDAX NEW XL-30 detection unit. Argon (nitrogen) adsorption/desorption isotherms of the bulk material were recorded at 87 K (77 K) with either an Autosorb iQ instrument (Quantachrome Instruments, Boynton Beach, FL, USA) or with a BELSORP-max apparatus (BEL Japan Inc.). Samples were outgassed in vacuo at 100 °C for 12 h (ZIF-8, HKUST-1, TiO $_2$) or at 130 °C for 3 h (CAU-1-NH $_2$). Apparent specific surface areas were calculated by using the BET method as described in the literature.⁴⁸ Micropore volumes were calculated from the adsorption branch at $p/p_0 = 0.5$. For liquid state $^1\text{H-NMR}$ investigations, the samples were dissolved in a solution of 5% NaOD in D $_2\text{O}$. The NMR spectra were recorded on a Bruker DRX500 NMR spectrometer operating at 500 MHz. Elemental analysis was carried out on an Eurovektor EuroEA elemental analyzer. Ellipsometric measurements were carried out using a Woollam M2000D at angles of 65°, 70°, and 75° in the spectral range of 190–1000 nm. The data were fitted between 300 and 1000 nm. Further fitting details are provided in the [SI](#). Sorption reflectance measurements were recorded with the same instrument using s-polarized light at an incident angle of 75°, whereas a fiber optic spectrometer (USB2000+, Ocean Optics) interfaced with an optical light microscope (DM2500 M, Leica) was used for time-dependent reflection measurements. Further sorption measurement details are provided in the [SI](#). Color image analysis was performed using the program FIJI. PCA analysis was carried out with the help of the program XLSTAT. Further analytical details are provided in the [SI](#).

3.2.3 Results and Discussion

Characterization of TiO₂/MOF Bragg stacks and tandem MOF Bragg stacks

The fabrication of MOF-based BSs was pursued by alternately spin-coating colloidal suspensions of the MOFs ZIF-8, HKUST-1, and CAU-1-NH₂ and/or the high-RI material TiO₂, yielding either BSs consisting of a single MOF species periodically stacked with TiO₂ or purely MOF-based BSs composed of two different types of MOFs (denoted tandem MOF BSs in the following). For the fabrication of the tandem MOF BSs, we used the combinations ZIF-8/HKUST-1 and ZIF-8/CAU-1-NH₂, each starting with ZIF-8 as the first layer. XRD patterns of the MOF particles gained before film deposition are depicted in **Figs. 1a–c**. Apart from peak broadening, which we attribute to the small particle size of the MOFs, the patterns show good agreement with the respective simulated patterns of the MOFs.

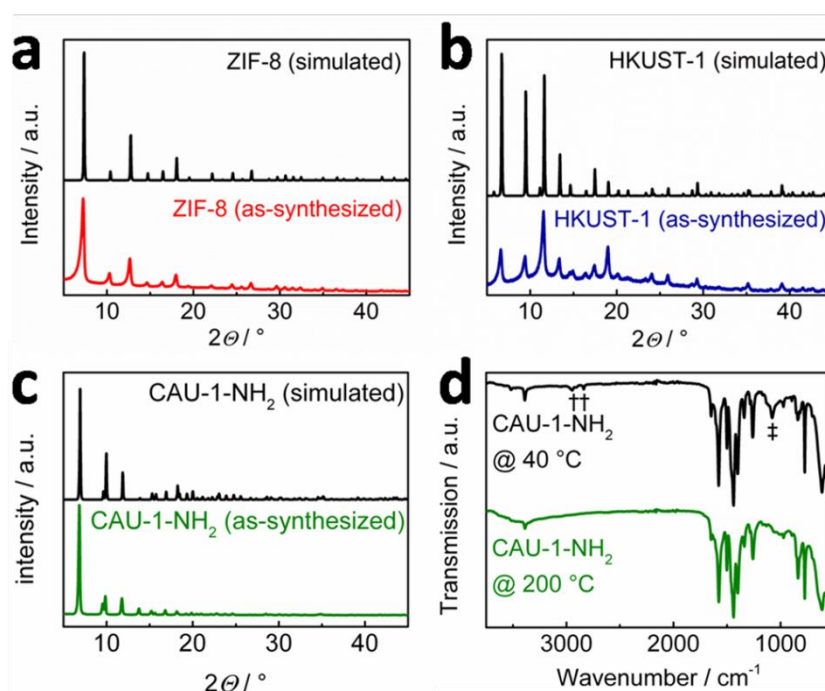


Figure 1. Powder XRD patterns of (a) ZIF-8 nanoparticles (red), (b) HKUST-1 nanoparticles (blue), (c) CAU-1-NH₂ nanoparticles (green), and respective simulated XRD patterns (black). (d) IR spectra of CAU-1-NH₂ after different thermal treatments. IR bands corresponding to C–H and C–O stretching vibrations of methoxy groups are marked by † and ‡, respectively.

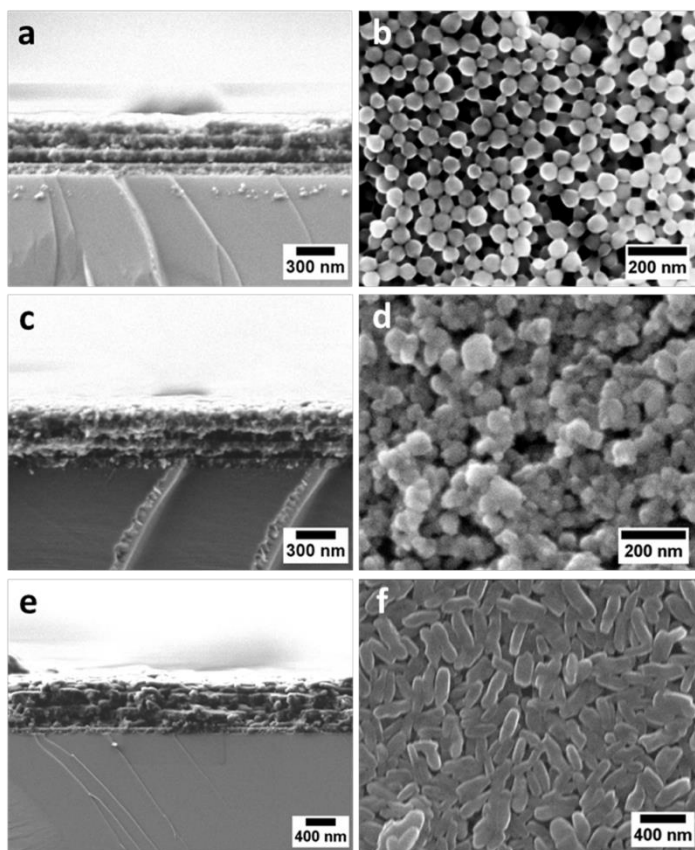


Figure 2. Cross-sectional SEM images of TiO₂/MOF BSs and top views of MOF nanoparticles on silicon substrates: (a) TiO₂/ZIF-8, (b) ZIF-8, (c) TiO₂/HKUST-1, (d) HKUST-1, (e) TiO₂/CAU-1-NH₂, and (f) CAU-1-NH₂.

The BSs were annealed at 200 °C, except for CAU-1-NH₂-based BSs, in order to remove residual solvent molecules from the porous structures as well as to enhance their mechanical stability. In contrast to HKUST-1- and ZIF-8-containing BSs, the respective CAU-1-NH₂ multilayers were dried at 40 °C to retain their composition, as CAU-1-NH₂ was shown to undergo a postsynthetic transformation from [Al₄(OH)₂(OCH₃)₄(BDC-NH₂)₃] to [Al₄(OH)₆(BDC-NH₂)₃] in air at elevated temperatures.⁴⁶ We observed the reported postsynthetic exchange of methoxy by hydroxy groups upon heating at 200 °C, as evidenced by the reduction of the IR bands for the aliphatic C–H stretching vibrations at 2950 and 2840 cm⁻¹ as well as for the C–O stretching vibration at 1080 cm⁻¹ (**Fig. 1d**). The respective IR spectra for ZIF-8 and HKUST-1, confirming the retention of these structures after heating at 200 °C, are shown in **Fig. S2** (**SI**). Besides IR spectroscopy, argon and nitrogen sorption experiments were conducted for further characterization of the bulk material (MOFs and TiO₂). The respective isotherms and derived specific surface areas and micropore volumes are provided in the **SI** (**Fig. S3** and **Table S1**). Bulk CAU-1-NH₂ was also characterized by

CHNS and EDX analysis as well as NMR spectroscopy to obtain the actual composition of the material. As-obtained CAU-1-NH₂ was washed in methanol instead of water to keep the dispersion stable for the spin-coating process. Therefore, some of the amino groups are still protonated, with Cl⁻ acting as a counterion.⁴⁶ According to the analytical data, the precise sum formula of the product washed in methanol and dried in air is [Al₄(OH)_{2.34}(CH₃O)_{3.66}(BDC-NH₂)_{1.68}(BDC-NH₃)_{1.19}(BDC-NHCH₃)_{0.13}] \cdot 1.19Cl \cdot H₂O. Despite the large counterions, the pores are still accessible, which was demonstrated by the nitrogen sorption experiments. The results of NMR spectroscopic measurements, elemental analysis, and EDX analysis are presented in the [SI](#) (**Fig. S4**, **Tables S2** and **S3**).

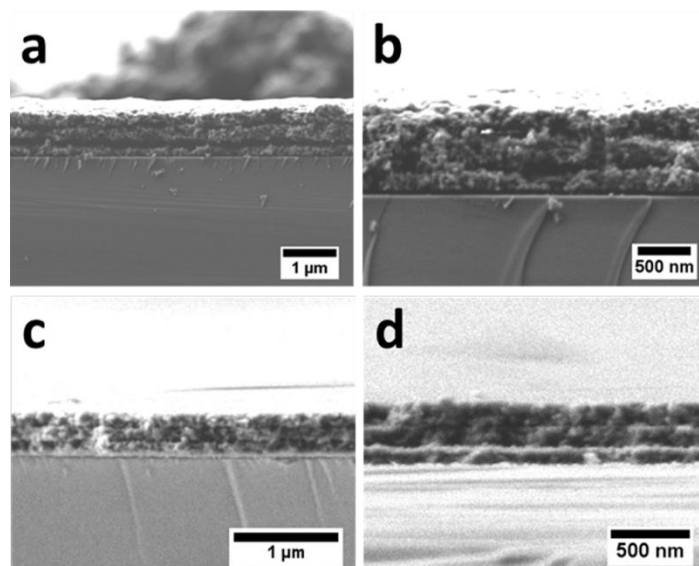


Figure 3. Cross-sectional SEM images of a ZIF-8/HKUST-1 BS (a, b) and a ZIF-8/CAU-1-NH₂ BS (c, d) on silicon substrates.

The realization of the multilayered structures is illustrated by cross-sectional SEM. Representative three-bilayer stacks for each investigated TiO₂/MOF combination as well as top-view images of MOF single layers are shown in **Fig. 2**, whereas the respective tandem MOF BSs are presented in **Fig. 3**. The successful integration of the different MOF species is demonstrated by the particulate appearance of the films, reflecting the characteristic morphology of the MOF nanoparticles. For the ZIF-8/HKUST-1 BS, the discrimination of the individual layers is impeded, as both types of MOF nanoparticles exhibit similar sizes and the scattering contrast is low due to only marginal differences in electron density of the building blocks involved. To confirm the presence of all MOFs, we used EDX analysis and

recorded IR spectra for all BSs on silicon substrates, which ascertain the successful integration and retention of the MOF structures (**Table S4** and **Fig. S5**, SI). Besides, we determined the effective RI of single MOF layers (1.20, 1.25, and 1.30 for ZIF-8, HKUST-1, and CAU-1-NH₂, respectively; see also **Table S5**, SI) and their thickness using spectroscopic ellipsometry. From the SEM images shown in **Fig. 2**, we deduce average thickness values of 71, 77, and 133 nm for ZIF-8, HKUST-1, and CAU-1-NH₂ layers, respectively, although lateral thickness variations in the stacks are observed. More SEM images showing larger details as well as photographic images of the stacks are provided in the SI (**Fig. S6**).

Vapor sorption and optical sensing with MOF-based Bragg stacks

The combination of high- and low-RI materials in a multilayer, such as TiO₂ and a MOF, creates a periodic lattice in one dimension that strongly scatters photons with wavelengths commensurate with the lattice period. The periodic potential thus gives rise to the formation of a photonic bandgap that prevents light with particular frequencies from traveling through the BS. According to the Bragg–Snell law for normal incidence, the position of the diffraction maximum λ_{\max} can be modulated by varying the optical thickness of the layers, i.e., the product of the effective RI (n) and the physical thickness h of the layers, in response to external stimuli such as adsorption of analytes, according to⁴⁹

$$m\lambda_{\max} = 2(n_L h_L + n_H h_H)$$

Here, the parameters for the low- and high-RI-material are marked with L and H, respectively, and m is the diffraction order. Due to a change in the RI contrast caused by infiltration with an analyte, the response to a stimulus can be detected by changes in the reflectance spectrum or even by the naked eye through a color change of the BS.

In order to evaluate whether our hybrid structures are suitable as sensing systems combining both sensitivity and selectivity, we exposed our TiO₂/MOF BSs to different organic vapors and monitored the response with the help of spectrophotometric ellipsometry. In **Fig. 4a**, exemplary reflectance spectra of a TiO₂/CAU-1-NH₂ BS show a significant optical shift (44 nm) upon exposure to ethanol at saturation pressure ($p/p_0 \approx 1$). The respective spectra of TiO₂/ZIF-8 and TiO₂/HKUST-1 BSs as well as the response of all TiO₂/MOF BSs to methanol at $p/p_0 \approx 1$ are presented in **Figs. S7** and **S8** (SI). The structures show pronounced shifts upon exposure to both ethanol (42 and 32 nm for ZIF-8- and

HKUST-1-based BSs, respectively) and methanol (36, 35, and 50 nm for ZIF-8, HKUST-1, and CAU-1-NH₂ BSs, respectively), which illustrates the sensitivity of all three BSs toward the investigated analytes. It should be noted that the wavelength shift of a Bragg maximum positioned at higher wavelengths (which may, for example, be due to a larger physical thickness of the layers) is generally larger compared to Bragg maxima at lower wavelengths. Hence, besides the adsorption capacity being unique for every MOF type, the response magnitude of a specific multilayer structure will also be affected by the thickness of its layers, at least to a certain extent. In addition, the apparent thickness variations in each multilayer (see **Figs. 2** and **3**) will lead to slight differences in the respective Bragg maxima for different spots on the film. A more detailed discussion concerning the validity of the shifts in terms of sample quality and experimental limitations is provided in the **SI** (Characterization Details). To make the results for different TiO₂/MOF BSs more comparable, we thus calculated the shifts ($\lambda_n - \lambda_0 = \Delta\lambda$) normalized with respect to the wavelength of the maxima λ_n (for calculation details, see **SI**, Characterization Details).

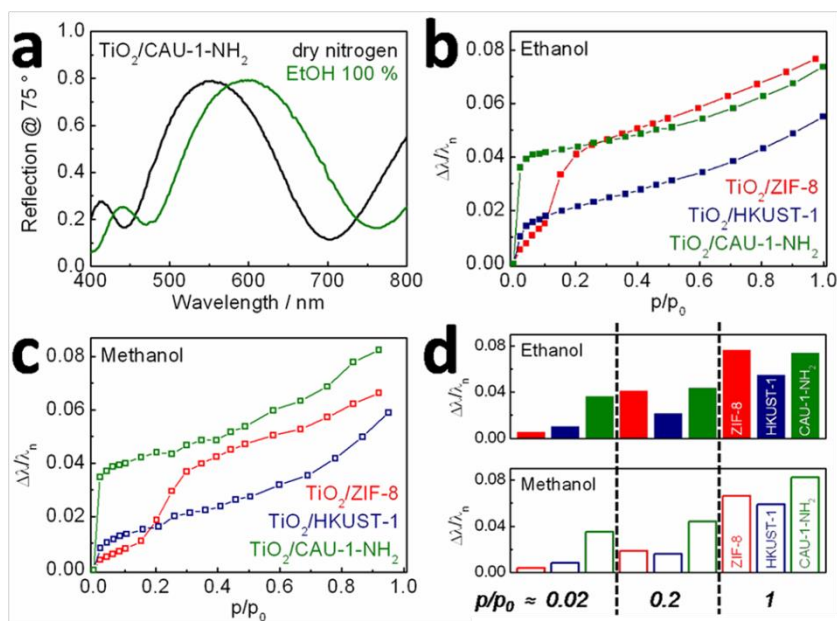


Figure 4. (a) Reflectance spectra for a TiO₂/CAU-1-NH₂ BS kept in dry nitrogen (black line) and after exposure to ethanol (green line) at the highest partial pressure ($p/p_0 \approx 1$). Optical adsorption isotherms for TiO₂/MOF BSs for ethanol (b) and methanol vapor (c). (d) Normalized peak shifts for three TiO₂/MOF BSs after adsorption of ethanol and methanol at three different pressure ranges.

3 Interference-Based Readout

By plotting the (normalized) peak shift of TiO₂/MOF BSs as a function of vapor pressure, optical vapor adsorption isotherms are obtained that demonstrate the adsorption performance of the different MOF BSs in the presence of ethanol (**Fig. 4b**) and methanol (**Fig. 4c**) at different concentrations. The ZIF-8-based BS shows an S-type isotherm at low pressures ($p/p_0 \leq 0.1$ for ethanol adsorption), which is in agreement with our previously reported results³⁰ as well as with other ZIF-8 adsorption studies.^{50,51} This particular shape is often associated with a certain flexibility of the framework induced by the interaction with analytes (gate opening), which may result in the uptake of molecules with even larger kinetic diameters than the pore entrances of ZIF-8.⁵² According to Zhang *et al.*⁵⁰ and Cousin Saint Remi *et al.*,⁵¹ the adsorption isotherms of various alcohols are shifted for ZIF-8 to lower pressures with increasing chain length and, hence, hydrophobicity. Here, the uptake for ethanol is shifted to $p/p_0 \approx 0.1$. For methanol, despite its smaller diameter, the step in the isotherm is observed at $p/p_0 \approx 0.2$, which may originate from the larger polarity in comparison to ethanol and, hence, the less beneficial analyte–framework interaction.⁵⁰ The slow but continuous increase of the curve at even higher partial pressures is attributed to the textural porosity of both TiO₂ and ZIF-8 layers.³⁰ In contrast to TiO₂/ZIF-8, HKUST-1- and CAU-1-NH₂-based BSs show a steep increase at very low vapor pressures associated with the instant uptake of the analytes in the micropores and in agreement with the rather hydrophilic nature of both MOF structures. Compared to the HKUST-1 BS, the CAU-1-NH₂ BS shows a significantly larger shift at low vapor pressures for both sorptives. The shape of the ethanol sorption isotherm for TiO₂/CAU-1-NH₂ is in good agreement with the isotherm of CAU-1 thin films on QCM gold electrodes,⁵³ which is indicative of a MOF-dominated sensing performance of the BS. Both isotherms for TiO₂/CAU-1-NH₂ and TiO₂/HKUST-1 exhibit continuously increasing curves at $p/p_0 > 0.1$, consistent with the presence of a comparatively high fraction of textural porosity. The sorption isotherms presented here suggest a lower adsorption capacity of HKUST-1 in comparison to that of the other MOFs, ZIF-8 and CAU-1-NH₂, which is in line with the sorption data of the bulk material (see **Table S1, SI**).

To evaluate the sensing performance, i.e., adsorption capacity and selectivity of the individual MOFs, the normalized shifts for each MOF BS are compared (**Fig. 4d**) by the example of three different analyte concentrations ($p/p_0 \approx 0.02$, 0.2, and 1.0). According to this chart, TiO₂/CAU-1-NH₂ shows superior sensitivity at low vapor pressures ($p/p_0 \approx 0.02$) toward both analytes in comparison to that for the other BSs. The high sensitivity of the CAU-1-NH₂ BS toward the investigated alcohols is in good agreement with the response

demonstrated for CAU-1-coated QCM electrodes.^{53,54} For HKUST-1- and ZIF-8-based BSs, a somewhat opposite sensing behavior is observed at low partial pressures: While the ZIF-8 BS shows only marginal shifts for both analytes at $p/p_0 \approx 0.02$ in comparison to $\text{TiO}_2/\text{HKUST-1}$, a pronouncedly higher shift for ethanol is observed at $p/p_0 \approx 0.2$ for $\text{TiO}_2/\text{ZIF-8}$. For methanol vapor ($p/p_0 \approx 0.2$), we found rather similar uptakes for both $\text{TiO}_2/\text{HKUST-1}$ and $\text{TiO}_2/\text{ZIF-8}$ BSs. At high vapor pressures ($p/p_0 \approx 1$), the largest sensitivity for ethanol and methanol is shown by $\text{TiO}_2/\text{ZIF-8}$ and $\text{TiO}_2/\text{CAU-1-NH}_2$ BSs, respectively, whereas a general lower adsorption capacity for the HKUST-1 BS is observed in comparison to that for the other BSs. This finding complies with the results published by Wu *et al.*,³³ which state the significantly lower sensitivity of HKUST-1 opals as compared to that of ZIF-8-based structures. However, such observations have to be treated with care, as the precise comparison is possible only under similar experimental conditions (such as analyte concentration and measurement setup) as well as comparable sample properties (e.g., thickness of the investigated films, textural porosity, accessibility of the pores). In this context, the potential presence of residual water content during the sensing experiments constitutes another important parameter in evaluating the performance of HKUST-1 sensors, as the degree of humidity has been shown to greatly influence its sorption capacity toward other analytes.^{55,56} Aside from these general considerations, the chemoselective behaviour of our MOF multilayer systems is clearly demonstrated by the different optical shifts at various partial pressures.

Besides selectivity and sensitivity, a key issue of sensing devices is the recoverability of such systems, including the ease of sorptive removal within a reasonable amount of time as well as preferably low response times toward small concentration changes. To probe the response time of our platforms, we exposed TiO_2/MOF BSs to different ethanol concentrations that were varied within short time intervals and monitored the change in reflectivity in situ at certain wavelength positions (**Fig. 5**). According to the measurements presented in **Fig. 5**, the reflectivity of all BSs changes within seconds when the concentration is altered in increments of $\geq 10\%$ and occurs reversibly with no apparent delay after concentration change. Depending on the MOF type, it takes a few seconds to reach at least 90% of the final response, as can be deduced from the graphs. For instance, upon a change from 0 to 25% ethanol vapor in the nitrogen stream, we calculated response times of about 4.5, 7.7, and 10.1 s for $\text{TiO}_2/\text{ZIF-8}$, $\text{TiO}_2/\text{HKUST-1}$, and $\text{TiO}_2/\text{CAU-1-NH}_2$, respectively (see also **Fig. S9**, **S1**), which is comparable to that of other MOF sensors.^{28,33} The initial response of our BSs upon small concentration changes is, hence, fast and produces

clearly distinguishable signals. For an estimation of the detection limit of our BSs, see the [SI](#) (Characterization Details).

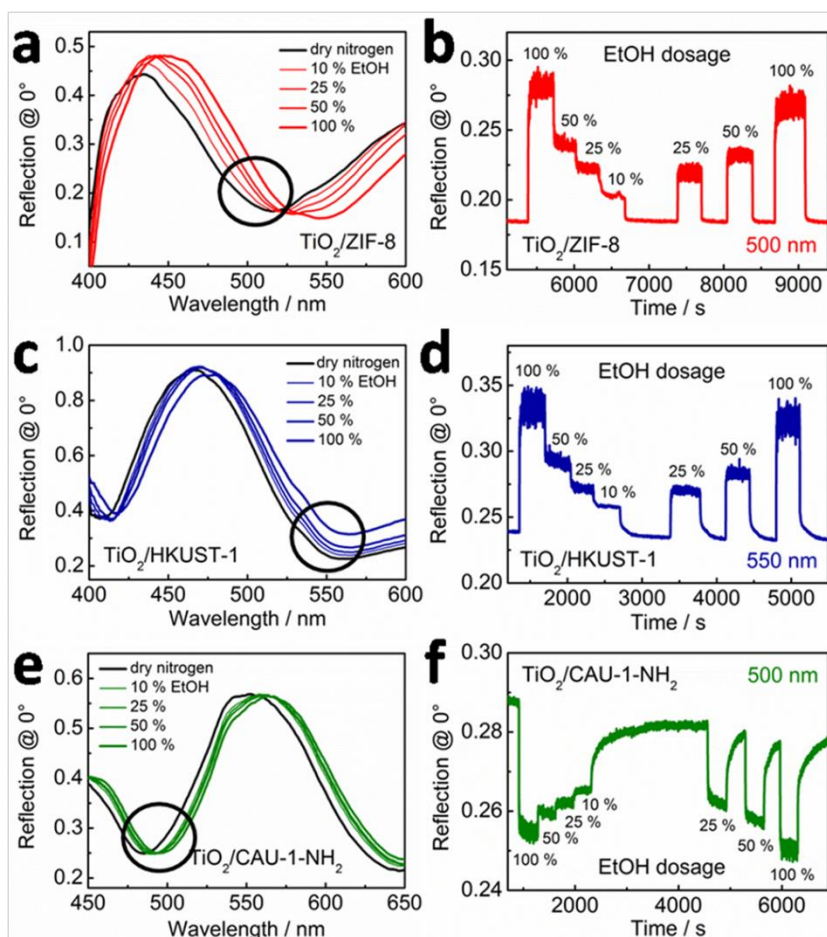


Figure 5. Reflectance spectra of TiO_2/MOF BSs and time-dependent responses of the BSs upon exposure to varying concentrations of ethanol vapor: (a, b) $\text{TiO}_2/\text{ZIF-8}$, (c, d) $\text{TiO}_2/\text{HKUST-1}$, and (e, f) $\text{TiO}_2/\text{CAU-1-NH}_2$. The response was monitored by recording the change in reflection at distinct wavelength positions (marked in the respective spectra). Close-up views of the graph positions used for calculating the response time are provided in the SI (Fig. S9).

The presented results demonstrating both high sensitivity and selectivity of TiO_2/MOF BSs as well as fast response times suggest their utility for the analyte-specific detection in arrayed sensing devices. To obtain a high level of specificity, we pursued two different strategies, both taking advantage of the combination of the characteristic sorption properties of the individual MOFs: In our first approach, we integrated two MOF species into a single sensing platform, whereas in the second approach, all three TiO_2/MOF BSs are

assembled in a basic color pattern (optical fingerprint). Both methods are envisaged to allow for the simultaneous encoding of different types of host–guest interactions. In our first approach, we evaluated the sensing performance of the tandem MOF BSs (i.e., the combination of ZIF-8 layers with either HKUST-1 or CAU-1-NH₂) by conducting similar sorption measurements as those for the TiO₂/MOF BSs (see **Figs. S10–S13** for reflectance spectra, **SI**). In **Fig. 6**, the ethanol and methanol sorption isotherms of TiO₂/MOF BSs (MOF = ZIF-8, HKUST-1) are presented in comparison to ZIF-8/HKUST-1. The ethanol sorption isotherm (**Fig. 6a**) for the tandem MOF BS shows characteristic features of the isotherms for the TiO₂/ZIF-8 BS: At $p/p_0 \approx 0.1$, an increase in the isotherm is observed that is comparable to the isotherm obtained for TiO₂/ZIF-8. This similarity can be also found in the methanol sorption isotherm of the tandem MOF BS (**Fig. 6d**): Here, a shift of the step from $p/p_0 \approx 0.1$ to $p/p_0 \approx 0.2$ in comparison to the ethanol sorption isotherm is observed, which matches well with the sorption data obtained for TiO₂/ZIF-8. In addition, we observe another step at $p/p_0 < 0.1$ in both the ethanol and methanol isotherms, matching the response of TiO₂/HKUST-1 toward methanol at very low partial pressures. The signal height, however, turns out to be rather small in comparison to the clearly visible step at $p/p_0 \approx 0.1$ (0.2) for ethanol (methanol). We rationalize this finding with the different adsorption capacities of the MOFs: By taking into account the low adsorption capacity of HKUST-1, which we deduce from the sorption data of the bulk material (**Fig. S3** and **Table S1**, **SI**), and the sorption measurements of TiO₂/HKUST-1 (**Figs. 4b** and **c**), the signal for the uptake in the pores of HKUST-1 is likely overlapped by the comparatively larger signal caused by the interaction of the sorptive with ZIF-8. By increasing the thickness of HKUST-1 layers, which can be facilely done through multiple spin-coating steps, the magnitude of the HKUST-1 response may increase as well. In order to test this assumption, we prepared a series of tandem MOF BSs with different relative layer thicknesses of the individual MOFs and repeated the adsorption experiments. The integration of differing amounts of MOFs is confirmed by EDX analysis (**Table S4**, **SI**). In **Fig. 6b**, we depict exemplarily the adsorption performance of three ZIF-8/HKUST-1 BSs toward ethanol vapor with gradually increasing layer thicknesses of HKUST-1. At high ZIF-8 content, two clearly distinguishable steps ($p/p_0 < 0.1$ and $p/p_0 \approx 0.1$) in the ethanol sorption isotherm are observed. When the thickness of the HKUST-1 layers is increased, the step height at $p/p_0 < 0.1$ seems to increase as well, which is consistent with the larger amount of available HKUST-1 micropores. We observed a similar trend when subjecting the BSs to methanol vapor (**Fig. 6e**).

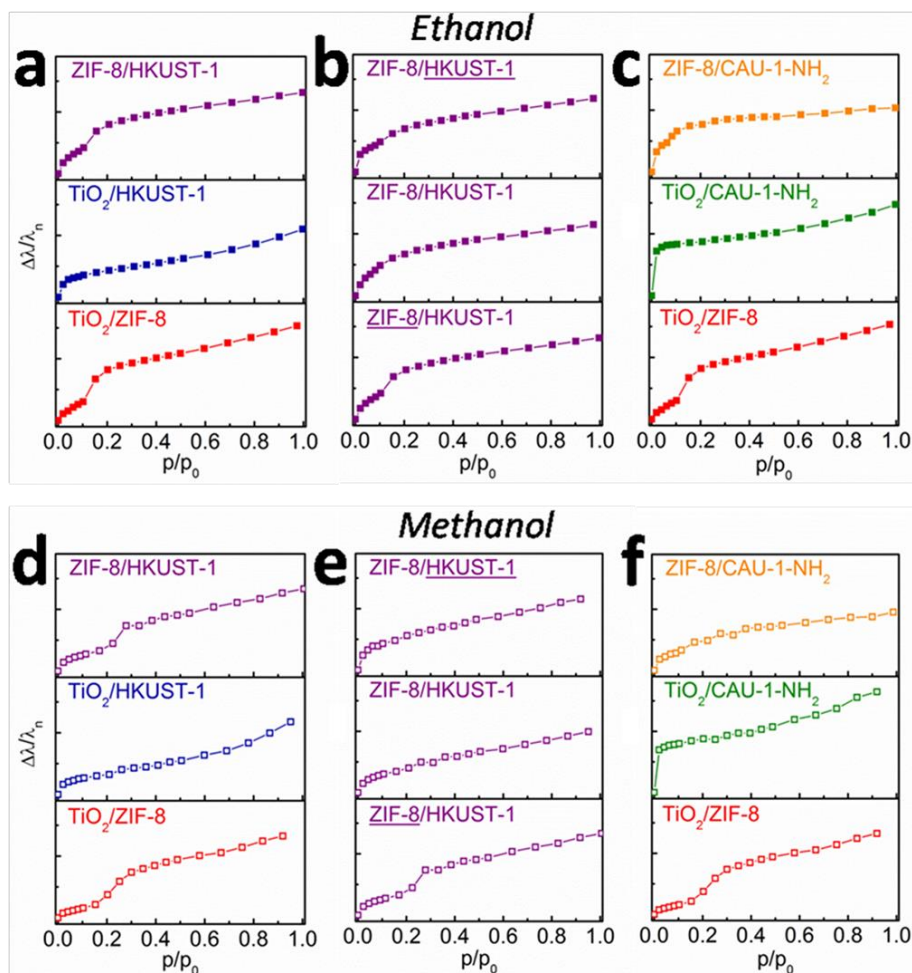


Figure 6. (a) Ethanol and (d) methanol sorption isotherms of a ZIF-8/HKUST-1 BS in comparison to the respective isotherms of $\text{TiO}_2/\text{HKUST-1}$ and $\text{TiO}_2/\text{ZIF-8}$ BSs. (b) Ethanol and (e) methanol sorption isotherms of three ZIF-8/HKUST-1 BSs with different layer thicknesses. The thickness of the ZIF-8 layers is increased from top to bottom (highlighted by underlines), whereas the HKUST-1 content is decreased. (c) Ethanol and (f) methanol sorption isotherms of a ZIF-8/CAU-1-NH₂ BS in comparison to the respective isotherms of $\text{TiO}_2/\text{CAU-1-NH}_2$ and $\text{TiO}_2/\text{ZIF-8}$ BSs.

In order to probe the versatility of our tandem MOF multilayers, we conducted similar adsorption experiments with another heterostructure (ZIF-8/CAU-1-NH₂) and compared them to the adsorption isotherms measured for $\text{TiO}_2/\text{ZIF-8}$ and $\text{TiO}_2/\text{CAU-1-NH}_2$ (Figs. 6c and f). The isotherms for ZIF-8/CAU-1-NH₂ show clear, yet somewhat less pronounced, characteristic features of the respective single-component BSs compared to ZIF-8/HKUST-1. This finding may be explained by a mutual influence arising from the presence of direct interfaces between the two MOFs, which, along with the sequence of the multilayer, may affect the individual sorption behavior of the MOFs. Such effects have been already described for oxide bilayers exhibiting different (textural) porosities⁵⁷ or binary Janus MOF

3 Interference-Based Readout

coatings⁵⁸ and may also occur in our tandem MOF BSs, leading to a somewhat synergistic sensing behavior. Tuning the layer thicknesses of either ZIF-8 or CAU-1-NH₂ (see **Fig. S14**, **SI**, for the isotherms) leads to no apparent enhancement of one or the other MOF signature in contrast to the case of ZIF-8/HKUST-1. While the response of ZIF-8/HKUST-1 toward the investigated analytes seems to be characterized by the sorption properties of the individual BS components, the ZIF-8/CAU-1-NH₂ BS shows a more complex response that may be mediated by the mutual interactions between its layers. Despite these differences in the sensing behavior of the two tandem MOF BSs, the versatility of such multilayers is demonstrated by tailoring the sorption properties toward a particular analyte through the judicious choice of the constituting MOF structures as well as by fine-tuning the dimensions of the individual layers. The impact of these parameters and their tailoring toward a specific sorption profile is currently being investigated in our group.

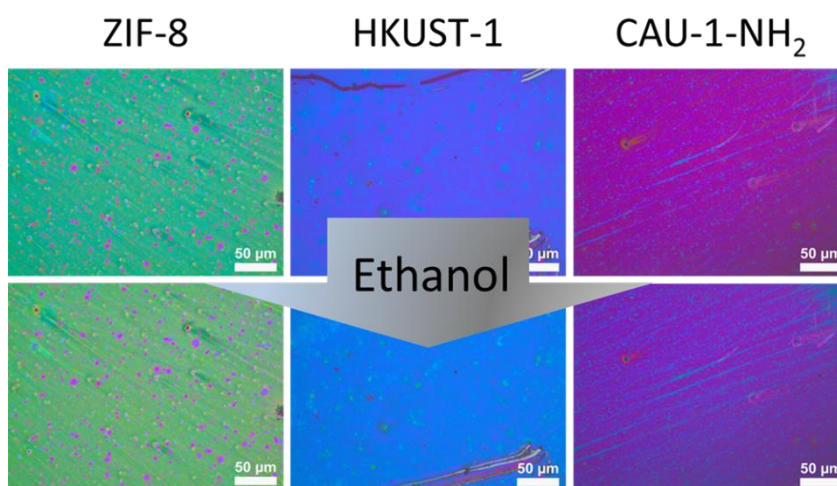


Figure 7. Photographic images of an array assembled from ZIF-8/TiO₂, TiO₂/HKUST-1, and TiO₂/CAU-1-NH₂ BSs, illustrating the color change of the array upon exposure to ethanol vapor (lower row) in comparison to pure nitrogen (upper row).

In our second approach toward enhanced analyte specificity, we pursued the fabrication of an arrayed setup assembled from multiple MOF-based multilayers. In general, arrayed sensing devices are built up of different sensing films arranged in a specific pattern. Depending on the transduction scheme, the sensor–analyte interaction generates a unique signature with enhanced analyte specificity in comparison to that of the individual sensors, owing to the combinatorial response. As a first step toward such an array derived from

3 Interference-Based Readout

photonic MOF multilayer structures, we arranged all three MOF-based BSs on a glass substrate in a home-built chamber (see **Fig. S15**, [SI](#) for images of the setup and the array). In this chamber, a stream of nitrogen saturated with the analyte was injected, and the evolution of the color upon analyte uptake was monitored in situ with a camera attached to the microscope.

As illustrated in **Fig. 7**, showing optical images of the individual films, the PC array exposed to ethanol vapor shows a clearly visible color change in comparison to the array subjected to pure nitrogen. The response, i.e., color signature of a similar arrayed setup to a range of different analytes including ethanol, water, 2-propanol, and 1-hexanol, is shown in **Fig. S16** ([SI](#)). We confirmed these changes by simultaneously recording the evolution of the reflection spectra for each BS (**Figs. S17–S19**, [SI](#)) and determined the respective spectral shifts for each sorptive after 5 min exposure. By assigning these values to the respective TiO₂/MOF BSs, we obtain unique numerical codes that are specific for each investigated analyte (**Table 1**; see **Table S6**, [SI](#) for normalized values). According to **Table 1**, HKUST-1- and CAU-1-NH₂-based BSs show comparatively high sensitivity to water, which agrees well with the hydrophilic nature of both MOF structures. A moderate shift is observed for the TiO₂/ZIF-8 BS upon exposure to water due to the hydrophobicity of ZIF-8, which is somewhat counterbalanced by adsorption of water in the TiO₂ nanoparticulate layers. For all TiO₂/MOF BSs, we observe a reduced uptake of 1-hexanol, which may be related to its bulkiness in comparison to that of the other analytes.

Table 1. Peak shifts for an array assembled from three TiO₂/MOF BSs upon exposure to different sorptives.

Sorptive	Peak shifts (nm) ^a		
	TiO ₂ /ZIF-8	TiO ₂ /HKUST-1	TiO ₂ /CAU-1-NH ₂
Water	5.4	8.0	9.3
Ethanol	18.0	11.9	7.5
2-Propanol	15.9	13.4	10.0
1-Hexanol	3.9	2.5	1.1

^aValues derived from the respective reflection spectra shown in Figs. S17–S19 ([SI](#)).

To interpret and classify the individual sorption characteristics of the stacks, we have recorded photographic images of the samples before and after exposure to the vapors and extracted the respective RGB values by image analysis. Such approaches based on color image analysis rather than on spectroscopic shifts have already been successfully implemented in the analysis of colorimetric combinatorial platforms.⁴² Here, we exposed our samples to an alternate stream of either pure nitrogen or nitrogen saturated with a solvent and recorded images for specific spots on the samples under constant light conditions. The analysis of the images was performed using a code developed with the program FIJI that involves alignment of the images, area selection, and calculation of the mean RGB intensities (see [SI](#) for a more detailed description of the experimental setup and image processing). In **Fig. 8a**, the extracted mean RGB values and channel images are exemplarily shown as unique patterns for all three BS samples upon exposure to nitrogen (left side) in comparison to ethanol adsorption (right side). The as-obtained values were then used to determine the differences ΔR , ΔG , and ΔB for each BS sample (**Fig. 8b**, calculated for ethanol) and each investigated analyte (**Fig. 8c**, values represented by gray X's in the matrix). Note that the values represent mean values derived from three measurements per solvent and BS sample (see **Tables S7–S9**, [SI](#), for complete lists of all extracted and calculated intensities). The reproducibility of the measurements is demonstrated by the reversibility of the respective RGB intensities upon switching from pure nitrogen to the solvent or solvent mixture (**Figs. S20 and S21**, [SI](#)).

The extracted values can then be used to analyze the individual capability of the BSs to discriminate between different analyte vapors. To this end, we performed principal component analysis (PCA) based on the characteristic RGB codes for each stack. The thus-obtained PCA plots are depicted in **Figs. 9a–c** for $\text{TiO}_2/\text{ZIF-8}$, $\text{TiO}_2/\text{HKUST-1}$, and $\text{TiO}_2/\text{CAU-1-NH}_2$ BSs, respectively. Each plot shows a 2D projection of the factor scores calculated for each observation (i.e., solvent), whereas the first component, F1, and the second, F2, account for the largest variance of the measurements. From **Fig. 9a**, we can see that $\text{TiO}_2/\text{ZIF-8}$ BS shows a rather poor discrimination capability for methanol, ethanol, and 2-propanol, as these points cluster in similar regions, whereas the points for water and 1-hexanol are clearly separated from the former solvents. The first two principal components (F1 and F2) account for 93.25% of the variance. For $\text{TiO}_2/\text{HKUST-1}$ BS (**Fig. 9b**), we observe a separation of methanol from the groups 2-propanol/ethanol and 1-hexanol/water (F1 + F2: 99.89%). The CAU-1-NH₂ BS shows a comparatively better distribution and, hence, discrimination of the analytes (**Fig. 9c**), indicated by a clear separation of all five points (F1

3 Interference-Based Readout

+ F2: 100%). The three MOF BSs hence show clearly different degrees of discrimination between the investigated analytes, which could be useful in a combinatorial response for analyzing, for instance, mixtures of vapors.

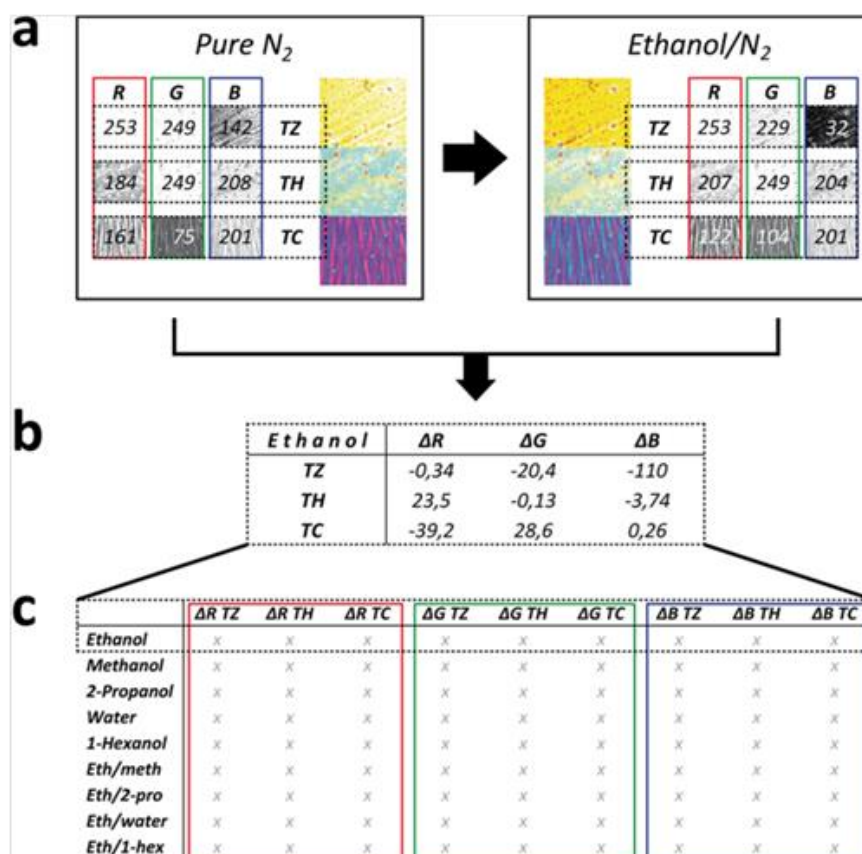


Figure 8. Scheme illustrating the basic steps of color image analysis and determination of analyte-specific numerical codes. (a) Photographic images of an array assembled from TiO₂/ZIF-8, TiO₂/HKUST-1, and TiO₂/CAU-1-NH₂ BSs are recorded for the exposure to nitrogen and a sorptive, respectively (exemplarily shown for ethanol). After alignment and area selection, the images are split in the respective color channels, and the mean RGB intensities are extracted. (b) On the basis of average RGB intensities obtained for three measurements, the differences ΔR (G, B) = R_{sorptive} (G, B) - R_{N_2} (G, B) are calculated. (c) Image processing and calculation of ΔR (G, B) are performed for all investigated analytes, yielding a 9 × 9 matrix.

As a proof of concept, we used the extracted data for four solvent mixtures (ethanol with methanol, 2-propanol, water, or 1-hexanol in volume ratios of 1:1) to perform PCA with all nine variables (i.e., ΔR (TZ, TH, TC) and so forth) which allows us to evaluate the combinatorial capability of the stacks for analyte discrimination. According to **Fig. 9d**, the array shows a clear separation and, hence, discrimination of all analytes (F1 + F2: 91.64%). If we calculate individual plots for each of the RGB channels (see **Fig. S22**, **SI**), then the best

separation result is obtained when monitoring the B channel (F1 + F2: 86.73%). In this case, already the extraction of the B intensities would be sufficient to allow the solvent mixtures to be discriminated. If the PCA is performed as a function of the individual BS samples (i.e., only the RGB values for TiO₂/ZIF-8 are considered and so forth), then both TiO₂/ZIF-8 and TiO₂/CAU-1-NH₂ BSs show a comparatively high degree of separation for three of the four solvents (**Fig. S23, SI**; F1 + F2: 92.07 and 99.32%, respectively), which may be the reason for the good discrimination capability of the complete array.

Our BS array hence shows clearly visible color changes upon analyte exposure and allows for the instantaneous detection of different guest species by monitoring both the color profile and the respective reflectance spectra. Evaluating these coupled detection routes (i.e., color signature and reflection spectra) thus provides an efficient tool to monitor adsorption events at low concentrations, and the precision of the generated analyte signatures is enhanced owing to the dual readout.

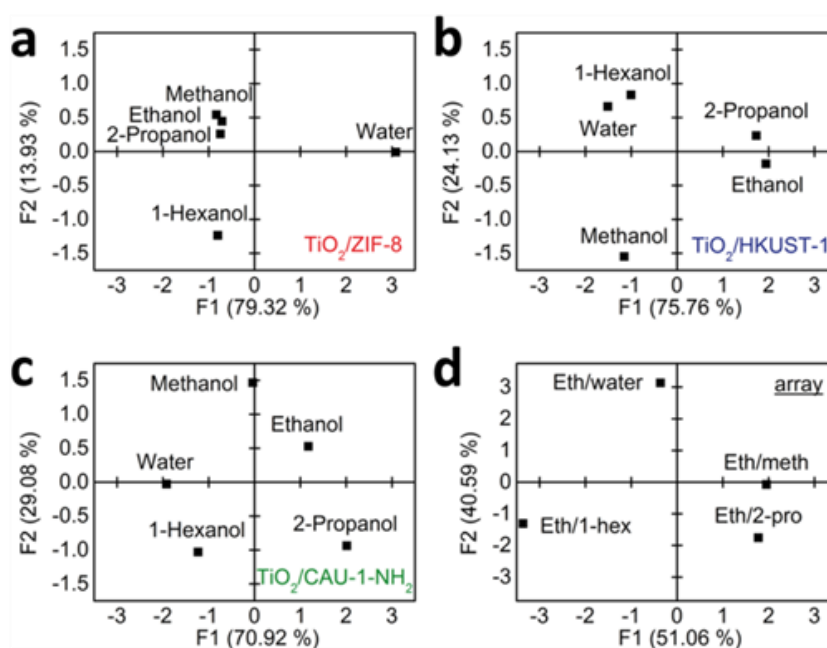


Figure 9. PCA plots for (a) TiO₂/ZIF-8, (b) TiO₂/HKUST-1, and (c) TiO₂/CAU-1-NH₂ BSs, illustrating the individual discrimination capability of each BS toward pure solvent vapors (ethanol, methanol, 2-propanol, water, and 1-hexanol). (d) PCA plot for an array assembled from TiO₂/ZIF-8, TiO₂/HKUST-1, and TiO₂/CAU-1-NH₂ BSs, illustrating the combinatorial capability for discriminating between solvent mixtures (ethanol with methanol, 2-propanol, water, and 1-hexanol).

3.2.4 Conclusions

In summary, we have presented the fabrication of photonic multilayers based on three prototypic MOFs (ZIF-8, HKUST-1, CAU-1-NH₂), which allow for the macroscopic optical detection of analyte-selective host–guest interactions occurring on the molecular level. The sensing performance of our systems was analyzed by vapor sorption experiments under ambient conditions, which allow for both identifying and quantifying the analyte. Our results thus demonstrate, in accordance with other transduction methods such as surface acoustic wave sensors³⁸ or workfunction-based detection,⁵⁶ that MOF coatings possess excellent sensitivity. The shapes of the optical adsorption isotherms of TiO₂/MOF BSs show the signature of the active MOF species, pointing to a MOF-dominated response. Moreover, along with the large variety of MOF structures, the use of MOFs as active components in PC sensors provides a convenient means to discriminate between mutually interfering analytes. We show that cross-responsivity can be minimized by using specific types of MOFs with different polarities combined with principal component analysis of their color-coded optical response.

The isotherms of tandem MOF BSs show enhanced complexity and increased analyte specificity. By simultaneously encoding multiple host–guest interactions in a single BS, we demonstrate the potential for MOF-based analyte detection *via* multiplexing schemes. We hypothesize that the interfaces between two MOFs as well as the sequence of the MOF layers in a BS influence their individual sorption behavior and may lead to synergistic behavior or a slowing of analyte uptake. This possibility will be explored further. Furthermore, we have developed a MOF-based BS array to enhance the analyte-specific readout, similar to the color-coding principles used in a biochip. The color pattern obtained after analyte exposure can ultimately be used as an analyte-specific fingerprint, which we demonstrated through principal component analysis. Important performance parameters of our MOF-based sensors were investigated, revealing good recoverability and response times on the order of 5–10 s.

Acknowledgments

We thank Prof. T. Bein for granting access to the ellipsometer and V. Duppel, C. Minke, S. Hug, C. Argyo, and L. Nichols for their assistance with the material analysis.

3.2.5 References

- 1 M. Eddaoudi, D. B. Moler, H. Li, B. Chen, T. M. Reineke, M. O'Keeffe and O. M. Yaghi, *Acc. Chem. Res.* **2001**, *34*, 319-330.
- 2 M. Eddaoudi, J. Kim, N. Rosi, D. Vodak, J. Wachter, M. O'Keeffe and O. M. Yaghi, *Science* **2002**, *295*, 469-472.
- 3 A. K. Cheetham, C. N. R. Rao and R. K. Feller, *Chem. Commun.* **2006**, 4780-4795.
- 4 R. Haldar and T. K. Maji, *CrystEngComm* **2013**, *15*, 9276-9295.
- 5 M. I. H. Mohideen, B. Xiao, P. S. Wheatley, A. C. McKinlay, Y. Li, A. M. Z. Slawin, D. W. Aldous, N. F. Cessford, T. Düren, X. Zhao, R. Gill, K. M. Thomas, J. M. Griffin, S. E. Ashbrook and R. E. Morris, *Nat. Chem.* **2011**, *3*, 304-310.
- 6 S. M. Cohen, *Chem. Rev.* **2012**, *112*, 970-1000.
- 7 M. Lammert, S. Bernt, F. Vermoortele, D. E. De Vos and N. Stock, *Inorg. Chem.* **2013**, *52*, 8521-8528.
- 8 J. Lee, O. K. Farha, J. Roberts, K. A. Scheidt, S. T. Nguyen and J. T. Hupp, *Chem. Soc. Rev.* **2009**, *38*, 1450-1459.
- 9 M. Ranocchiari and J. A. v. Bokhoven, *Phys. Chem. Chem. Phys.* **2011**, *13*, 6388-6396.
- 10 E. L. First, C. E. Gounaris and C. A. Floudas, *Langmuir* **2013**, *29*, 5599-5608.
- 11 Q. Yang, D. Liu, C. Zhong and J.-R. Li, *Chem. Rev.* **2013**, *113*, 8261-8323.
- 12 R. J. Kuppler, D. J. Timmons, Q.-R. Fang, J.-R. Li, T. A. Makal, M. D. Young, D. Yuan, D. Zhao, W. Zhuang and H.-C. Zhou, *Coordin. Chem. Rev.* **2009**, *253*, 3042-3066.
- 13 L. E. Kreno, K. Leong, O. K. Farha, M. Allendorf, R. P. Van Duyne and J. T. Hupp, *Chem. Rev.* **2012**, *112*, 1105-1125.
- 14 A. Carne, C. Carbonell, I. Imaz and D. MasPOCH, *Chem. Soc. Rev.* **2011**, *40*, 291-305.
- 15 N. Stock and S. Biswas, *Chem. Rev.* **2012**, *112*, 933-969.
- 16 E. A. Flügel, A. Ranft, F. Haase and B. V. Lotsch, *J. Mater. Chem.* **2012**, *22*, 10119-10133.

- 17 S. Cao, G. Gody, W. Zhao, S. Perrier, X. Peng, C. Ducati, D. Zhao and A. K. Cheetham, *Chem. Sci.* **2013**, *4*, 3573-3577.
- 18 M. D. Allendorf, C. A. Bauer, R. K. Bhakta and R. J. T. Houk, *Chem. Soc. Rev.* **2009**, *38*, 1330-1352.
- 19 Z.-Z. Lu, R. Zhang, Y.-Z. Li, Z.-J. Guo and H.-G. Zheng, *J. Am. Chem. Soc.* **2011**, *133*, 4172-4174.
- 20 A. J. Fletcher, E. J. Cussen, T. J. Prior, M. J. Rosseinsky, C. J. Kepert and K. M. Thomas, *J. Am. Chem. Soc.* **2001**, *123*, 10001-10011.
- 21 M. D. Allendorf, R. J. T. Houk, L. Andruszkiewicz, A. A. Talin, J. Pikarsky, A. Choudhury, K. A. Gall and P. J. Hesketh, *J. Am. Chem. Soc.* **2008**, *130*, 14404-14405.
- 22 S. Henke, D. C. Florian Wieland, M. Meilikhov, M. Paulus, C. Sternemann, K. Yussenko and R. A. Fischer, *CrystEngComm* **2011**, *13*, 6399-6404.
- 23 Y. Jiang, J. Huang, B. Kasumaj, G. Jeschke, M. Hunger, T. Mallat and A. Baiker, *J. Am. Chem. Soc.* **2009**, *131*, 2058-2059.
- 24 E. Biemmi, A. Darga, N. Stock and T. Bein, *Microporous Mesoporous Mater.* **2008**, *114*, 380-386.
- 25 C.-Y. Huang, M. Song, Z.-Y. Gu, H.-F. Wang and X.-P. Yan, *Environ. Sci. Technol.* **2011**, *45*, 4490-4496.
- 26 H. Gliemann and C. Wöll, *Mater. Today* **2012**, *15*, 110-116.
- 27 O. Zybaylo, O. Shekhah, H. Wang, M. Tafipolsky, R. Schmid, D. Johannsmann and C. Wöll, *Phys. Chem. Chem. Phys.* **2010**, *12*, 8093-8098.
- 28 A. Demessence, C. Boissière, D. Grosso, P. Horcajada, C. Serre, G. Férey, G. J. A. A. Soler-Illia and C. Sanchez, *J. Mater. Chem.* **2010**, *20*, 7676-7681.
- 29 G. Lu and J. T. Hupp, *J. Am. Chem. Soc.* **2010**, *132*, 7832-7833.
- 30 F. M. Hinterholzinger, A. Ranft, J. M. Feckl, B. Rühle, T. Bein and B. V. Lotsch, *J. Mater. Chem.* **2012**, *22*, 10356-10362.
- 31 G. Lu, O. K. Farha, W. Zhang, F. Huo and J. T. Hupp, *Adv. Mater.* **2012**, *24*, 3970-3974.

- 32 G. Lu, O. K. Farha, L. E. Kreno, P. M. Schoenecker, K. S. Walton, R. P. Van Duyne and J. T. Hupp, *Adv. Mater.* **2011**, *23*, 4449-4452.
- 33 Y.-n. Wu, F. Li, W. Zhu, J. Cui, C.-a. Tao, C. Lin, P. M. Hannam and G. Li, *Angew. Chem. Int. Ed.* **2011**, *50*, 12518-12522.
- 34 C. Cui, Y. Liu, H. Xu, S. Li, W. Zhang, P. Cui and F. Huo, *Small* **2014**, *10*, 3672-3676.
- 35 H. Guo, Y. Zhu, S. Qiu, J. A. Lercher and H. Zhang, *Adv. Mater.* **2010**, *22*, 4190-4192.
- 36 A. Schoedel, C. Scherb and T. Bein, *Angew. Chem. Int. Ed.* **2010**, *49*, 7225-7228.
- 37 J. Kobler, B. V. Lotsch, G. A. Ozin and T. Bein, *ACS Nano* **2009**, *3*, 1669-1676.
- 38 A. L. Robinson, V. Stavila, T. R. Zeitler, M. I. White, S. M. Thornberg, J. A. Greathouse and M. D. Allendorf, *Anal. Chem.* **2012**, *84*, 7043-7051.
- 39 T. A. Dickinson, J. White, J. S. Kauer and D. R. Walt, *Nature* **1996**, *382*, 697-700.
- 40 N. A. Rakow and K. S. Suslick, *Nature* **2000**, *406*, 710-713.
- 41 A. Hierlemann and R. Gutierrez-Osuna, *Chem. Rev.* **2008**, *108*, 563-613.
- 42 L. D. Bonifacio, D. P. Puzzo, S. Breslav, B. M. Willey, A. McGeer and G. A. Ozin, *Adv. Mater.* **2010**, *22*, 1351-1354.
- 43 F. Cunin, T. A. Schmedake, J. R. Link, Y. Y. Li, J. Koh, S. N. Bhatia and M. J. Sailor, *Nat. Mater.* **2002**, *1*, 39-41.
- 44 J. Cravillon, S. Münzer, S.-J. Lohmeier, A. Feldhoff, K. Huber and M. Wiebcke, *Chem. Mater.* **2009**, *21*, 1410-1412.
- 45 A. Ranft, S. B. Betzler, F. Haase and B. V. Lotsch, *CrystEngComm* **2013**, *15*, 9296-9300.
- 46 T. Ahnfeldt, D. Gunzelmann, J. Wack, J. Senker and N. Stock, *CrystEngComm* **2012**, *14*, 4126-4136.
- 47 B. V. Lotsch, F. Scotognella, K. Moeller, T. Bein and G. A. Ozin, *Proc. SPIE* **2010**, *7713*, 77130V-77110.
- 48 J. Rouquerol, P. Llewellyn and F. Rouquerol, *Stud. Surf. Sci. Catal.* **2007**, *160*, 49-56.

3 Interference-Based Readout

- 49 L. D. Bonifacio, B. V. Lotsch, D. P. Puzzo, F. Scotognella and G. A. Ozin, *Adv. Mater.* **2009**, *21*, 1641-1646.
- 50 K. Zhang, L. Zhang and J. Jiang, *J. Phys. Chem. C* **2013**, *117*, 25628-25635.
- 51 J. Cousin Saint Remi, T. Rémy, V. Van Hunskerken, S. van de Perre, T. Duerinck, M. Maes, D. De Vos, E. Gobechiya, C. E. A. Kirschhock, G. V. Baron and J. F. M. Denayer, *ChemSusChem* **2011**, *4*, 1074-1077.
- 52 D. Fairen-Jimenez, S. A. Moggach, M. T. Wharmby, P. A. Wright, S. Parsons and T. Düren, *J. Am. Chem. Soc.* **2011**, *133*, 8900-8902.
- 53 F. Hinterholzinger, C. Scherb, T. Ahnfeldt, N. Stock and T. Bein, *Phys. Chem. Chem. Phys.* **2010**, *12*, 4515-4520.
- 54 X. Si, C. Jiao, F. Li, J. Zhang, S. Wang, S. Liu, Z. Li, L. Sun, F. Xu, Z. Gabelica and C. Schick, *Energy Environ. Sci.* **2011**, *4*, 4522-4527.
- 55 T. R. C. Van Assche, T. Duerinck, J. J. Gutiérrez Sevillano, S. Calero, G. V. Baron and J. F. M. Denayer, *J. Phys. Chem. C* **2013**, *117*, 18100-18111.
- 56 P. Davydovskaya, A. Ranft, B. V. Lotsch and R. Pohle, *Anal. Chem.* **2014**, *86*, 6948-6958.
- 57 M. C. Fuertes, S. Colodrero, G. Lozano, A. R. González-Elipe, D. Grosso, C. Boissière, C. Sanchez, G. J. d. A. A. Soler-Illia and H. Míguez, *J. Phys. Chem. C* **2008**, *112*, 3157-3163.
- 58 M. Meilikhov, S. Furukawa, K. Hirai, R. A. Fischer and S. Kitagawa, *Angew. Chem. Int. Ed.* **2013**, *52*, 341-345.

3.3 1D PHOTONIC DEFECT STRUCTURES BASED ON COLLOIDAL POROUS FRAMEWORKS: REVERSE PORE ENGINEERING AND VAPOR SORPTION

Annekathrin Ranft, Ida Pavlichenko, Katalin Szendrei, Peter M. Zehetmaier, Yinghong Hu, Alberto von Mankowski, Bettina V. Lotsch

published in *Microporous Mesoporous Mater.* **2015**, 216, 216-224

DOI: 10.1016/j.micromeso.2015.05.031

<http://dx.doi.org/10.1016/j.micromeso.2015.05.031>

Reprinted with permission from Elsevier. © 2015 Elsevier Inc.

Abstract

Stimuli-responsive 1D photonic crystals, referred to as Bragg stacks, are capable of translating environmental changes into a color read-out through changes in the effective refractive index (RI) of the multilayer system upon infiltration with an analyte. The sensitivity and versatility of prototypic SiO₂/TiO₂ multilayers can be greatly enhanced by the use of nanoparticulate or mesoporous building blocks, or inherently microporous structures such as metal-organic frameworks (MOFs). Here, we introduce a stimuli-responsive ZIF-8 “defect” layer into SiO₂/TiO₂ multilayers in order to combine the high optical quality of a Bragg stack with the characteristic sorption properties of the MOF. The addition of a planar defect layer, either embedded in or deposited on top of the Bragg stack acts as a “dopant” and introduces a narrow band of allowed states in the photonic band gap, which can be utilized for the precise determination of the optical response of the Bragg stack. We demonstrate the impact of layer morphology, layer sequence and the position of the defect on the optical and vapor sorption properties of the photonic architectures. Moreover, a facile process is presented which allows for the clean inversion of the acid-sensitive ZIF-8 defect layer into a mesoporous layer in a one-step fashion, while the layer structure and optical quality of the stack architecture is preserved.

3.3.1 Introduction

Periodic multilayer structures built up from dielectric materials with different refractive indices have recently been developed into versatile sensing platforms based on color-tunable, analyte-specific optical readout.¹⁻⁷ The capability of these structures, referred to as 1D photonic crystals (PCs) or Bragg stacks (BSs), to translate subtle changes in their chemical environment or internal host-guest interactions into a color read-out has been demonstrated, for instance, by the exposure to gaseous and liquid analytes.⁴⁻⁸ The presence of guest molecules in the textural pores of the multilayer constituents induces a change in the effective refractive index (RI) and, hence, the structural color of the infiltrated photonic architecture. SiO₂ and TiO₂ layers derived from low-cost sol-gel processing routes are typically used as building blocks in 1D PCs,^{9,10} as they allow for a high RI contrast and well-defined Bragg reflection peaks with only a few bilayers (BLs) in the stack. A variety of modification schemes have been explored to enhance the response toward environmental changes including the variation of the morphology of the constituting layers such as porosity, size or shape of the building blocks.^{5,6,11,12} The sensitivity of sol-gel derived architectures could thus be improved by the use of mesoporous oxides.^{7,13} Another possibility is the fabrication of cavity structures whose symmetry is disrupted by a defect layer deposited either inside or on top of a regular BS (referred to as “sandwich” and “top” defect structure, respectively).^{6,9,10,14} The addition of such a layer leads to a narrow band range of allowed frequencies within the photonic stop band, and the well-defined spectral position of the narrow defect mode can be employed as a precise measure for gradually differing analyte concentrations.¹⁰ Finally, the implementation of inherently microporous, chemically functional materials such as metal-organic frameworks (MOFs) may help to improve the selectivity of 1D PCs towards molecular-scale analytes. Owing to the modular construction principle of these porous networks built up from metal ions joint by bridging organic linkers, the selectivity and specificity may be greatly enhanced in comparison to conventional metal oxide-based PCs by means of size or shape exclusion and specific host-guest interactions.^{15,16} Compared to mesostructured metal oxides, MOFs benefit from well-defined pore systems thus allowing for enhanced analyte specificity as a function of the kinetic diameter of the analyte. Moreover, as a result of the structural variability of MOFs, the affinity toward particular analytes can be fine-tuned from hydrophobic to polar sorptives without the need for additional post-synthetic functionalization steps. The possibility to fabricate MOFs with dimensions reduced down to the nanoscale allows for

their integration into thin film devices,¹⁷⁻²⁰ which has recently been demonstrated for ZIF-8 as a component in various multilayer structures.^{21,22}

In this work, we demonstrate the fabrication of MOF-based defect structures for the first time by depositing ZIF-8 layers on top of regular periodic multilayers, thus breaking their symmetry, as well as by embedding the MOF between two BSs. We show that via both approaches clean defect structures are obtained, which are characterized by well-defined Bragg reflection peaks and high reflectivity values. By using different TiO₂ layers derived from either a colloidal dispersion or a sol, we can fine-tune the morphology of the defect architectures which allows for enhanced control of their porosity, while the chemical composition of the PC building blocks remains unchanged. Moreover, we show that the nanoparticulate MOF defect slab can be converted into a mesoporous layer *via* a simple one-step synthesis, alluding to the way in which inverse opal structures are synthesized. The transformation into the reversed pore structure takes place without destroying the original photonic architecture, and the spectral characteristics of the defect structure are preserved, rendering this strategy beneficial for smart defect engineering. Besides the optical quality, we investigated the sensing capability of our samples by exposing them to ethanol vapor at various relative pressures and monitoring *in situ* the spectral shift upon analyte adsorption.

3.3.2 Experimental Section

Syntheses

All chemicals used in the syntheses are commercially available and were used without further purification. 2-Methylimidazole (C₄H₆N₂, 99%), titanium isopropoxide (Ti(OiPr)₄, 97%), 2-propanol (pure) and methanol (puriss) were purchased from SigmaAldrich. Tetramethylammonium hydroxide (N(CH₃)₄OH·5H₂O, 99%) and nitric acid (HNO₃, puriss) were purchased from Acros. Ethanol (absolute) was purchased from BfB, hydrochloric acid (HCl, puriss) was purchased from Brenntag, tetraethoxysilane (Si(OEt)₄, 99%) was purchased from Merck and zinc nitrate hexahydrate (Zn(NO₃)₂·6H₂O, 99%) was purchased from Grüssing.

SiO₂ sol was prepared according to ref. 14. Si(OEt)₄ (1.0 g, 4.8 mmol) and absolute ethanol (8.5 mL) were stirred for 5 min. To this solution, deionized water (0.43 mL) and 0.5 M HCl (0.02 mL) were added consecutively under stirring and the clear mixture was kept stirring at RT until further use. In an alternative route, the SiO₂ sol suspension was obtained by

3 Interference-Based Readout

mixing $\text{Si}(\text{OEt})_4$, ethanol and 0.1 M HCl (without the addition of water) in volume ratios of 1:10:1 or 2:10:2.

TiO_2 sol was prepared in an analogous fashion to a literature protocol.¹⁴ $\text{Ti}(\text{OiPr})_4$ (0.81 g, 2.8 mmol) and 2-propanol (8.3 mL) were stirred for 5 min. To this solution, deionized water (0.026 mL) and 0.1 M HNO_3 (0.02 mL) were added consecutively under stirring and the turbid mixture was kept stirring at RT until further use.

TiO_2 particles were synthesized according to ref. 23. $\text{Ti}(\text{OiPr})_4$ (19.2 g, 65.5 mmol, 20 mL) was added dropwise to deionized water (36 mL) under vigorous stirring. After stirring for 1 h, the resultant white solid was filtered with a 1.2 mm glass microfibers filter (VWR) and washed with deionized water. The solid was mixed with 0.6 M $\text{N}(\text{CH}_3)_4\text{OH}\cdot 5\text{H}_2\text{O}$ (7.13 g, 39 mmol, 3.9 mL) and transferred to a Teflon autoclave reactor. The mixture was heated at 120 °C for 3 h and subsequently centrifuged at 14,000 rpm for 10 min to remove potential agglomerates from the suspension. The remainder was redispersed in methanol, and before each spin-coating process an appropriate amount of the diluted and sonicated mixture was filtrated with a 0.45 mm syringe filter (VWR) which allowed for enhanced homogeneity of the deposited film.

ZIF-8 nanoparticles were prepared according to a literature synthesis.²⁴ In a typical experiment, $\text{Zn}(\text{NO}_3)_2\cdot 6\text{H}_2\text{O}$ (0.73 g, 2.44 mmol) was dissolved in methanol (50 mL) and rapidly added to a solution of $\text{C}_4\text{H}_6\text{N}_2$ (1.62 g, 19.6 mmol) in 50 mL methanol. The mixture was stirred constantly throughout the reaction until the solution turned turbid. After 1 h, the nanocrystals were separated from the solvent by centrifugation and washed 3 times with fresh methanol. Stable colloidal suspensions of ZIF-8 were obtained by redispersing the particles after centrifugation in methanol, and repeated sonication.

$\text{SiO}_2/\text{TiO}_2$ multilayers were obtained by spin-coating SiO_2 sol and TiO_2 nanoparticles or sol alternately on silicon substrates until the desired number of BLs (3–4) was obtained. For depositing the layers within 30–60 s, a rotational speed of 4000 rpm was used at an acceleration speed of 4000 rpm s^{-1} (WS-650SZ-6NPP/LITE, Laurell Technologies Corporation). Different thicknesses of the individual layers were achieved by using either multiple coating steps or by adjusting the material concentration in the respective solvents. After each coating step, the stack was calcined on a hot plate (PZ 28-3TD, Harry Gestigkeit GmbH) at 200 °C for 10–15 min to suppress further thickness changes of the freshly deposited layer. Before the deposition of TiO_2 on top of a SiO_2 layer, the samples were

plasma-cleaned for 1 min (Femto plasma-cleaner, Diener Electronic GmbH, air, power: 50%) which significantly improved the adhesion to the SiO₂ surface.

Defect structures were prepared by spin-coating the MOF suspension on a SiO₂/TiO₂ multilayer, using similar spin-coating conditions (4000 rpm at 4000 rpm s⁻¹). The thickness of the MOF layer was adjusted by the number of the deposition steps. After heating at 200 °C for 10–15 min, the stacks were either directly used for characterization and vapor sorption experiments or employed as substrate for sandwich defect structures by coating additional TiO₂/SiO₂ BLs (1–4) on top of the MOF layer. Similarly to the regular SiO₂/TiO₂ BSs, the films were heated after every coating step.

Characterization

Scanning electron (SE) micrographs and EDX measurements were recorded either with a JEOL JSM-6500F SEM equipped with an Oxford EDX analysis system or with a Merlin (Zeiss) FE-SEM. Additional EDX measurements (for investigating sample F where the surface was partially removed by sputtering with Ga ions) were performed with a Crossbeam 1540 EsB workstation (Zeiss). IR spectra were recorded with a JASCO FT/IR-4100 spectrometer. Grazing incidence XRD measurements were conducted with an Empyrean diffractometer (PANalytical). Ellipsometric measurements were carried out using a Woollam M2000D at angles of 65°, 70° and 75° in the spectral range of 190–1000 nm. The data were fitted between 300 and 1000 nm using a Cauchy-type material as the model layer for MOF thin films, and the respective metal oxide models for SiO₂ and TiO₂ layers. Reflectance spectra for regular BSs and defect structures were simulated using a MATLAB code.²⁵ In the first step, experimentally obtained thicknesses (derived from SEM images and/or ellipsometric data) and RI values (derived from ellipsometric simulations at 530 nm by definition) were used as starting points and then fitted to the experimental spectra in an iterative approach (see [SL Tables S2](#) and [S3](#), for experimental and simulated values). To facilitate the simulation process, equal thicknesses were assumed for each material in samples A–E. However, for the fourth TiO₂ layer in sample F (i.e. the one adjacent to the defect slab), a considerably lower thickness was assumed in order to account for the apparent shrinking of this layer as compared to all other TiO₂ layers. Spectrophotometric measurements were recorded with the same ellipsometer using *s*-polarized light at an incident angle of 75°. Vapor sorption measurements were recorded at ambient temperature using gas mixing systems and the

3 Interference-Based Readout

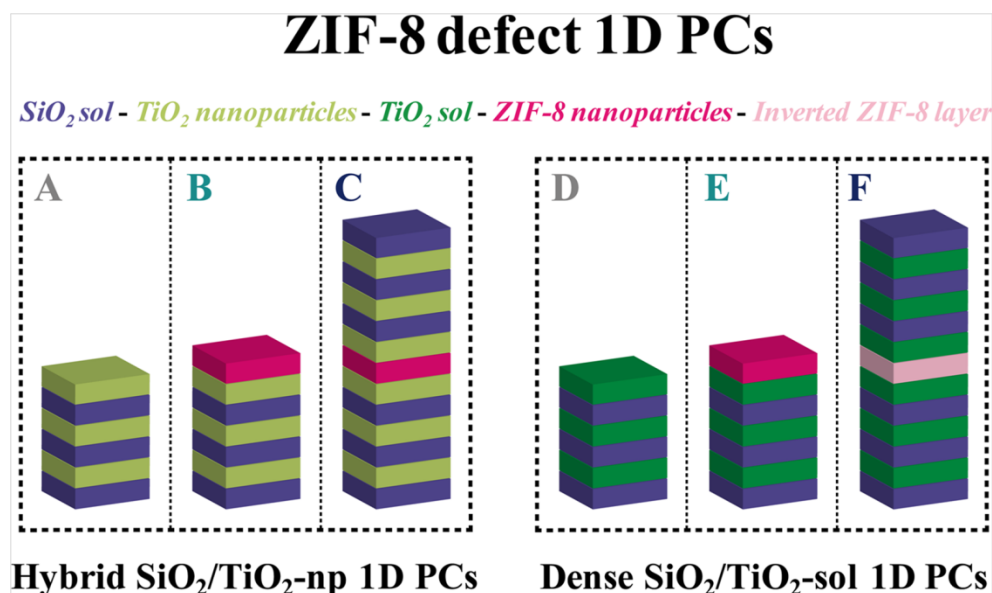
ellipsometer. Relative pressures p/p_0 ranging from 0 to 1 (step sizes: 0.02 for $0 \leq p/p_0 \leq 0.1$, 0.05 for $0.1 \leq p/p_0 \leq 0.5$ and 0.1 for $0.5 \leq p/p_0 \leq 1$) were achieved in our measurements by mixing a nitrogen stream at a fixed flow rate with the liquid sorptive (i.e. ethanol in our case) at different concentrations (0–100% saturation). Both the flow rate of the nitrogen stream and the flow of the liquid analyte were controlled by the percentage of valve opening of the respective mass flow controllers (for the gas and the liquid; W-101A-110-P, F-201C, Bronkhorst High-Tech), before they were mixed and evaporated in a so-called “controlled evaporation and mixing” (CEM) element (W-101A, Bronkhorst High-Tech). For each target partial pressure p the sorptive volume (in L/min) was calculated using the van der Waals equation and by taking into account the respective room temperature and atmospheric pressure of the measurement day. With the help of the online software FLUIDAT, the liquid conversion factor (in g/h) and the saturation pressure p_0 were calculated as a function of the employed controlling elements, at room temperature and atmospheric pressure. For the vapor sorption experiments, the samples were placed in a chamber with two openings: One for the tube connecting the gas mixing system with the chamber and transporting the vapor, and another one designed as outlet for the excessive vapor stream. In a typical measurement, the samples were exposed to a specific vapor concentration for 1–5 min and the optical response was measured via spectrophotometry before switching to the next analyte concentration. We used exposure times as low as 1 min as at least 90% of the final response of the stacks occurs within seconds as deduced from kinetic reflectance measurements that we have recently shown for various MOF-based multilayers.²⁶

Time-dependent measurements were recorded with a fiber optic spectrometer (USB2000+, Ocean Optics) integrated with an optical microscope (DM2500 M, Leica). The sample was therefore placed in a home-made chamber which was assembled as described elsewhere.²⁷ The chamber was pierced three times to create an outlet and two separate inlets: The first one for the connection to a constant nitrogen stream, the second one for connecting to the carrier gas saturated with ethanol vapor at a constant analyte concentration. The saturation of the carrier gas was achieved by bubbling nitrogen through a washing bottle filled with ethanol at a constant velocity. The response of the sample was monitored by recording the change in reflectance at a specific wavelength of the spectrum, and the sample was alternatingly exposed to the nitrogen/ethanol mixture and pure nitrogen with an approximate delay of 2 min.

3.3.3 Results and Discussion

Structuring of the ZIF-8 defect 1D photonic crystals

For the fabrication of the BSs, either a combination of SiO₂ sol and TiO₂ sol or TiO₂ nanoparticles were used, leading to BS architectures with gradually differing textural porosities and, hence, analyte accessibility. In **Scheme 1**, an overview is given on the architectures examined in this work. The stacks are classified as either a member of hybrid 1D PCs based on SiO₂ sol and TiO₂ nanoparticles (np in the scheme; samples A–C), or 1D photonic structures built entirely from rather dense and, hence, less sensitive SiO₂/TiO₂ sol-based multilayers (samples D–F).



Scheme 1. Schematic drawings of the multilayer structures described in this work. Besides illustrating the periodic layer sequence, the differences in the individual RIs and morphologies are stressed by using specific colors for each material (SiO₂: blue, TiO₂-np: bright green, TiO₂-sol: dark green, ZIF-8 nanoparticles: red, inverted ZIF-8 layer: pink).

Periodic SiO₂/TiO₂ multilayers were obtained by spin-coating and annealing alternately a SiO₂ sol and TiO₂ suspensions on silicon substrates until the desired number of BLs was achieved. For the deposition of TiO₂ thin films, either colloidal TiO₂ suspensions or a TiO₂ sol was used to produce mixed-porous or purely sol-based architectures denoted as SiO₂/TiO₂-np (sample A) and SiO₂/TiO₂-sol (sample D) BSs, respectively. We observed that a number of

three to five BLs was sufficient to yield BSs with a high optical quality indicated by the formation of a pronounced stop-band with high reflectivity of >90% (see **Fig. 3** and the respective paragraph for a more detailed discussion of the optical quality). In **Figs. 1a** and **d**, cross-sectional SEM micrographs are shown for A and D, respectively, which were built up from three BLs in each case. The alternate assembly of SiO₂ and TiO₂ layers is confirmed by the periodic array of darker and brighter slabs in the SE micrographs, which is attributed to the different electron densities and, hence, scattering contrast of the metal oxides.

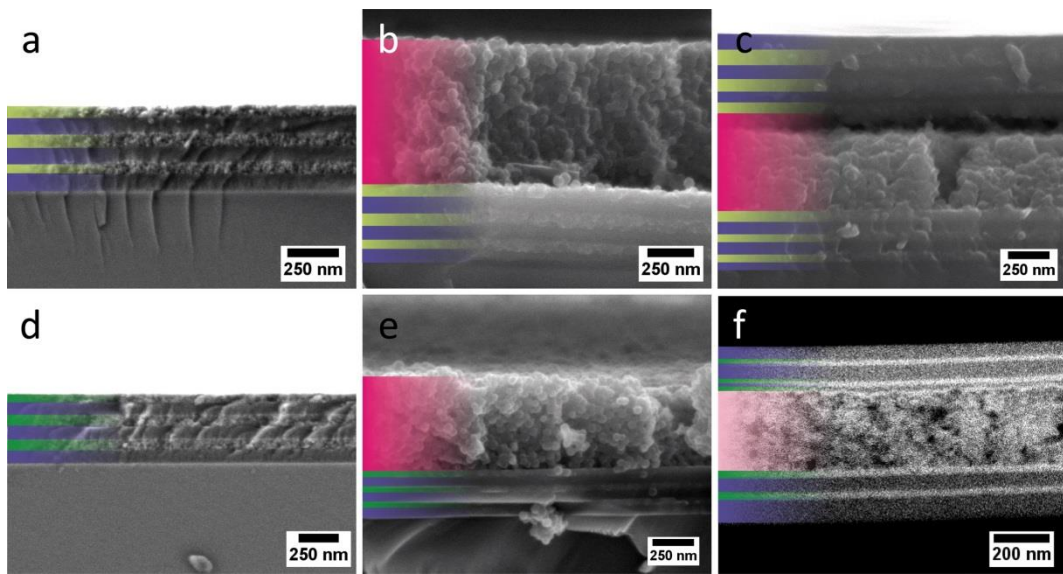
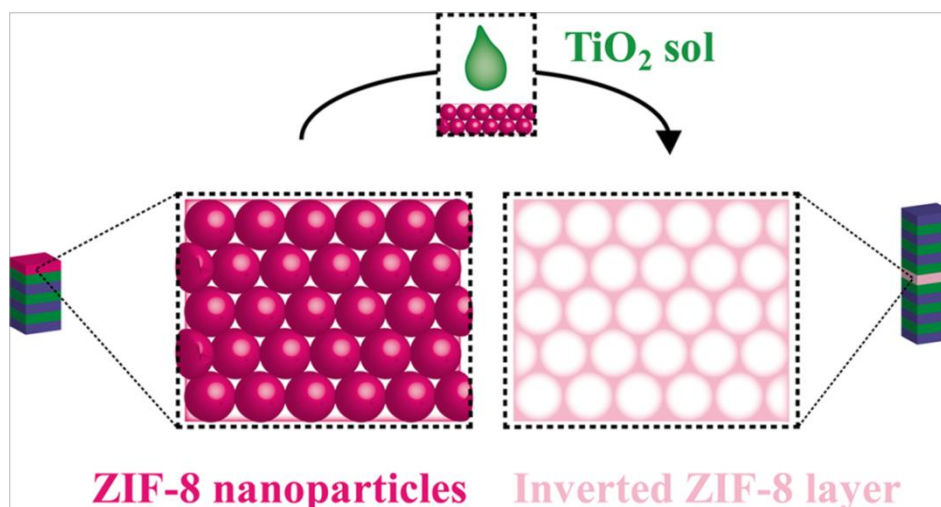


Figure 1. Cross-sectional SEM images of hybrid 1D PCs (a–c: samples A, B and C) and dense multilayer structures (d–f: samples D, E and F). The individual layers are highlighted with the respective colors introduced for the schematically drawn stacks (SiO₂: blue, TiO₂-np: bright green, TiO₂-sol: dark green, ZIF-8 nanoparticles: red, inverted ZIF-8 layer: pink). Note that the stack shown in (f) has inhomogeneously peeled off the surface of the silicon substrate.

The fabrication of defect MOF-based structures was accomplished by using the SiO₂/TiO₂ multilayers prepared in the first step as substrate, and depositing a layer of ZIF-8 nanoparticles on top. In **Figs. 1b** and **e**, the formation of a smooth particulate layer on top of three-bilayered BSs is shown, indicating the successful deposition of ZIF-8 particles on the surface of both the particulate and the dense TiO₂ layer (samples B and E, respectively). The cross-section images of exemplary defect sandwich structures, with 3 additional BLs on top, are shown in **Figs. 1c** and **f** for the mixed-porous (C) and the sol-based (F) BSs, respectively. In C, the retention of the particles in the defect layer is confirmed by the particulate appearance of the middle slab. For F, however, the morphology of the defect seems to be

significantly changed as compared to the original uncovered ZIF-8 layer (see **Fig. 1e**). In place of the nanoparticles with textural porosity between the particles an inverted structure is observed which appears as mesoporous replica of ZIF-8 with voids in the size range of the original particles (~50 nm). This observation alludes to the way in which inverse opal structures are typically synthesized, although the process used here is intriguingly simple: In opal fabrication a template – SiO₂ or polymer microparticles – are either co-assembled with a void-filling material such as TiO₂ sol or infiltrated with the sol subsequent to the assembly process.²⁸ In the next step, the template spheres are removed by thermal treatment or solvent extraction. We assume that a similar templating process takes place in our samples, albeit in a one-step fashion: The ZIF-8 particles act as a template layer, which is inverted through the application of TiO₂ sol (**Scheme 2**). To explore the conditions required to induce the one-step formation of the porous layer and its composition, we firstly deposited 1–3 TiO₂/SiO₂ BLs on a ZIF-8 top-coated BS, while in a second experiment a BL with reversed stacking order (SiO₂/TiO₂) was used, and monitored the resulting morphology of the defect layer with crosssectional SEM. In all cases, formation of the porous structure was observed, demonstrating the reproducibility of this phenomenon on the one hand; on the other hand, it appears sufficient to use only 1 BL to create the reverse pore system. In **Figs. S1a** and **b** (**SI**), this observation is illustrated by SEM images of a sandwich structure with one overhead TiO₂/SiO₂ BL (**Fig. S1a**) in comparison to a structure with one BL with reversed order (SiO₂/TiO₂) on top (**Fig. S1b**). Although it is difficult to distinguish the individual oxide layers due to issues that we discuss further below, the porous nature of the underlying inverted “ZIF-8” layer is clearly visible in the SEM images. In fact, we observed that already the deposition of either TiO₂ or SiO₂ sol onto ZIF-8 entails the formation of the porous structure (**Fig. 2a** for TiO₂; see **SI, Fig. S1c**, for SiO₂), which we attribute to the low pH of the sol layers (synthesized in 0.5 M HCl/0.1 M HNO₃, respectively, for SiO₂/TiO₂) likely entailing the dissolution of the acid-sensitive ZIF-8. When the colloidal (basic) TiO₂ suspension was used, however, the morphology of the ZIF-8 particles remained unchanged (**SI, Fig. S1d**). A similar templating process, yet proceeding in a two-step synthesis, has been described for carbonate nanoparticles which were incorporated in a polymer film,²⁹ and by utilizing the acid lability of the particles porous polymer membranes were formed. Complete infiltration of the defect layer and, hence, inversion is supported by the observation of various dips and cavities penetrating the entire height of the defect layer (**Fig. 2b**, green arrows), which act as reservoirs from which the sol spreads out and reaches the interparticle voids.



Scheme 2. Schematic illustration of the reverse pore engineering as observed in the fabrication of purely sol-based sandwich defect structures. Upon contact with TiO₂ sol (represented as green drop), the ZIF-8 layer (red spheres) is transformed into a mesoporous inverted layer (pink mesh).

According to **Figs. 1f** and **2c**, the fourth TiO₂ layer (i.e. the one following the inverted MOF film) and the adjacent SiO₂ layer turn out thinner as compared to the other layers, additionally suggesting the leakage of the sols into the subjacent layer. The thickness change of the SiO₂ layer is, however, less pronounced than for TiO₂ and has not been observed for all our samples. We thus assume that the probability of SiO₂ sol leaking into the defect slab is controlled by the “density” of the remaining fourth TiO₂ layer and therefore varies with its thickness. As can be seen in **Fig. 2d**, the newly formed inverted layer shows a high scattering contrast similar to the TiO₂ slabs, and is less sensitive to the electron beam than the original ZIF-8 defect, which indicates the transformation into a mesoporous oxide layer. As EDX measurements suggest that Zn is still present in the inverted layer (SI, **Table S1** and **Fig. S2b**), partial conversion from ZIF-8 to ZnO also seems plausible. To clarify whether the original ZIF-8 layer is completely dissolved or at least partially still intact, we conducted further analytical measurements including XRD and IR spectroscopy. According to **Figs. S2c** and **d** (SI), the presence of ZIF-8 or a Zn containing product can be concluded in both the top defect (E) and the sandwich structure (F). Hence, we assume that after the conversion process residual Zn and N are still present in the inverted slab aside from Si and Ti suggesting that no pure sol layer has formed. Additional evidence for the conversion is obtained from sorption experiments which we conducted with a sandwich defect structure built up from rather porous TiO₂ sol layers. The recorded optical response no longer shows

the prominent adsorption steps characteristic for ZIF-8 (see [SI, Fig. S3](#), and the corresponding paragraph for a more detailed discussion of the sorption experiments). We thus assume that the formation process of the porous layers takes place in a similar way to that used in the fabrication of inverse opal structures or porous polymers,³⁰ i.e. via a templating process. With regards to costs, ease of handling and synthesis time, this process therefore has the potential to outperform the conventional fabrication strategy, as the formation of the porous structure (i.e. infiltration and template removal) is executed in one single step.

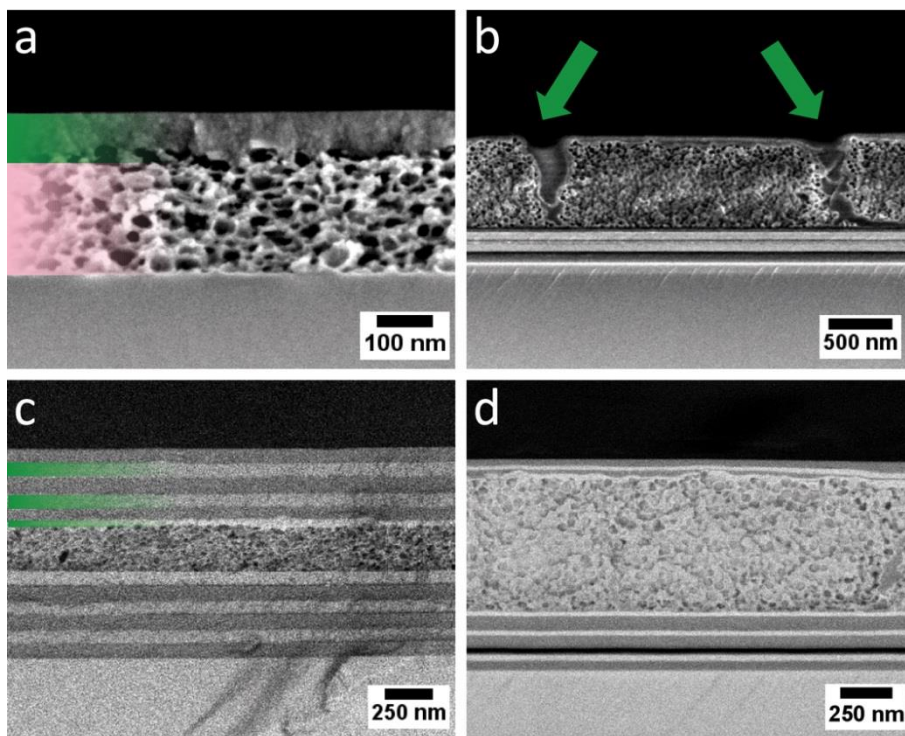


Figure 2. Cross-sectional SEM images of (a) a single ZIF-8 layer coated with TiO₂ sol, and three exemplary dense sandwich structures, (b) illustrating the leakage of overhead layers into the defect layer, (c) demonstrating the comparatively lower thickness of the TiO₂ layer following the inverted MOF film in comparison to the other TiO₂ slabs, and (d) recorded in backscattering mode, visualizing the high scattering contrast of the inverted layer. The reversed ZIF-8 layer in (a) is highlighted in pink, while TiO₂ slabs in (a) and (c) are shown in dark green.

We investigated the optical characteristics and quality of our structures by measuring their reflection spectra at normal incidence by means of a fiber optic spectrometer interfaced with an optical microscope, and by comparing the experimentally obtained data with simulated spectra. In general, the stop-band position of the BSs (λ_{\max}) depends on the optical

thickness (i.e. physical thickness d times refractive index n) of the constituent building blocks, which can be modulated by changing the deposition conditions such as the spinning speed, or the solution concentration:¹

$$m\lambda_{\max} = 2(n_L h_L + n_H h_H)$$

Here, m is the diffraction order and L and H denote the thickness d and RI n of the low- and high-RI materials, respectively, at normal incidence.

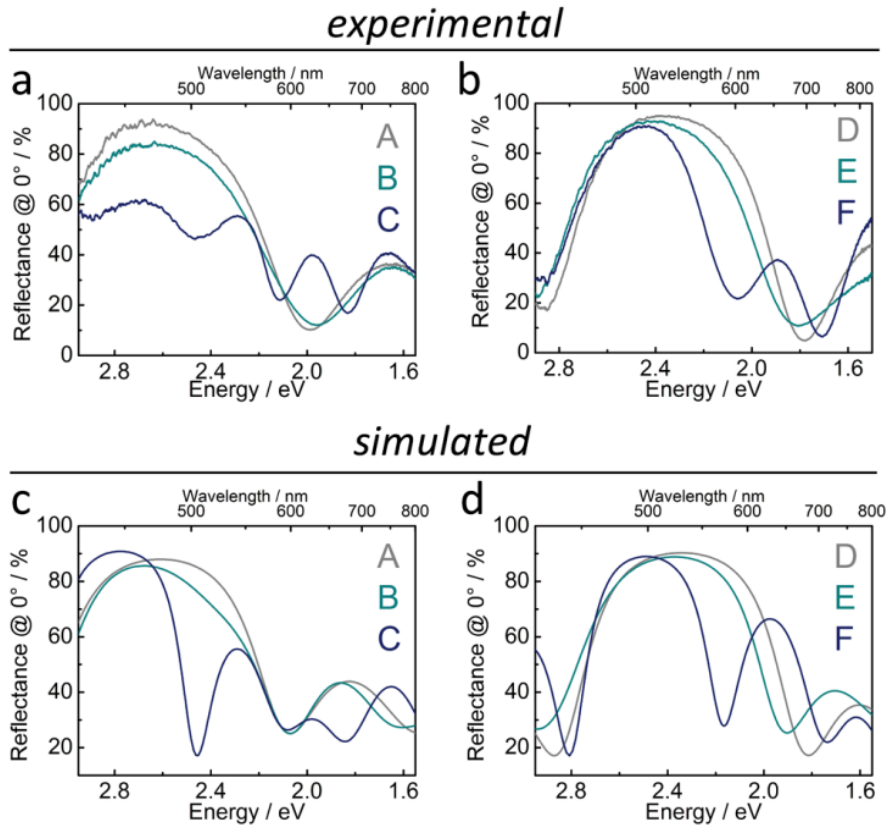


Figure 3. Experimentally obtained (top row) and simulated (bottom row) reflection spectra of hybrid 1D PCs (a, c: samples A, B and C) and dense multilayer structures (b, d: samples D, E and F). Gray lines represent $\text{SiO}_2/\text{TiO}_2$ BSs without defect, top defect structures are shown in dark cyan and sandwich defect structures in blue.

In the corresponding UV-vis spectra of the top defect structures (dark cyan lines in **Figs. 3a** and **b**), a slight decrease in reflectivity is observed in comparison to the original BSs (gray lines). This observation is in accordance with top defect BSs coated with mesoporous TiO_2 ,¹⁰ where sizeable effects on the spectrum by localization of defect modes in the stop band are only seen for very thick top layers, while embedded layers give rise to pronounced

reflectance dips, irrespective of their thickness. Indeed, by adding more BLs to our heterostructures, we also observe the appearance of a reflectance dip in the stop band (blue lines in **Figs. 3a** and **b**, at ca. 2.46 eV/504 nm and 2.06 eV/602 nm, respectively). Compared with the top defect structure, the reflectivity of sample C is considerably reduced ($\approx 65\%$), while the sol-sol-based sandwich structure F maintains its high optical quality ($\approx 90\%$). This finding may be rationalized by the comparatively large particles of the colloidal TiO₂ suspension (10–20 nm) leading to enhanced diffuse scattering losses and, hence, lower optical quality with increasing numbers of BLs in comparison to sol-based multilayers having a higher homogeneity (see [SI Fig. S4](#), for the spectral evolution with each BL deposition).

In order to evaluate the quality and validity of the experimentally obtained data, we calculated simulated spectra of the stacks on the basis of ellipsometric measurements for single oxide and MOF films, respectively, and SE micrographs of the final BS architectures. Based on average thicknesses determined from SEM data and spectroscopic ellipsometry, and the respective RIs of the individual oxide layers (see [SI Tables S2](#) and [S3](#), for a complete list of all experimental and simulated thickness values and RIs), we calculated Bragg maxima of 2.61 eV (475 nm) and 2.34 eV (530 nm) for A and D (**Figs. 3c** and **d**, gray lines), which is comparable to the experimentally measured ones (2.64 eV/470 nm and 2.36 eV/526 nm for A and D, respectively, gray lines in **Figs. 3a** and **b**). Similarly to the recorded spectra, the simulations for top defect stacks B and E (**Figs. 3c** and **d**, dark cyan lines) show a slight reduction in reflectivity compared to the original multilayer structures. The calculated maxima of both stacks coated with ZIF-8 (2.68 eV/463 nm and 2.37 eV/524 nm for B and E, respectively) are in the same range as the measured ones (2.63 eV/472 nm and 2.40 eV/517 nm). In contrast to the experimental spectrum recorded for sandwich defect structure C, the simulated spectrum shows a comparatively higher reflectivity which is in the same range as for the SiO₂/TiO₂ BS and the top-coated stack, and a better resolved reflectance dip (**Fig. 3c**, blue line). Nevertheless, the shape of both spectra in the range below 2.4 eV are in good agreement, and the dips in the maxima are at equal positions (2.46 eV/504 nm in both cases) suggesting the plausibility of the assumed optical thickness values for C. The experimental spectrum of F is in good agreement with the simulated one (**Fig. 3d**, blue line), indicated by a similar shape of the Bragg maximum, reflectivity and similar dip positions (2.06 eV/602 nm for the recorded data and 2.16 eV/574 nm for the calculated spectrum). For the calculation, we assumed an average RI of 1.60 for the defect layer, which is in between those for a nanoparticulate ZIF-8 layer (1.21) and TiO₂ sol (1.93) (see also

Fig. S5, SI). According to the prominent dip in both the experimental and the calculated spectrum of F, the inversion of the original ZIF-8 film into a mesoporous layer, hence, does not prevent the formation of a clean defect structure. Nevertheless, its sensitivity and selectivity to analytes is of course expected to change with respect to the samples with an intact MOF layer.

Sorption experiments with ZIF-8 defect 1D photonic crystals

To test the sensitivity of our defect structures to molecular analytes, vapor sorption measurements were conducted at room temperature using mass flow controllers and spectrophotometry at a viewing angle of 75° to monitor spectral changes at different analyte concentrations (0–100%, corresponding to relative pressures of $0 \leq p/p_0 \leq 1$). To this end, the sample was placed in a measurement chamber with two openings such that the sample was exposed to a constant stream of flowing gas/vapor mixture for 1–5 min. We used exposure times as low as 1 min as we observed that the full response of the stack toward the analyte is achieved within the first minute and remains constant upon further exposure (see ref. 26 and **Fig. S6, SI**). In the first run, we investigated in situ the response of the two top defect structures (samples B and E) toward ethanol vapor while gradually increasing the analyte concentration. The spectra shown in **Figs. 4a** and **c** illustrate the change of the optical properties of each stack upon exposure to ethanol vapor at the highest analyte concentration in comparison to pure nitrogen. For both structures, a pronounced red-shift of the respective spectra is observed (66 nm/0.18 eV for B and 61 nm/0.13 eV for E, determined at 1.9 eV/16% reflectivity and 1.7 eV/40% reflectivity, respectively). By comparing a range of top defect samples with differing ZIF-8 layer thicknesses, we observed that stacks with a large thickness of the top defect layer show a comparatively higher response in comparison to thinner ones, which is consistent with the larger total pore volume available for the uptake of guest molecules (see **SI, Fig. S7**, for the comparison of two top defect structures based on colloidal TiO_2). By using a distinct position in the spectrum to determine the shift for each stack at various analyte concentrations, we obtain optically encoded isotherms revealing the individual sorption behavior of the structures as a consequence of their differing porosities. For both top defect samples, we observe a similar behavior with increasing analyte concentration in the nitrogen stream (**Figs. 4b** and **d**): At $p/p_0 \approx 0.1$, the spectrum strongly red-shifts, while at both lower and higher ethanol concentrations less pronounced changes are observed. This finding indicates pore size or

chemo-specific analyte uptake at a certain threshold pressure, as typically found for adsorption in ordered pore systems. Indeed, delayed ethanol adsorption into the micropores of bulk ZIF-8 around $p/p_0 = 0.1$ is associated with a polarity-driven gate opening effect³¹ and was likewise reported for ZIF-8/TiO₂ BSs.²¹ Thus, the adsorption behavior of both top defect structures seems to be dominated by the structural pores of ZIF-8, which is rationalized by the larger layer thickness in comparison to the subjacent multilayer. Besides the sensitivity of the individual materials (i.e. TiO₂, SiO₂ and ZIF-8), the response may also be influenced by the assembly order of the stack: As the top ZIF-8 layer is most exposed to the infiltrating analyte vapor and hence most accessible, the optical response may be dominated by ZIF-8 rather than by the underlying, less accessible oxide layers.

We also tested the response of the two sandwich defect structures toward ethanol vapor (**Figs. 4e–h**). The reflection spectrum of C (**Fig. 4e**) shifts to higher wavelengths upon ethanol adsorption similarly to its counterpart without the overlying additional BLs. The magnitude of the shift, however, is reduced suggesting that the response of the stacks is, amongst others, mediated by the stacking architecture. In the vapor adsorption isotherm (**Fig. 4f**), we observe two major steps at $p/p_0 \leq 0.02$ and $p/p_0 \approx 0.1$. As the adsorption in micropores is typically accompanied by a strong signal increase at very low relative pressures, we attribute the first pronounced shift to the analyte uptake in the textural micropores of the overhead BS (with an average particle size of 10–20 nm for TiO₂-np, up to 25% porosity can be expected³²). To confirm this assumption, we conducted similar vapor sorption experiments with a regular hybrid multilayer (**SI, Fig. S8**) which indeed shows strong uptake of alcohol molecules at low relative pressures, similarly to the observations reported in ref. 5. The second signal increase is again attributed to the adsorption event taking place in the structural pores of ZIF-8. Apparently, the signal height for sample C is drastically reduced as compared to the shift observed for sample B (**Fig. 4b**), indicating a relatively weaker interaction with the analyte vapor for C. This observation agrees well with the results obtained for a defect sandwich structure with only 1 instead of 3 overhead BLs (**SI, Fig. S9**): While the overall response is in between that of B and C, the ZIF-8 response (i.e. the step at $p/p_0 \approx 0.1$) turns out to be higher relative to the defect structure C with 3 BLs.

3 Interference-Based Readout

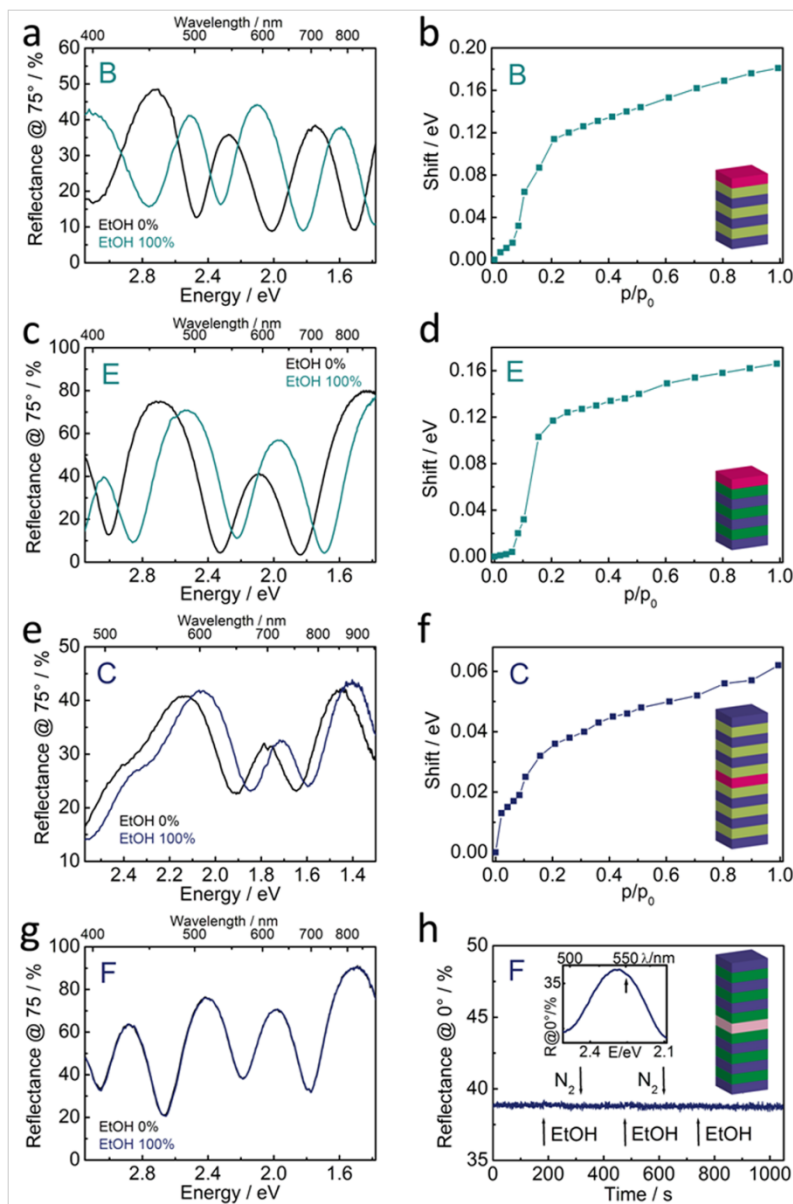


Figure 4. Reflection spectra and optical vapor sorption isotherms of hybrid 1D PCs (a, b: sample B; e, f: sample C) and dense multilayer structures (c, d: sample E; g: sample F) illustrating the change of the optical properties after adsorption of ethanol vapor. Note that the spectra look different from those shown in Fig. 3 as they are recorded at 75. In the reflection spectra, the respective spectral shift upon exposure to the highest analyte concentration (100%, $p/p_0 \approx 1$) is shown in comparison to pure nitrogen, while the respective isotherms illustrate the individual sorption behaviors of the stacks at various relative pressures. The time-dependent response of F (h) was recorded by switching back and forth from pure nitrogen to nitrogen/ethanol and monitoring the reflectivity at a distinct wavelength of the spectrum. Dark cyan lines represent top defect structures and sandwich defect structures are shown in blue.

In contrast to the hybrid structures, sol-sol-based sample F shows no response at all upon analyte exposure (Fig. 4g), which is illustrated in Fig. 4h by a time-dependent monitoring of the reflectivity at 2.26 eV (550 nm). Although the defect layer possesses a considerable

degree of textural porosity, as we deduce from the SEM images (**Fig. 1f**), no response and, hence, no ethanol adsorption is observed in the sol-based defect BS. Apparently, the overhead BS hampers the infiltration of analyte vapor into the underlying layers, which suggests that the stack-analyte interaction is mediated by both the BS architecture (i.e. top vs internal defect, number of BLs) and the type and morphology (i.e. structural and/or textural porosity) of the layers directly exposed to the incoming vapor. Similar phenomena have been described for metal oxide based BLs and multilayers with differing porosities, where the shape of the isotherms showed a dependency on the stacking order of the layers.²⁵ The low sensitivity of sol-based multilayers is reported in ref. 32 and additionally demonstrated through vapor sorption measurements with a regular SiO₂/TiO₂-sol BS sample (SI Fig. S10).

We thus hypothesize that the vapor penetrates the stack in a successive way by entering from the top side of the sample, and that the ultimate sensing behavior of the stack is controlled by the upmost layers. To further corroborate this assumption, we performed two additional sensing experiments with a porous SiO₂/TiO₂ BS sample: In the first run, we covered the four edges of the stack with adhesive tape to prevent potential analyte adsorption leaving only the surface available to the vapor atmosphere, while in the second run the top side was covered. In each case, the sample was exposed to ethanol vapor at a constant concentration while monitoring the spectrum and the change in reflectivity (at normal incidence). From **Fig. S11** (SI) showing the respective spectra and kinetic measurements for both scenarios, it can be clearly seen that the sample with blocked edges readily responds to the analyte stream by showing a pronounced spectral shift (**Fig. S11a**) and a prompt increase in reflectivity (**Fig. S11b**). In comparison, no signal is observed for the stack with the covered surface upon analyte exposure (**Figs. S11c, d**) suggesting that the analyte transport through the BS indeed starts from the top layer only.

In summary, the sorption behavior of both top defect structures seems to be predominantly governed by the response of ZIF-8, while the vapor sorption isotherms of the sandwich structures are determined by the constituents of the respective uppermost layers. Using colloidal TiO₂ layers, partial accessibility to the underlying layers is granted, whereas the deposition of purely sol-sol-based multilayers strongly hampers the analyte transfer to the rest of the stack. For both types of sandwich structures, the pore accessibility shows a dependency on the number of overhead BLs, which especially affects the sensitivity of the dense defect structures.

3.3.4 Conclusion

We have demonstrated the successful integration of MOFs into 1D photonic defect multilayers using two different approaches, namely by depositing thin ZIF-8 layers either on top of a regular PC built up from SiO₂ and TiO₂ as low- and high-refractive index materials, or embedded between two multilayers. The conversion of a ZIF-8 layer into an optically homogenous mesoporous film upon sol contact occurs via a templating process in a simple one-step procedure with retention of the original stack architecture. This method is generic and lends itself well for the fabrication of complex photonic cavity structures or membranes with different porosities from only three basic building blocks. Vapor sorption experiments reveal a pronounced higher sensitivity and selectivity for top defect structures in comparison to stacks with embedded MOFs, which we attribute to the larger exposed surface area of the external ZIF-8 layer resulting in superior stack-analyte interactions. Despite the porosity of the inverted defect layer the purely sol-based sandwich structure showed no response upon analyte contact, thus stressing the “gating” function of the uppermost layers for the sensitivity of the overall detection platform. Further experiments exploring the sorption properties of different MOF-based defect structures are currently underway to tailor the selectivity of the stacks toward specific host-guest interactions.

Acknowledgments

Financial support by the Max Planck Society, Deutsche Forschungsgemeinschaft (SPP-1362), the Fond der Chemischen Industrie (FCI), the cluster of excellence Nanosystems Initiative Munich (NIM), and the Center for NanoScience (CeNS) is gratefully acknowledged. We thank Prof. T. Bein for granting access to the ellipsometer, and V. Duppel, C. Minke, H. Hoier, B. Fenk, and L. Stegbauer for their assistance with the material analysis.

3.3.5 References

- 1 L. D. Bonifacio, B. V. Lotsch, D. P. Puzzo, F. Scotognella and G. A. Ozin, *Adv. Mater.* **2009**, *21*, 1641-1646.
- 2 H. Xu, P. Wu, C. Zhu, A. Elbaz and Z. Z. Gu, *J. Mater. Chem. C* **2013**, *1*, 6087-6098.
- 3 B. V. Lotsch and G. A. Ozin, *Adv. Mater.* **2008**, *20*, 4079-4084.

3 Interference-Based Readout

- 4 M. Oliva-Ramírez, L. González-García, J. Parra-Barranco, F. Yubero, A. Barranco and A. R. González-Elipe, *ACS Appl. Mater. Interfaces* **2013**, *5*, 6743-6750.
- 5 S. Colodrero, M. Ocaña, A. R. González-Elipe and H. Míguez, *Langmuir* **2008**, *24*, 9135-9139.
- 6 B. V. Lotsch and G. A. Ozin, *ACS Nano* **2008**, *2*, 2065-2074.
- 7 M. N. Ghazzal, O. Deparis, A. Errachid, H. Kebaili, P. Simonis, P. Eloy, J. P. Vigneron, J. De Coninck and E. M. Gaigneaux, *J. Mater. Chem.* **2012**, *22*, 25302-25310.
- 8 B. V. Lotsch, C. B. Knobbe and G. A. Ozin, *Small* **2009**, *5*, 1498-1503.
- 9 M. Barhoum, J. M. Morrill, D. Riassetto and M. H. Bartl, *Chem. Mater.* **2011**, *23*, 5177-5184.
- 10 N. Hidalgo, M. E. Calvo, M. G. Bellino, G. J. A. A. Soler-Illia and H. Míguez, *Adv. Funct. Mater.* **2011**, *21*, 2534-2540.
- 11 I. Pavlichenko, A. T. Exner, M. Guehl, P. Lugli, G. Scarpa and B. V. Lotsch, *J. Phys. Chem. C* **2012**, *116*, 298-305.
- 12 M. N. Ghazzal, O. Deparis, J. De Coninck and E. M. Gaigneaux, *J. Mater. Chem. C* **2013**, *1*, 6202-6209.
- 13 S. Y. Choi, M. Mamak, G. von Freymann, N. Chopra and G. A. Ozin, *Nano Lett.* **2006**, *6*, 2456-2461.
- 14 N. Hidalgo, M. E. Calvo and H. Míguez, *Small* **2009**, *5*, 2309-2315.
- 15 M. Eddaoudi, D. B. Moler, H. Li, B. Chen, T. M. Reineke, M. O'Keeffe and O. M. Yaghi, *Acc. Chem. Res.* **2001**, *34*, 319-330.
- 16 H. Furukawa, K. E. Cordova, M. O'Keeffe and O. M. Yaghi, *Science* **2013**, *341*, 12304441-123044412.
- 17 E. A. Flügel, A. Ranft, F. Haase and B. V. Lotsch, *J. Mater. Chem.* **2012**, *22*, 10119-10133.
- 18 P. Falcaro, R. Ricco, C. M. Doherty, K. Liang, A. J. Hill and M. J. Styles, *Chem. Soc. Rev.* **2014**, *43*, 5513-5560.

- 19 D. Bradshaw, A. Garai and J. Huo, *Chem. Soc. Rev.* **2012**, *41*, 2344-2381.
- 20 O. Shekhah, J. Liu, R. A. Fischer and C. Wöll, *Chem. Soc. Rev.* **2011**, *40*, 1081-1106.
- 21 F. M. Hinterholzinger, A. Ranft, J. M. Feckl, B. Rühle, T. Bein and B. V. Lotsch, *J. Mater. Chem.* **2012**, *22*, 10356-10362.
- 22 G. Lu, O. K. Farha, W. Zhang, F. Huo and J. T. Hupp, *Adv. Mater.* **2012**, *24*, 3970-3974.
- 23 M. E. Calvo, S. Colodrero, T. C. Rojas, J. A. Anta, M. Ocaña and H. Míguez, *Adv. Funct. Mater.* **2008**, *18*, 2708-2715.
- 24 J. Cravillon, S. Münzer, S.-J. Lohmeier, A. Feldhoff, K. Huber and M. Wiebcke, *Chem. Mater.* **2009**, *21*, 1410-1412.
- 25 M. C. Fuertes, S. Colodrero, G. Lozano, A. R. González-Elipe, D. Grosso, C. Boissière, C. Sanchez, G. J. D. A. A. Soler-Illia and H. Míguez, *J. Phys. Chem. C* **2008**, *112*, 3157-3163.
- 26 A. Ranft, F. Niekietel, I. Pavlichenko, N. Stock and B. V. Lotsch, *Chem. Mater.* **2015**, *27*, 1961-1970.
- 27 A. T. Exner, I. Pavlichenko, D. Baierl, M. Schmidt, G. Derondeau, B. V. Lotsch, P. Lugli, G. Scarpa, *Laser Photon. Rev.* **2014**, *8*, 726-733.
- 28 B. Hatton, L. Mishchenko, S. Davis, K. H. Sandhage and J. Aizenberg, *Proc. Natl. Acad. Sci.* **2010**, *107*, 10354-10359.
- 29 C. R. Kellenberger, N. A. Luechinger, A. Lamprou, M. Rossier, R. N. Grass and W. J. Stark, *J. Membr. Sci.* **2012**, *387-388*, 76-82.
- 30 D. Wu, F. Xu, B. Sun, R. Fu, H. He and K. Matyjaszewski, *Chem. Rev.* **2012**, *112*, 3959-4015.
- 31 J. Cousin Saint Remi, T. Rémy, V. Van Hunskerken, S. van de Perre, T. Duerinck, M. Maes, D. De Vos, E. Gobechiya, C. E. A. Kirschhock, G. V. Baron and J. F. M. Denayer, *ChemSusChem* **2011**, *4*, 1074-1077.
- 32 I. Pavlichenko, A. T. Exner, G. Logvenov, G. Scarpa, P. Lugli and B. V. Lotsch, *Can. J. Chem.* **2012**, *90*, 1069-1077.

4 SUMMARY AND OUTLOOK

4.1 METAL-ORGANIC FRAMEWORKS AS OPTICAL SENSOR MATERIALS?

In this thesis, we have demonstrated that nanosized versions of MOFs can serve as versatile building blocks for optically homogenous thin films (**chapter 2**) and multilayers (**chapter 3**). For the latter, the integration of nanoMOFs into several light-guiding patterns has been shown, ranging from single MOF BSs (in combination with TiO₂; **chapter 3.1**), to tandem MOF BSs and arrayed platforms (**chapter 3.2**), to photonic defect structures (**chapter 3.3**). The optical features of these materials (i.e. interference color) have been used for sensing molecular events in the porous layers; by monitoring *in situ* the response toward particular solvent vapors (water, alcohols, and other organic vapors; see also refs. 1 and 2), the sensitivity and chemical selectivity of the stacks have been demonstrated. Besides, the response toward the investigated analytes has shown to occur reversibly on the scale of a few seconds, and may be correlated with prevalent analyte concentrations (measured in partial pressures). Changes in the structural colors have been monitored through UV-vis reflectance spectroscopy, and by recording optical photographs which allow for complex color image analysis. –Besides, new routes for controlling morphologies have been found on the one hand by the inversion of a particulate film into an optically homogenous mesoporous layer (**chapter 3.3**), and on the other hand by the additive-mediated size control of two prototypic MOFs (**chapter 2**).

The particularly short response times of our photonic MOF sensors, their strong capability for sensing alcohols and the overall easy handling (no external wires needed for signal indication!) suggest that MOF based platforms are promising candidates for environmental sensing; this could be in the form of breathalyzers, e.g. for estimating blood alcohol contents *via* the breath. However, there are some issues to be considered for real-life applications, which partially relate to experiences that we have made with MOF thin films during this thesis:

- 1) sensitivity,
- 2) cross-responsivity,
- 3) iridescence,
- 4) stability.

The following sections specify these particular issues and suggest ideas how they could be overcome.

Starting with the sensitivity, MOF thin films are in general highly responsive toward molecular analytes which has been demonstrated, for instance, through quartz crystal microbalance (QCM) sensing and workfunction-based readout.^{1,2} Briefly, the latter reveals host-guest interactions in MOFs by visualizing changes in the electronic structure of the sensing layer (i.e. work function), while for the former the event of molecular adsorption is monitored by changes in the oscillation frequency of the sensor. These changes are in turn proportional to the mass loading resulting from the adsorption of the analyte. Both readout strategies allow for the detection of even very low analyte concentrations (2–50 ppm).¹ – The capability of detecting molecules at such low levels is mandatory for a potential sensory material. These are, however, not attainable by the MOF platforms discussed in this thesis: In fact, the lowest concentration that has been investigated with the interference-based readout was $p/p_0 \approx 0.02$ (ca. 20000 ppm or 20‰). This is attributed to the comparatively low resolutions of the applied optical set-ups, which permit the detection of sub-nm shifts, and the moderate spectral shifts induced through RI variation alone (see **chapter 5.3** for a discussion of the detection limit). Effective changes in the lattice constants (i.e. through shrinking or swelling) could have a much higher impact on the optical properties than RI variations.³ On the other hand, RI variations are usually much faster detected by the observer when induced through vapor adsorption, than swelling processes by diffusion. – Signal enhancement may thus eventually be achieved by counterbalancing the (dis-)advantages of both methods through one or more of the following possibilities:

a) Increased layer thicknesses (while maintaining the accessibility of the active MOF component for the desired analyte);

b) Implementation of even more sensitive MOF structures, or dynamic MOFs which respond through transformational changes, such as “breathing”;⁴

c) Embedding in elastic materials that are capable of swelling or shrinking;⁵ here, the analyte should be adsorbed in the MOF pores only, and the MOF response may act as a switch to induce a lattice change in the soft stretchable material.

Beside the general sensitivity, the selectivity of a certain MOF type will ultimately determine the performance of a sensor, such as its capability for discriminating between several analytes. Cross-responsivity induced by molecules other than ethanol in one’s breath (e.g. water droplets) may be bypassed by arrayed platforms such as the ones presented in this work (tandem MOFs BSs or BS arrays; see **chapter 3.2**); i.e. a combination of different MOFs having characteristic sorption capabilities can serve for indicating complex breath mixtures. Here, the implementation of more “structured” MOFs, e.g. SURMOFS (surface-mounted metal-organic frameworks),⁶ heterostructured “Janus” materials⁷ or core-shell structures⁸ could be useful: Only target molecules would be allowed to enter the active core (a MOF or another functional material) and thus to concentrate in the pores, while the outer MOF shell acts as a protecting molecular sieve; this way, the sensing signal may be less prone to “broadband” detection. – In a more general approach, specific MOF structures may be chosen, such as the rather hydrophobic ZIF-8, which thus hamper the free diffusion of water molecules inside the sensing platform.

Furthermore, structural colorations generated through multilayers are typically characterized by interference (i.e. change in hue and intensity for different viewing angles). For an optical breathalyzer, however, precise color definitions for specific ethanol concentrations are necessary to guarantee a correct result. Even if an optimal viewing angle could be found to achieve maximal intensity and defined hue, it would not be practicable to use breathalyzers at only one specific angle. Here, the color generating principle in *Morpho* butterflies can serve as an inspiration source for achieving a specific color at given conditions and for a broad angle region.⁹

Concerning the stability, we have experienced (in accordance with the literature) that MOF coatings are not particularly stable against chemicals such as acids,¹⁰ or high temperatures (e.g. max. 200 °C for ZIF-8)¹¹, and mechanical forces (if deposited *via* spin-coating). Moreover, the MOF platforms investigated as part of this thesis have shown to lose their sensitivity toward vapors after prolonged exposure times (see also ref. 1); hence, it is to be doubted that they may be used for long-time purposes or much less sensing liquids. – Nevertheless, the life-time of MOF sensors may be probably significantly enhanced by using SAMs (self-assembled monolayers of organic molecules) or SURMOFS which covalently attach the MOF structure to the substrate;^{6,12} this way, the structures may be less prone to mechanical strength *and* be sufficiently stable in solutions than when being deposited *via* spin-coating. In addition, the MOF particles could be embedded in polymers or other suitable materials, or the stack may be fashioned with a polymeric top layer as a robust shield; however, it must be guaranteed that the underlying MOF component is still accessible to the analyte which most likely enters through the top site (see **chapter 3.3**). Another option would be to regenerate MOF structures after they have been used for a certain time period: This could be done, for instance, through exposure to specific solvents¹³ or through soaking in the respective precursor solution. The latter has been shown for the (partially) reversible substitution of metal nodes or linkers in a given framework structure.¹⁴

Along with these lines, it will be increasingly important to have the possibility to post-synthetically modify given stacks to adapt or enhance their functionality. This possibility resembles the way in which nature fabricates its materials: Instead of fabricating specific materials for specific functions, a few basic building units are appropriately assembled, and subsequently modified with respect to actual and/or local needs. This approach may also allow for a more environmentally friendly and efficient fabrication of devices as a lower variety of building units and, hence, chemicals are needed, and the MOF may be also recycled if necessary. – Modification of MOF-based sensing platforms can be achieved either through post-synthetic modification of the organic linkers,¹⁵ or hybridization approaches (e.g. metathesis reactions involving partial linker/metal substitution;^{14,16,17} **Fig. 1a**): This can be done, for instance, by soaking the parent MOF structure in the respective precursor solution. For both modification routes, it is expected that the sorption properties of the new MOF can thus be optimized for a desired sensing reaction (e.g. through strengthening desired host–guest interaction forces). At the same time, if the MOF is implemented in a photonic device, such substitution reactions could be monitored with great ease (and *in*

situ!) as the introduction of other building blocks (functional groups, metal or linker) into the MOF structure is expected to induce changes in the effective RI and, hence, optical appearance (**Fig. 1b**).

Along with the implementation of ZIF-8 as a defect layer in regular $\text{SiO}_2/\text{TiO}_2$ BSs (**chapter 3.3**), we have shown that the ZIF-8 defect layer may be inverted into a mesoporous layer by simply depositing metal oxide sols onto the MOF slab; the stack architecture (i.e. ordering of the individual layers) thereby remained unaltered during the transformation. Such one-step inversion processes may be used as an alternative route for hybridization with MOFs: For example, the inverted pores may be fashioned with functionality by either grafting desired molecules to the pore walls,¹⁸ or by accommodating active guests in the mesopores, such as gold nanoparticles or dyes.¹⁶ The pores could also be filled with a precursor material and thus used as templates for opal-like structures;¹⁹ likewise the pores can serve as confined reaction containers, e.g. in order to yield polymers with properties strictly dictated by pore size, geometry and pore chemistry of the host lattice.¹⁷ Epitaxial growth of different MOF phases on the pore walls in a layer-by-layer fashion, e.g. for the synthesis of core-shell structures or tandem MOF PCs, seems also feasible.

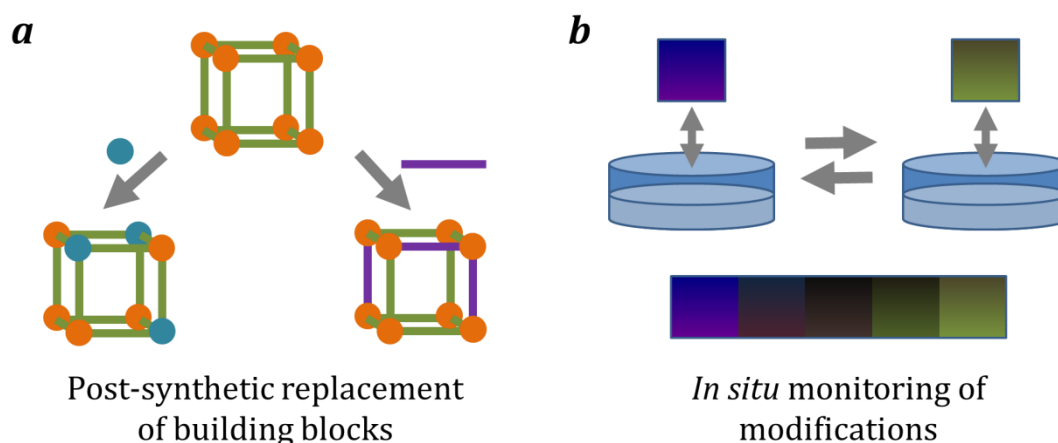


Figure 1. Metathesis reactions with MOFs. (a) Post-synthetic strategies (here: replacement of metal nodes and organic linkers; routes on the left and right, respectively) allow for altering the composition of a MOF structure at specific positions, while maintaining its overall topology. (b) The process and the outcome of such exchange reactions may be monitored *in situ* by implementing the desired MOF type into a photonic multilayer (colored squares). Upon soaking into an appropriate reaction solution (e.g. with another metal source), the PC's color is expected to change depending on the exchange rate (visualized with the color bar). This reaction may occur reversibly, thus allowing for the regeneration of the parent MOF structure.

Another interesting research field would be to experiment with the material's porosity: Here, the fabrication of the mesoporous layer may be studied as a function of different MOF nanoparticles having characteristic particle diameters and shapes, or as a function of the particle ordering in the thin film (**Fig. 2**). In this context, the co-assembly of MOF particles, differing either in size, shape or composition, may lead to well-defined hierarchical pore systems. As MOFs possess different stabilities with respect to temperature, solvents and chemicals (owing to their structural diversity), both the pore topology and functionality could be thus tailored toward a desired sensing performance (e.g. molecular sieving or preferential adsorption).^{20,21}

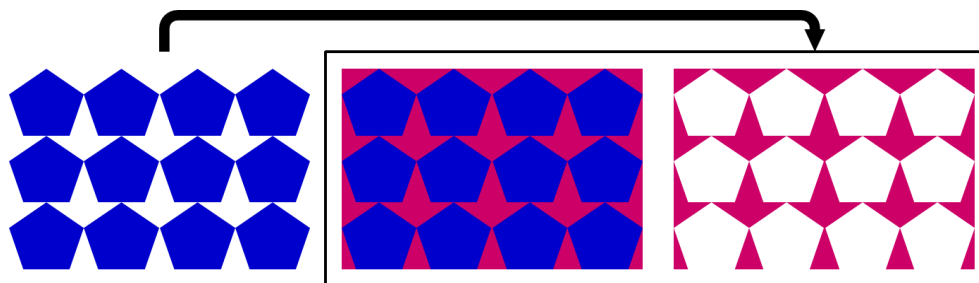


Figure 2. Pore engineering with MOF nanoparticles (blue) as templates for meso-/macroporous films. The transformation into the inverted layer through a stimulus (e.g. an infiltrating sol, as shown above in pink) may be studied as a function of particle size, shape, composition or ordering, to achieve either uniform or hierarchical pore systems.

To conclude, the performance of optical MOF detection platforms may be improved by several approaches related to hierarchically controlled structuring (structural microporosity, nanoparticulate layers, mesoporous opaline assemblies, building block replacement, SURMOFs etc.), or the directed mixing of color generating principles (diffraction gratings and multilayer interference for iridescenceless colors); using both approaches, the realization of novel “emerging” properties seems feasible which have not yet been (fore)seen. In particular, the concepts of 1) metathesis reactions, 2) controlled pore engineering, and 3) embedding in soft materials for enhanced spectral changes may render a powerful tool toward the fabrication of smart optical sensing devices based on MOFs.

4.2 REFERENCES

- 1 P. Davydovskaya, A. Ranft, B. V. Lotsch and R. Pohle, *Anal. Chem.* **2014**, *86*, 6948-6958.
- 2 P. Davydovskaya, A. Ranft, B. V. Lotsch and R. Pohle, *Proc. Eng.* **2014**, *87*, 1433-1436.
- 3 Y. Kang, J. J. Walsh, T. Gorishnyy and E. L. Thomas, *Nature Mater.* **2007**, *6*, 957-960.
- 4 A. Schneemann, V. Bon, I. Schwedler, I. Senkovska, S. Kaskel and R. A. Fischer, *Chem. Soc. Rev.* **2014**, *43*, 6062-6096.
- 5 K.-I. Jang, H. U. Chung, S. Xu, C. H. Lee, H. Luan, J. Jeong, H. Cheng, G.-T. Kim, S. Y. Han, J. W. Lee, J. Kim, M. Cho, F. Miao, Y. Yang, H. N. Jung, M. Flavin, H. Liu, G. W. Kong, K. J. Yu, S. I. Rhee, J. Chung, B. Kim, J. W. Kwak, M. H. Yun, J. Y. Kim, Y. M. Song, U. Paik, Y. Zhang, Y. Huang and J. A. Rogers, *Nat. Commun.* **2015**, *6*, doi: 10.1038/ncomms7566.
- 6 L. Heinke, M. Tu, S. Wannapaiboon, R. A. Fischer and C. Wöll, *Microporous Mesoporous Mater.* **2015**, *216*, 200-215.
- 7 M. Meilikhov, S. Furukawa, K. Hirai, R. A. Fischer and S. Kitagawa, *Angew. Chem. Int. Ed.* **2013**, *52*, 341-345.
- 8 K. Koh, A. G. Wong-Foy and A. J. Matzger, *Chem. Commun.* **2009**, 6162-6164.
- 9 S. Kinoshita and S. Yoshioka, *ChemPhysChem* **2005**, *6*, 1442-1459.
- 10 L. Huang, H. Wang, J. Chen, Z. Wang, J. Sun, D. Zhao and Y. Yan, *Microporous Mesoporous Mater.* **2003**, *58*, 105-114.
- 11 J. Cravillon, S. Münzer, S.-J. Lohmeier, A. Feldhoff, K. Huber and M. Wiebcke, *Chem. Mater.* **2009**, *21*, 1410-1412.
- 12 E. Biemmi, A. Darga, N. Stock and T. Bein, *Microporous Mesoporous Mater.* **2008**, *114*, 380-386.

4 Summary and Outlook

- 13 G. Majano, O. Martin, M. Hammes, S. Smeets, C. Baerlocher and J. Pérez-Ramírez, *Adv. Funct. Mater.* **2014**, *24*, 3855-3865.
- 14 P. Deria, J. E. Mondloch, O. Karagiari, W. Bury, J. T. Hupp and O. K. Farha, *Chem. Soc. Rev.* **2014**, *43*, 5896-5912.
- 15 S. M. Cohen, *Chem. Rev.* **2012**, *112*, 970-1000.
- 16 H. Furukawa, U. Müller and O. M. Yaghi, *Angew. Chem. Int. Ed.* **2015**, *54*, 3417-3430.
- 17 M. L. Foo, R. Matsuda and S. Kitagawa, *Chem. Mater.* **2014**, *26*, 310-322.
- 18 H.-L. Jiang, D. Feng, T.-F. Liu, J.-R. Li and H.-C. Zhou, *J. Am. Chem. Soc.* **2012**, *134*, 14690-14693.
- 19 B. Hatton, L. Mishchenko, S. Davis, K. H. Sandhage and J. Aizenberg, *Proc. Natl. Acad. Sci.* **2010**, *107*, 10354-10359.
- 20 S. Furukawa, J. Reboul, S. Diring, K. Sumida and S. Kitagawa, *Chem. Soc. Rev.* **2014**, *43*, 5700-5734.
- 21 M. D. Allendorf and V. Stavila, *CrystEngComm* **2015**, *17*, 229-246.

5 APPENDIX

Supporting information for *chapters 2.1, 3.1, 3.2* and *3.3* is provided in this section, followed by a list of all publications and presentations.

5.1 SUPPORTING INFORMATION FOR CHAPTER 2.1

adapted from A. Ranft, S. B. Betzler, F. Haase and B. V. Lotsch, „Additive-mediated size control of MOF nanoparticles”, *CrystEngComm* **2013**, 15, 9296-9300.

Cover image^a



^aImage designed by Christoph Hohmann (NIM), reproduced by permission of the authors from The Royal Society of Chemistry.

Materials and methods

Chemicals

Benzene-1,3,5-tricarboxylic acid (H₃BTC, 98%), N,N-dimethylformamide (DMF, p.a.) and copper acetate monohydrate (Cu(OAc)₂ · H₂O, 98+%) were purchased from Acros. Poly(acrylic acid) (PAA, MW = 1,800), 2-aminoterephthalic acid (H₂BDC-NH₂, 99+%) and polyvinylpyrrolidone (PVP, MW = 40,000) were purchased from Sigma-Aldrich. Zinc acetate dihydrate (Zn(OAc)₂ · 2H₂O, p. a.) was purchased from ACS. Hexadecyltrimethylammonium bromide (CTAB, 98%) was purchased from Alfa Aesar. Ethanol (99%) was purchased from BfB. All chemicals were used as received without further purification.

Synthesis of HKUST-1

In a typical synthesis, H₃BTC (73.8 mg, 0.344 mmol) was dissolved in ethanol (1.4 mL) and DMF (4.2 mL) under stirring and combined with PAA (221 mg, 0.123 mmol). To this mixture, a solution of Cu(OAc)₂ · H₂O (70 mg, 0.344 mmol) in 2.8 mL deionized water was added under vigorous stirring, which rapidly induced the formation of a blue precipitate. The product was separated from the reaction mixture by centrifugation and washed in DMF, ethanol and water for at least 3 times. Stable colloidal suspensions were obtained by redispersing the washed product in DMF using ultrasound (Elmasonic S100H ultrasonic bath, 550 W).

For further experiments, the reaction conditions were varied, including reaction time (5 min, 30 min), reaction temperature (0 °C, room temperature (RT), 55 °C) and amount of PAA (depending on the weight ratio of H₃BTC:PAA = 1:2, 1:3, 1:4, 1:5, 1:6, 1:15, corresponding to 0.082 mmol, 0.123 mmol, 0.164 mmol, 0.205 mmol, 0.246 mmol, 0.615 mmol of PAA).

Synthesis of IRMOF-3

In a typical synthesis, Zn(OAc)₂ · 2H₂O (35.12 mg, 0.160 mmol) was dissolved in DMF (2 mL) and rapidly added to a solution of H₂BDC-NH₂ (10.86 mg, 0.059 mmol), CTAB (10 mg, 0.027 mmol) and PVP (10 mg, 0.00025 mmol) in 3 mL DMF under stirring. The reaction mixture turned turbid within the first minute and was stirred additionally for at least 5 min. The product was separated by centrifugation and washed in DMF and ethanol for at least 3 times. Stable colloidal suspensions were obtained by redispersing the washed product in DMF using ultrasound (Elmasonic S100H ultrasonic bath, 550 W).

For further experiments, the reaction conditions were varied, including reaction time (5 min, 30 min, 60 min, 3 d, 11 d) and amount of additive (0.0135 mmol/0.00013 mmol, 0.027 mmol/0.00025 mmol, 0.054 mmol/0.0005 mmol of CTAB/PVP; 0.00013 mmol, 0.00025 mmol, 0.0005 mmol, 0.00125 mmol of PVP).

Thin film deposition

Thin films consisting of HKUST-1 and IRMOF-3 nanoparticles, respectively, were obtained by spin-coating the respective colloidal suspensions on pre-cleaned silicon substrates. Prior to film deposition, silicon substrates (1x1 cm²) were treated with piranha acid (96% H₂SO₄/30% H₂O₂, 2:1) for 1 h, rinsed intensively with water, dried under nitrogen stream and plasma-cleaned (Femto plasma cleaner, Diener Electronic GmbH, air, 100 W) for 5 min. A rotational speed of 4000 rpm for 1 min was used for the deposition of the layers, while the acceleration speed was fixed to 1500 rpm/s. Thicker films were obtained by multiple coating steps.

Characterization

Powder X-ray diffraction (XRD) measurements were carried out on a Huber G670 diffractometer in Guinier geometry or on a Stadi P type diffractometer (Stoe & Cie) in transmission using Ge(111)-monochromated Cu-K_{α1} radiation ($\lambda = 1.54051 \text{ \AA}$). Data were collected between 5° and 50°.

Dynamic light scattering (DLS) measurements were carried out with a Nano ZS Zetasizer with a 4 mW HeNe laser ($\lambda = 633 \text{ nm}$). The scattered light was detected in back-scattering geometry at an angle of 173°.

Infrared (IR) spectroscopy was carried out with the help of a Perkin Elmer Spektrum BX II spectrometer with an attenuated total reflectance unit.

Scanning electron (SE) micrographs were recorded either with a JEOL JSM-6500F SEM equipped with an Oxford EDX analysis system or with a Merlin (Zeiss) FE-SEM.

Atomic force microscopy (AFM) measurements were performed on a MFP-3D Stand alone AFM (Asylum Research, Santa Barbara). Tapping-mode was applied using OMCL-AC160TS-R3 (Olympus, Tokio) cantilevers with a resonant frequency of 300 kHz.

Ellipsometric measurements were carried out using a Woollam M2000D at angles of 65°, 70° and 75° in the spectral range of 190-1000 nm. The data were fitted between 300 and

1000 nm using a Cauchy-type material as the model layer to determine the effective refractive index (RI) and the thickness of the investigated layers (using average values deduced by SEM images as starting values). The effective RI of the MOF layer is made up of RI contributions from textural porosity ($RI_{\text{por}} = 1$), the MOF itself, and possible residues of the additives ($RI_{\text{res}} > 1$).

Additional analytical data

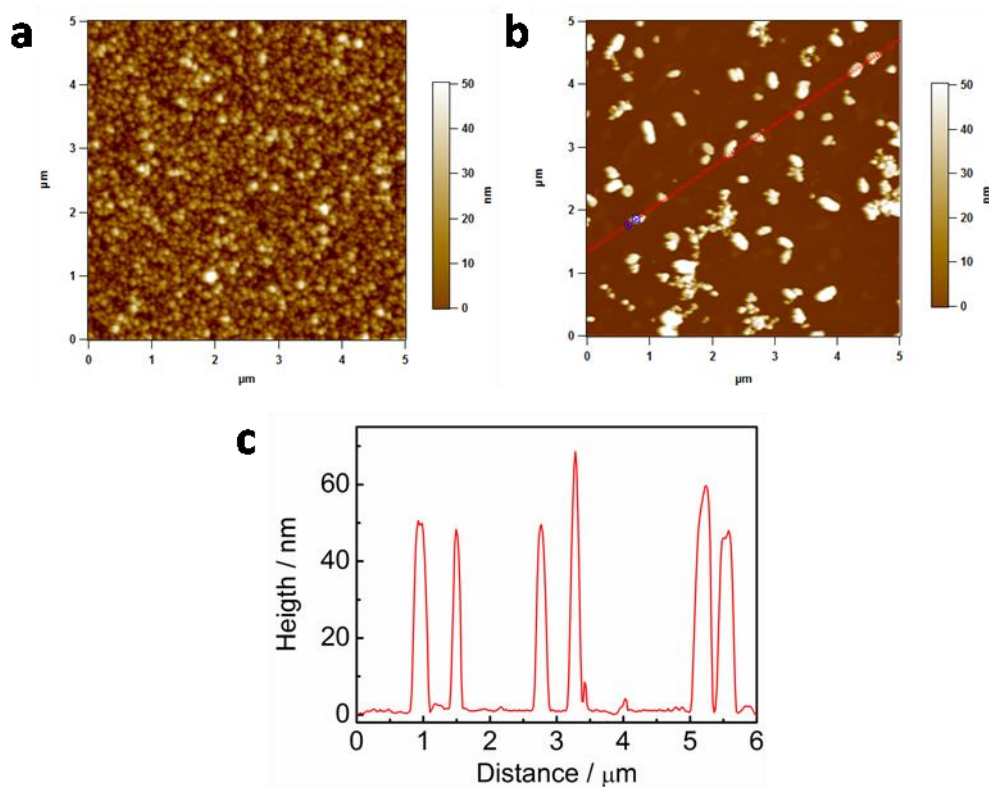


Figure S1. AFM measurements (a, b) and height profile (c) of HKUST-1 particles synthesized at 0 °C.

5 Appendix

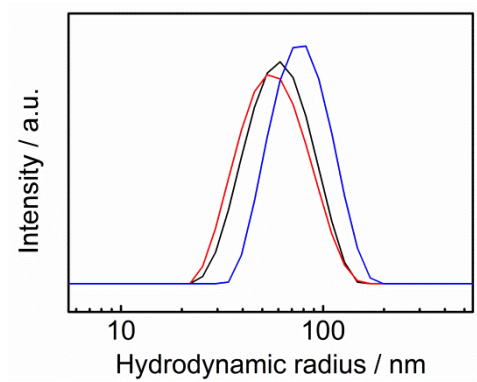


Figure S2. DLS measurements of HKUST-1 particles synthesized at different temperatures (black: 0 °C, red: RT, blue: 55 °C) after centrifugation and redispersion in DMF.

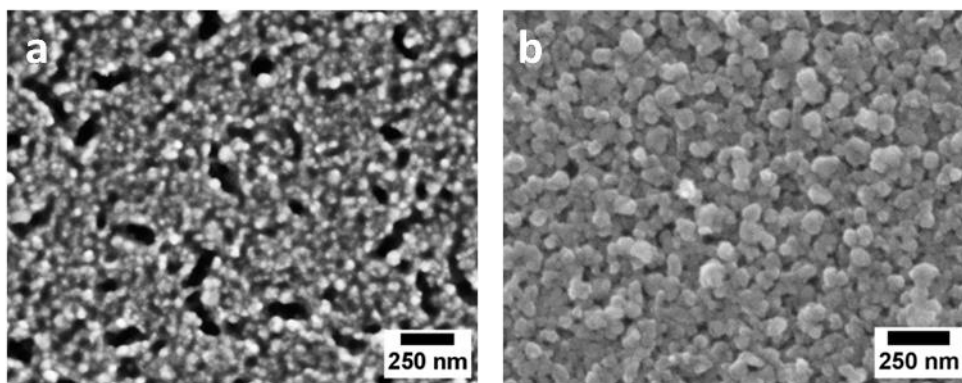


Figure S3. SEM images of HKUST-1 particles synthesized at different temperatures: a) 0 °C, b) RT.

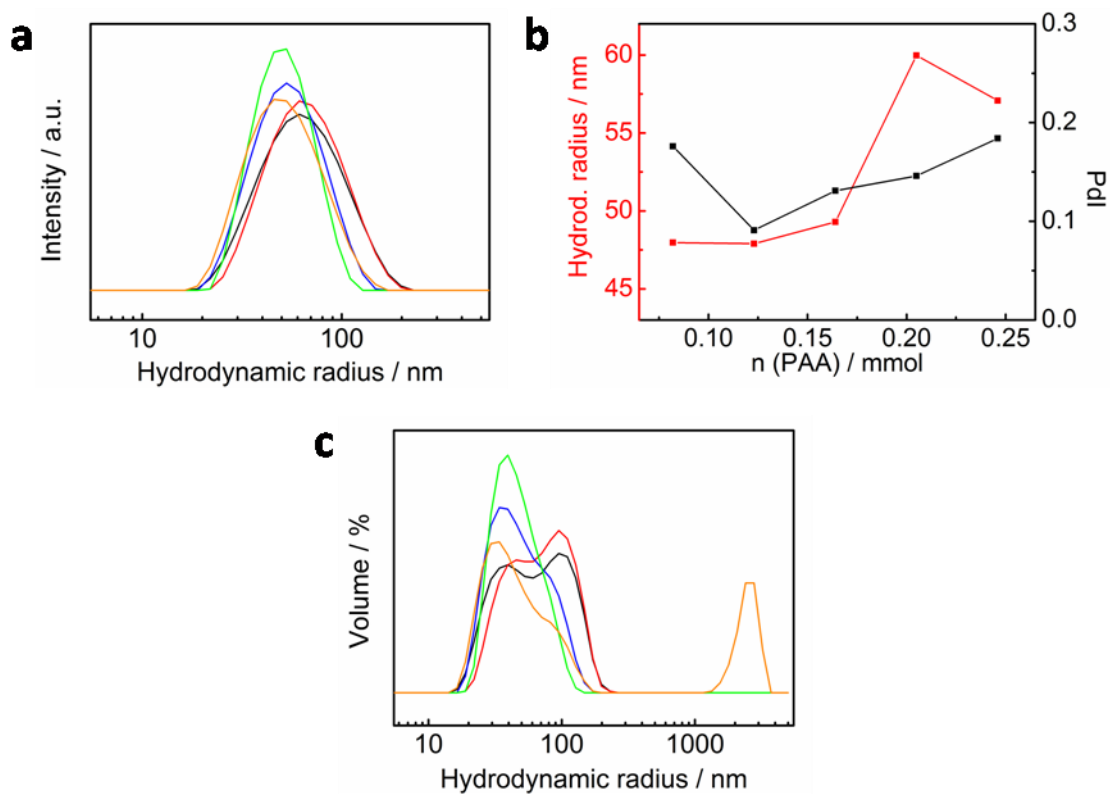


Figure S4. DLS measurements (shown as a) intensity distribution and c) volume distribution) of HKUST-1 particles synthesized at 0 °C with different ratios of H₃BTC:PAA (black: 1:6 / 0.246 mmol PAA, red: 1:5 / 0.205 mmol PAA, blue: 1:4 / 0.164 mmol PAA, green: 1:3 / 0.123 mmol PAA, orange: 1:2 / 0.082 mmol PAA) after centrifugation and redispersion in DMF; b) evolution of the size (red) and the polydispersity index (PDI) (black), with the PAA concentration.

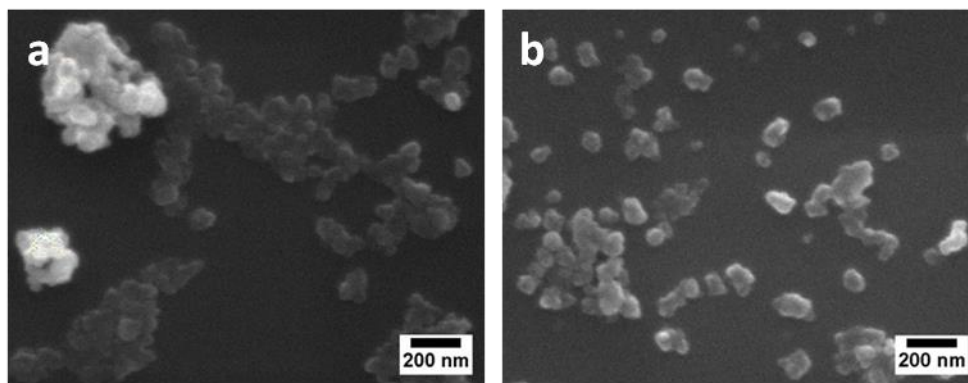


Figure S5. SEM images of HKUST-1 particles synthesized at RT after different reaction times: a) 5 min, b) 30 min.

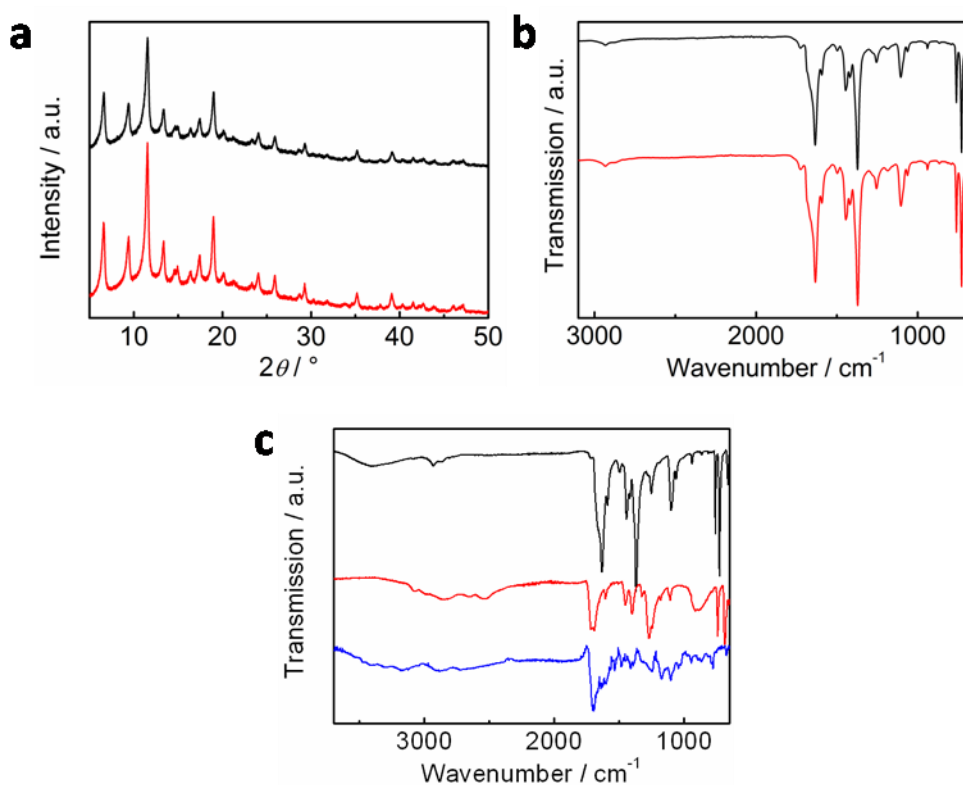


Figure S6. PXRD patterns (a) and IR spectra (b) of HKUST-1 particles synthesized at RT after different reaction times (black: 5 min, red: 30 min). c) IR spectra of HKUST-1 (black, synthesized without additives), H₃BTC (red) and PAA (blue), showing good agreement between the products synthesized with and without PAA (note that PAA and H₃BTC have similar IR bands, in particular around 1700 cm^{-1} corresponding to C=O vibrations of carboxylic acid groups).

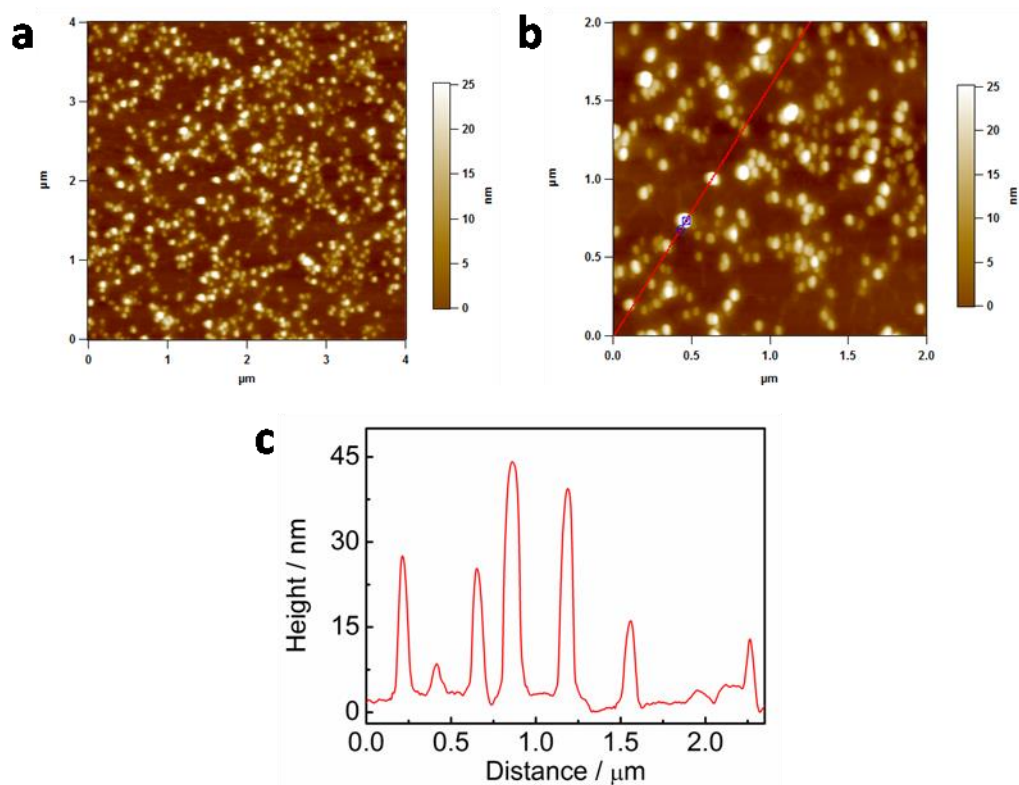


Figure S7. AFM measurements (a, b) and height profile (c) of IRMOF-3 particles.

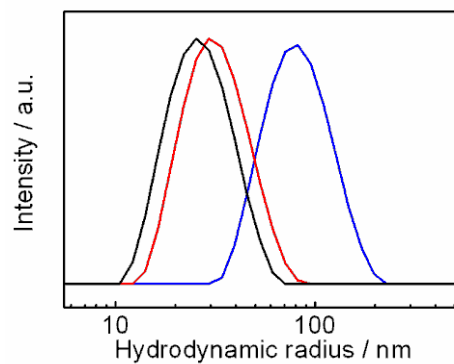


Figure S8. DLS measurements of IRMOF-3 particles synthesized with different total amounts of CTAB/PVP at weight ratios of 1:1 (black: 0.054 mmol/0.0005 mmol, red: 0.027 mmol/0.00025 mmol, blue: 0.0135 mmol/0.00013 mmol) after centrifugation and redispersion in DMF.

5 Appendix

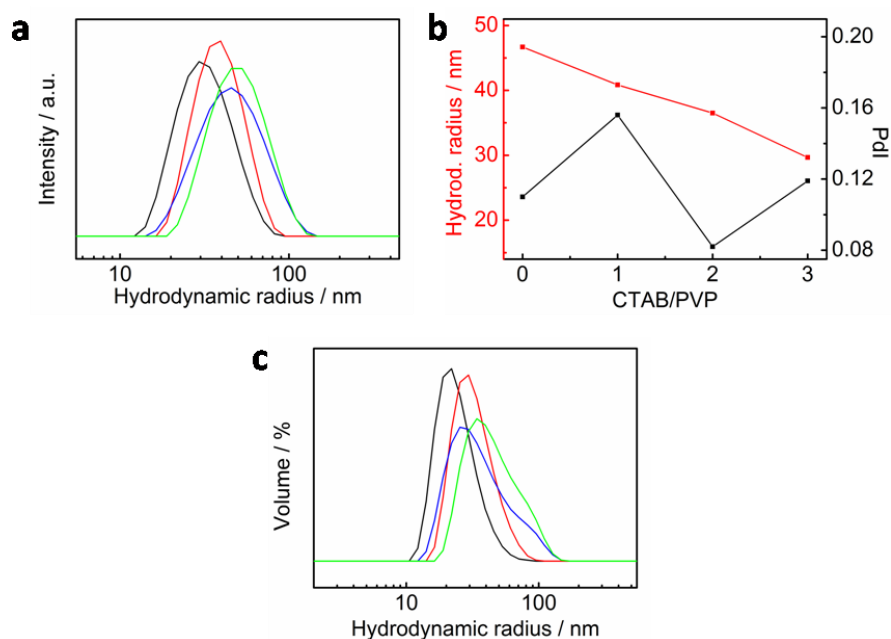


Figure S9. DLS measurements (shown as a) intensity distribution and c) volume distribution) of IRMOF-3 particles synthesized with different amounts of CTAB and/or PVP (black: weight ratio 1:1 of CTAB/PVP (0.027 mmol/0.00025 mmol), red: 0.027 mmol of CTAB, blue: 0.00025 mmol of PVP, green: no additives) after 5 min reaction time; b) evolution of the mean radius and the PDI with the amount of additives (0: no additives, 1: 0.027 mmol of CTAB, 2: 0.00025 mmol of PVP, 3: 0.027 mmol/0.00025 mmol of CTAB/PVP).

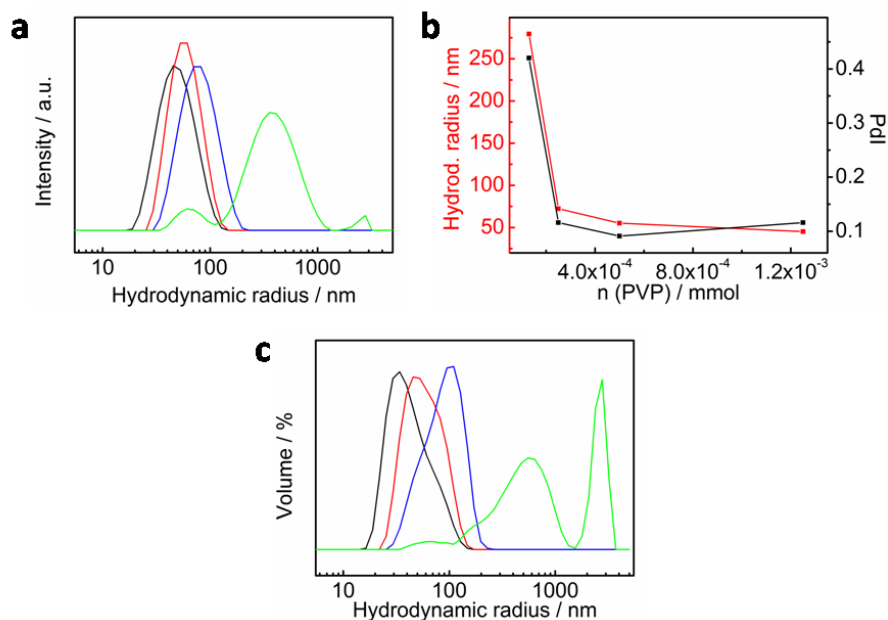


Figure S10. DLS measurements (shown as a) intensity distribution and c) volume distribution) of IRMOF-3 particles synthesized with different amounts of PVP (black: 0.00125 mmol, red: 0.0005 mmol, blue: 0.00025 mmol, green: 0.00013 mmol) after centrifugation and redispersion in DMF; b) evolution of the size (red) and the PDI (black) with the amount of PVP.

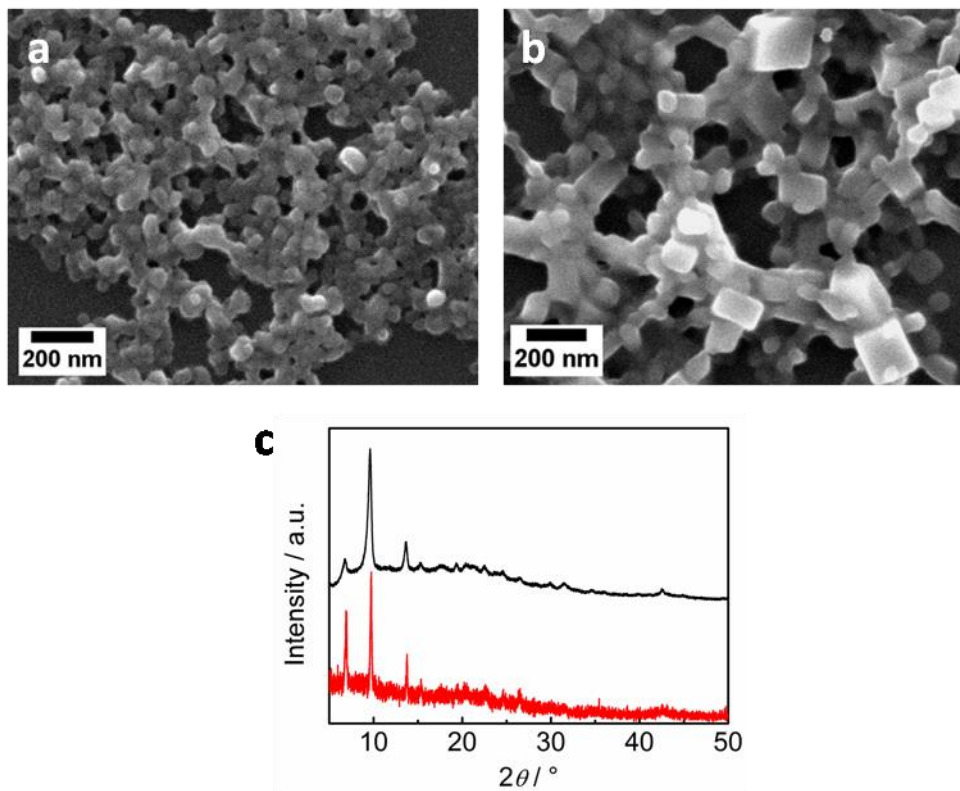


Figure S11. SEM images of IRMOF-3 particles synthesized a) with CTAB/PVP (0.027 mmol/0.00025 mmol) and b) without additives; c) corresponding PXRD patterns of IRMOF-3 particles synthesized with additives (black) and without additives (red).

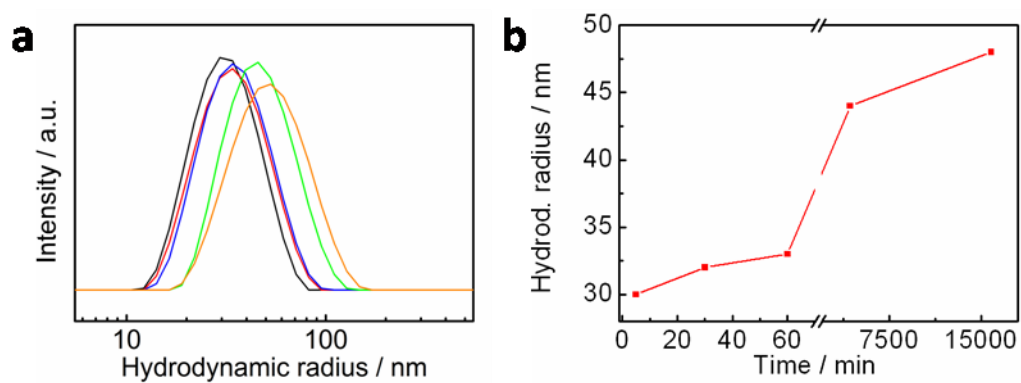


Figure S12. DLS measurements of IRMOF-3 particles as a function of time: a) evolution of the size distribution of the reaction mixture (black: 5 min, red: 30 min, blue: 60 min, green: 3 d, orange: 11 d); b) evolution of the mean radius.

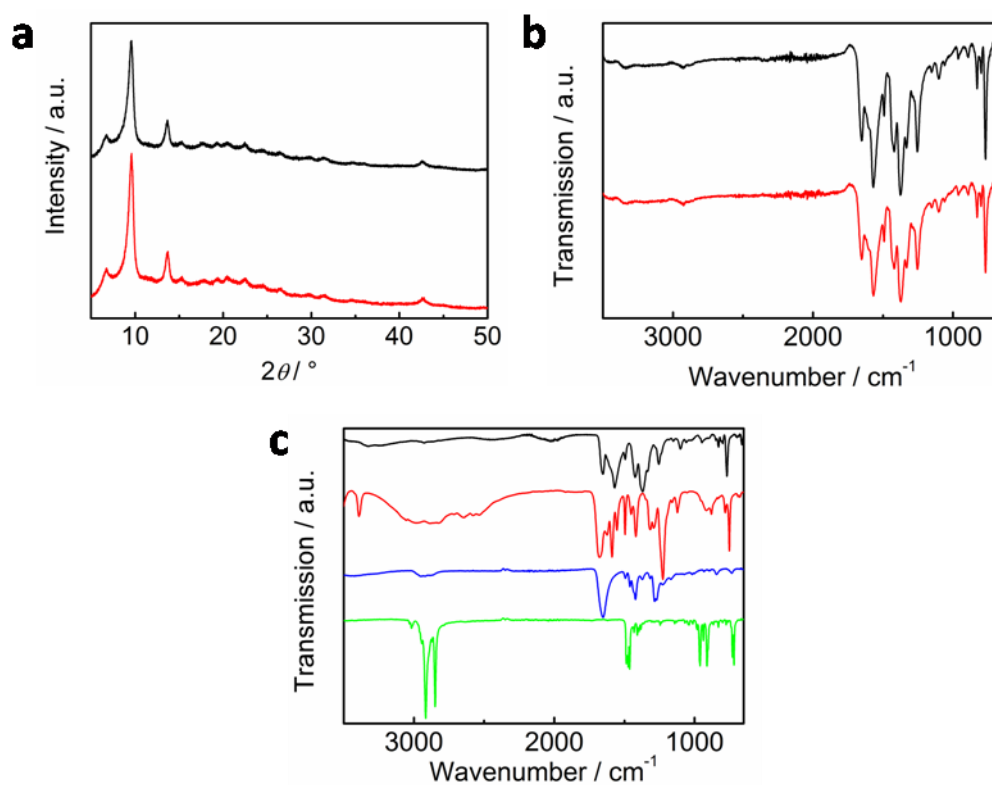


Figure S13. PXRD patterns (a) and IR spectra (b) of IRMOF-3 particles synthesized at different reaction times (black: 5 min, red: 30 min). c) IR spectra of IRMOF-3 (black, synthesized without additives), H₂BDC-NH₂ (red), PVP (blue) and CTAB (green), demonstrating the good agreement of the IR spectra of the products synthesized with and without CTAB/PVP as well as the absence of major residues from the additive mixture.

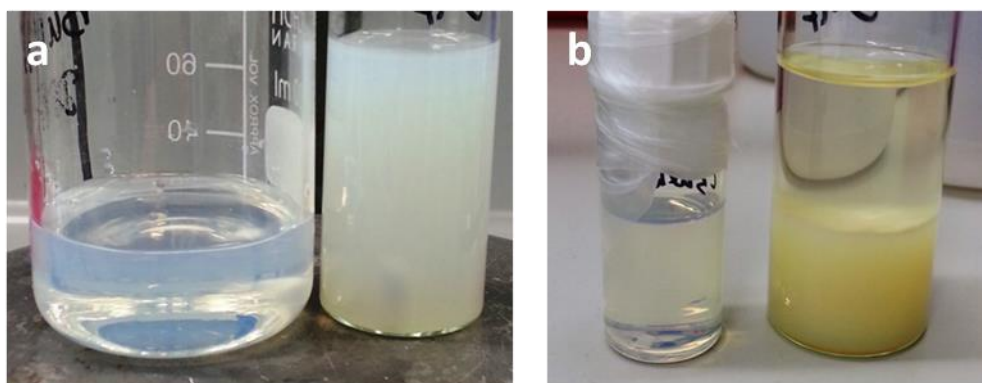


Figure S14. Photographs of suspensions of IRMOF-3 particles synthesized with additives (vessel on the left) and without additives (vessel on the right) after a) 30 min and b) 1 day.

5.2 SUPPORTING INFORMATION FOR CHAPTER 3.1

adapted from F. M. Hinterholzinger, A. Ranft, J. M. Feckl, B. Rühle, T. Bein and B. V. Lotsch, „One-dimensional metal-organic framework photonic crystals used as platforms for vapor sorption”, *J. Mater. Chem.* **2012**, *22*, 10356-10362.

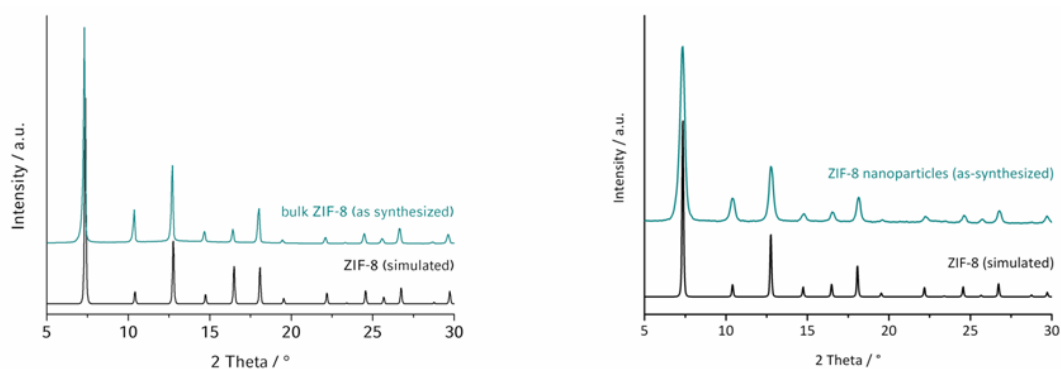
Additional analytical data

Figure S1. X-ray diffraction patterns (background corrected) of as-synthesized bulk ZIF-8 material (left) as well as of ZIF-8 nanoparticles (right) compared to simulated data.

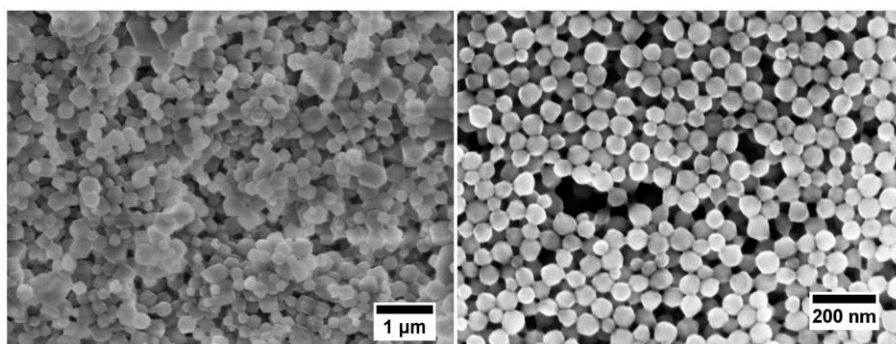


Figure S2. Scanning electron microscopy (SEM) images showing a bulk ZIF-8 powder sample obtained from the mixture solution used for the fabrication of BS-1 (left) as well as ZIF-8 nanoparticles used for the preparation of BS-2 (right).

5 Appendix

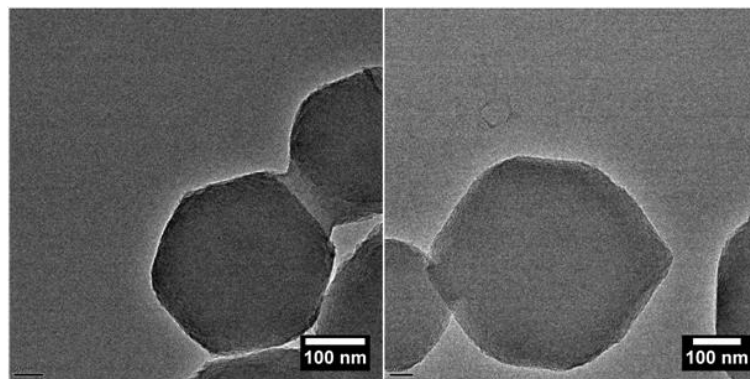


Figure S3. Transmission electron microscopy (TEM) micrographs showing as-synthesized ZIF-8 nanocrystals isolated from a powder sample obtained from the reaction solution used for dense ZIF-8 film growth.

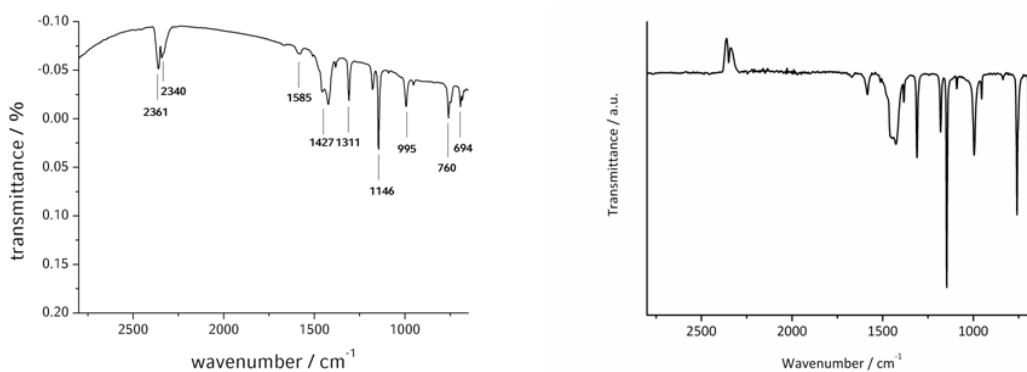


Figure S4. IR spectra of bulk ZIF-8 (left) as well as of ZIF-8 nanoparticles (right).

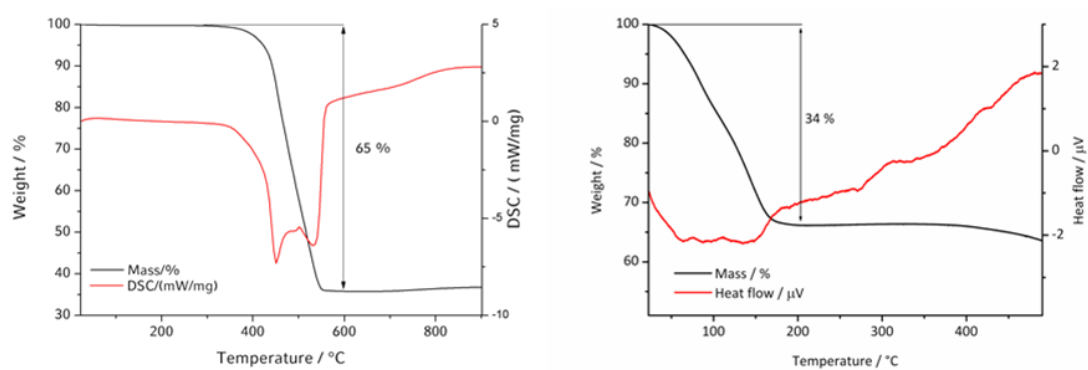


Figure S5. Thermogravimetric analysis (TGA), differential scanning calorimetry (DSC) and differential thermal analysis (DTA) of bulk ZIF-8 (left) and ZIF-8 nanoparticles (right), respectively, illustrating a one-step weight loss as well as the decomposition of bulk ZIF-8.

5 Appendix

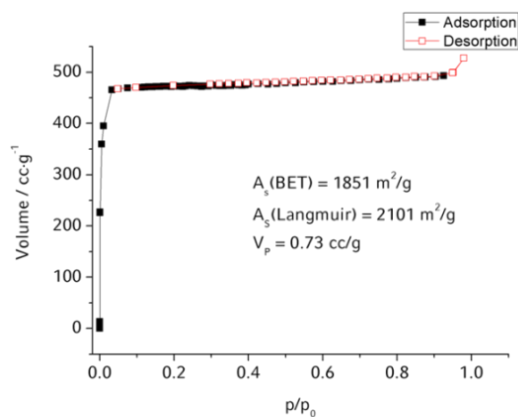


Figure S6. Physisorption measurement performed with nitrogen at 77 K for bulk ZIF-8 showing a type I isotherm, the specific surface area (BET/Langmuir) and the pore volume.

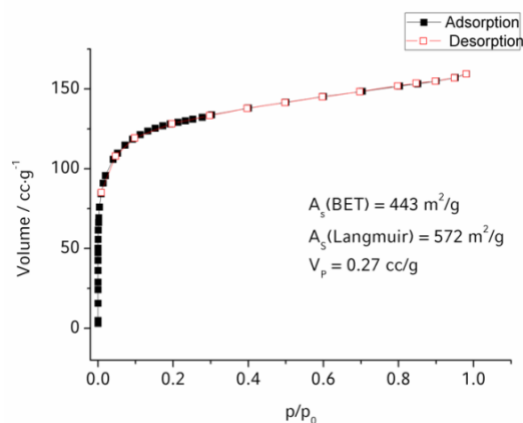


Figure S7. Physisorption measurement at 77 K performed on a titania nanoparticle sample synthesized without structure-directing agent (F127) showing a type I isotherm, the specific surface area (BET/Langmuir) and the pore volume.

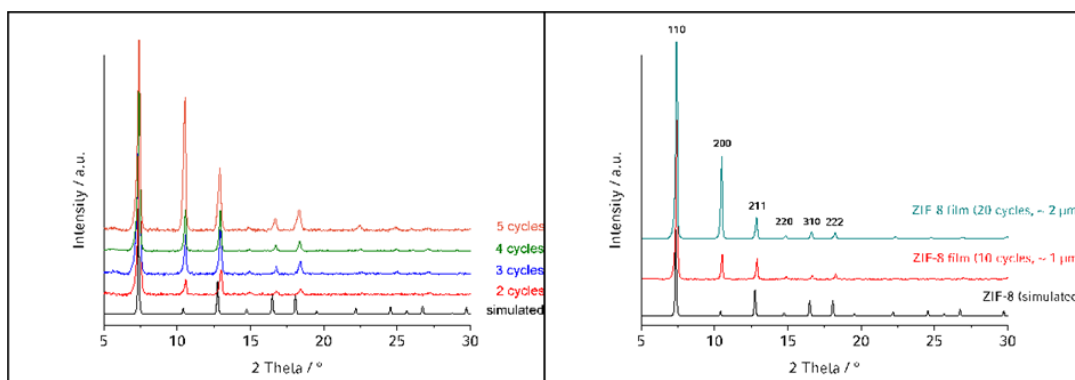


Figure S8. X-ray diffraction patterns (background corrected) of ZIF-8 thin films after different growing cycles compared to simulated data.

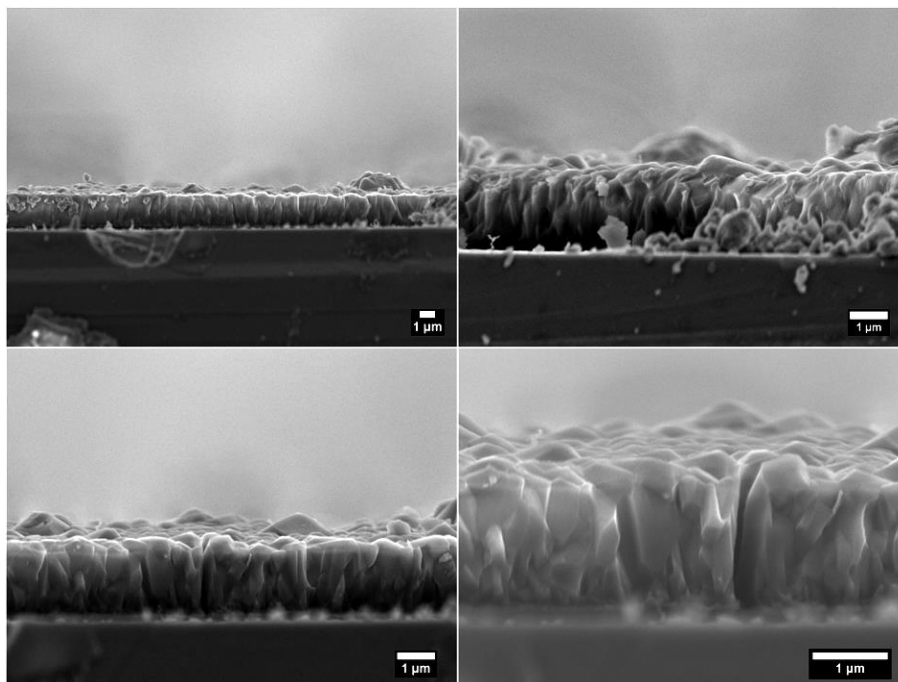


Figure S9. SEM micrographs showing a 10-cycled ZIF-8 thin film (magnification: x4.000 (top, left); x10.000 (top, right); x10.000 (bottom, left); x20.000 (bottom, right)).

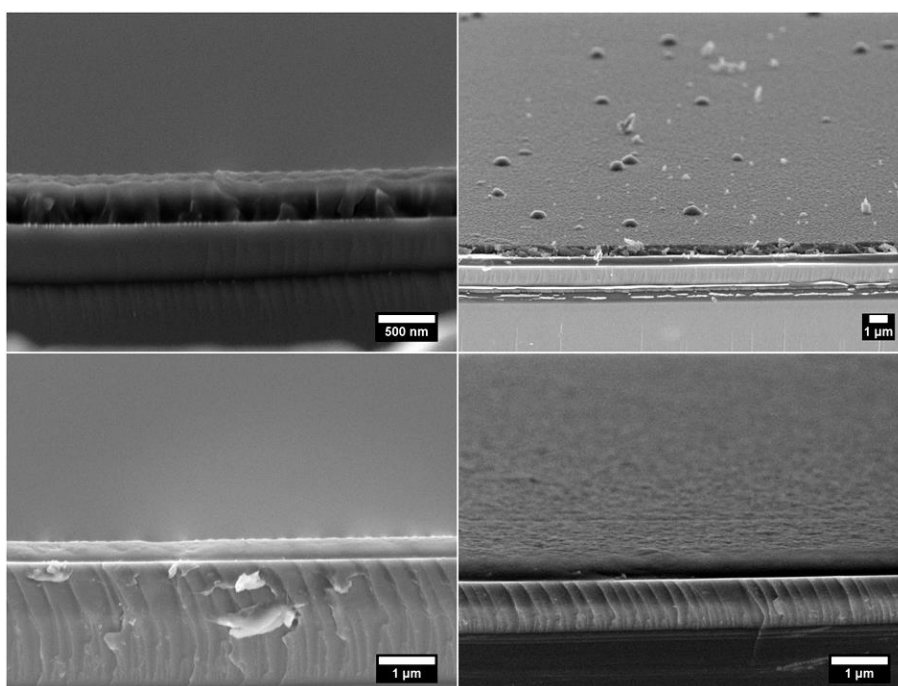


Figure S10. SEM micrographs showing ZIF-8 thin films grown in a crystallization solution while shaking (top) as well as under ultrasonic irradiation (bottom) (magnification: x5.000 (top, left); x30.000 (top, right); x15.000 (bottom, left); x15.000 (bottom, right)).

5 Appendix

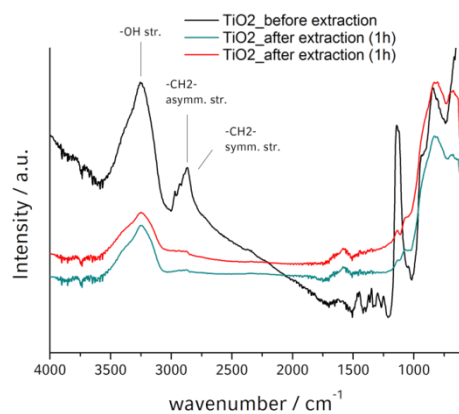


Figure S11. RAIR spectra of a TiO₂ thin film before and after the ethanol extraction procedure.

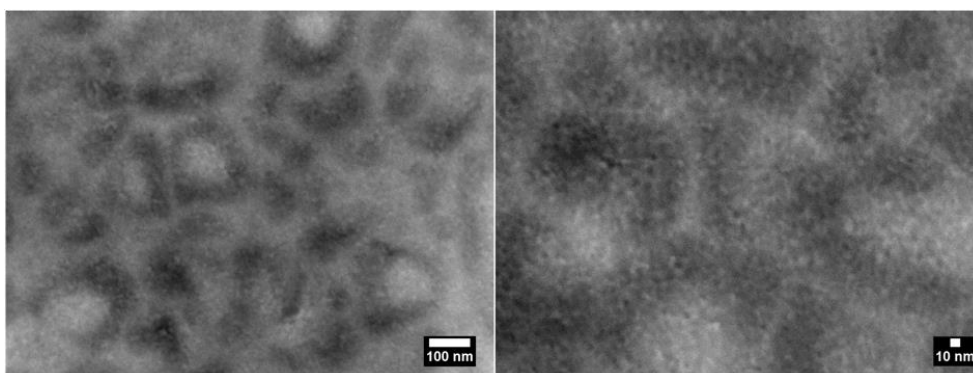


Figure S12. SEM micrographs demonstrating the mesoporous structure of a thin TiO₂ film after ethanol extraction (magnification: x100.000 (left); x250.000 (right)).

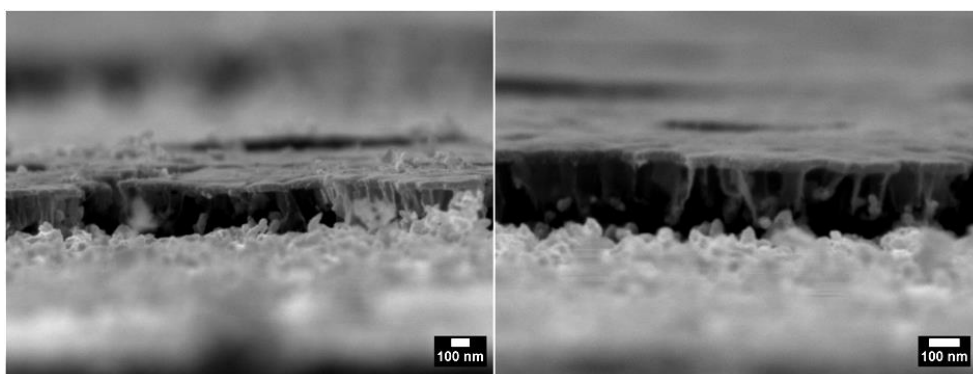


Figure S13. SEM micrographs showing bilayered BS-1 with an average film thickness of ~ 50 nm for each titania layer and ~ 200 nm for each ZIF-8 layer, respectively. The ZIF-8/mp-TiO₂ Bragg stack is depicted for different magnifications (x45.000 (left); x75.000 (right)).

5 Appendix

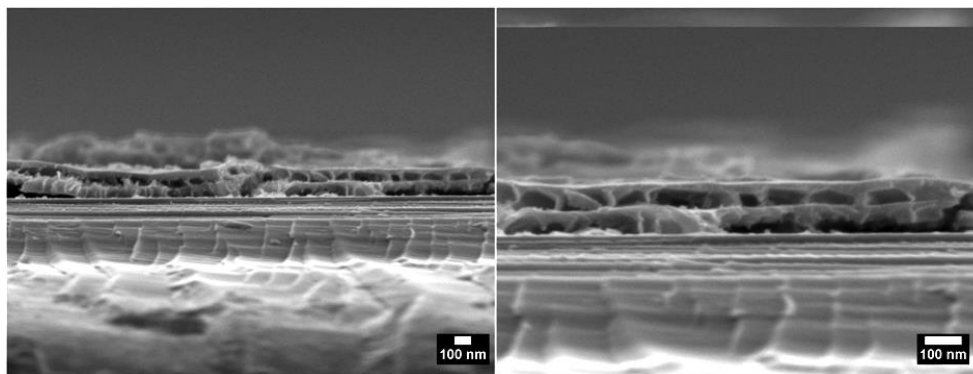


Figure S14. SEM micrographs showing the two-bilayered BS-1 with an average film thickness of ~ 50 nm for each titania layer and ~ 70 nm for each ZIF-8 layer, respectively. The ZIF-8/mp-TiO₂ Bragg stack is depicted for different magnifications ($\times 40,000$ (left); $\times 90,000$ (right)).

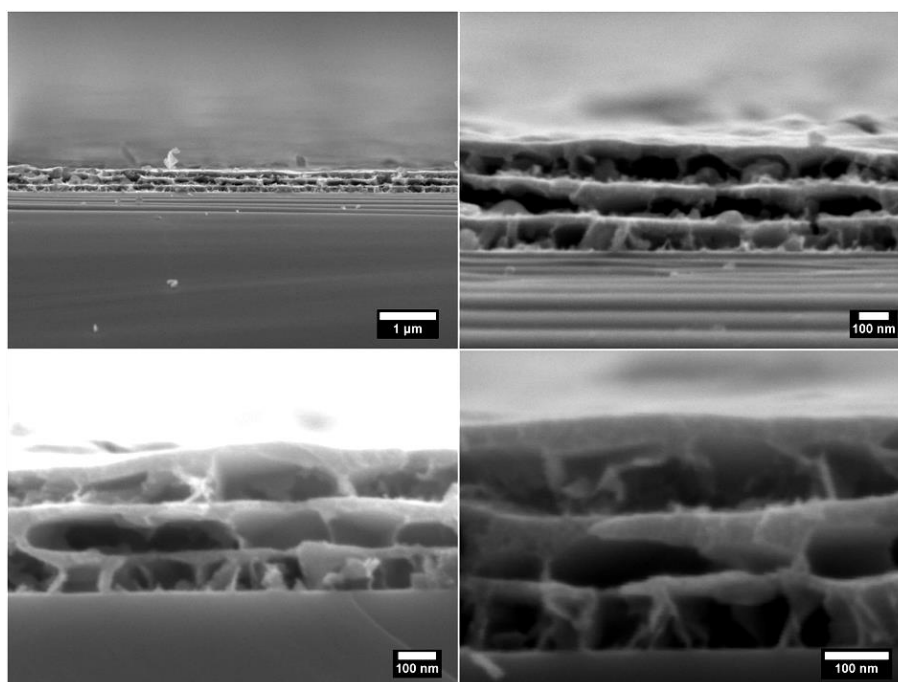


Figure S15. SEM micrographs showing the three-bilayered BS-1 with an average film thickness of ~ 50 nm for each titania layer and ~ 70 nm for each ZIF-8 layer, respectively. ZIF-8/mp-TiO₂ Bragg stack is depicted for different magnifications ($\times 15,000$ (top, left); $\times 80,000$ (top, right); $\times 100,000$ (bottom, left); $\times 170,000$ (bottom, right)).

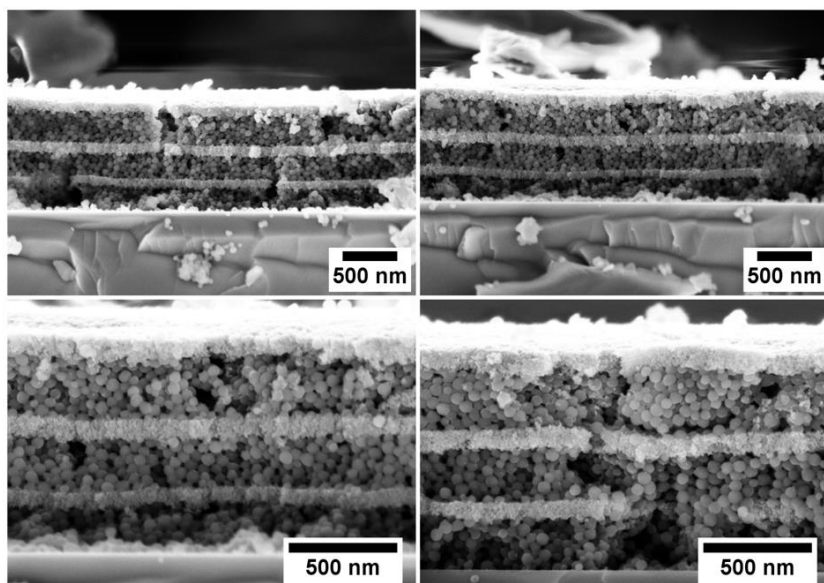


Figure S16. SEM micrographs showing the three-bilayered BS-2 with an average film thickness of ~ 50 nm for each titania layer and ~ 200 nm for each ZIF-8 layer, respectively. ZIF-8/TiO₂-BS is depicted for different magnifications (x30.000 (top); x60.000 (bottom)).

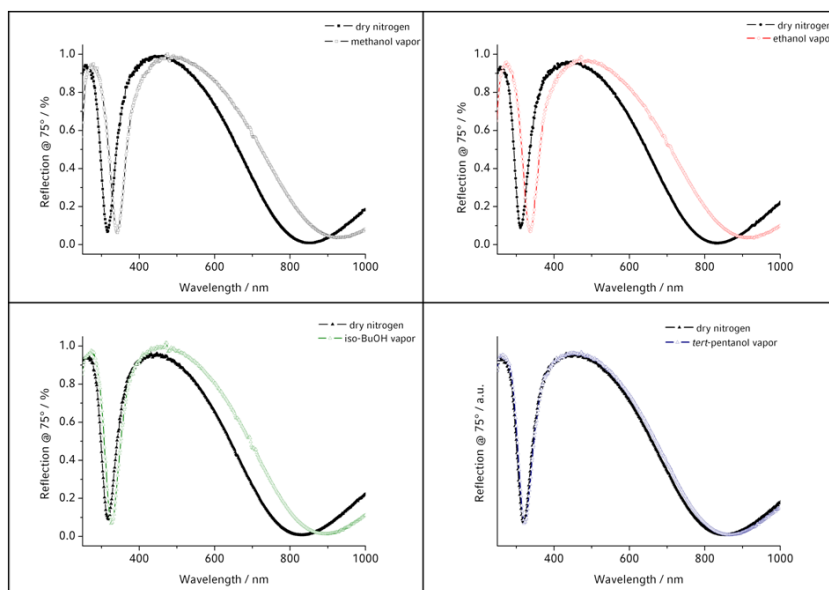


Figure S17. Reflectance spectra of a dense 200 nm single-layered ZIF-8 reference sample showing the pronounced optical shift monitored at saturation pressure upon exposure to methanol (top, left), ethanol (top, right) and isobutanol (bottom, left), respectively, as well as no optical response upon *tert*-pentanol (bottom, right) sorption.

5 Appendix

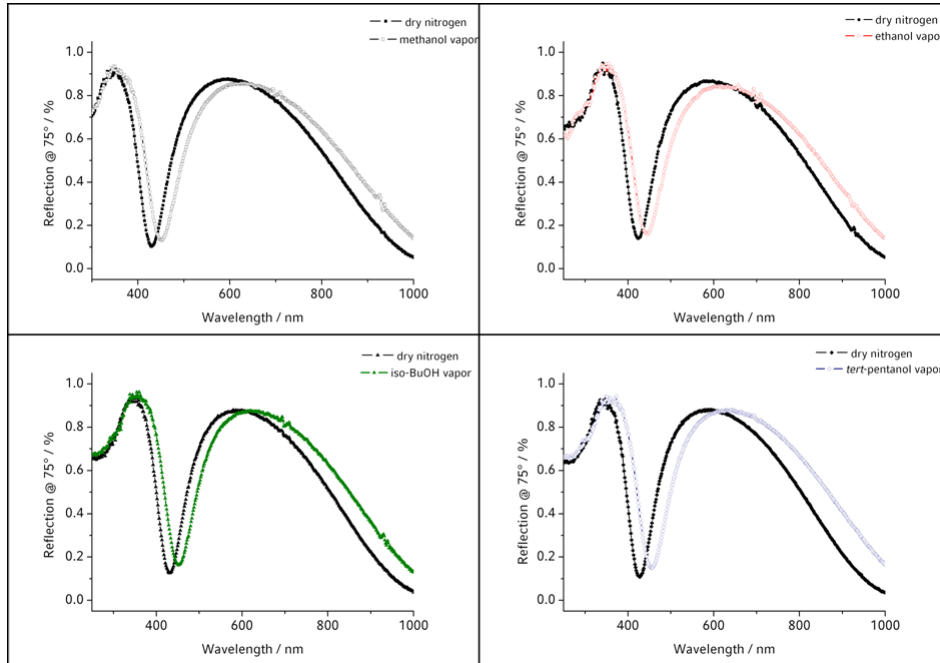


Figure S18. Reflectance spectra of the three-bilayered BS-1 showing the pronounced optical shift monitored at saturation pressure upon exposure to methanol (top, left), ethanol (top, right) and isobutanol (bottom, left) as well as upon *tert*-pentanol (bottom, right) sorption.

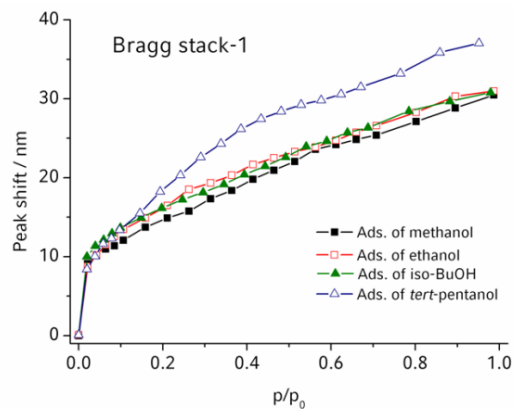


Figure S19. Optical vapor sorption isotherms demonstrating the adsorption performance of BS-1 during exposure to a series of alcohol vapors.

5 Appendix

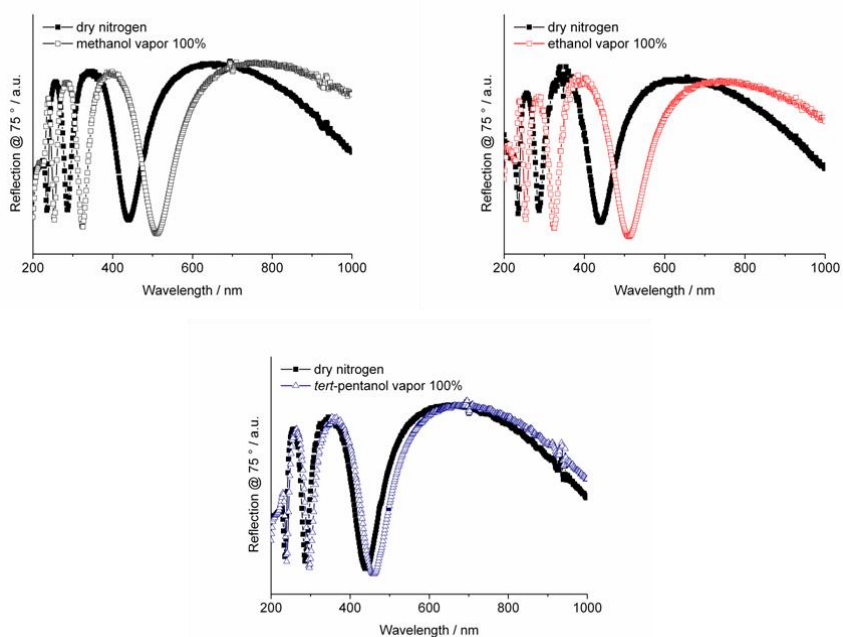


Figure S20. Reflectance spectra of a porous 400 nm single-layered ZIF-8 reference sample showing the pronounced optical shift monitored at saturation pressure upon exposure to methanol (top, left), ethanol (top, right) and *tert*-pentanol (bottom).

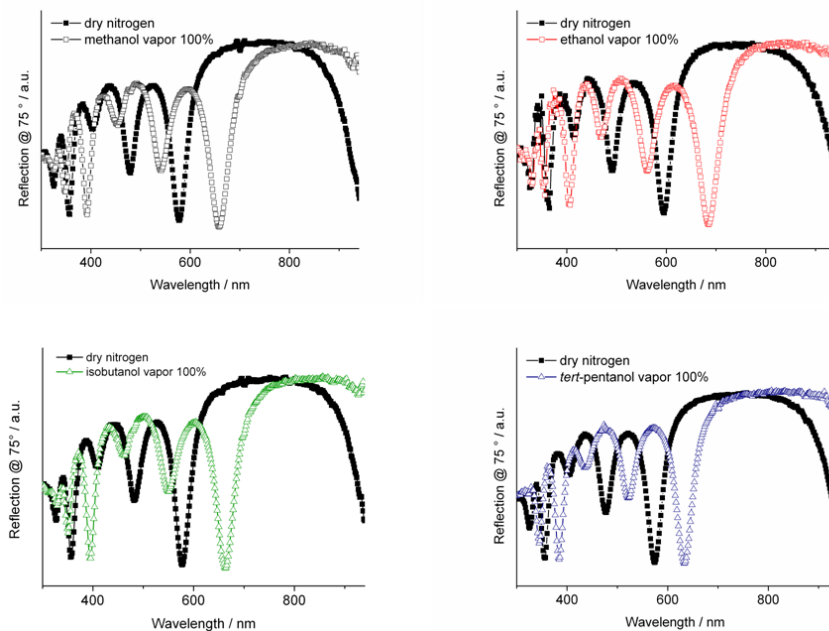


Figure S21. Reflectance spectra of the three-bilayered BS-2 (DMF) showing the pronounced optical shift monitored at saturation pressure upon exposure to methanol (top, left), ethanol (top, right), isobutanol (bottom, left) and *tert*-pentanol (bottom, right).

5 Appendix

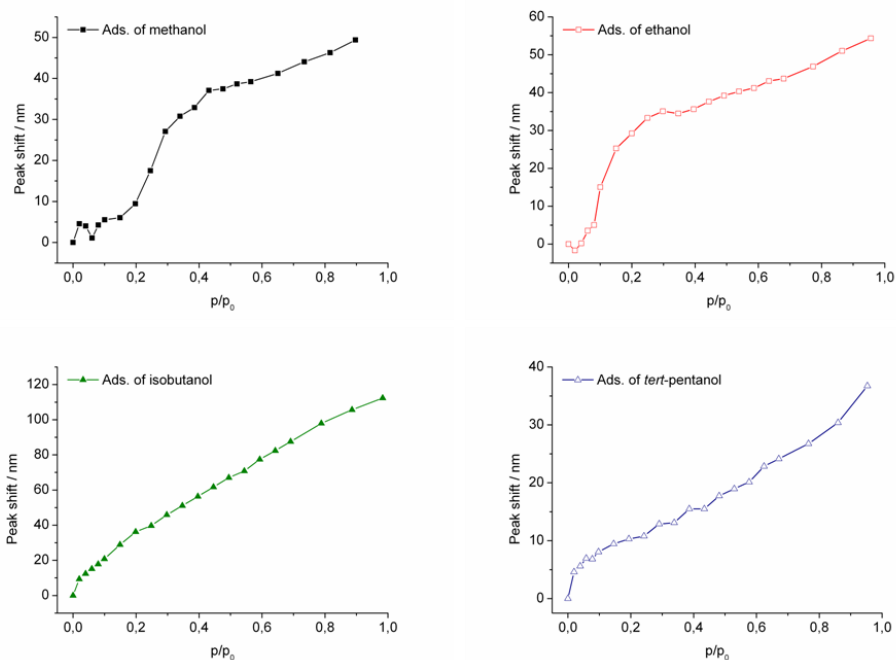


Figure S22. Reproduced optical vapor sorption isotherms demonstrating the adsorption of methanol, ethanol and *tert*-pentanol performed with BS-2 which was fabricated by redispersing the ZIF-8 nanoparticles in methanol (BS-2 (MeOH), see Experimental Section) as well as the adsorption of isobutanol into BS-2 prepared with nanoparticles redispersed in DMF (BS-2 (DMF)). Owing to the different fabrication methods and the resulting differences in the ZIF-8 layer thicknesses, less pronounced absolute shifts of about 50 nm are recorded using the BS-2 (MeOH) as compared to BS-2 (DMF) used in Fig. 5c and for isobutanol adsorption (Fig. S22). Therefore, the optical shift for isobutanol agrees well with the results obtained with BS-2 (DMF) shown in Fig. 5c, whereas the absolute shifts for the other solvent vapors are smaller. Nevertheless, note that the shapes of all four optical isotherms are in good agreement with the isotherms shown in Fig. 5c, indicating the same host-guest interactions as in BS-2 and thus, the same analyte selectivity to operate.

5.3 SUPPORTING INFORMATION FOR CHAPTER 3.2

adapted from A. Ranft, F. Niekiel, I. Pavlichenko, N. Stock and B. V. Lotsch, „Tandem MOF-Based Photonic Crystals for Enhanced Analyte-Specific Optical Detection”, *Chem. Mater.* **2015**, *27*, 1961-1970.

Characterization details

Sorption measurements

Sorption reflectance measurements were carried out with a Woollam M2000D ellipsometer using s-polarized light at an incident angle of 75°. Sorption isotherms were recorded at ambient temperature using home-made Labview-controlled gas mixing systems. Digital mass flow controllers (W-101A-110-P, F-201C, Bronkhorst High-Tech) were used to control the dosing of the carrier gas nitrogen and the liquid analyte, which was vaporized in a controlled evaporation and mixing element (CEM, W-101A, Bronkhorst High-Tech). For the sorption measurements, partial pressures p were calculated using the van der Waals equation. The relative pressure p/p_0 relates to the saturation pressure p_0 .

Time-dependent reflectance measurements were conducted using a fiber optic spectrometer (USB2000+, Ocean Optics) integrated with an optical light microscope (DM2500 M, Leica). The measurements were recorded at ambient temperature using gas mixing systems. Digital mass flow controllers (L-01RAD, F-201CV, Bronkhorst High-Tech) were used to control the dosing of the carrier gas nitrogen and the liquid analyte which was vaporized in a CEM element (W-101A, Bronkhorst High-Tech). The analyte concentration was calculated using the software FLUIDAT (Bronkhorst High-Tech) in the section “CEM calculation”. The calculation is based on the respective values for the atmospheric pressure, temperature and pressure of the individual components to determine the relative humidity degree.

The response of the MOF-based BS array toward different solvent vapors (ethanol, methanol, 2-propanol, water, 1-hexanol, ethanol/methanol, ethanol/2-propanol, ethanol/water and ethanol/1-hexanol at volume ratios of 1:1) was measured using the same setup (spectrometer, microscope and camera attached to the microscope). Instead of the gas mixing system, a washing bottle filled with the respective solvent(s) was used, and the vapor was transported to the array by bubbling nitrogen through the solvent.

The home-made chamber used for the time-dependent measurements and recording of the response of the array was assembled from two object slides and a 2.5x2.5 cm² square piece of PDMS (for a more detailed description of the fabrication of the PDMS mold refer to ¹). In this PDMS piece, a window of 2x2 cm² was cut out. The PDMS chamber was pierced three times to create an outlet and two separate inlets on the neighbouring sides. The first inlet was used for connecting the chamber to a constant nitrogen stream, the second one for the connection to the carrier gas saturated with the solvent vapor. For sorption measurements, the chamber was sandwiched between the two object slides and fixed with clamps to ensure a tight contact (see **Fig. S15** for photographic images of the setup). To achieve constant light conditions, the microscope was shielded from external light sources by using a box and black cloths.

Determination of the thickness and RI from ellipsometric data

Ellipsometric measurements were carried out using a Woollam M2000D ellipsometer at incident angles of 65°, 70° and 75° in the spectral range of 190 nm – 1000 nm. The data were fitted between 300 nm and 1000 nm. To determine the effective RI and the thickness of the individual layers, a Cauchy-type material was used as the model layer for MOFs. The effective RI is made up of RI contributions from textural porosity ($RI_{\text{por}} = 1$), the material itself and possible residues of the solvent ($RI_{\text{res}} > 1$). RI values presented in the **SI** are measured at $\lambda = 589$ nm. For fitting, average thickness values were used as starting values deduced from fitting thin layers prepared similarly.

Calculation of normalized values of Bragg diffraction peak shifts

In order to compensate for the inherent non-linearity of wavelength based reflectance spectra (as opposed to the energy scale), leading to apparent larger shifts for diffraction peaks at high wavelengths (and hence, for thicker BSs), we calculated normalized values of the Bragg diffraction peak shifts. In our approach, normalized values were obtained by dividing each peak shift $\lambda_n - \lambda_0 (= \Delta\lambda)$ by the wavelength position λ_n of a distinct maximum at

a given partial pressure (see **Fig. S1**). For BSs with layer thicknesses corresponding to an ideal “quarter wave stack” (i.e. $\lambda_m/n_1 = 4d_1$ and $\lambda_m/n_2 = 4d_2$ where λ_m is the mid-gap wavelength) the normalized wavelength shifts should be independent of the stop band position. To prove that the validity of this approach also roughly holds for non-quarter wave stack BS compositions, we calculated the normalized values for two exemplary TiO₂/ZIF-8 BSs consisting of 10 bilayers with different thicknesses of the ZIF-8 layers (150 nm and 200 nm, respectively). The spectra shown in **Fig. S1** were simulated by using the respective RI values obtained for single films in dry nitrogen (ZIF-8: 1.188, TiO₂: 1.718) and after adsorption of ethanol at $p/p_0 \approx 1$ (ZIF-8: 1.244, TiO₂: 1.75), respectively. Based on the spectra of these “hypothetical” BSs, we calculated normalized values of 0.038 (corresponding to a shift of 20 nm) for the first BS (**Fig. S1a**, ZIF-8: 150 nm), and 0.040 (corresponding to a shift of 26 nm) for the second BS (**Fig. S1b**, ZIF-8: 200 nm). For calculations based on our experimentally obtained spectra, we used fitted values of the maxima shown in **Figs. S7, S8** and **S10-13** (for vapor adsorption isotherms) and **Figs. S17-19** (for **Table S6** in the **SI**), respectively.

Determination of the response time

To estimate general response times of TiO₂/MOF BSs, we used the spectra shown in **Fig. 5** (main article) and determined exemplary values at the transition from 0% to 25% ethanol vapor. The response time values presented in the article are derived from evaluating the baselines for 0% and 25% uptake (see **Fig. S9** for details). By aligning the measured curve, a right triangle is formed from which the response time (= opposite leg) can be determined.

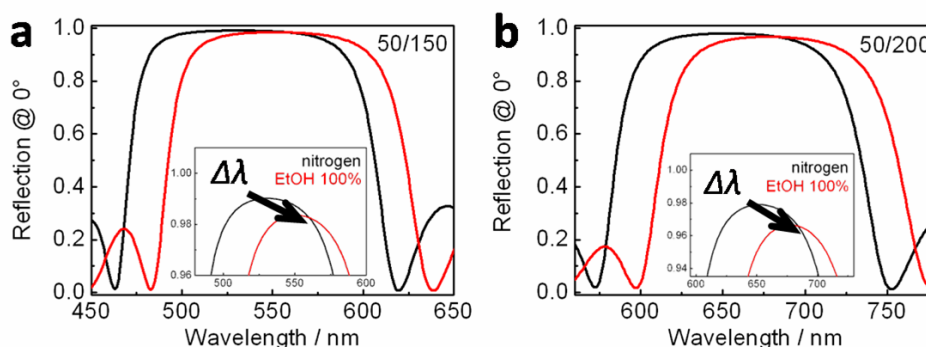


Figure S1. Simulated reflectance spectra for exemplary TiO₂/ZIF-8 BSs with different layer thicknesses in dry nitrogen and upon the adsorption of ethanol ($p/p_0 \approx 1$): a) TiO₂: 50 nm, ZIF-8: 150 nm, b) TiO₂: 50 nm, ZIF-8: 200 nm. The insets show a magnification of the range that was used for the calculation of normalized peak shift values.

Precision of spectral shifts

The precision of the spectral shifts shown in this work mainly depends on two parameters, i.e. sample quality and experimental limitations, which are discussed in the following in more detail.

Based on the SEM images shown in the main text (**Figs. 2** and **3**) we need to assume apparent thickness variations in our multilayers which can result in small red- or blue-shifts of the respective Bragg maxima depending on the spot that is investigated in a BS. This effect (i.e. a shift being induced by another factor besides analyte adsorption) can be excluded by choosing a distinct spot on the film, which is then maintained for all sorption measurements. To ensure that the same spot is used in every experiment, we took photographic images of the films with the help of a camera attached to the sensing setup. After finding the right spot the sample was fixed in this position to exclude sample movement, and the spectral changes upon adsorption were monitored in situ by tracing the change in reflectivity and recording optical images.

Thickness variations within different samples also result in different positions of the Bragg maximum and can lead to apparently larger shifts for thicker layers as we also mentioned in the main text. We faced this phenomenon by normalizing each shift ($\lambda_n - \lambda_0 = \Delta\lambda$) to the wavelength position (λ_n) to make the results for different BSs more comparable (see also section above). Although thickness variations and lateral inhomogeneities can affect the optical quality of photonic crystals, the spectral properties of our multilayers are sufficiently robust and pronounced (i.e. characterized by distinct Bragg peaks) as can be seen, for instance, in **Fig. 4a** (main text). Even more importantly, despite structural imperfections of the stacks the sensing properties of our systems are maintained as they predominantly arise from the inherent structural properties of the MOFs.

Besides the sensing material, the measurement settings (resolution of the optical fiber/ellipsometer, flow setup) have to be taken into account to assess the validity of the observed shifts. We therefore estimated the smallest concentration change (i.e. the limit of detection) that can be detected with our instrumental setup. For the time-dependent measurements shown in **Fig. 5** (main text), well-detectable shifts of 3.2 nm for both TiO₂/ZIF-8 and TiO₂/HKUST-1 BSs, and 7.2 nm for TiO₂/CAU-1-NH₂, respectively, were observed applying the lowest possible flow of 0.1 g/h (at 200 mln/min) at 10% ethanol dosage ($p/p_0 = 0.1$). For the sorption measurements shown in **Figs. 4b-d** (main text), shifts

of at least 1.9 nm were detected for an increase of the relative pressure from 0 to 0.02. Beside the sorption setup, the spectral detection system determines the detection limit, which is 0.38 nm for the optical fiber and 1.6 nm for the ellipsometer, as well as the goodness of the fitting to determine the peak shift. By using gas mixing systems and spectrometers with a higher resolution, it is thus expected that our MOF BSs are capable of detecting even lower analyte concentrations.

Evaluation of image-based sorption measurements

In a general procedure, the BSs were alternately exposed to nitrogen and the nitrogen stream saturated with one of the investigated solvents or solvent mixtures for 2 min each, and the respective color changes were monitored by recording images of specific spots on the samples with a camera attached to the microscope. The measurements were repeated three times to evaluate the reproducibility of the changes. In some cases, prolonged terms of flooding with nitrogen were used to enhance sorptive removal (up to 10 min). Data analysis was performed equally for each BS by conducting preprocessing steps in the first place, and subsequently calculating numerical codes for each analyte. For simultaneous processing of the images, we ran two macros which we developed with the program FIJI². The processing includes alignment of the images, area selection, cropping, splitting in color channels and measuring the mean intensities for each image. We determined average values from three measurements ($R_{\text{average}}(G, B)$ for all BSs) and calculated the differences between images recorded upon exposure to pure nitrogen and the sorptive ($\Delta R(G, B) = R_{\text{sorptive}}(G, B) - R_{\text{N}_2}(G, B)$ for each BS). By repeating these steps for all investigated analytes and all color channels, a 9 x 9 matrix is obtained (9 sorptives, 9 variables) representing the unique numerical codes for each solvent or solvent mixture. The thus determined values were used for principal component analysis (PCA) using the program XLSTAT³. Complete lists of the measured RGB intensities and calculated values are provided in **Tables S7-S9**.

Reproducibility of image-based sorption measurements

To test the reproducibility of the observed color changes, the measurements were repeated three times for each solvent and each stack. The intensity values extracted from the images for each cycle (N_2 vs sorptive/ N_2) alternate evenly for each color channel (see **Figs. S20** and **S21** for single solvents and solvent mixtures, respectively) except for a few cases for which we observed slight intensity changes with each cycle (compare with **Table S7-S9** for standard deviations). As the images were aligned before extraction of the color

intensities, a shift of the spot position eventually leading to differing intensity values can be excluded. It is therefore assumed that the slight changes are caused by a comparatively high affinity of the BSs toward different sorptives, or hampering of transport events due to the rather small pore sizes of the stack constituents leading to partially blocked pores after a sorption measurement. In both cases, complete recovery of the samples requires more exhaustive flooding with nitrogen (> 10 min) or more rigorous methods to remove the analyte from the sample (e.g. evacuation or heat).

1 A. T. Exner, I. Pavlichenko, D. Baierl, M. Schmidt, G. Derondeau, B. V. Lotsch, P. Lugli, and G. Scarpa, *Laser Photon. Rev.* **2014**, *8*, 726-733.

2 ImageJ 1.49m, Wayne Rasband, National Institutes of Health, USA, Java 1.8.0_25 (32-bit), <http://imagej.nih.gov/ij>.

3 XLSTAT Version 2014.5.03 (64-bit), Copyright Addinsoft 1995-2014, Microsoft Excel 14.0 7140 (7) (64-bit), <http://www.xlstat.com>.

Additional analytical data

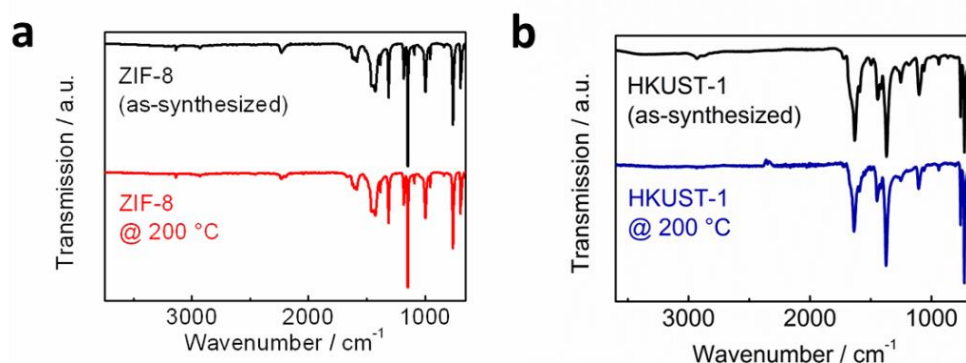


Figure S2. IR spectra of nanoparticle powder of MOFs prior to and after thermal treatment: (a) ZIF-8 and (b) HKUST-1.

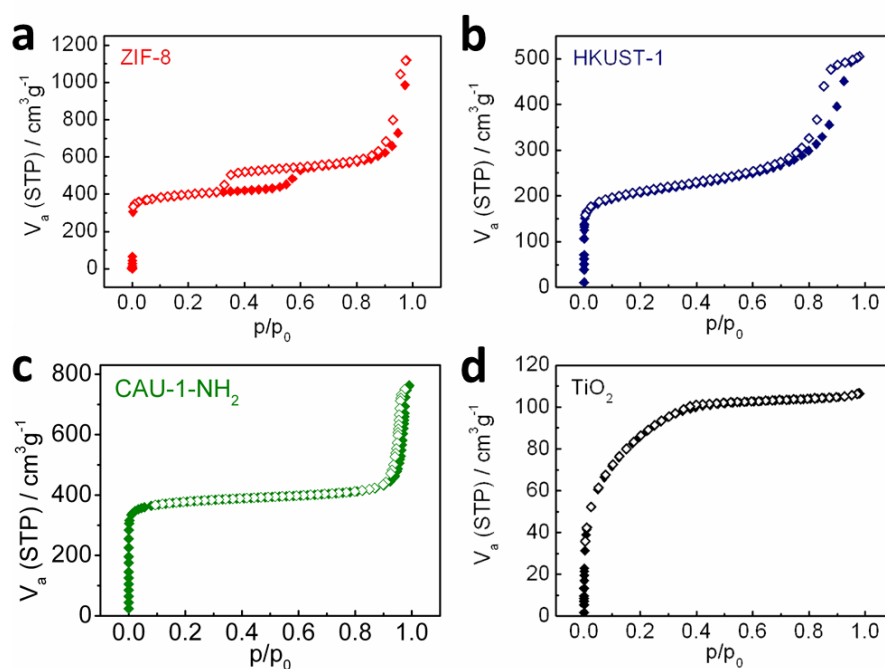


Figure S3. Sorption isotherms of nanoparticle powder of MOFs and TiO₂: (a) ZIF-8 (argon), (b) HKUST-1 (argon), (c) CAU-1-NH₂ (nitrogen) and (d) TiO₂ (argon).

Table S1. Sorption data of bulk MOFs and TiO₂. The values derive from the sorption isotherms shown in Fig. S3.

Compound	$a_{s,BET} / \text{m}^2\text{g}^{-1}$	$V_{\text{mikro}} / \text{cm}^3\text{g}^{-1}$
ZIF-8	1352	0.48
HKUST-1	675	0.30
CAU-1-NH ₂	1482	0.61
TiO ₂	278	0.07

5 Appendix

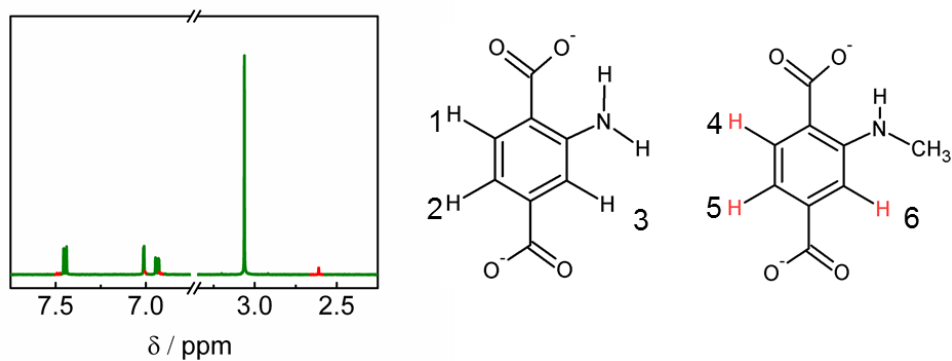


Figure S4. NMR data of bulk CAU-1-NH₂. Left: ¹H-NMR spectrum of bulk CAU-1-NH₂. Signals corresponding to BDC-NHCH₃²⁻ are marked in red. Right: Proton labeling of BDC-NH₂²⁻ and BDC-NHCH₃²⁻. ¹H-NMR (500 MHz, NaOD/D₂O): δ = 7.48 (d, ³J = 8.3 Hz, 0.04 H, H4), 7.45 (d, ³J = 8.1 Hz, 1 H, H1), 7.01 (d, ⁴J = 1.7 Hz, 1 H, H3), 7.00 (d, ⁴J = 1.8 Hz, 0.04 H, H6), 6.94 (dd, ³J = 8.1 Hz, ⁴J = 1.6 Hz, 1H, H2), 6.90 (dd, ³J = 7.9 Hz, ⁴J = 1.4 Hz, 0.04 H, H4), 3.06 (s, 3.67 H, OCH₃), 2.61 (s, 0.13 H, NH-CH₃) ppm.

Table S2. Elemental analysis of bulk CAU-1-NH₂. Calculated values refer to [Al₄(OH)_{2.34}(CH₃O)_{3.66}(BDC-NH₂)_{1.68}(BDC-NH₃)_{1.19}(BDC-NHCH₃)_{0.13}·1.19Cl·H₂O.

	C / %	H / %	N / %
Found	39.5	3.53	5.00
Calculated	38.5	3.82	4.88

Table S3. EDX analysis of bulk CAU-1-NH₂.

	Al		Cl	
Found	67.3 %	75.4 %	21.6 %	20.9 %
Averaged	71.4 %		21.3 %	
Normalized to 4 Al ³⁺	4		1.19	

5 Appendix

Table S4. EDX analysis of TiO₂/MOF BSs and tandem MOF BSs on Si substrates.

	Zn / %	Cu / %	Al / %	Ti / %
TiO ₂ /ZIF-8	0.22			1.62
TiO ₂ /HKUST-1		0.24		2.16
TiO ₂ /CAU-1-NH ₂			0.53	2.43
ZIF-8/HKUST-1	0.61	0.43		
ZIF-8/HKUST-1	0.31	0.80		
ZIF-8/CAU-1-NH ₂	0.87		0.58	
ZIF-8/CAU-1-NH ₂	0.35		0.44	

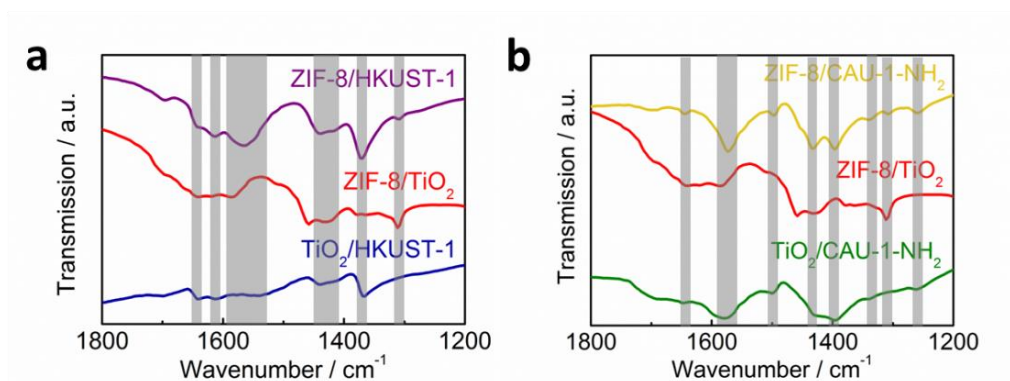


Figure S5. IR spectra of tandem MOF and TiO₂/MOF BSs on Si substrates: (a) ZIF-8/HKUST-1 in comparison to ZIF-8/TiO₂ and TiO₂/HKUST-1, (b) ZIF-8/CAU-1-NH₂ in comparison to ZIF-8/TiO₂ and TiO₂/CAU-1-NH₂.

Table S5. Simulated thicknesses and refractive indices (RI) derived from ellipsometric data of thin MOF films on Si substrates.

Material	Thickness	RI
ZIF-8	153 nm	1.20
HKUST-1	110 nm	1.25
CAU-1-NH ₂	236 nm	1.30

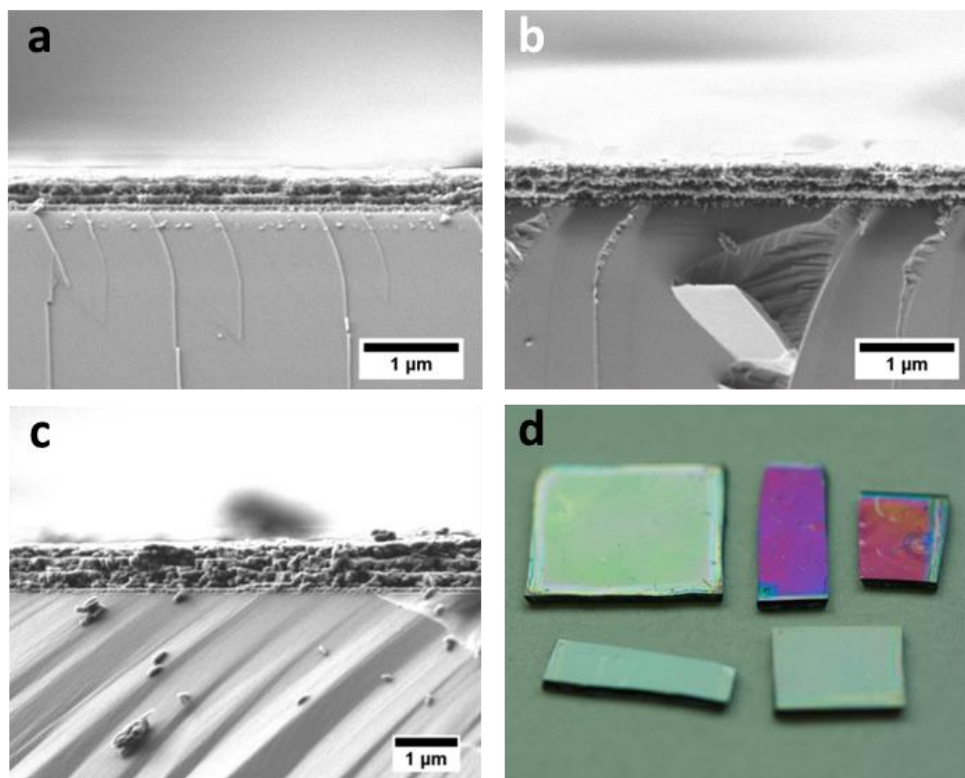


Figure S6. SEM images of (a) TiO₂/ZIF-8 BS, (b) TiO₂/HKUST-1 BS, (c) TiO₂/CAU-1-NH₂ BS and a photographic image (d) of five representative BS samples (from left to right, top: TiO₂/ZIF-8, TiO₂/HKUST-1, TiO₂/CAU-1-NH₂, bottom: ZIF-8/HKUST-1, ZIF-8/CAU-1-NH₂).

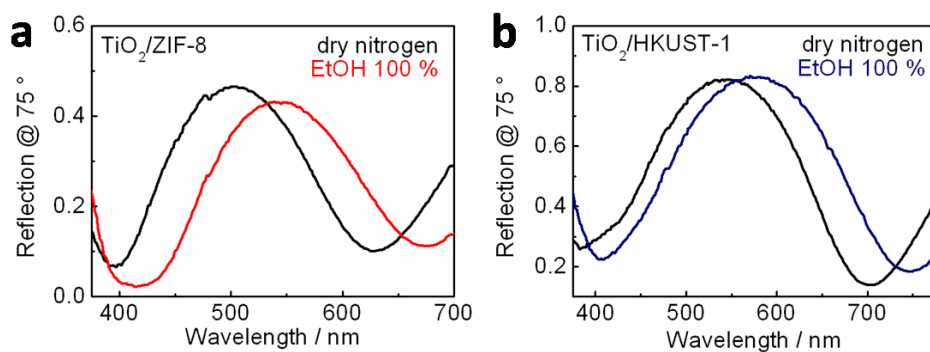


Figure S7. Reflectance spectra of (a) TiO₂/ZIF-8 BS and (b) TiO₂/HKUST-1 BS kept in dry nitrogen and after adsorption of ethanol at the highest partial pressure ($p/p_0 \approx 1$).

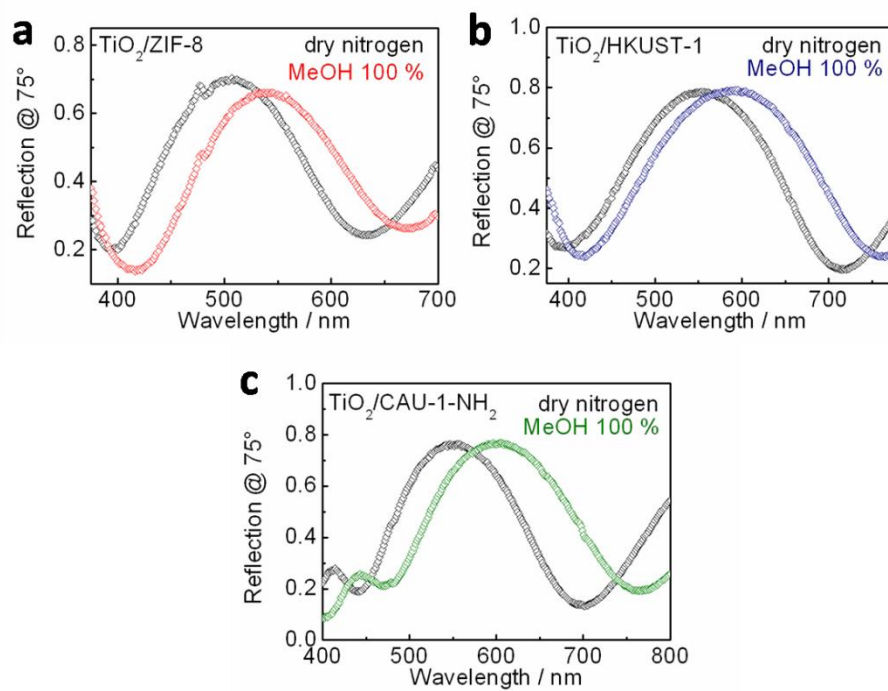


Figure S8. Reflectance spectra of (a) $\text{TiO}_2/\text{ZIF-8}$ BS, (b) $\text{TiO}_2/\text{HKUST-1}$ BS and (c) $\text{TiO}_2/\text{CAU-1-NH}_2$ BS kept in dry nitrogen and upon the adsorption of methanol at the highest partial pressure ($p/p_0 \approx 1$).

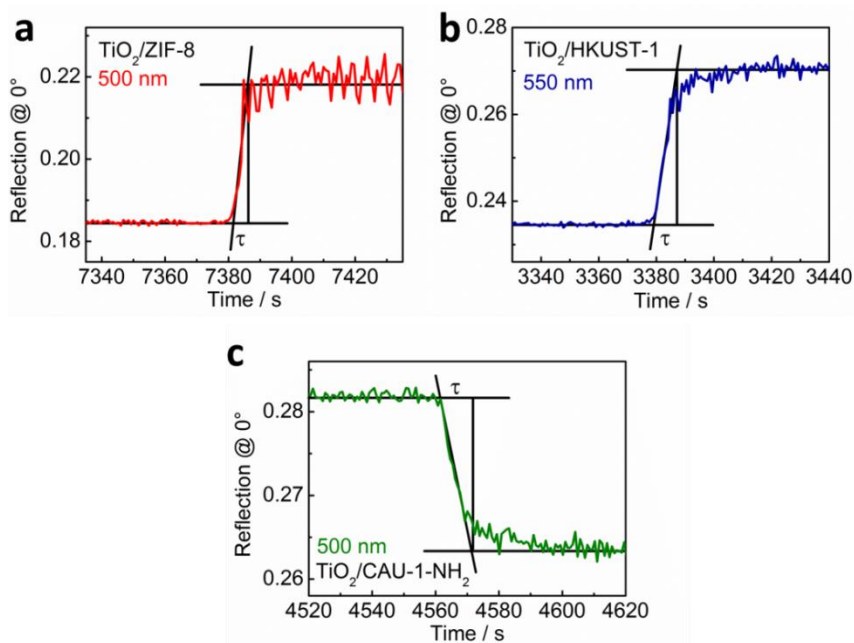


Figure S9. Determination of the response time using details of the time-dependent measurements shown in Fig. 5 (main article). The response time of each BS (a) $\text{TiO}_2/\text{ZIF-8}$, (b) $\text{TiO}_2/\text{HKUST-1}$, (c) $\text{TiO}_2/\text{CAU-1-NH}_2$ was determined exemplarily for the exposure to 0 % to 25 % ethanol vapor.

5 Appendix

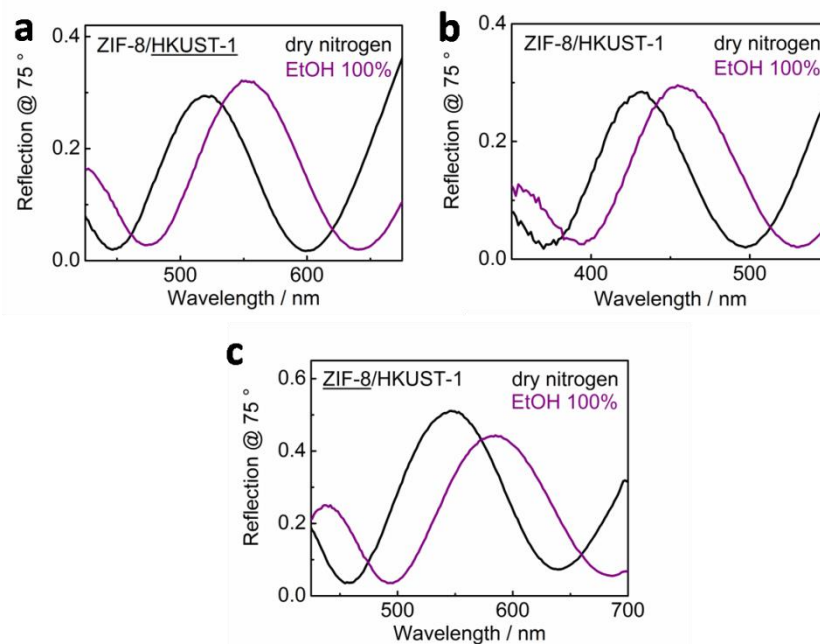


Figure S10. Reflectance spectra of ZIF-8/HKUST-1 BSs with different layer thicknesses kept in dry nitrogen and upon the adsorption of ethanol at the highest partial pressure ($p/p_0 \approx 1$). The thickness of the ZIF-8 layers is increased from (a) to (c) (highlighted by underlines), while the HKUST-1 content is decreased.

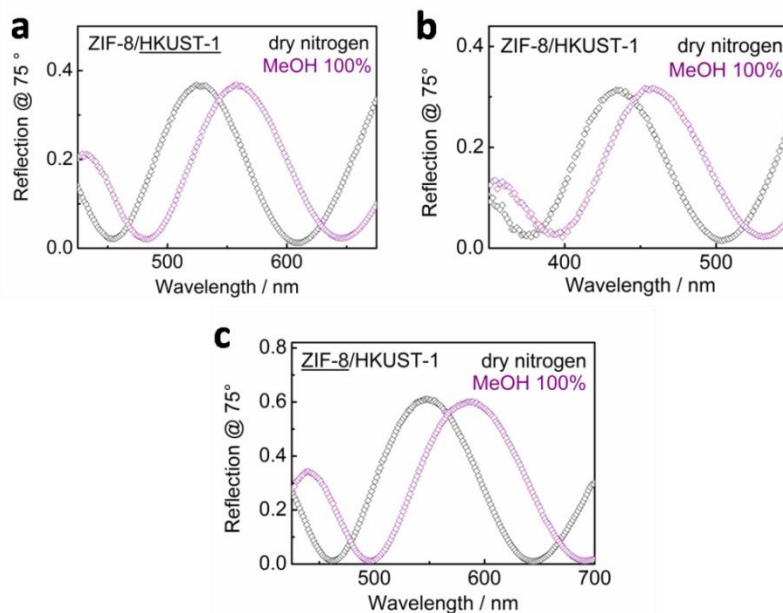


Figure S11. Reflectance spectra of ZIF-8/HKUST-1 BSs with different layer thicknesses kept in dry nitrogen and upon the adsorption of ethanol at the highest partial pressure ($p/p_0 \approx 1$). The thickness of the ZIF-8 layers is increased from (a) to (c) (highlighted by underlines), while the HKUST-1 content is decreased.

5 Appendix

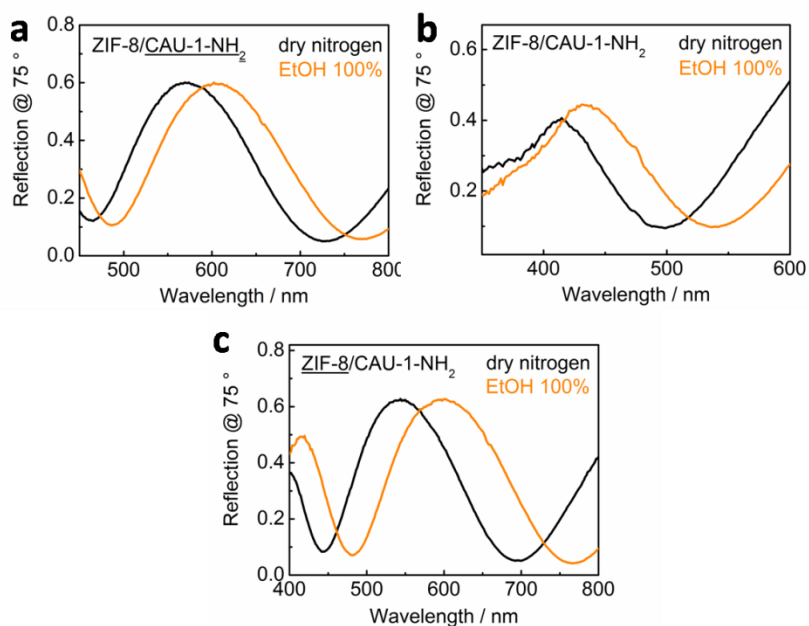


Figure S12. Reflectance spectra of ZIF-8/CAU-1-NH₂ BSs with different layer thicknesses kept in dry nitrogen and upon the adsorption of ethanol at the highest partial pressure ($p/p_0 \approx 1$). The thickness of the ZIF-8 layers is increased from (a) to (c) (highlighted by underlines), while the CAU-1-NH₂ content is decreased.

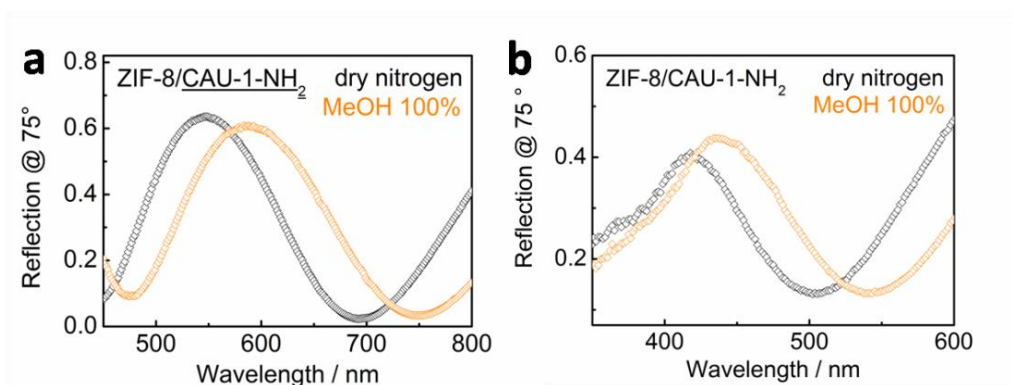


Figure S13. Reflectance spectra of ZIF-8/CAU-1-NH₂ BSs with different layer thicknesses kept in dry nitrogen and upon the adsorption of methanol at the highest partial pressure ($p/p_0 \approx 1$). The thickness of the ZIF-8 layers is increased from (a) to (b) (highlighted by underlines), while the CAU-1-NH₂ content is decreased.

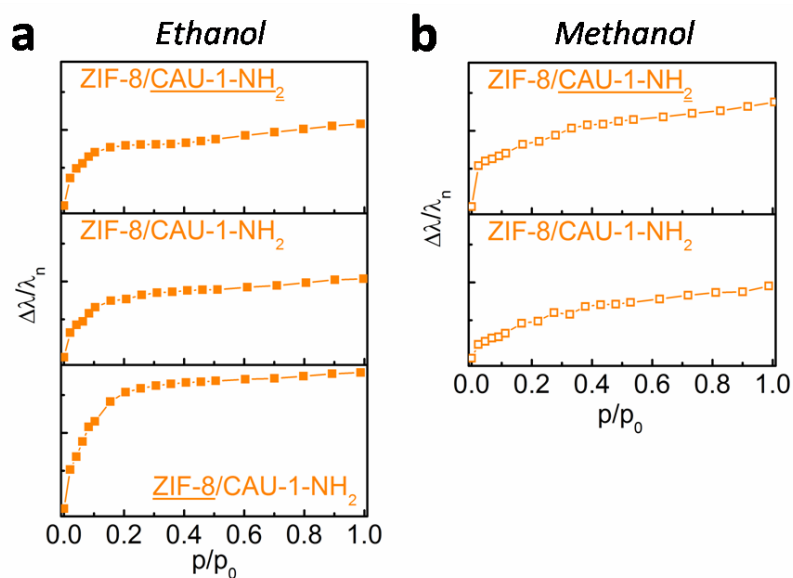


Figure S14. Sorption isotherms of ZIF-8/CAU-1-NH₂ BSs with different layer thicknesses for (a) ethanol and (b) methanol. The thickness of the ZIF-8 layers is increased from top to bottom (highlighted by underlines), while the CAU-1-NH₂ content is decreased. The graphs show normalized peak shifts which were calculated by fitting the maximum of each spectrum obtained at different partial pressures (exemplarily shown in Fig. S12 (S13) for 0% and 100% ethanol (methanol), respectively; see also subsection “Characterization details” (SI) for the calculation). For a better comparison of the isotherms, all axes of ordinates are arranged such that the same range is shown.

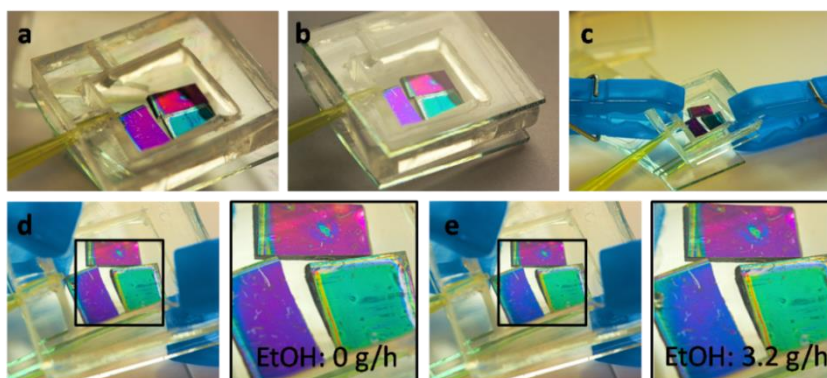


Figure S15. Photographic images of an array assembled from three TiO₂/MOF BSs (bottom-right: ZIF-8/TiO₂, left: TiO₂/HKUST-1, top-right: TiO₂/CAU-1-NH₂) arranged in a home-built chamber. The response of the BSs upon exposure to a specific ethanol concentration is illustrated by the change in color of each BS.

5 Appendix

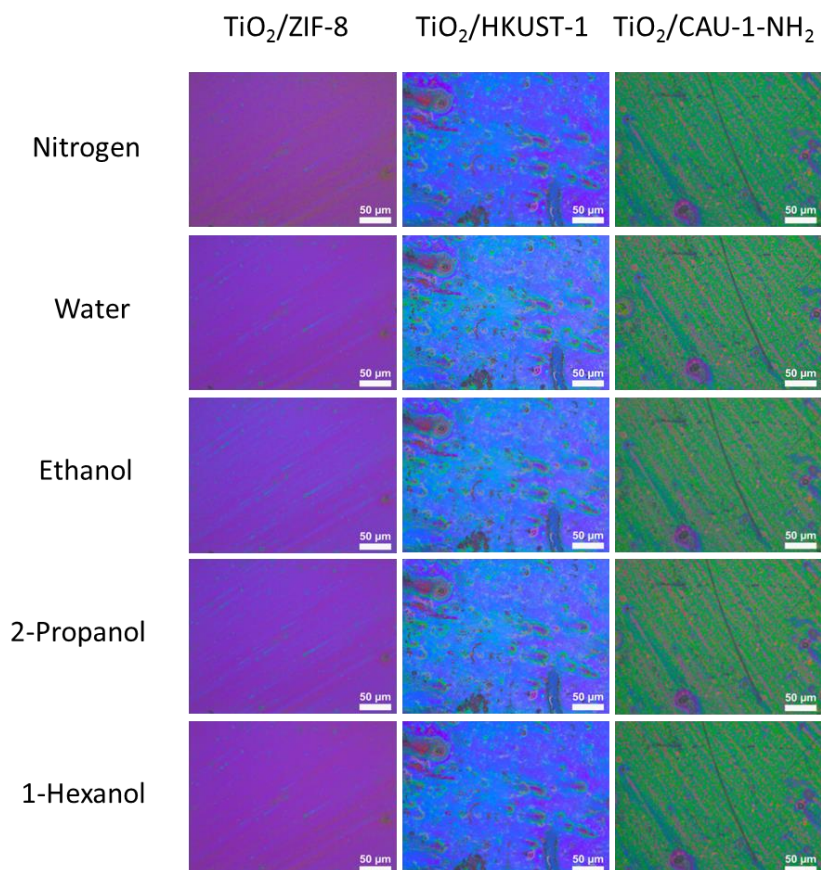


Figure S16. Photographic images of TiO₂/MOF BSs illustrating the color change upon exposure to a nitrogen stream saturated with a single sorptive (water, ethanol, 2-propanol or 1-hexanol) in comparison to pure nitrogen. The BSs were exposed one by one to the stream and the color change was recorded in situ with a camera attached to the microscope.

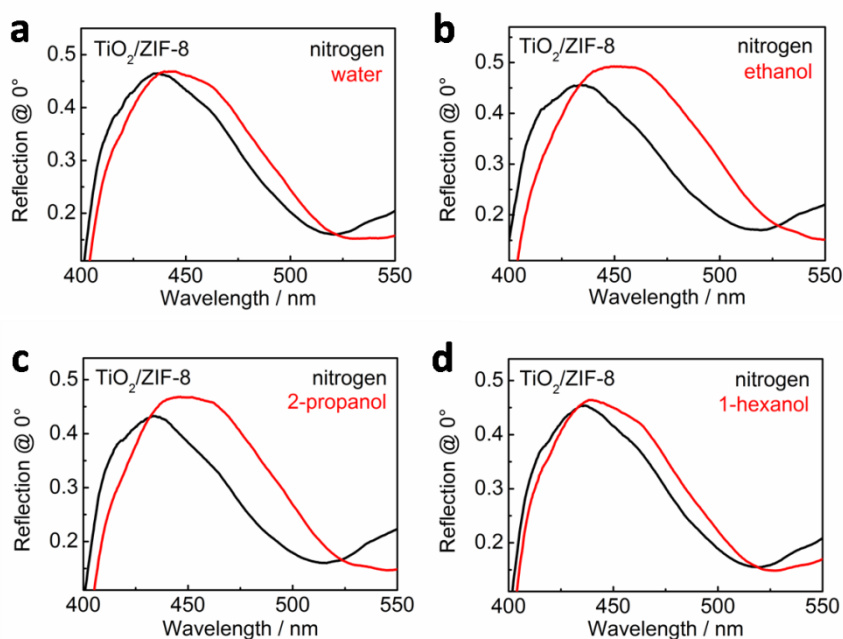


Figure S17. Reflectance spectra of a $\text{TiO}_2/\text{ZIF-8}$ BS exposed to a nitrogen stream saturated with (a) water, (b) ethanol, (c) 2-propanol and (d) 1-hexanol. The spectra were monitored simultaneously with the photographic images shown in Fig. S16 for $\text{TiO}_2/\text{ZIF-8}$.

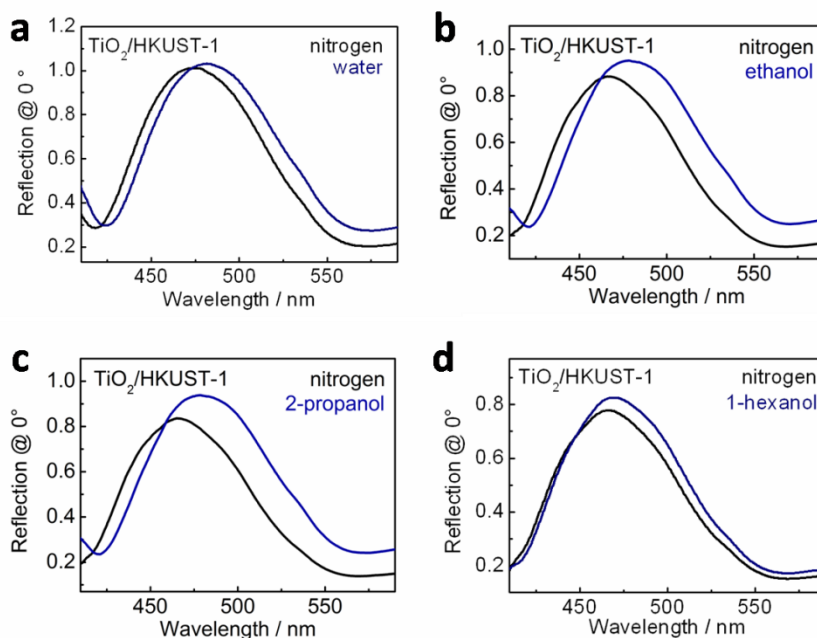


Figure S18. Reflectance spectra of a $\text{TiO}_2/\text{HKUST-1}$ BS exposed to a nitrogen stream saturated with (a) water, (b) ethanol, (c) 2-propanol and (d) 1-hexanol. The spectra were monitored simultaneously with the photographic images shown in Fig. S16 for $\text{TiO}_2/\text{HKUST-1}$.

5 Appendix

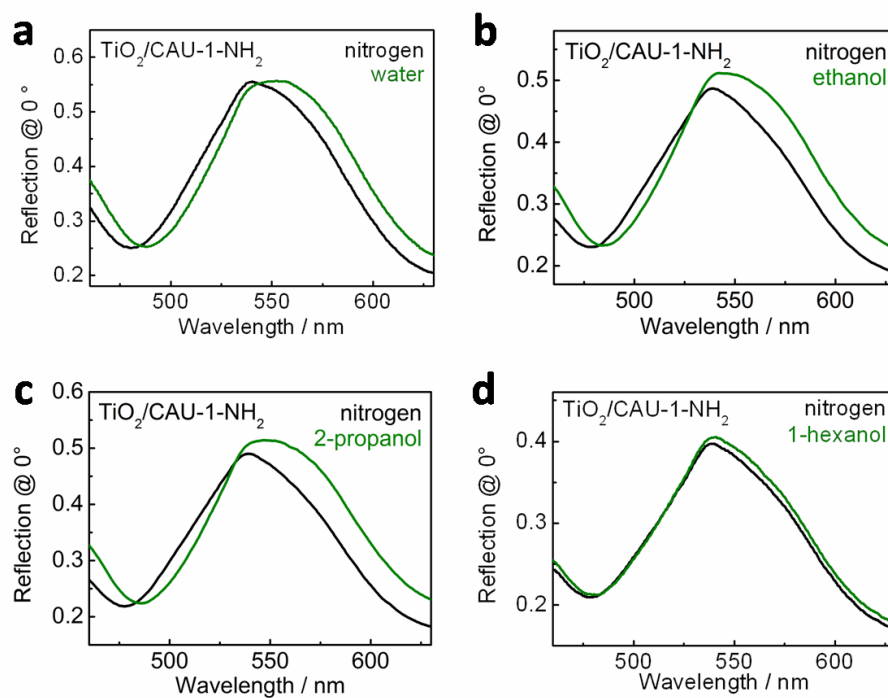


Figure S19. Reflectance spectra of a $\text{TiO}_2/\text{CAU-1-NH}_2$ BS exposed to a nitrogen stream saturated with (a) water, (b) ethanol, (c) 2-propanol and (d) 1-hexanol. The spectra were monitored simultaneously with the photographic images shown in Fig. S16 for $\text{TiO}_2/\text{CAU-1-NH}_2$.

Table S6. Normalized peak shifts for the array assembled from TiO_2/MOF BSs shown in Fig. S16 upon exposure to different sorptives. The values derive from the respective reflection spectra shown in Figs. S17-S19.

	Normalized peak shifts		
	$\text{TiO}_2/\text{ZIF-8}$	$\text{TiO}_2/\text{HKUST-1}$	$\text{TiO}_2/\text{CAU-1-NH}_2$
Water	0.012	0.017	0.017
Ethanol	0.040	0.025	0.014
2-Propanol	0.035	0.028	0.018
1-Hexanol	0.009	0.005	0.002

5 Appendix

Table S7a. Measured intensities (R channel) derived from photographic images and calculated ΔR values for the TiO₂/MOF BS array upon exposure to pure nitrogen and single solvents.

Sorptive	No.	R								
		TiO ₂ /ZIF-8			TiO ₂ /HKUST-1			TiO ₂ /CAU-1-NH ₂		
		N ₂	Sorptive	Δ	N ₂	Sorptive	Δ	N ₂	Sorptive	Δ
Ethanol	1	253.35	253.00	-0.34	179.79	206.31	23.48	164.83	122.73	-39.16
	2	253.37	253.08		185.09	207.76		159.76	121.77	
	3	253.46	253.09		186.71	207.95		158.47	121.10	
	<i>stand. dev.</i>	0.06	0.05	0.04	3.62	0.90	2.73	3.36	0.82	2.57
Methanol	1	253.28	252.95	-0.34	184.07	203.60	17.99	161.09	123.12	-33.50
	2	253.36	253.02		184.82	203.15		161.30	127.96	
	3	253.45	253.11		185.27	201.39		160.34	131.16	
	<i>stand. dev.</i>	0.09	0.08	0.00	0.61	1.17	1.73	0.51	4.04	4.40
2-Propanol	1	252.74	252.28	-0.36	187.02	207.90	20.04	159.52	117.03	-40.07
	2	252.66	252.34		189.27	209.07		155.50	116.16	
	3	252.72	252.41		190.03	209.48		154.18	115.80	
	<i>stand. dev.</i>	0.04	0.07	0.08	1.57	0.82	0.75	2.78	0.63	2.15
Water	1	252.78	252.49	-0.15	185.93	192.98	5.06	154.82	133.12	-14.28
	2	252.85	252.72		188.93	193.11		143.58	132.64	
	3	252.94	252.90		189.25	193.20		142.56	132.35	
	<i>stand. dev.</i>	0.08	0.20	0.12	1.83	0.11	1.73	6.81	0.39	6.44
1-Hexanol	1	252.63	252.13	-0.50	196.15	201.35	6.63	143.39	125.42	-15.97
	2	252.69	252.23		198.89	205.03		137.05	121.36	
	3	252.74	252.21		203.78	212.34		133.19	118.96	
	<i>stand. dev.</i>	0.05	0.06	0.04	3.87	5.59	1.73	5.15	3.27	1.88

5 Appendix

Table S7b. Measured intensities (R channel) derived from photographic images and calculated ΔR values for the TiO₂/MOF BS array upon exposure to pure nitrogen and solvent mixtures.

		R								
		TiO ₂ /ZIF-8			TiO ₂ /HKUST-1			TiO ₂ /CAU-1-NH ₂		
<i>Sorptive</i>	<i>No.</i>	<i>N₂</i>	<i>Sorptive</i>	Δ	<i>N₂</i>	<i>Sorptive</i>	Δ	<i>N₂</i>	<i>Sorptive</i>	Δ
Eth/meth	1	253.32	252.99	-0.34	190.21	201.88	14.16	149.08	117.91	-33.18
	2	253.33	252.98		186.92	202.84		153.12	117.55	
	3	253.32	252.99		187.94	202.82		152.95	120.14	
<i>stand. dev.</i>		0.00	0.01	0.01	1.68	0.55	2.21	2.28	1.41	2.22
Eth/2-pro	1	253.14	252.73	-0.34	191.35	205.38	14.22	148.03	116.73	-32.60
	2	253.13	252.81		191.54	205.99		148.32	115.64	
	3	253.15	252.85		192.20	206.37		149.05	115.22	
<i>stand. dev.</i>		0.01	0.06	0.05	0.44	0.50	0.21	0.53	0.77	1.26
Eth/water	1	253.31	253.13	-0.24	189.23	200.31	11.43	142.10	123.02	-27.45
	2	253.45	253.18		189.35	201.27		154.55	122.66	
	3	253.50	253.22		190.42	201.72		153.69	122.31	
<i>stand. dev.</i>		0.10	0.05	0.05	0.65	0.72	0.43	6.96	0.36	7.26
Eth/1-hex	1	252.50	252.11	-0.42	192.45	205.14	9.65	150.91	124.07	-24.05
	2	252.53	252.10		192.37	201.83		148.59	125.06	
	3	252.55	252.10		194.92	201.72		147.08	125.29	
<i>stand. dev.</i>		0.02	0.01	0.03	1.45	1.95	2.95	1.93	0.65	1.88

5 Appendix

Table S8a. Measured intensities (G channel) derived from photographic images and calculated ΔG values for the TiO₂/MOF BS array upon exposure to pure nitrogen and single solvents.

<i>Sorptive</i>	<i>No.</i>	G								
		TiO ₂ /ZIF-8			TiO ₂ /HKUST-1			TiO ₂ /CAU-1-NH ₂		
		<i>N₂</i>	<i>Sorptive</i>	Δ	<i>N₂</i>	<i>Sorptive</i>	Δ	<i>N₂</i>	<i>Sorptive</i>	Δ
Ethanol	1	249.15	229.88	-20.36	249.13	248.73	-0.13	73.83	103.03	28.63
	2	249.06	228.55		248.80	248.82		75.55	103.83	
	3	249.09	227.79		248.91	248.89		75.60	104.01	
	<i>stand. dev.</i>	0.04	1.06	1.02	0.17	0.08	0.23	1.01	0.52	0.50
Methanol	1	248.57	223.00	-23.61	248.42	247.97	-0.64	74.03	100.99	22.09
	2	248.89	225.11		248.49	247.83		74.16	95.63	
	3	249.29	227.81		248.50	247.69		73.86	91.69	
	<i>stand. dev.</i>	0.36	2.41	2.05	0.04	0.14	0.18	0.15	4.67	4.60
2-Propanol	1	249.00	222.08	-27.12	248.80	248.41	-0.14	73.25	105.58	32.03
	2	246.98	220.21		248.62	248.57		74.85	106.70	
	3	246.63	218.96		248.63	248.66		75.22	107.12	
	<i>stand. dev.</i>	1.28	1.57	0.48	0.10	0.13	0.22	1.05	0.79	0.27
Water	1	247.97	237.93	-5.42	247.99	247.05	-0.70	74.85	86.16	7.51
	2	247.73	243.50		247.74	247.12		80.99	86.74	
	3	248.29	246.29		247.66	247.14		81.51	86.97	
	<i>stand. dev.</i>	0.28	4.26	4.15	0.17	0.05	0.22	3.71	0.42	3.30
1-Hexanol	1	248.06	230.02	-18.26	247.41	246.60	-0.63	77.78	89.10	10.41
	2	247.65	230.34		246.93	246.55		81.86	92.11	
	3	247.42	227.98		246.79	246.09		84.07	93.74	
	<i>stand. dev.</i>	0.32	1.28	1.09	0.32	0.28	0.22	3.19	2.35	0.84

5 Appendix

Table S8b. Measured intensities (G channel) derived from photographic images and calculated ΔG values for the TiO₂/MOF BS array upon exposure to pure nitrogen and solvent mixtures.

		G								
		TiO ₂ /ZIF-8			TiO ₂ /HKUST-1			TiO ₂ /CAU-1-NH ₂		
<i>Sorptive</i>	<i>No.</i>	<i>N₂</i>	<i>Sorptive</i>	Δ	<i>N₂</i>	<i>Sorptive</i>	Δ	<i>N₂</i>	<i>Sorptive</i>	Δ
Eth/meth	1	250.00	237.02	-13.91	247.59	246.96	-0.83	74.43	98.20	24.27
	2	249.81	235.60		247.90	246.95		72.78	98.68	
	3	249.67	235.12		247.86	246.95		72.85	95.99	
<i>stand. dev.</i>		0.16	0.99	0.83	0.17	0.01	0.17	0.93	1.43	1.44
Eth/2-pro	1	249.36	230.74	-19.06	247.87	246.96	-0.82	74.81	98.59	25.25
	2	248.51	229.76		247.78	246.97		74.36	100.02	
	3	248.25	228.45		247.73	247.00		74.21	100.54	
<i>stand. dev.</i>		0.58	1.15	0.65	0.07	0.02	0.09	0.31	1.01	1.32
Eth/water	1	249.03	235.96	-11.90	248.12	247.39	-0.70	81.05	93.56	17.26
	2	249.86	237.99		248.08	247.38		73.81	93.62	
	3	250.11	239.36		248.07	247.39		73.61	93.07	
<i>stand. dev.</i>		0.56	1.71	1.16	0.03	0.01	0.03	4.23	0.30	4.11
Eth/1-hex	1	248.25	230.49	-17.64	247.54	246.76	-0.98	74.05	91.60	16.09
	2	247.84	230.43		247.55	246.40		74.61	90.50	
	3	247.77	230.02		247.38	246.36		75.37	90.21	
<i>stand. dev.</i>		0.26	0.26	0.20	0.09	0.22	0.19	0.66	0.74	1.37

5 Appendix

Table S9a. Measured intensities (B channel) derived from photographic images and calculated ΔB values for the TiO₂/MOF BS array upon exposure to pure nitrogen and single solvents.

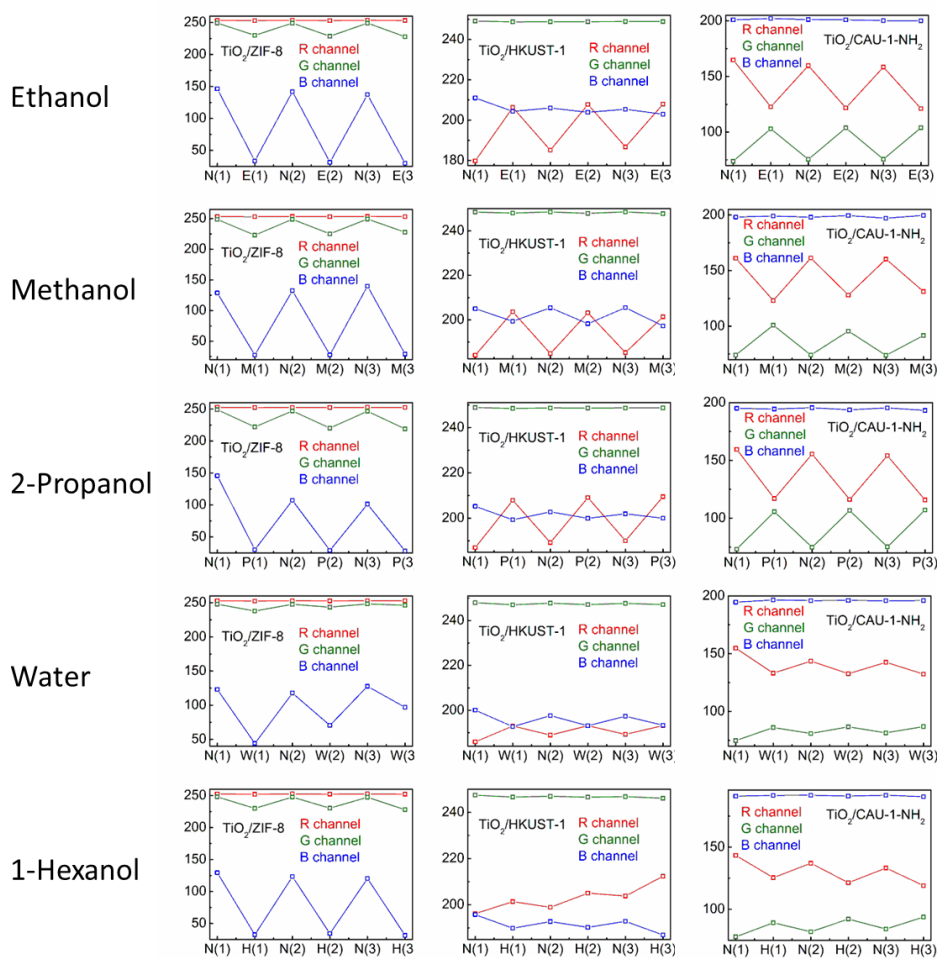
Sorptive	No.	B								
		TiO ₂ /ZIF-8			TiO ₂ /HKUST-1			TiO ₂ /CAU-1-NH ₂		
		N ₂	Sorptive	Δ	N ₂	Sorptive	Δ	N ₂	Sorptive	Δ
Ethanol	1	146.36	33.47	-110.30	210.97	204.37	-3.74	200.90	202.13	0.26
	2	141.82	31.37		206.00	203.87		201.13	200.93	
	3	137.37	29.81		205.41	202.92		200.21	199.95	
	<i>stand. dev.</i>	4.49	1.84	2.66	3.05	0.74	2.48	0.48	1.09	0.85
Methanol	1	128.89	27.61	-105.60	205.03	199.35	-7.03	198.10	199.02	1.65
	2	132.47	27.82		205.43	198.25		197.97	199.45	
	3	139.91	29.02		205.46	197.24		197.06	199.60	
	<i>stand. dev.</i>	5.62	0.76	4.88	0.24	1.06	1.28	0.57	0.30	0.82
2-Propanol	1	145.64	30.01	-89.04	205.24	199.30	-3.58	195.07	194.50	-1.53
	2	107.13	28.89		202.78	199.94		195.60	193.79	
	3	101.32	28.08		201.94	199.99		195.48	193.28	
	<i>stand. dev.</i>	24.09	0.97	23.17	1.72	0.39	2.10	0.28	0.61	0.85
Water	1	123.11	44.02	-52.42	200.06	192.70	-5.30	194.51	196.52	0.81
	2	117.76	70.37		197.63	193.10		195.93	196.17	
	3	127.69	96.91		197.35	193.34		195.80	195.99	
	<i>stand. dev.</i>	4.97	26.44	24.54	1.49	0.32	1.80	0.78	0.27	1.04
1-Hexanol	1	129.42	32.42	-91.67	195.72	189.87	-4.74	191.08	191.60	-0.46
	2	123.26	34.20		192.71	190.24		191.81	191.13	
	3	120.38	31.42		192.84	186.94		191.82	190.61	
	<i>stand. dev.</i>	4.62	1.41	4.61	1.70	1.80	1.96	0.43	0.49	0.89

5 Appendix

Table S9b. Measured intensities (B channel) derived from photographic images and calculated ΔB values for the TiO₂/MOF BS array upon exposure to pure nitrogen and solvent mixtures.

		B								
		TiO ₂ /ZIF-8			TiO ₂ /HKUST-1			TiO ₂ /CAU-1-NH ₂		
<i>Sorptive</i>	<i>No.</i>	<i>N₂</i>	<i>Sorptive</i>	Δ	<i>N₂</i>	<i>Sorptive</i>	Δ	<i>N₂</i>	<i>Sorptive</i>	Δ
Eth/meth	1	171.13	46.70	-121.60	198.84	193.29	-7.16	191.37	190.88	-0.08
	2	164.62	42.57		201.40	193.41		190.59	190.47	
	3	159.44	41.12		201.20	193.24		190.57	190.95	
<i>stand. dev.</i>		5.85	2.89	3.08	1.42	0.08	1.40	0.45	0.26	0.43
Eth/2-pro	1	155.74	35.15	-103.14	199.51	191.52	-7.32	190.34	189.58	-1.11
	2	130.59	33.00		198.72	191.48		190.32	189.13	
	3	122.17	30.93		198.22	191.51		190.24	188.86	
<i>stand. dev.</i>		17.47	2.11	15.45	0.65	0.02	0.64	0.05	0.36	0.32
Eth/water	1	133.46	40.21	-107.09	198.61	192.51	-6.26	195.08	194.42	0.62
	2	157.68	45.33		199.28	192.81		192.97	194.27	
	3	165.37	49.69		199.50	193.29		192.21	193.43	
<i>stand. dev.</i>		16.65	4.74	12.10	0.46	0.39	0.19	1.49	0.53	1.11
Eth/1-hex	1	129.33	33.06	-92.47	197.61	190.67	-7.26	190.65	191.59	0.97
	2	123.19	32.85		197.11	189.10		190.85	192.05	
	3	123.23	32.42		195.64	188.82		191.14	191.93	
<i>stand. dev.</i>		3.53	0.33	3.30	1.02	1.00	0.66	0.24	0.24	0.21

5 Appendix



5 Appendix

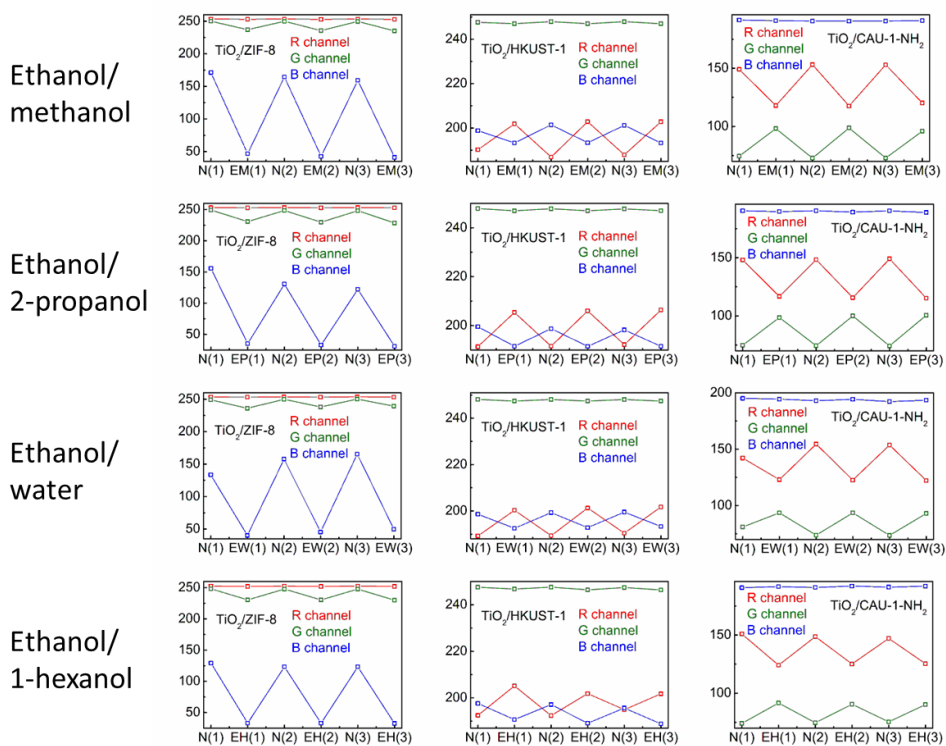


Figure S21. Evolution of the R, G and B channels of photographic images for TiO_2/MOF BSs alternately exposed to pure nitrogen (N) in comparison to the nitrogen stream saturated with a solvent mixture (ethanol with either methanol (EM), 2-propanol (EP), water (EW) or 1-hexanol (EH) using a volume ratio of 1:1). The images were recorded in situ with a camera attached to the microscope, and subsequently processed to extract the average R, G and B values which were then used in this Fig. to illustrate the reversible sorption behavior of the stacks.

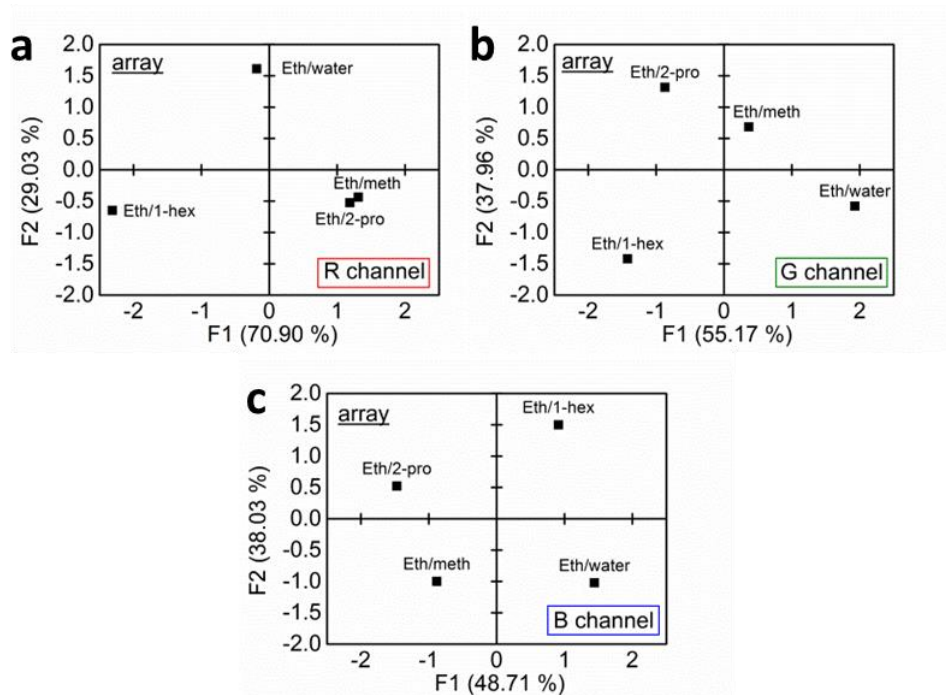


Figure S22. PCA plots for (a) R, (b) G and (c) B channels, illustrating the different correlations of the channels for the investigated solvent mixtures.

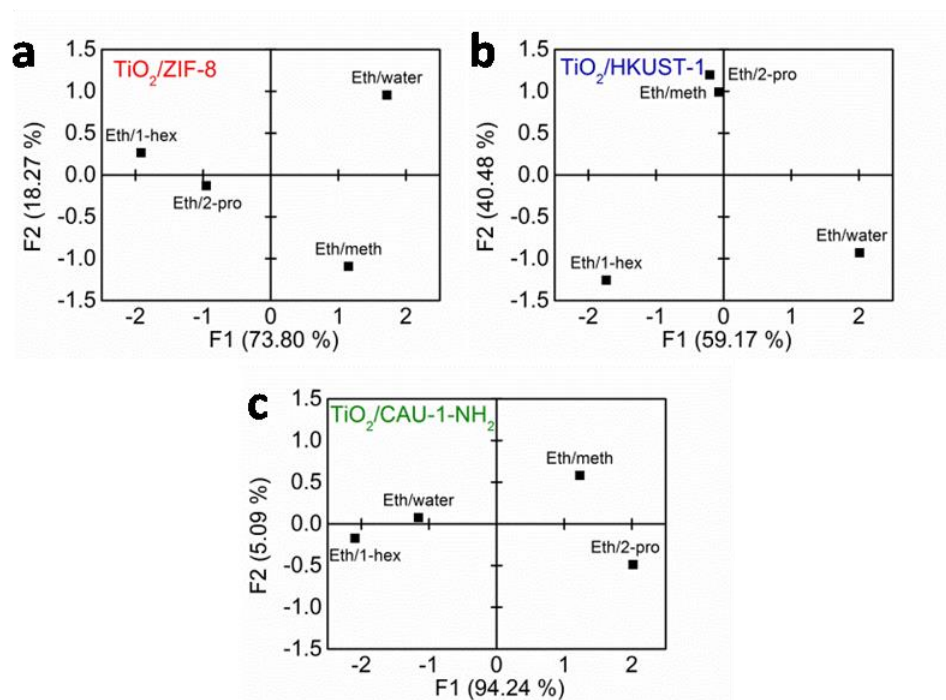


Figure S23. PCA plots for (a) $\text{TiO}_2/\text{ZIF-8}$ BS, (b) $\text{TiO}_2/\text{HKUST-1}$ BS and (c) $\text{TiO}_2/\text{CAU-1-NH}_2$ BS, illustrating the different response correlations of the stacks for the investigated solvent mixtures.

5.4 SUPPORTING INFORMATION FOR CHAPTER 3.3

adapted from A. Ranft, I. Pavlichenko, K. Szendrei, P. M. Zehetmaier, Y. Hu, A. von Mankowski, B. V. Lotsch, „1D photonic defect structures based on colloidal porous frameworks: Reverse pore engineering and vapor sorption”, *Microporous Mesoporous Mater.* **2015**, *86*, 6948-6958.

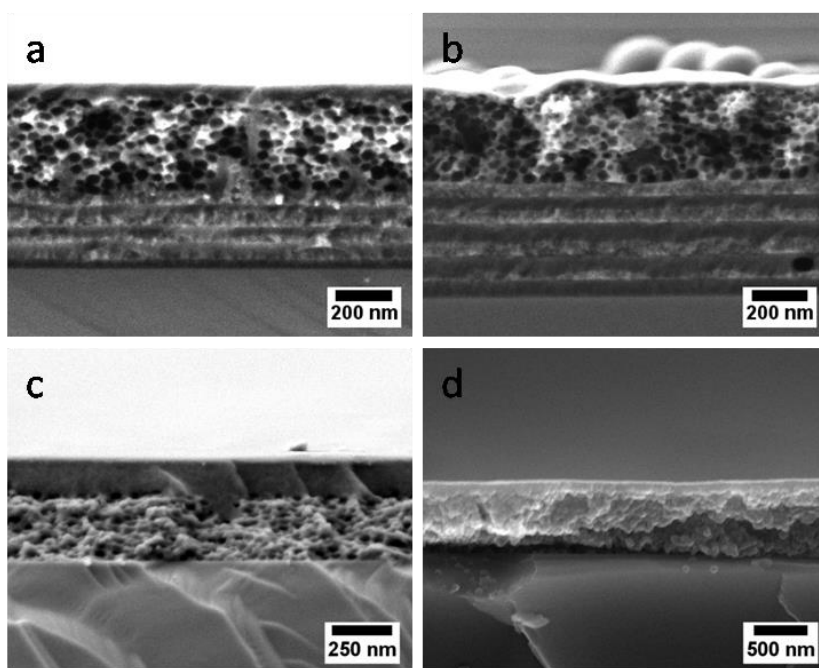
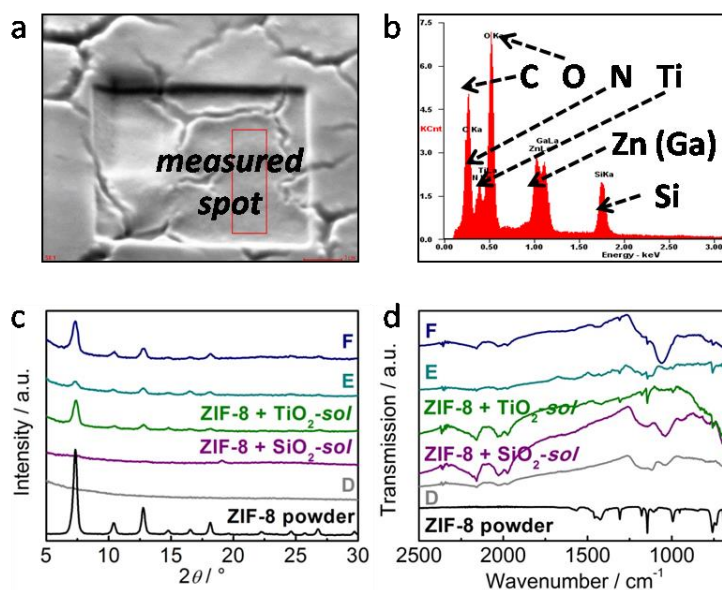
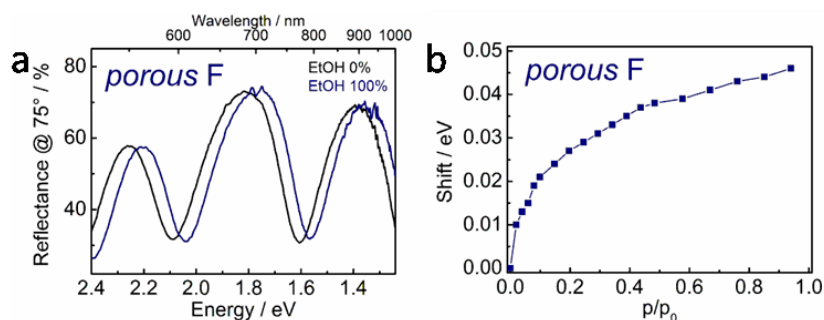
Additional analytical data

Figure S1. Cross-sectional SEM images of (a) a dense sandwich structure with 1 overhead TiO₂/SiO₂ BL, (b) a similar structure with 1 overhead SiO₂/TiO₂ BL, (c) a single ZIF-8 layer coated with SiO₂-sol and (d) a single ZIF-8 film coated with TiO₂-np.

Table S1. EDX measurements gained from cross-sectional SEM images of defect structures on silicon substrates (samples E and F).

	Si / %	Ti / %	Zn / %
E	33.6	1.59	2.24
F	30.2	2.65	1.52

**Figure S2.** (a) Top-view SEM image of sample F showing the spot that has been investigated with EDX (b). Note that the measured spot has been treated with Ga ions to remove the upper BS from the sample thereby suggesting the presence of Ga in the sample. (c) XRD patterns and (d) IR spectra for samples D, E, F and ZIF-8 layers coated with either SiO₂ or TiO₂ sol in comparison to ZIF-8 powder.**Figure S3.** Reflection spectrum (a) and optical vapor sorption isotherm (b) of a porous sol-based sandwich structure, illustrating the change of the optical properties upon adsorption of ethanol vapor. In the reflection spectrum, the spectral shift upon exposure to the highest analyte concentration (100%, $p/p_0 \approx 1$) is shown in comparison to pure nitrogen, while the isotherm illustrates the sorption behavior of the stack at various relative pressures.

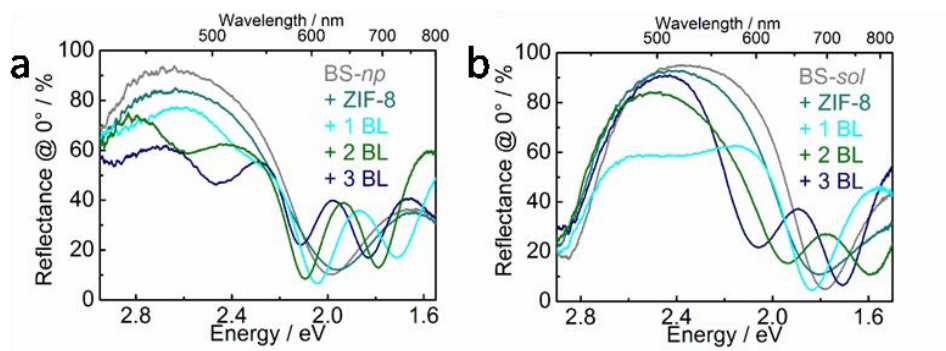


Figure S4. Spectral evolution of a hybrid 1D PC (a) and a dense multilayer structure (b) after the deposition of ZIF-8 and with each following BL deposition.

Table S2. Experimental layer thicknesses (“exp.”) deduced from cross-sectional SEM images of defect structures and ellipsometric measurements with single films on silicon substrates, and simulated thickness values (“sim.”) obtained from model fits to the respective spectra of samples A-F.

	$d(\text{SiO}_2) / \text{nm}$		$d(\text{TiO}_2) / \text{nm}$		$d(\text{defect layer}) / \text{nm}$	
	<i>exp.</i>	<i>sim.</i>	<i>exp.</i>	<i>sim.</i>	<i>exp.</i>	<i>sim.</i>
A	89	82	54	65	-	-
B	85	85	58	62	603	550
C	79	68	61	65	456	466
D	88	93	67	70	-	-
E	98 ^a	92	67 ^a	66	293 ^a	250
F	86	92	62	66+30 ^b	259	260

^a Values derived solely from ellipsometric measurements

^b First value simulated for all TiO_2 layers except for the one adjacent to the defect slab (fourth layer), second value simulated for the fourth TiO_2 layer

5 Appendix

Table S3. Experimental RIs (“exp.”) determined from ellipsometric measurements with single films on silicon substrates, and simulated RIs (“sim.”) obtained from model fits to the respective spectra of samples A-F.

	<i>n</i> (SiO ₂) @ 530 nm		<i>n</i> (TiO ₂) @ 530 nm		<i>n</i> (defect layer) @ 530 nm	
	<i>exp.</i>	<i>sim.</i>	<i>exp.</i>	<i>sim.</i>	<i>exp.</i>	<i>sim.</i>
A	1.41	1.40	1.87	1.88	1.21	-
B		1.42		1.86		1.21
C		1.41		1.85		1.21
D		1.41	1.93	1.93		-
E		1.42		1.93		1.21
F		1.41		1.93	-	1.60

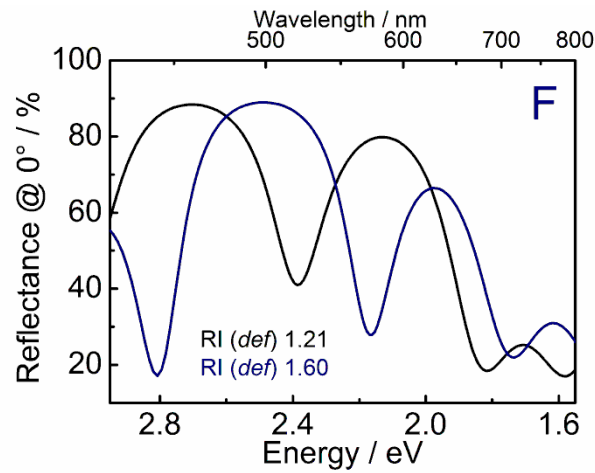


Figure S5. Simulated reflection spectra of sample F obtained for different refractive indices of the defect slab (black line: 1.21, blue line: 1.60). Thickness values and refractive indices simulated for SiO₂ and TiO₂ layers, respectively, are listed in Tables S2 and S3.

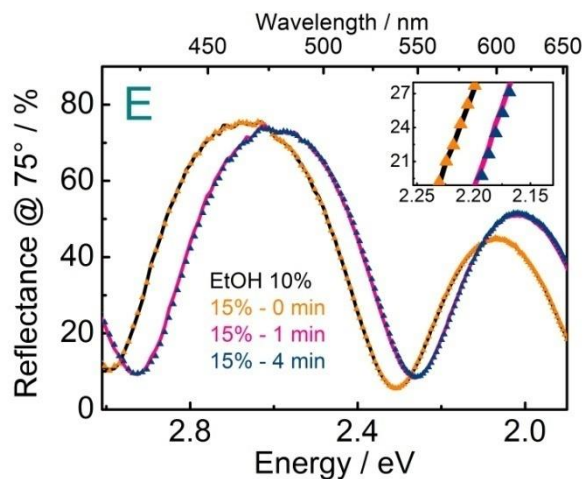


Figure S6. Reflection spectra of sample E recorded after different exposure times toward various ethanol vapor concentrations. After exposing the sample to 10%, the concentration was changed to 15% and spectra were recorded every 60 s for 5 min. The figure illustrates that the response toward the analyte is completed within the first minute.

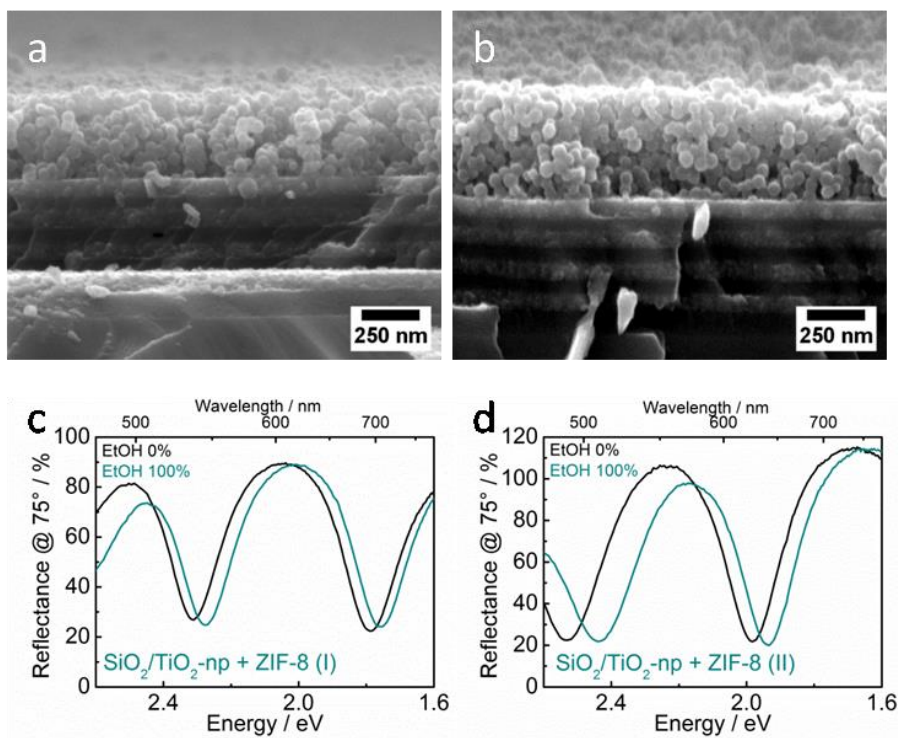


Figure S7. Cross-sectional SEM images (a, b) and reflection spectra (c, d) of two hybrid top defect structures with different ZIF-8 layer thicknesses. In the reflection spectrum, the spectral shift upon exposure to the highest analyte concentration (100%, $p/p_0 \approx 1$) is shown in comparison to pure nitrogen. The image and spectrum on the right side (b, d) were recorded for the stack with the larger ZIF-8 thickness (sample II).

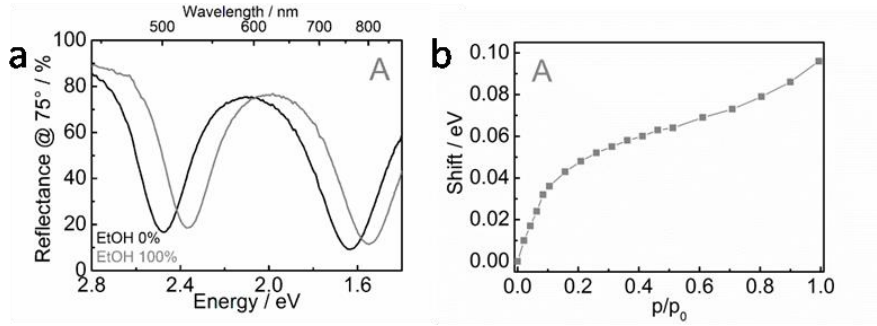


Figure S8. Reflection spectrum (a) and optical vapor sorption isotherm (b) of a regular hybrid 1D PC illustrating the change of the optical properties upon the adsorption of ethanol vapor. In the reflection spectrum, the spectral shift upon exposure to the highest analyte concentration (100%, $p/p_0 \approx 1$) is shown in comparison to pure nitrogen, while the isotherm illustrates the sorption behavior of the stack at various relative pressures.

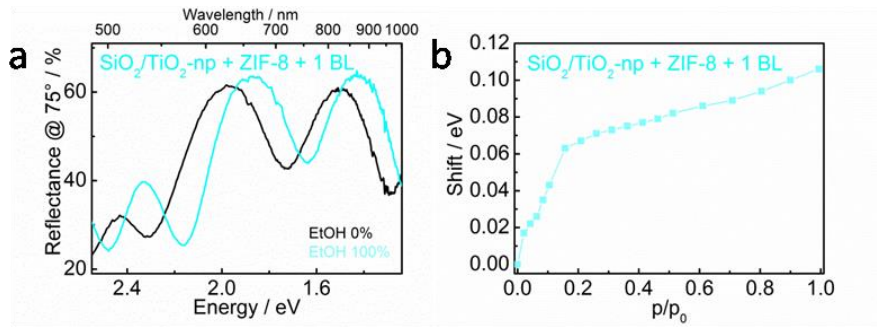


Figure S9. Reflection spectrum (a) and optical vapor sorption isotherm (b) of a hybrid sandwich structure with 1 overhead BL, illustrating the change of the optical properties upon the adsorption of ethanol vapor. In the reflection spectrum, the spectral shift upon exposure to the highest analyte concentration (100%, $p/p_0 \approx 1$) is shown in comparison to pure nitrogen, while the isotherm illustrates the sorption behavior of the stack at various relative pressures.

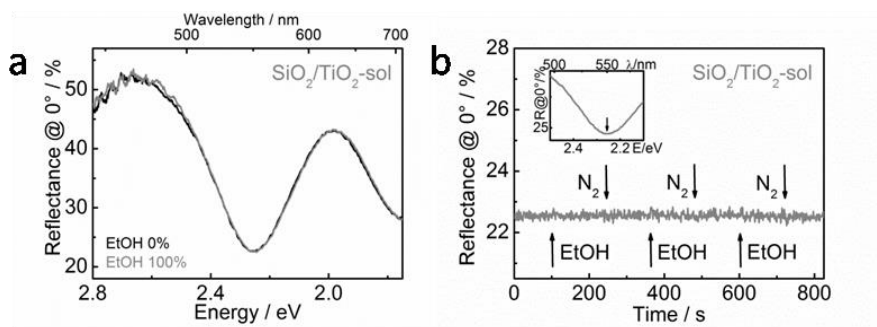


Figure S10. Reflection spectrum (a) and time-dependent response (b) of a regular dense 1D PC illustrating the sorption behavior upon exposure to ethanol vapor. In the reflection spectrum, the spectral shift upon exposure to a nitrogen stream saturated with ethanol (denoted as “100%”) is shown in comparison to pure nitrogen. The time-dependent response was recorded by switching back and forth from pure nitrogen to nitrogen/ethanol and monitoring the reflectivity at a distinct wavelength (550 nm \approx 2.26 eV) of the spectrum.

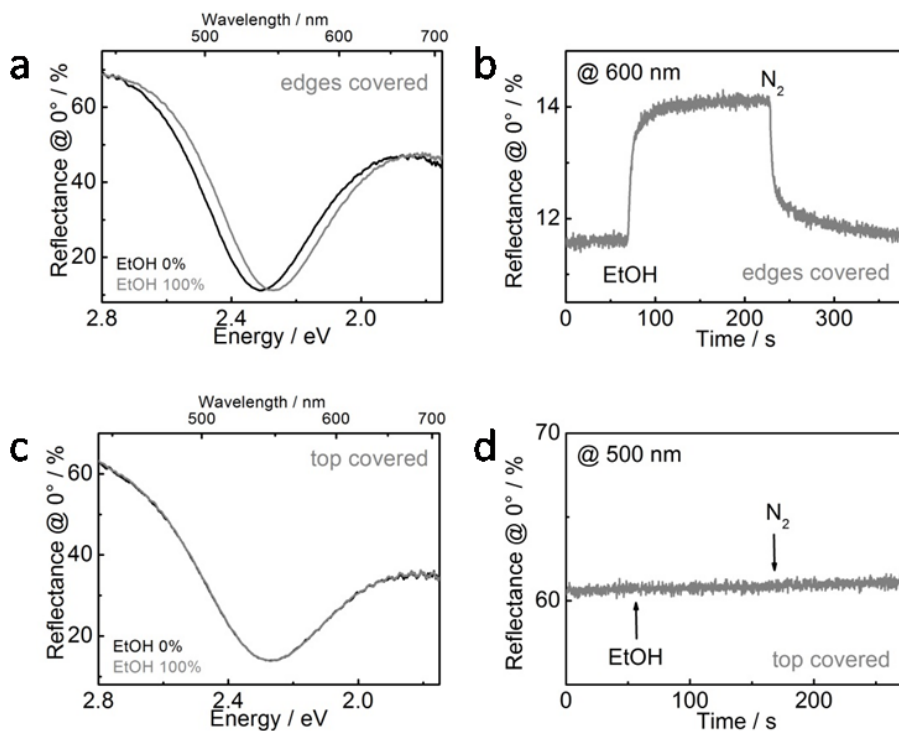


Figure S11. Reflection spectra and time-dependent response of (a, b) a regular porous $\text{SiO}_2/\text{TiO}_2$ BS with covered edges; (c, d) the same stack with covered surface and free edges. In the reflection spectra, the spectral shift upon exposure to a nitrogen stream saturated with ethanol (denoted as “100%”) is shown in comparison to pure nitrogen. The time-dependent responses were recorded by switching back and forth from pure nitrogen to nitrogen/ethanol and monitoring the reflectivity at a distinct wavelength of the spectrum. The observed changes in the spectra and the reflectivity suggest that infiltration of the stack occurs from the top layer only.

List of Publications

Published as part of this thesis

Chapter 2

- 1 A. Ranft, S. B. Betzler, F. Haase and B. V. Lotsch, „Additive-mediated size control of MOF nanoparticles”, *CrystEngComm* **2013**, *15*, 9296-9300.

Writing the manuscript, literature research and creation of graphical material were done by Annekathrin Ranft. Synthesis of the samples, conduction and evaluation of analytical data were carried out by Annekathrin Ranft, Sophia Betzler and Frederik Haase in close collaboration. Bettina Lotsch directed and supervised the work. All authors revised the manuscript.

Chapter 3

- 2 F. M. Hinterholzinger, A. Ranft, J. M. Feckl, B. Rühle, T. Bein and B. V. Lotsch, „One-dimensional metal-organic framework photonic crystals used as platforms for vapor sorption”, *J. Mater. Chem.* **2012**, *22*, 10356-10362.

Writing the manuscript and literature research were done by Florian Hinterholzinger. Synthesis of the samples, conduction and evaluation of analytical data and creation of graphical material were performed by Florian Hinterholzinger, Annekathrin Ranft and Johann Feckl in close collaboration. Sensing measurements were performed by Florian Hinterholzinger and Annekathrin Ranft. Development of automatically performed sensing measurements, fitting of the experimental data and evaluation of the fits were done by Bastian Rühle. Thomas Bein and Bettina Lotsch directed and supervised the work. All authors revised the manuscript.

- 3 A. Ranft, F. Niekietel, I. Pavlichenko, N. Stock and B. V. Lotsch, „Tandem MOF-Based Photonic Crystals for Enhanced Analyte-Specific Optical Detection”, *Chem. Mater.* **2015**, *27*, 1961-1970.

Writing the manuscript, literature research and the main part of creating graphical material were done by Annekathrin Ranft. Synthesis of the samples, conduction and evaluation of analytical data were performed by Annekathrin Ranft and Felicitas Niekietel in close collaboration. Parts of the graphical material concerning further

analysis (IR measurements, nitrogen sorption, NMR, EDX and elemental analysis for the in-depth characterization of CAU-1-NH₂) were done by Felicitas Niekiet. Sensing measurements were performed by Annekathrin Ranft. Instruction on the sensing measurements with the optical fibre, supply of the home-made measurement chamber and creation of the TOC graphic were done by Ida Pavlichenko. Norbert Stock and Bettina Lotsch directed and supervised the work. All authors revised the manuscript.

- 4 A. Ranft, I. Pavlichenko, K. Szendrei, P. Zehetmaier, Y. Hu, A. von Mankowski and B. V. Lotsch, „1D photonic defect structures based on colloidal porous frameworks: Reverse pore engineering and vapor sorption”, *Microporous Mesoporous Mater.* **2015**, *216*, 216-224.

Writing the manuscript, literature research, creation of graphical material and evaluation of analytical data were done by Annekathrin Ranft. Synthesis of the samples and sensing measurements were performed by Annekathrin Ranft, Ida Pavlichenko, Peter Zehetmaier, Yinghong Hu and Alberto von Mankowski in close collaboration. Simulation of spectra were carried out by Katalin Szendrei. Bettina Lotsch directed and supervised the work. All authors revised the manuscript.

Published articles in conjunction with this thesis

- 5 E. A. Flügel, A. Ranft, F. Haase and B. V. Lotsch, „Synthetic routes toward MOF nanomorphologies”, *J. Mater. Chem.* **2012**, *22*, 10119-10133.

Writing the review article and requesting figures for reproduction were done by Erik Flügel. Literature research was carried out by Erik Flügel, Annekathrin Ranft and Frederik Haase. Bettina Lotsch directed and supervised the work.

- 6 P. Davydovskaya, A. Ranft, B. V. Lotsch and R. Pohle, „Analyte Detection with Cu-BTC Metal-Organic Framework Thin Films by Means of Mass-Sensitive and Work-Function-Based Readout”, *Anal. Chem.* **2014**, *86*, 6948-6958.

Writing the manuscript, conduction of sensing experiments, evaluation of analytical data and the main part of creating graphical material were done by Polina Davydovskaya. Literature research and synthesis of the samples were performed by Polina Davydovskaya and Annekathrin Ranft in close collaboration. Parts of the graphical material and further analysis (XRD and SEM analysis for testing the water stability of Cu-BTC nanoparticles) were done by Annekathrin Ranft. Bettina Lotsch and Roland Pohle directed and supervised the work. All authors revised the manuscript.

- 7 P. Davydovskaya, A. Ranft, B. V. Lotsch and R. Pohle, „Selective and Sensitive Detection of C3 Molecules with Cu-BTC Metal-organic Framework by Means of Mass Sensitive and Work Function Based Read-out”, *Proc. Eng.* **2014**, *87*, 1433-1436.

Writing the manuscript, literature research, conduction of sensing experiments, evaluation of analytical data and creation of graphical material were done by Polina Davydovskaya. Synthesis of the samples was done by Polina Davydovskaya and Annekathrin Ranft in close collaboration. Bettina Lotsch and Roland Pohle directed and supervised the work. All authors revised the manuscript.

List of Presentations

Oral presentations

02/2012, Kreuth: Ringberg Meeting

A. Ranft, B. Lotsch, „Colloidal Porous Frameworks for the Fabrication of Optical Sensors”.

11/2012, Dresden: MOF2012, Status Report Meeting

A. Ranft, F. Hinterholzinger, F. Niekiet, B. Lotsch, T. Bein, N. Stock, „One-Dimensional Metal-Organic Framework Photonic Crystals Used as Platforms for Vapor Sorption”.

04/2015, München: Kerschensteiner Kolleg (Deutsches Museum), Seminar

A. Ranft, A. von Mankowski, K. Szendrei, B. Lotsch, „1D Photonic Crystals for Sensing Applications”.

Poster presentations

03/2011, Erlangen: 23. Deutsche Zeolith-Tagung

A. Ranft, B. Lotsch, „Colloidal porous frameworks for the fabrication of photonic multilayer systems”.

09/2011, Venedig: Center for NanoScience Workshop

A. Ranft, B. Lotsch, „Colloidal porous frameworks for the fabrication of photonic multilayer systems”.

03/2012, Magdeburg: 24. Deutsche Zeolith-Tagung

A. Ranft, B. Lotsch, „Colloidal porous frameworks for the fabrication of optical sensors”.

09/2012, Stuttgart: Max-Planck-Institut für Festkörperforschung, Workshop

A. Ranft, F. Hinterholzinger, F. Niekiet, J. Feckl, B. Rühle, N. Stock, T. Bein, B. Lotsch, „One-dimensional MOF photonic crystals used as platforms for vapor sorption”.

11/2012, Stuttgart: Max-Planck-Institut für Festkörperforschung, Evaluierung

A. Ranft, B. Lotsch, „One-dimensional MOF photonic crystals used as platforms for vapor sorption“.

03/2013, Sorrent: Third International Conference on Multifunctional, Hybrid and Nanomaterials

A. Ranft, F. Hinterholzinger, F. Niekiel, J. Feckl, B. Rühle, N. Stock, T. Bein, B. Lotsch, „MOF-based photonic crystal sensors“.

07/2013, Lenggries: Nanosystems Initiative Munich Summer Retreat

A. Ranft, S. Betzler, F. Haase, B. Lotsch, „Additive-mediated size control of MOF nanoparticles“.

09/2013, Dresden: International Symposium on Metal-Organic Frameworks

A. Ranft, P. Davydovskaya, F. Niekiel, N. Stock, R. Pohle, B. Lotsch, „MOF-based sensing platforms“.

TABLE OF CONTENTS

1 INTRODUCTION	9
1.1 HIERARCHY AND EMERGENCE:	9
ORDER IN NATURE AND SYNTHETIC CHEMISTRY	9
1.1.1 Materials and Voids.....	9
1.1.2 Metal-Organic Frameworks.....	14
1.2 BIO-INSPIRATION:.....	19
FROM COLOR TO OPTICAL DEVICES	19
1.2.1 Color Generating Principles.....	19
1.2.2 Sensor Performance Parameters.....	25
1.3 OBJECTIVES OF THIS THESIS.....	29
1.4 REFERENCES	31
2 NOVEL STRATEGIES IN NANOSCALE MOF SYNTHESIS	37
SUMMARY.....	37
2.1 ADDITIVE-MEDIATED SIZE CONTROL OF MOF NANOPARTICLES	39
2.1.1 Introduction	39
2.1.2 Results and Discussion	41
2.1.3 Conclusions.....	47
2.1.4 References.....	48
3 INTERFERENCE-BASED READOUT OF SORPTION EVENTS IN MOF MULTILAYER SYSTEMS	53
SUMMARY.....	53
3.1 ONE-DIMENSIONAL METAL-ORGANIC FRAMEWORK PHOTONIC CRYSTALS USED AS PLATFORMS FOR VAPOR SORPTION	57
3.1.1 Introduction	58
3.1.2 Experimental.....	60
3.1.3 Characterization	63

3.1.4 Results and Discussion	63
3.1.5 Conclusions.....	70
3.1.6 References.....	71
3.2 TANDEM MOF-BASED PHOTONIC CRYSTALS FOR ENHANCED ANALYTE-SPECIFIC OPTICAL DETECTION	75
3.2.1 Introduction	76
3.2.2 Experimental Section.....	78
3.2.3 Results and Discussion	82
3.2.4 Conclusions.....	97
3.2.5 References.....	98
3.3 1D PHOTONIC DEFECT STRUCTURES BASED ON COLLOIDAL POROUS FRAMEWORKS: REVERSE PORE ENGINEERING AND VAPOR SORPTION	103
3.3.1 Introduction	104
3.3.2 Experimental Section.....	105
3.3.3 Results and Discussion	109
3.3.4 Conclusion.....	120
3.3.5 References.....	120
4 SUMMARY AND OUTLOOK.....	123
4.1 METAL-ORGANIC FRAMEWORKS AS OPTICAL SENSOR MATERIALS?	123
4.2 REFERENCES.....	129
5 APPENDIX.....	131
5.1 SUPPORTING INFORMATION FOR CHAPTER 2.1.....	133
5.2 SUPPORTING INFORMATION FOR CHAPTER 3.1.....	145
5.3 SUPPORTING INFORMATION FOR CHAPTER 3.2.....	155
5.4 SUPPORTING INFORMATION FOR CHAPTER 3.3.....	181
List of Publications	189
List of Presentations	192